

JAERI - M
93-241

JAERI TIARA ANNUAL REPORT
1992 (VOL. 2)
APRIL 1992 - MARCH 1993

December 1993

Department of Advanced Radiation Technology

日 本 原 子 力 研 究 所
Japan Atomic Energy Research Institute

JAERI-Mレポートは、日本原子力研究所が不定期に公刊している研究報告書です。
入手の間合わせは、日本原子力研究所技術情報部情報資料課（〒319-11茨城県那珂郡東海村）あて、お申しこしてください。なお、このほかに財団法人原子力弘済会資料センター（〒319-11茨城県那珂郡東海村日本原子力研究所内）で複写による実費頒布をおこなっております。

JAERI-M reports are issued irregularly.

Inquiries about availability of the reports should be addressed to Information Division
Department of Technical Information, Japan Atomic Energy Research Institute, Tokai-mura, Naka-gun, Ibaraki-ken 319-11, Japan.

©Japan Atomic Energy Research Institute, 1993

編集兼発行 日本原子力研究所
印刷 いばらき印刷(株)

JAERI TIARA Annual Report
1992 (Vol. 2)
April 1992 - March 1993

Department of Advanced Radiation Technology

Takasaki Radiation Chemistry Research Establishment
Japan Atomic Energy Research Institute
Watanuki-cho, Takasaki-shi, Gunma-ken

(Received November 22, 1993)

This annual report describes research activities which have been performed with the JAERI TIARA (Takasaki Ion Accelerators for Advanced Radiation Application) facilities from April 1, 1992 to March 31, 1993. Summary reports of 60 papers and brief descriptions on status of TIARA in the period are contained. A list of publications, the type of research collaborations and organization of TIARA are also given as appendices.

Keywords: JAERI TIARA, Ion Accelerators, Solid State Physics, Radiation Effects in Materials, Materials for Space, Semiconductors, Organic Materials, Inorganic Materials, Nuclear Fusion Reactor, Functional Materials, Radiation Chemistry, Radiation Biology, Nuclear Medicine, Biotechnology, Radioisotope Production, Nuclear Chemistry, Materials Analysis, Accelerator Technology, Safety Control

Editors: Isao Ishigaki, Ryuichi Tanaka, Isamu Nashiyama, Hiroshi Naramoto,
Hideki Omichi, Akio Toraishi, Hiromasa Watanabe, Hiroshi
Watanabe

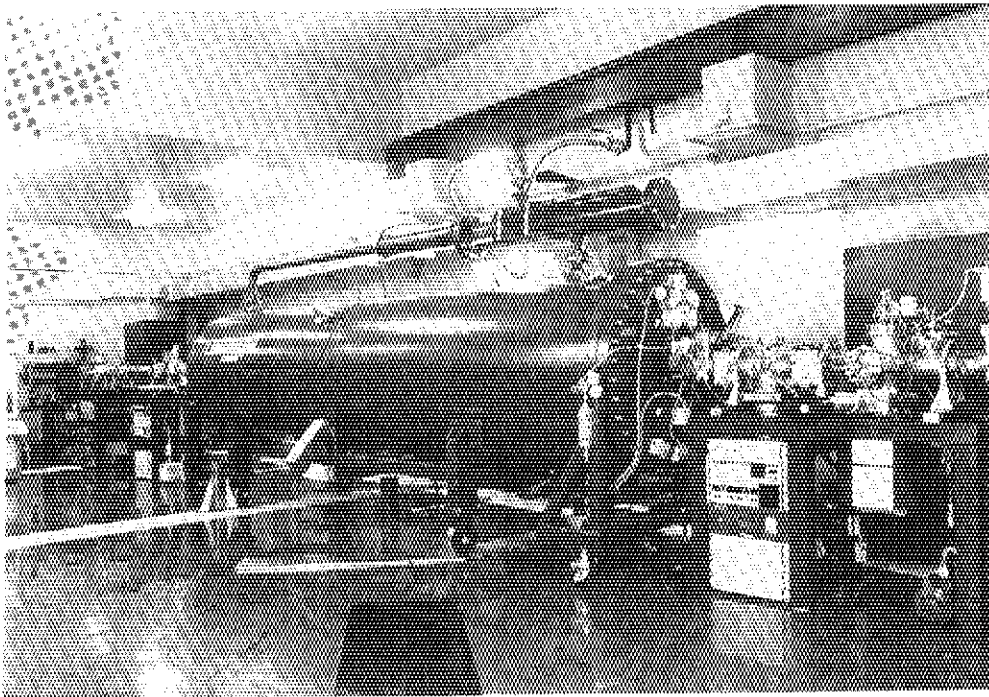
原研イオン照射研究施設平成4年度年次報告

日本原子力研究所高崎研究所
放射線高度利用推進室

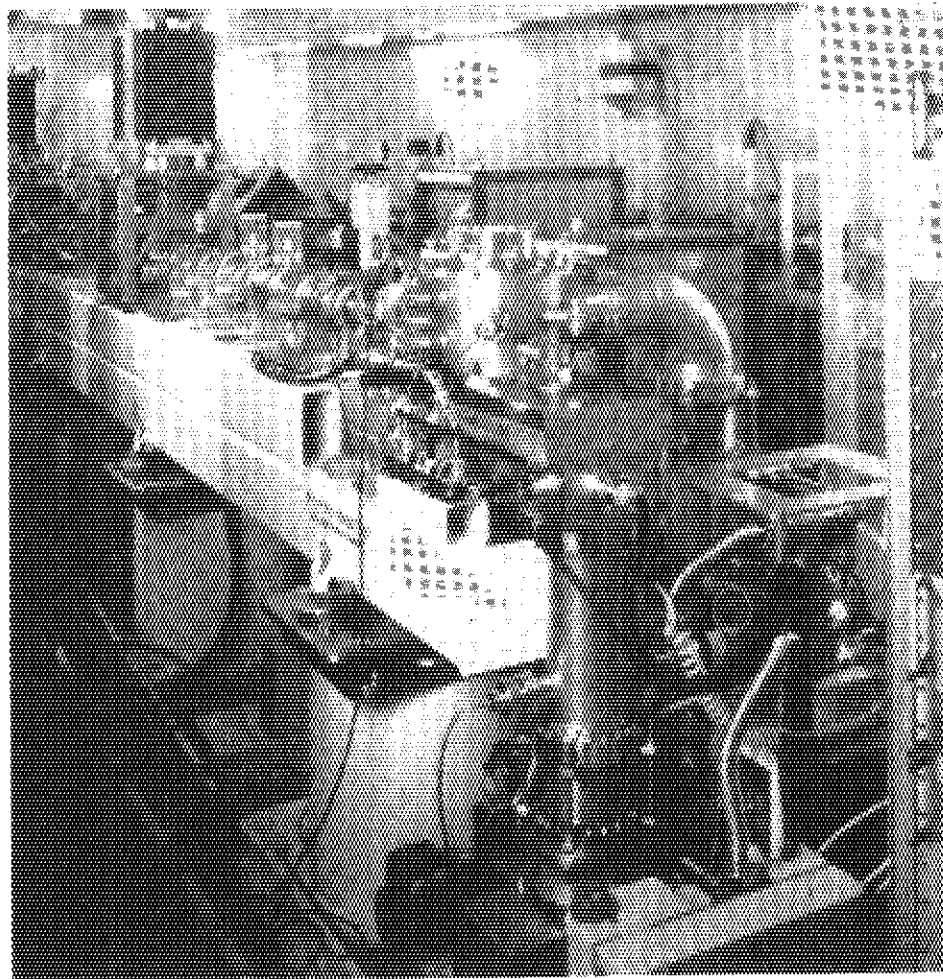
(1993年11月22日受理)

本年次報告は、原研イオン照射研究施設で、1992年4月1日から1993年3月31日までの間に行われた研究活動の概要をまとめたものである。

1) 宇宙用半導体, 2) バイオテクノロジー, 3) 放射線化学, 4) 有機材料, 5) 無機材料, 6) 材料解析, 7) 核化学およびラジオアイソトープ製造, 8) 加速器技術, 9) 施設建屋および安全システムの9部門にわたる60編の研究報告に加えて、施設の運転・利用状況、公表された文献、企業・大学等との研究協力関係、研究開発・施設運営組織を収録する。



3MV Tandem Accelerator



Microbeam Line (Target Room 1)


PREFACE

This report covers research and development activities which have been performed with the JAERI TIARA (Takasaki Ion Accelerators for Advanced Radiation Application) facilities during the period from April 1992 until March 1993, and also gives an outline of the operation and utilization of the TIARA in the same period.

The AVF cyclotron and the 3MV tandem accelerator which were completed in 1990, have been operated satisfactorily through the period, though the latter was stopped from January (until October 1993) because of the construction of a new beam line connected to a newly constructed target room. Other two accelerators, i.e. the 3MV sigle-ended accelerator and the 400kV ion implanter were under construction, they will start serving to research activities from January 1994.

The Second TIARA Research Review Meeting was held on June 30 and July 1 1993 in Tokyo, where many subjects in this issue were reported. 39 reports and an invited lecture were presented; 222 persons including 137 from outside of JAERI participated the meeting: All figures were much increased in compair with the first meeting and suggest the utilization of TIARA have started successfully to some extent. We owe this to advices of the Consultative Committee for the Research and Development of Advanced Radiation Technology, the Consultative Committee for the JAERI/Universities Collaborative Project Research Program, the TIARA General Program Committee, and their subcommittees.

I sincerely hope the utilization of TIARA will be more prosperous and successful in coming years.



Isao Ishigaki

Director

Department of Advanced

Radiation Technology,

Takasaki Radiation Chemistry

Research Establishment

Contents

1. Semiconductors for Space	1
1.1 Scattered-beam Irradiation Method for SEU Testing	3
1.2 Study on Local Control of the Electrical Resistivity by Ion Irradiation	7
1.3 Measurement of Transient Current Induced by Microbeams	9
1.4 A Study on Radiation Proof of Solar Cell for Space Application	13
1.5 Study of Single Event Upset Induced by Energetic Heavy Ions in a 256kbits SRAM for Space Application	17
1.6 Charge Distribution in a Small Sensitive Volume due to the Si(p,x) Nuclear Reactions	20
2. Biotechnology	25
2.1 Ion Beam Apparatus for Biological Samples(II)	27
2.2 Cellular Proteins of <u>Deinococcus radiodurans</u> R ₁ Irradiated by Ion Beams	31
2.3 DNA Double-strand Breaks and the Repair in Radioresistant Bacterium, <u>Deinococcus radiodurans</u> , Irradiated by Ion Beams .	34
2.4 Morphology of <u>Deinococcus radiodurans</u> Irradiated by Heavy Ion Beams	38
2.5 Repair of Transforming Capacity of Cells Irradiated with High-LET Ions in a Radiation Resistant Bacterium, <u>Deinococcus radiodurans</u>	42
2.6 Resistance to Heavy Ion Particles on Radioresistant Bacterium, <u>Deinococcus radiodurans</u> Dry Cells Packed in Gelatin	46
2.7 The Use of Pollen Irradiated with Helium Ion Beam for Interspecific Hybridization in <u>Nicotiana</u>	50
2.8 Studies on Induced Mutations by Ion Beam in Plants	54
2.9 Optical Spectra of Rabbit Red Blood Cells Irradiated with Heavy Ion Beams	57
2.10 Effect of Ion Beam Irradiation on Seed Germination and Growth of <u>Phalaenopsis</u>	59
2.11 Radiation Sensitivities of Protoplasts of Cabbage (<u>Brassica Oleracea</u>) Irradiated by Ion Beams or X-rays	61
3. Radiation Chemistry	63

3.1	Characteristics of Various Film Dosimeters for Ion Beams	65
3.2	Microdosimetry with Heavy Ions	69
3.3	The Study of Chemical Processes Induced by Heavy Ions	72
4.	Organic Materials	77
4.1	High Energy Ion Irradiation Effects on Polymers(I) Changes in Mechanical Properties Induced by 10 MeV Protons	79
4.2	Uniformity of Beam Fluence Distribution Obtained by the Multiple Coulomb Scattering Using Thin Metal Foils	83
4.3	Irradiation Effects on Mechanical Properties of CFRP for Spacecraft	87
5.	Inorganic Materials	91
5.1	Metastable Phase Formation by Ion Implantation	93
5.2	Irradiation Effects on Electrical Resistivity of Ceramic Materials	96
5.3	Effects of Helium on Microstructures and Mechanical Properties of Stainless Steels	98
5.4	Electrical Properties of Ion-beam-irradiated Semi-insulating GaAs	101
5.5	High Energy Ni Ion Implantation and Thermal Annealing for α -SiC Single Crystal	105
5.6	PKA Energy Spectrum Dependence of Defect Cluster Formation in Gold by High Energy Self-ion Irradiation	109
5.7	Molybdenum Silicide Formation by Means of Ion Mixing	113
6.	Materials Analysis	117
6.1	Ion Beam Analysis on Sapphire Implanted with Vanadium Ions ..	119
6.2	Light Elements Analysis in Thin Films by RBS	123
6.3	High-energy Shadowing Effect Studied with Ion-induced Secondary Electron Spectroscopy	126
6.4	Application of Heavy Ions to Rutherford Backscattering	130
6.5	Optical Measurement System for Study of Electron-hole Pairs Induced in Semiconductors by High-energy Ion Irradiation	134
6.6	Positron Annihilation Study of Defects in Si: An Internal Source Method	138
6.7	Time-resolved X-ray Absorption Spectroscopy of Laser Ablated Silicon and Carbon Particles	143
6.8	In-situ Measurement of Secondary Ions During Hydrocarbon Ion Beam Deposition	145

6.9	XPS Studies on the Charge States of Cr and Cu Atoms Implanted into α -Al ₂ O ₃ and MgO Single Crystals	149
6.10	In-situ Observation of Effect of Hydrogen and Helium Dual-ion Irradiation in Aluminum	153
7.	Nuclear Chemistry and Radioisotope Production	157
7.1	Study of Unstable Nuclei Using the TIARA-ISOL	159
7.2	Production of Radioisotopes with Ion Beam: ¹³⁹ Ce	161
8.	Accelerator Technology	165
8.1	Heavy Ion Microbeam Apparatus for Single Event Upset Analysis	167
8.2	Accelerator Shielding Experiments with Monoenergetic Several Tens MeV Neutrons	171
8.3	Development of Visual Beam Adjustment Method for Cyclotron .	175
8.4	Design of JAERI 18GHz ECR Ion Source	179
8.5	Present Status and Beam Acceleration Tests on Cyclotron	183
8.6	Generation of Isochronous Fields	187
8.7	Electric Fields of Deflector	189
8.8	Orbit Calculation in the Central Region	192
8.9	Status of Ion Sources	194
8.10	Development of Beam Attenuator	196
8.11	Development of Parallel Plate Avalanche Counter for Fluence-rate Measurement	198
8.12	Performance and Some Operation Results of the Vacuum System for the Cyclotron	200
8.13	Radiation Resistance of Electronic Controller	204
8.14	Some Trials for Effective Operation of Negative Ion Sources for Tandem Accelerator	207
9.	Buildings and Safety Systems in TIARA Facilities	209
9.1	Design and Construction of TIARA Facilities	211
9.2	Radiation Monitoring System in TIARA Facility	221
9.3	Safety Interlock and Display Systems for Cyclotron Facility .	227
9.4	Personal Access Control System in TIARA	232
10.	Status of TIARA 1992	235
10.1	Utilization of TIARA Facilities	237
10.2	AVF Cyclotron	240
10.3	Status of 3MV Tandem Accelerator and Second-phase Accelerators Construction	242
10.4	Radiation and Radioactive Waste Controls in TIARA	244

Appendix	251
Appendix 1 List of Publications	253
Appendix 2 Type of Research Collaborations	259
Appendix 3 Organization and Personnel of TIARA	260

1. Semiconductors for Space

1.1	Scattered-beam Irradiation Method for SEU Testing	
	I.Nashiyama, Y.Morita, T.Hirao, H.Itoh and M.Yoshikawa	3
1.2	Study on Local Control of the Electrical Resistivity by Ion Irradiation	
	H.Akiyama, I.Takata, M.Yoshikawa and Y.Morita	7
1.3	Measurement of Transient Current Induced by Microbeams	
	T.Hirao, T.Nisijima, T.Kamiya, H.Yutoh, H.Itoh and I.Nashiyama..	9
1.4	A Study on Radiation Proof of Solar Cell for Space Application	
	S.Matsuda, Y.Yamamoto, M.Uesugi, Y.Morita and I.Nashiyama	13
1.5	Study of Single Event Upset Induced by Energetic Heavy Ions in a 256kbits SRAM for Space Application	
	S.Matsuda, T.Tamura, S.Kuboyama, I.Naito, H.Itoh, T.Hirao and I.Nashiyama	17
1.6	Charge Distribution in a Small Sensitive Volume due to the Si(p,x) Nuclear Reactions	
	Y.Takami, Y.Morita, I.Nashiyama, T.Tamura, Y.Shimano and M.Uesugi	20

1 . 1 SCATTERED-BEAM IRRADIATION METHOD FOR SEU TESTING

Isamu NASHIYAMA, Yousuke MORITA, Toshio HIRAO,
Hisayoshi ITOH, Masahito YOSHIKAWA

Department of Materials Development, JAERI

I. INTRODUCTION

Integrated circuits (ICs) destined for space applications will be exposed to several types of solar and galactic radiation. Random bombardment of the circuit by ionizing particles of very high-energy cosmic rays provokes the so called single events. Single events can lead to frustrating errors in electronic systems which may cause anything from annoying system responses to catastrophic system failures. The issue becomes even more important as smaller, denser, and more powerful integrated systems are placed in space applications. Therefore, evaluation of the single-event upset (SEU) tolerance of these modern ICs is strongly required for predicting the error probability caused by cosmic ray irradiation.

This report describes an outline of the scattered-beam irradiation method necessary for testing SEUs in memory ICs using the energetic heavy-ion irradiation facility at JAERI Takasaki.

II. CRITICAL LET AND UPSET CROSS-SECTION

In an idealized measurement of upsets in a memory IC, an incident heavy-ion has no effect on the errors (upsets) until its LET reaches a critical value. At that point, the particle causes enough charge to be collected to upset a memory cell. So far as all the cells are identical and the beam fluence is sufficiently high, the number of upsets increases abruptly at the critical LET from zero to the total number of memory cells. If the beam fluence is lower than the "one-hit-each-cell" value, not all cells will be struck by the beam. To account for the cells not exercised by the beam, the beam fluence is usually normalized out of the measured upsets : $\sigma = N/F$, where N is the total number of upsets observed, and F (particles /cm²) is the beam fluence. This parameter has units of area (cm²) and is called the upset cross-section for the circuit. In most cases, the saturated cross-section corresponds to the SEU sensitive area of the device, and is often used as such in the error-rate prediction codes.

Experimental evaluation of the critical LET and the saturated SEU cross-section is the purpose of the SEU testing of memory ICs, where we measure how the number of upsets per fluence varies with varying the LET value, and an upset cross-section is expressed as a function of LET. Appropriate beam intensity and beam homogeneity are mandatory for correct evaluation of the critical LET and the saturated SEU cross-section.

III. SCATTERED-BEAM IRRADIATION METHOD

The scattered-beam irradiation method, which is illustrated in Fig. 1, is convenient to provide low intensity and homogeneous ion beams. The energetic heavy ions from JAERI AVF cyclotron are scattered forward with a thin ($\sim 1\mu\text{m}$) gold foil and scattered ions are irradiated on the test devices placed at angles of 20 to 40 degrees. One can calculate the scattered ion intensity and homogeneity using Rutherford scattering formula.

Advantages of the scattered-beam irradiation method are, 1) beam intensity can be reduced by a several order of magnitude to a level convenient for SEU testing, 2) homogeneous irradiation fluence within the chip area of the device under test, 3) accurate evaluation of the fluence. Figure 2 shows ion-beam species, energies, ranges, and LETs which can be applicable to SEU testing.

One of the disadvantage of the scattered-beam irradiation method is that atoms recoiled from the scatter strike the specimen as well as scattered ions. These recoiled atoms cause SEUs, since their atomic number and therefore their LET value are higher than those of the scattered ions. In order to eliminate the recoiled atoms, a thin aluminum or Kapton absorber is placed in front of the device under test. Figure 3 shows how an aluminum absorber works, where 175 MeV Ar ions are scattered with $0.02\mu\text{m}$ thick Au target, and energies of the particles going out from the target are measured with a silicon surface barrier detector. The peak at 911 channel corresponds to 159 MeV scattered Ar ions and the small peak at 264 channel corresponds to recoiled Au atoms. With $12.5\mu\text{m}$ thick aluminum absorber, however, this recoiled Au peak disappears, indicating that the recoiled atoms stop in the absorber. The scattered Ar ions degrade their energy by about 52 keV and their energy purity becomes poor due to the straggling and the non-uniform thickness of the aluminum absorber. However, the LET value does not spread much since the LET is not a strong function of the particle energy. The LET values and ranges are tabulated in Table I for SEU testing.

IV. SEU TESTING USING VERY HIGH ENERGY HEAVY-IONS

In the case of very high energy heavy-ions of $E/M > 10\text{ MeV/amu}$, a strong nuclear reaction occurs between incident ions and the Au scatterer, and various unidentified reaction products hit the device under test. Therefore, the scattered-beam irradiation method based on Rutherford scattering principle is not applicable any more. A direct-beam irradiation method is applied instead, where the beam intensity is reduced by a beam attenuator installed between the ion source and the cyclotron, and the beam is defocused in order to obtain uniformity of irradiation fluence.

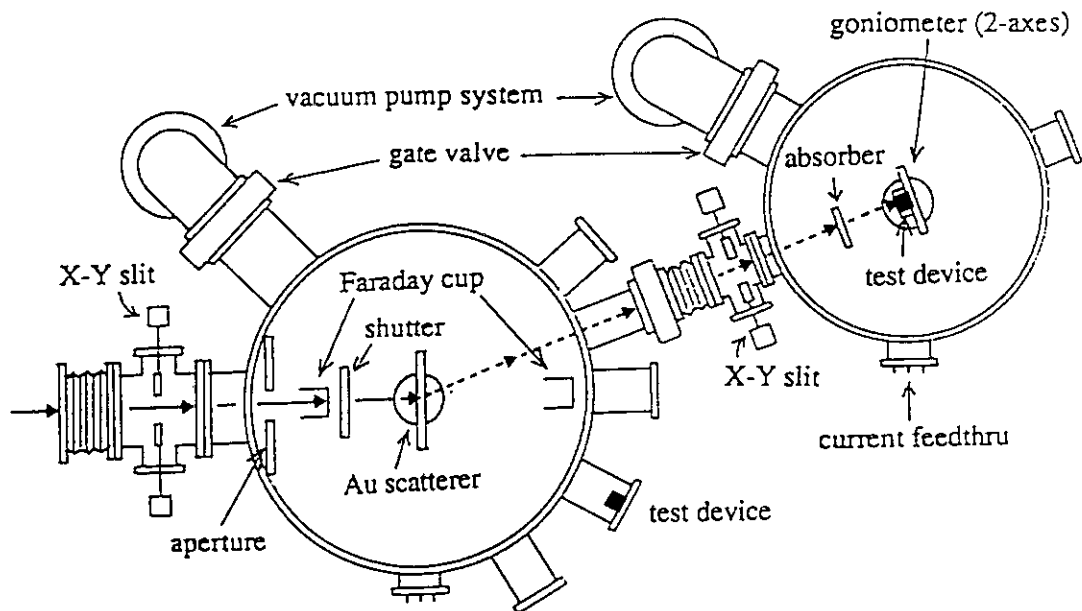


Fig. 1 Scattered-beam irradiation method for SEU testing.

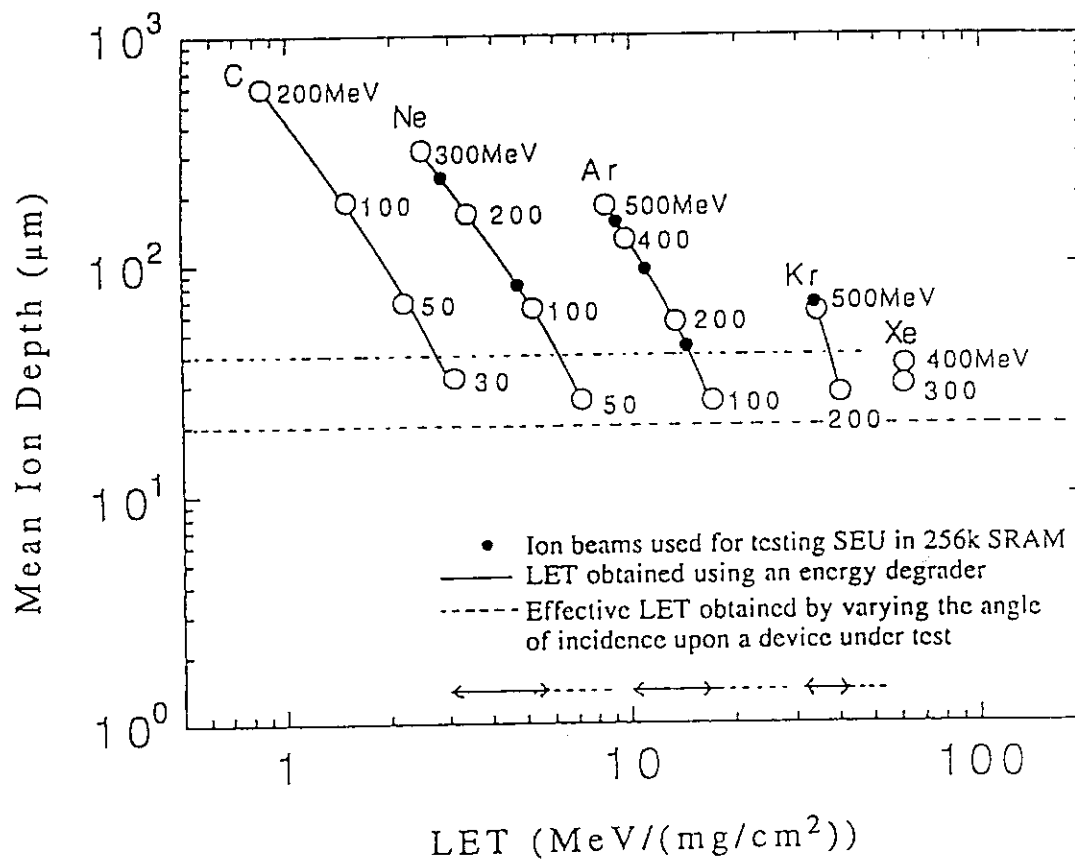


Fig. 2 LETs and ranges of energetic heavy-ions in silicon applicable to SEU testing.

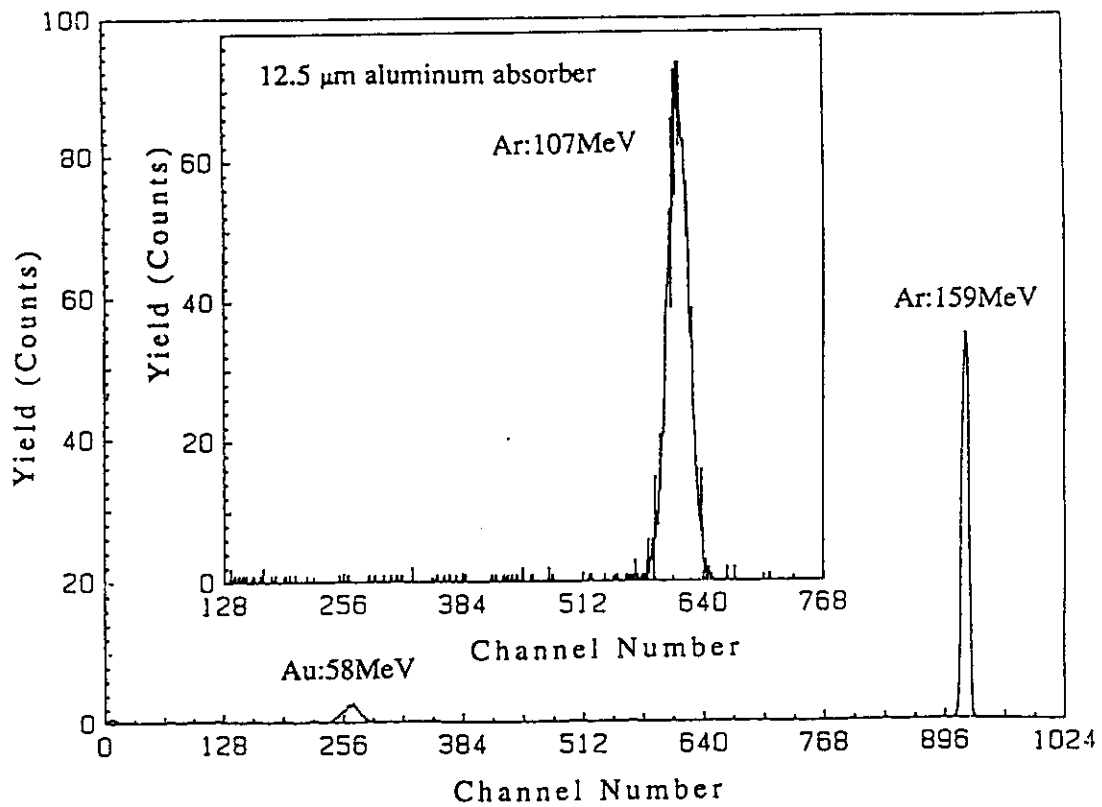


Fig. 3 Energy spectra of scattered Ar and recoiled Au atoms at an angle of 140 degree. The 175 MeV Ar-ion incidence upon 0.02 μ m thick Au scatterer.

Table I. LETs and Ranges of scattered and recoiled particles at 140 degree for SEU testing.

Beam	Incident ion energy (MeV)	Target (μ m)	without absorber		through 25 μ m Kapton absorber			
			Scattered ion energy (MeV)	Recoiled atom energy (MeV)	Scattered ion energy (MeV)	Recoiled atom energy (MeV)	LET (MeV cm^2/mg)	Range (μ m)
Ar	460	Au(1.0)	425 - 427	138 - 189	318 - 321	0	11.1 - 11.2	92.9 - 93.4
Ar	330	Au(1.0)	300 - 303	92 - 135	202 - 208	0	13.6 - 13.8	52.0 - 54.1
Ar	195	Au(1.0)	170 - 173	46 - 77	57 - 65	0	19.1 - 19.5	14.2 - 16.0
Ar	175	Au(1.0)	151 - 154	40 - 68	22 - 33	0	19.1 - 19.9	6.8 - 9.2
Ne	260	Au(1.0)	250	35 - 65	216 - 217	0	3.2 - 3.2	186 - 187
Ne	120	Au(1.0)	112 - 113	13 - 29	73 - 75	0	6.1 - 6.2	39.6 - 41.1
Kr	520	Au(1.0)	424 - 434	256 - 306	121 - 145	0	41.7 - 42.4	17.9 - 20.4
Kr	520	Ni(1.0)	-----	271 - 281	0	83 - 99	32.5 - 32.6	14.9 - 17.0

1.2 STUDY ON LOCAL CONTROL OF THE ELECTRICAL RESISTIVITY BY ION IRRADIATION

Hajime AKIYAMA, Ikunori TAKATA
Masato YOSHIKAWA*, Yousuke MORITA*

MITSUBISHI Electric Co. Ltd.
*JAERI, Takasaki

1. Introduction

High energy ion irradiations in silicon power devices, such as power thyristors, were studied for developing these devices into more high frequency and low power loss drive. Deep level defects in the band gap of silicon introduced by ionizing radiation or charged particles act as recombination centers of electrons and holes to reduce a lifetime of carriers in the semiconductor, and so these defects are useful to control the lifetime of carriers in the devices. Especially, when ion irradiation technique is used to this application, it is possible to obtain the best performance of their lifetime control for high speed drive on the devices, because localized defects around the mean ion depth in silicon are introduced, and control the lifetime of carriers around the narrow specified area of the devices¹⁾.

The aims of the study are following: (1) development on technique of uniform ion irradiation in large area (100mmx100mm), and on measurement of ion currents(nA-uA) under the large area irradiation of the wafers and the devices. (2) study of the relationship between induced defects and changes of electrical characteristics of silicon. (3) determination of the relationship between ion irradiation conditions and electrical characteristics(high frequency and low power loss) of the devices.

2. Experiments and Results

The silicon wafers(n-type, 0.5 ohm-cm) and p+n-diodes were irradiated by H^+ (10 MeV and 20 MeV) and He^{2+} (20 MeV) ions using AVF cyclotron at Takasaki, JAERI. The intensity profile of scanning beam(H^+ , 20 MeV) on irradiated area of 100mmx100mm is shown in Figure 1 using dosimeter of cellulose triacetate film(CTA film). In the intensity profile of scanning beam, the dose uniformity is within 5% except its central part(ca. 10% higher than that in other area). From the scanning profile, uniform irradiation of high energy ions in the wafers and devices of large area is capable of using AVF cyclotron at Takasaki.

Figure 2 shows the depth profile of electrical resistivity of silicon wafer irradiated by H^+ (10 MeV) through aluminum absorber (thickness: 525um). The resistivity profile shows a peak at 185um depth with a width of 60um, of which location is around the mean ion depth in silicon, and the peak height of the resistivity increases with increasing ion fluencies. Around the location in which the peak of the resistivity exist, the lifetime of carriers in the devices would be controlled. Figure 3 shows ICTS(Isothermal Capacitance Transient Spectroscopy) spectrums of p+n-diode irradiated by 10 MeV H^+ ion. The spectrums indicate increasing capacitance(defects) with increasing ion fluencies especially at a fluence of 5.0×10^{12} p/cm², and different increas-

ing rate of each capacitance peak related with each species of the defects induced by ion irradiation.

In further experiments, we interest in the irradiation of the devices in the ion fluence range of $10^{10} - 10^{12}$ p/cm², comparing with those in the low fluence of $10^8 - 10^{10}$ p/cm²).

References

- 1) H. Akiyama et al., Denkigakkai-kenkyukai SPC-89-49 (1989) p.7.
- 2) A. Hallen et al., J. Appl. Phys. 67(3) (1990) p.1266

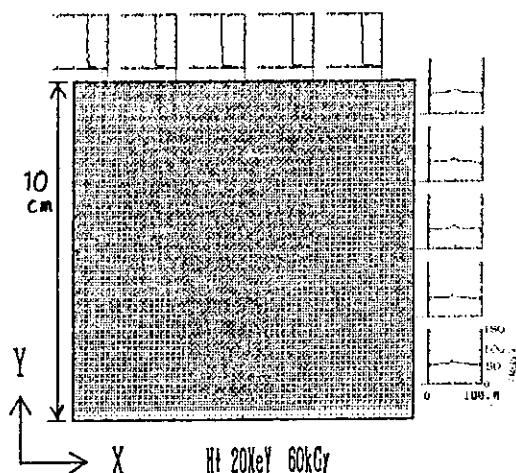


Fig. 1 Intensity profile of scanning beam on CTA
Beam: H⁺, 20 MeV,
Scan X; 50Hz, Y; 0.5Hz.
CTA Dosimeter: 60kGy,
100x100mm

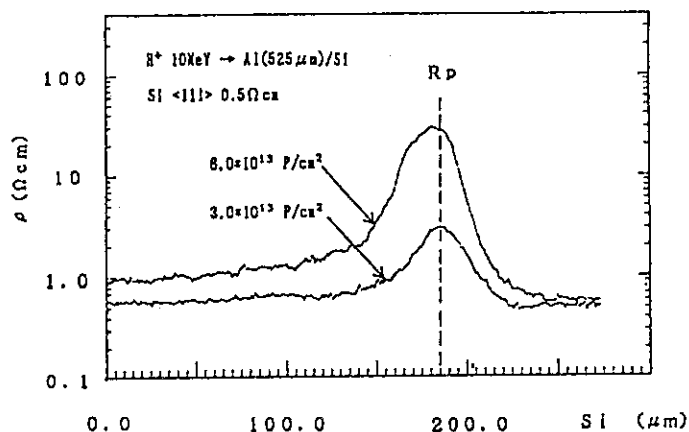


Fig. 2 Depth profile of electrical resistivity in silicon wafer
Beam: H⁺, 10 MeV
Al absorber: 525 μm
Si wafer: Si<111>, 0.5 ohm-cm

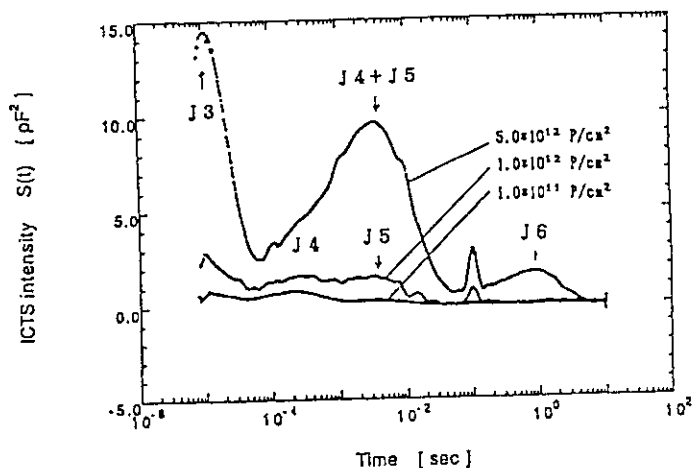


Fig. 3 ICTS spectrum of irradiated p⁺n-diode
Beam: H⁺, 10 MeV

1 . 3 MEASUREMENT OF TRANSIENT CURRENT INDUCED BY MICROBEAMS

Toshio HIRAO, Toshiji NISIJIMA*, Tommihiro KAMIYA, Hidenori YUTOH, Hisayosi ITOH, and Isamu NASHIYAMA

Department of Materials Development, JAERI

*Electrotechnical Laboratory

1. INTRODUCTION

Single-event upset (SEU) is triggered when an amount of electric charges induced by energetic ion incidence exceeds a value known as a critical charge in a very short time period. Therefore, accurate evaluation of electric charges and understanding of basic mechanisms of SEU are necessary for the improvement of SEU tolerance of electronic devices. Several attempts have been made for the direct measurements of extremely fast transient currents induced by single ion strikes on a p/n junctions, and charge collection mechanisms such as drift, funneling, and diffusion effects have been studied (1, 2, 3, 4).

In the present work, we apply microbeams of 15MeV-carbon, -silicon, -oxygen and -iron, and 6MeV-helium ions in order to measure picosecond current transients in a p⁺/n junction diode under various bias conditions. Total collected charges are evaluated from the current transients. We have obtained detailed information about the charge collection mechanism of SEU.

2. EXPERIMENTS

In order to attain an incident-ion positioning accuracy better than 1μm for current transient measurements, ion microbeams of about 1μm in diameter were provided using a high-energy ion microprobe system connected to the 3MV tandem accelerator at JAERI Takasaki (5, 6, 7, 8).

The experimental setup is schematically shown in Fig.1. Transient currents were measured using the microbeams of 6 MeV He-ion, and 15 MeV C-, O-, Si-, and Iron-ions under reverse bias conditions from 5V to 15V.

The test samples used in the present experiments were low-capacitance silicon p⁺/n junction diodes with substrate doping level from $2 \times 10^{15} \text{cm}^{-3}$ and with junction area of 50 μm in diameter as shown in Fig.2. The sample diode was mounted on a chip carrier with a 50 Ω double-ended microstripline(9).

Transient currents were measured using wide-band coaxial cables of 50 Ω impedance and a 40 GHz wide-band sampling oscilloscope (Textronix model CSA803).

3. RESULTS AND DISCUSSION

Some typical current transients obtained are shown in Fig. 3 for 6 MeV helium and 15 MeV heavy-ion incidence on a p/n SEU diode at -15 V bias. The peak height of the transient current increases with increasing the linear energy transfer LET of the incident ion. The curve for iron shows significantly fast decay compared with the other curves, which is explained by the fact that the penetration depth of 15 MeV Fe-ion in silicon is less than the depletion layer thickness, and therefore the transient current consists of only prompt drift component which terminates within a relatively short period of time.

The decay time varies with doping levels of the substrates as shown in Fig. 4, where the decay times of the prompt decaying portion are 434 ps and 137 ps for doping levels at $2 \times 10^{15} \text{cm}^{-3}$ and at $7 \times 10^{15} \text{cm}^{-3}$, respectively. Similar tendency was observed for all ion species and bias voltages, suggesting that prompt decaying portion is related to the charges collected by a strong electric field.

The whole current waveform is explained by the superposition of the prompt (drift and funneling) component and the delayed component with a nanosecond decay time. The drift current is due to charges collected from the inside of the depletion layer of the p/n junction diode. The funneling current is due to charges collected beyond the depletion layer from the electron-hole plasma column created along the trajectory of incident ions. The delayed component is due to diffusion of the excess minority carriers induced outside around the plasma column.

An amount of charges, QL, collected from the depletion layer is theoretically derived by the following equation,

$$QL = q \cdot \text{LET} \cdot \rho(\text{Si}) \cdot L / W = \text{LET} \cdot \rho(\text{Si}) \cdot L / 22.5 \text{ (pC)}$$

where, q is unit charge, LET linear energy transfer in $\text{MeV}/(\text{mg}/\text{cm}^2)$, $\rho(\text{Si})$ the density of silicon in g/cm^3 , L the depletion layer thickness, and W the energy necessary for creating one electron-hole pair in silicon.

Total charges collected are plotted in Fig. 5, as a function of bias voltage for p/n diode bombarded with 6 MeV He-ion, 15 MeV C-ion, and 15 MeV O-ion. It is found that collected charge increases with increasing the bias voltage and LET.

4. CONCLUSIONS

By applying high energy helium-and heavy-ion microbeams and a wide bandwidth digitizing sampling technique, we successfully measured SEU current transients. We measured prompt decay times and total collected charges of the transients, and found that both of them increase with increasing LET.

ACKNOWLEDGMENTS

The authors would like to acknowledge Mr.Suzuki for his assistance in setting up the experiments and Mr.Tajima who spent many long hours operating the accelerator for us.

REFERENCE

- 1) Ronald S.Wagner et al., IEEE Trans.Nucl.Sci.Vol.NS-34, No6(1987)1240
- 2) Ronald S.Wagner et al., IEEE Trans.Nucl.Sci.Vol.NS-35, No6(1988)1578
- 3) Toshiji Nisijima et al.Proc.of the Int.Workshop on Radiation Effects of Semiconductor Device for Space Application , Takasaki, Japan(1992)138.
- 4) Toshio Hirao et al. Proc. of the Int.workshop on Radiation Effects of Semiconductor Device for Space Application, Takasaki, Japan (1992) 142.
- 5) Toshio Hirao et al. TIARA Annual Report.Vol.1, (1992)100.
- 6) Tomihiro Kamiya et al.Proc.of the Int.Workshop on Radiation Effects of Semiconductor Device for Space Application, Takasaki, Japan(1992)112.
- 7) Tomihiro Kamiya et al.Proc.of the First Meeting on the ION Engineering Society of Japan(1992)105.
- 8) Tomihiro Kamiya et al.TIARA Annual Report.Vol.1, (1992)88
- 9) H.R.Kaupp, IEEE Trans.Elec.COM., 185(1967)4.

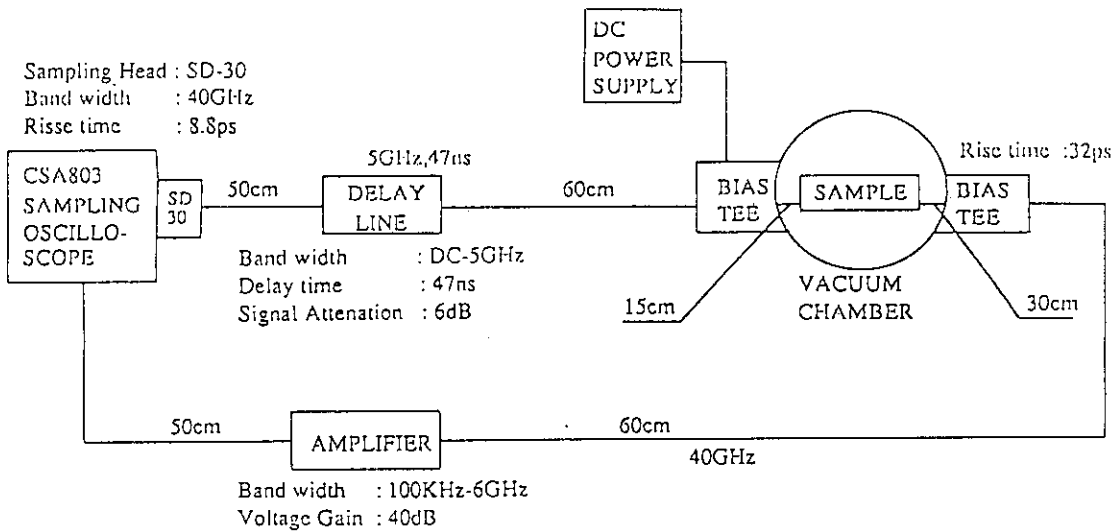


Figure 1. Block diagram of the electronic system for transient current measurements.

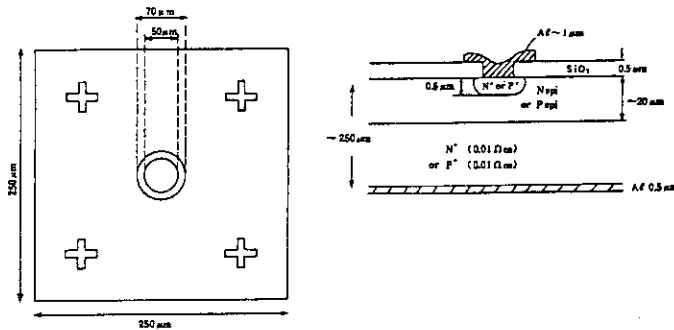


Fig.2 Schematics of silicon p/n junction diode for SEU experiments

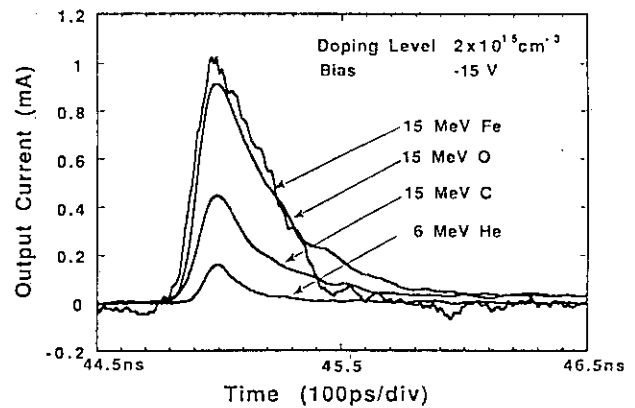


Fig.3 Current transients induced by the incidence of energetic ions on a p/n junction diode at -15V bias

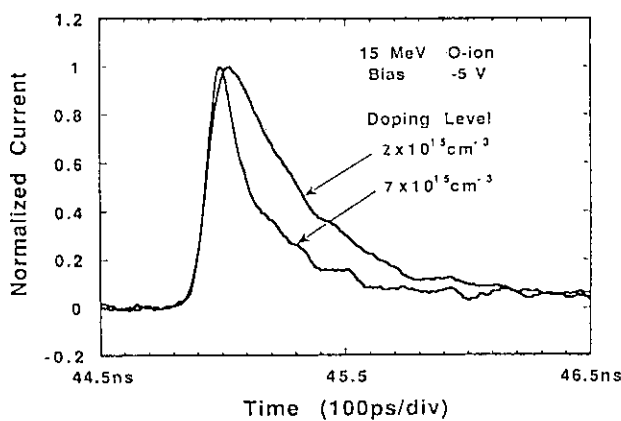


Fig.4 Normalized transient current for p/n junction diodes with different doping levels substrates

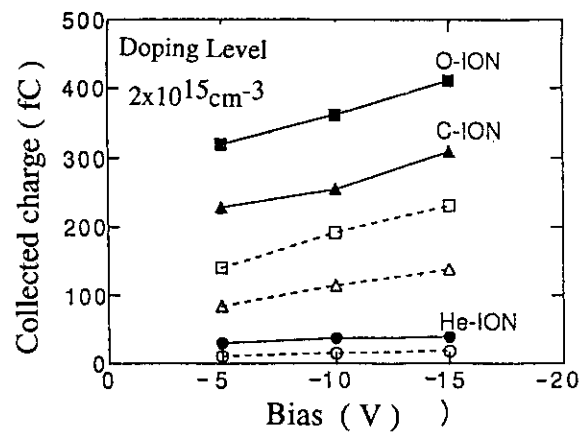


Fig.5 Relationship between collected charge and bias voltage, showing experimental values with solid and thoretical values with dashed lines

1.4 A Study on Radiation Proof of Solar Cell for Space Application

Sumio MATUDA*, Yasunari YAMAMOTO*, Masato UESUGI*
Yousuke MORITA**, Isamu NASHIYAMA**

*National Space Development Agency of Japan, **Japan Atomic Energy Research Institute

I. Introduction

Space radiation trapped by the Earth's magnetic fields can have serious effect on artificial satellites. This radiation belts called Van Allen belts have double structured fields surrounding the Earth. The inner zone of the Van Allen belts has altitude of 2,000-5,000km on the equator and the outer zone extends over 10,000-20,000km.

In addition to the trapped radiation, the galactic cosmic rays and solar radiation induced by solar activity can also have effects on artificial satellites.

Artificial satellites on low earth orbit of around 870km height are exposed in electrons(>0.1MeV) of annually approximate fluence of 1.6×10^{13} e/cm² (5.1×10^5 e/cm²·s) and in protons(>2MeV) of approximate fluence of 9.5×10^9 p/cm² (3.0×10^2 p/cm²·s).

An earth pointing satellites on geostationary orbit of about 36,000km height are exposed annually in electrons of 6.6×10^{14} e/cm² (2.1×10^7 e/cm²·s) and in proton of 1×10^6 p/cm²·s maximum during 30-50 minutes on each solar flare event.

Therefore, It is very important to evaluate radiation damage of the Solar Cell on satellites.

II. Abstract

To evaluate the radiation proof, irradiation tests of electron and proton to solar cell were performed and degradation of electrical characteristics (short circuit current, open circuit voltage, maximum power) were measured before and after irradiation using the solar simulator. The evaluation method was to clarify normalized electrical characteristics against fluence. Normalized electrical characteristic is a ratio of post irradiation electrical characteristics for pre-irradiation electrical characteristics. From that result, degradation comparison of electron and proton was done.

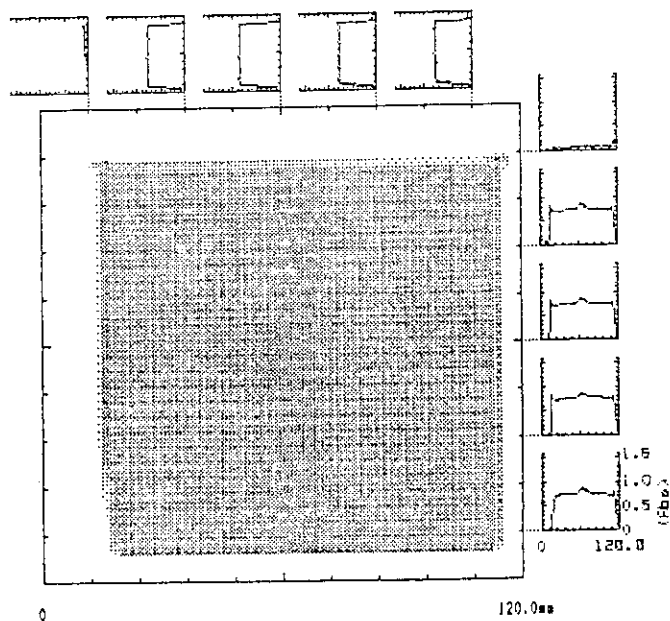


Fig.1 Uniformity of dose

III Samples and irradiation method

The samples used for the test are Si (silicon) and GaAs (gallium arsenide) solar cells. The Si solar cells were $2\text{cm} \times 2\text{cm} \times 100\text{ }\mu\text{m}$ in size with a BSFR(back surface field & reflector) structure, and GaAs solar cells were $2\text{cm} \times 2\text{cm} \times 200\text{ }\mu\text{m}$ in size, and both are without cover glass. Si solar cells are intended for ADEOS (Advanced Earth Observing Satellite) to be launched in 1995, and GaAs solar cells for COMETS (Communications and broadcasting engineering test satellite) to be launched in 1996.

The irradiation method is to utilize scan beam because of the largeness of irradiation area ($10 \times 10\text{cm}$). Using this method, 6-12 cells can be irradiated simultaneously.

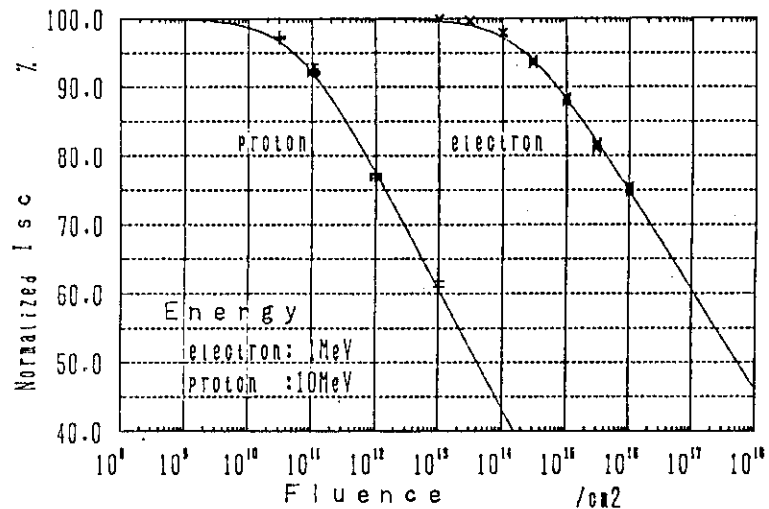


Fig.2 Calculation of degradation curve against each radiation (Si-100 Bare)

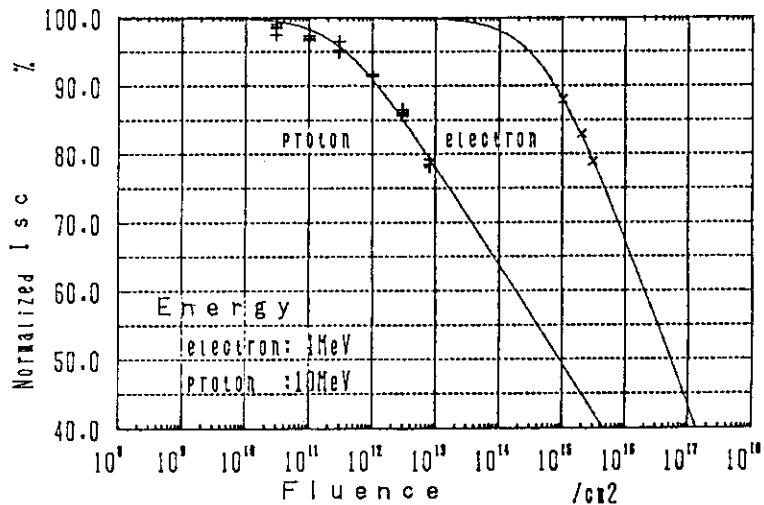


Fig.3 Calculation of degradation curve against each radiation (GaAs-200 Bare)

Table 1 Calculation of fitting parameter

	Si-100 Bare			
	electron		proton	
	C	$\phi\chi$	C	$\phi\chi$
short circuit current(Isc)	1.44E-01	1.83E+14	1.72E-01	5.13E+10
open circuit voltage(Voc)	7.36E-02	1.07E+13	8.76E-02	8.30E+09
maximum power(Pmax)	1.76E-01	3.52E+13	2.05E-01	1.24E+10

	GaAs-200 Bare			
	electron		proton	
	C	$\phi\chi$	C	$\phi\chi$
short circuit current(Isc)	2.43E-01	4.80E+14	1.44E-01	3.04E+11
open circuit voltage(Voc)	7.55E-02	1.31E+14	1.22E-01	3.93E+11
maximum power(Pmax)	2.69E-01	2.28E+14	2.11E-01	9.91E+10

Fig.1 shows the uniformity of dose measured with CTA (cellulose tridentate) film dosimeter.

It has a center area which is higher than the rest by 10%, but the other area is uniform within $\pm 3\%$.

IV Measurement

Results

When radiation is irradiated to a solar cell, electrical characteristics are degraded according to the kind of radiation energy and fluence.

The evaluation of lessening by fluence is done here. Normalized electrical characteristics and fluence are written by the eq.1.

$$\eta = 1 - C \times \log(1 + \phi / \phi_x) \quad 1)$$

η : normalized electrical characteristics
 ϕ : fluence
 C, ϕ_x : fitting parameters

Fig.2 and 3 show the fluence dependency of normalized I_{sc} (short circuit current) by electron and proton. The horizontal axis is fluence of radiation, the vertical axis is the normalized I_{sc} . Energy of electron is 1MeV and that of proton is 10MeV.

Table 1 shows the fitting parameters(C, ϕ_x) derived from approximation of the measurement results and least square of the eq.1. Fitting parameters of electron(1MeV) are listed as well for reference.

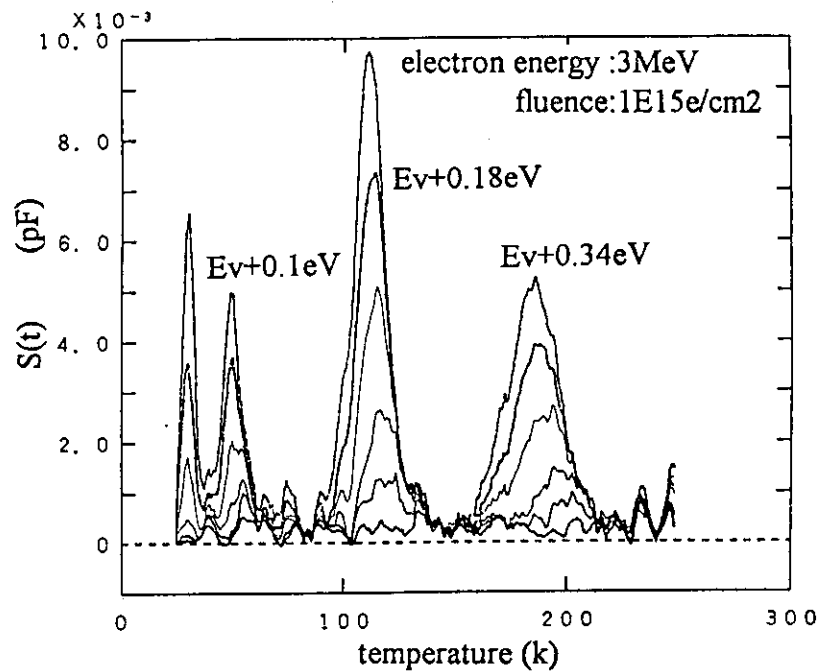


Fig.4 Measurement of deep level of Si cell irradiated electron

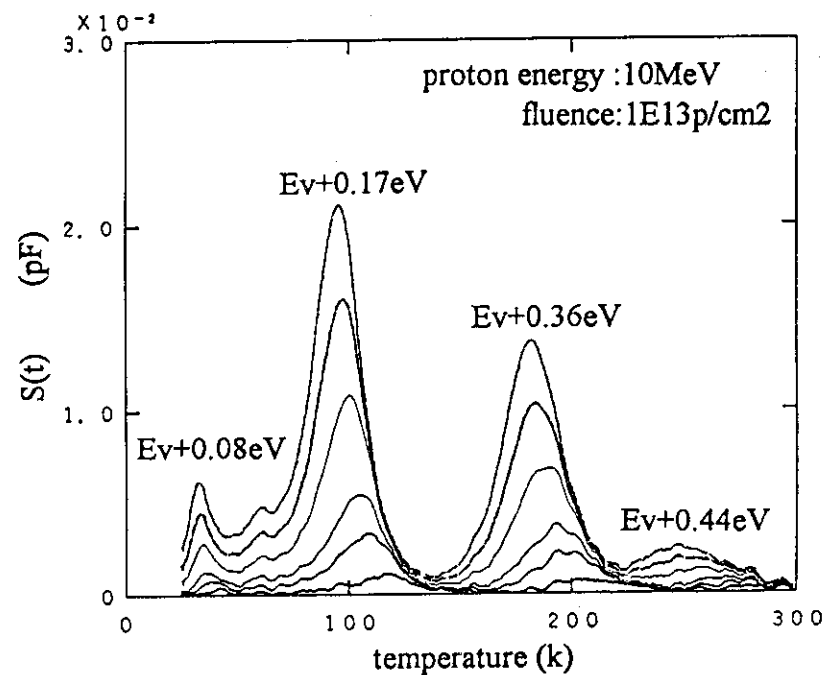


Fig.5 Measurement of deep level of Si cell irradiated proton

The designed life time of ADEOS/COMETS are 3years, total proton dose is considered to be about 3×10^{10} p/cm². Electrical characteristics for example I_{sc} are known to be sustained over 97% as shown Fig.2 and 3.

The evaluation result indicates that, for fluence giving the same normalized I_{sc} , electron(1MeV) : proton(10MeV)=6000 : 1(case of ratio 80%) GaAs solar cell has the same result of electron : proton=400 : 1(case of ratio 80%).

Furthermore, to research the cause of degradation of electrical characteristics, crystalline defects derived by proton are measured by DLTS(deep level transient spectroscopy) method. Fig.4 and 5 show the measurement results of deep level.

V. Conclusion

For both Si and GaAs, the evaluations of proton proof were done with the sample without cover glass. These solar cells were confirmed to be applicable to their own ADEOS/COMETS satellites. However, artificial satellites actually carry solar cell with cover glass. Therefore, proton beam tests of solar cell with cover glass will be done in near future. The effect of cover glass, in addition, can be evaluated by comparing the results.

VI. Future Plan

In order to predict the degradation to solar cell in real space radiation environment the evaluation of effect by proton with low energy(0.1-3MeV) will be performed, Also proton with high energy(20-100MeV) will be performed.

Moreover, a new type of Si solar cell under development will be examined in susceptibility to proton.

Acknowledgement

It is appreciated that Mr.T.Nakao of A.E.S took part in this study.

Reference

- 1) "Solar Cell Radiation Handbook " H.Y.Tada, Carter Jr. ,B.E.Anspaugh, and R.G.Downing, JPL Publication, Jet Propulsion Laboratory(1982)

1 . 5 STUDY OF SINGLE EVENT UPSET INDUCED BY ENERGETIC HEAVY IONS IN A 256KBITS SRAM FOR SPACE APPLICATION

Sumio MATSUDA, Takashi TAMURA, Satoshi KUBOYAMA, Ichiro NAITO, Hisayoshi ITOH*, Toshio HIRAO*, Isamu NASHIYAMA*

National Space Development Agency of Japan,

*Japan Atomic Energy Research Institute

I. INTRODUCTION

Space radiation particles trapped in radiation belts by the magnetic fields surrounding the Earth have serious effects on artificial satellites. These radiation belts called Van Allen belts have double structured fields. The inner zone of the Van Allen belts has altitude of 2,000-5,000 km on the equator and the outer zone extends over 10,000-20,000 km. In addition to the trapped radiation, the galactic cosmic rays and solar radiation induced by solar activity have strong effects on artificial satellites.

The satellites either in low earth orbit (400km - 900km) or in geostationary orbit (about 36,000km) are exposed to energetic electrons, protons and heavy ions. In the case of memory devices, single event upset (SEU) of memory cells caused by heavy ions is very important effect on artificial satellite.

The cross section of SEU is known to be a function of LET as shown in Fig.1. Threshold LET and saturated cross section are required as input parameters for upset rate predicting program codes, CREME (Cosmic Ray Effects on Microelectronics)¹⁾.

In the present paper, these two parameters are determined by measuring the upset cross sections for various LETs.

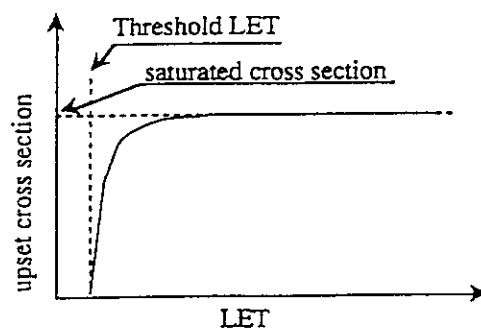


Fig.1 relationship between LET and upset cross section

II. SAMPLE AND IRRADIATION METHOD

(1) Samples

The sample used for the test is 256kbits SRAM (Static Random Access Memory) which is qualified by NASDA for space usage. Table 1 shows the specification of the test sample. Three samples out of the same manufacturing lot and one sample out of different lot were used in the following tests.

Table 1 Specification of test sample

Part Number	NASDA 38510/92001XBD
Technology	CMOS
Words	65,536
Bits	4 bit
Access Time	45ns (Max)
Package	24 pin 400 mil Ceramic Dip

(2) Irradiation Method

Heavy ions scattered into 30 degree with a thin Au foil were used in order to get uniform fluence at a sample. Fig.2 shows the concept of this testing system. The particle energy and the fluence were measured by a pulse height analyzer (PHA) which is connected to the SSD through pre-amplifier. A polyimide film is placed in front of the sample in order to absorb the scattered Au particles.

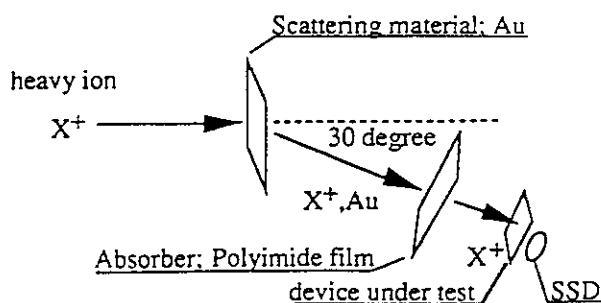


Fig. 2 Schematics of a scattered beam irradiation method.

Using this scattered beam irradiation method, three samples were tested simultaneously.

III. MEASUREMENT RESULTS

(I) Beam spectra

Table 2 shows the conditions of the scattered beams. Five different LETs were used for the tests. The normalized beam spectra are shown in Fig.3. The thickness of the polyimide film was chosen so that only recoiled Au was removed.

Table 2 Test conditions

Test	No.1		No.2	No.3	No.4		No.5
Particle	Ar	Ar	Ar	Ar	Ar	Ne	Ne
Accelerated Energy [MeV]	460	460	175	175	330	120	260
Scatt. Material (Au)[μm]	20	1	1	1	1	1	0
Absorber (Polyimide film)[μm]	25	25	25	25	12.5	12.5	0
Energy (After scattered) [MeV]	179	424	66	66	266	96	-
LET [MeV $\cdot\text{cm}^2/\text{mg}$]	14	9	19	19	12	5.2	2.8
Range [$\mu\text{m}(\text{Si})$]	417	138	15	15	73	60	258
Flux [ions/($\text{cm}^2\text{ sec}$)]	40	0.7	120	120	80	120	693

As shown in Fig.1, the upset cross-section in the low LET region varies radically. Energy spectrum that is corresponding to LET spectrum must be sharp. However, by inserting the polyimide film, the beam spectrum becomes broad. From this reason, when the beam spectrum did not have desired shape, the thicknesses of Au and polyimide films were changed.

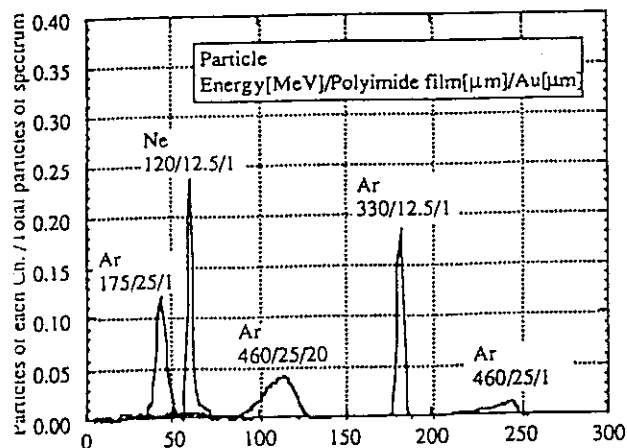


Fig.3 Beam spectra of each beam

Because the beam spectrum of scattered Ne 260MeV (Table 2, Test No.5) was enormously broad, the defocused direct beam was used in tests without Au and polyimide films.

(2) Dependence of write bit pattern

Because the configuration of this device is 4 bits per a word, 4 patterns of bit combination, "0000", "1111", "0101", "1010" were written in each word for various address ranges. As a result, the address and the write bit pattern dependence was found. In the gray area shown in Fig.4, the data "1" is easily changed to "0", but the data "0" is hardly changed to "1". In the white area, the data "0" is easily changed to "1", but the data "1" is hardly changed to "0". The ratio of gray area to white area in the device is 1 to 1. So, the upset rates became almost the same values in each bit pattern when the whole addresses were tested.

(3) Upset Cross Section

Figure 5 shows the upset cross section versus LET. Three data points that have the lowest cross section around 10^{-12} cm² were measured in a different way from that indicated in Fig.2. The sample number 4 comes from different lot had no remarkable difference. From this figure, threshold LET was determined to be about 2.8 MeV/(mg/cm²) and saturated cross section was 3×10^{-8} cm².

Upset rate of 256kbits SRAM in the space environment was estimated by using these parameters and CREME code. The result indicates that the probability of upset was negligibly small on low earth orbit of space station (altitude is 400km and inclination is 28.5 degree).

address	IO4	IO3	IO2	IO1
0- 64K	Gray	White	Gray	White
64K-128K	White	Gray	White	Gray
128K-192K	Gray	White	Gray	White
192K-256K	White	Gray	White	Gray

Fig.4 Dependency of write bit pattern

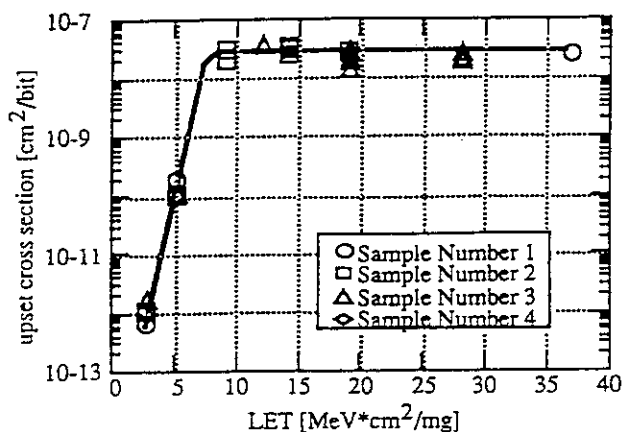


Fig.5 upset cross section versus LET

IV. SUMMARY

Two characteristic parameters of 256kbits SRAM such as threshold LET and saturated cross section for single event upset were obtained, and upset rate in space environment of this device was estimated.

Single-event upset phenomena to other devices will be investigated. Furthermore, upset phenomena caused by high energy protons will be studied in the near future.

REFERENCE

- 1) Adams, Jr. and James H., NRL Memorandum Report 5901 (1987).

1.6 Charge Distribution in a Small Sensitive Volume due to the Si(p,x) Nuclear Reactions.

Yasukiyo TAKAMI, Yosuke MORITA*, Isamu NASHIYAMA*,
Takashi TAMURA**, Yosuke SHIMANO* and
Masato UESYGI**

Institute for Atomic Energy, Rikkyo University,
*Takasaki JAERI, **NASDA

The purpose of this work is to investigate the adequacy of nuclear reaction models for Si(p,x) below 50 MeV, and establish a theoretical computation method for predicting SEU rate for protons below 50 MeV. In this report thin Si detector experimental results are theoretically analyzed with a new computation code based on adequate reaction models for this energy region. Finally, experimental results of 93L422(LTTL, RAM, AMD) are compared with theoretically derived values.

We adopted the pre-equilibrium model in the analysis of Si+p reactions. Although many pre-equilibrium models has been presented¹⁾, we chose an exciton model because the model reproduces experimental observations most successfully. Out of several exciton models, the random walk exciton models²⁾ seemed most adequate, because this model is able to take the multi-step pre-equilibrium process into consideration. The MCEXCITON code developed by Kishida and Kadotani³⁾ was modified to include the capability of computing compound particle emission and recoil nucleus energies. This code was then used for the series of computations. Fig. 1 illustrates calculated energy spectra of emitted particles from $^{28}\text{Si}+p$ reactions for 40 MeV incident protons.

Beams arriving at the Si target are seldom to be purely monochromatic. They are usually contaminated by energy degraded protons and other nuclear reaction products. This is because it is inevitable that some protons are scattered at beam ducts, slits, collimators and residual gases; and thus interacts with their nuclei. These contaminating particles often amount to 10^{-3} to 10^{-4} of incident protons. Since nuclear reactions by protons with Si nuclei are in the order of 10^{-4} for a target of a few hundred microns, signals given by these contaminated particles are a serious problem in the measurement of generated charge distributions by Si(p,x) reactions.

In order to discriminate these contaminating particles, two SBDs were closely set in face-to-face arrangement and placed perpendicularly to the incident proton beams. Coincident output pulses from the two SBDs were fed

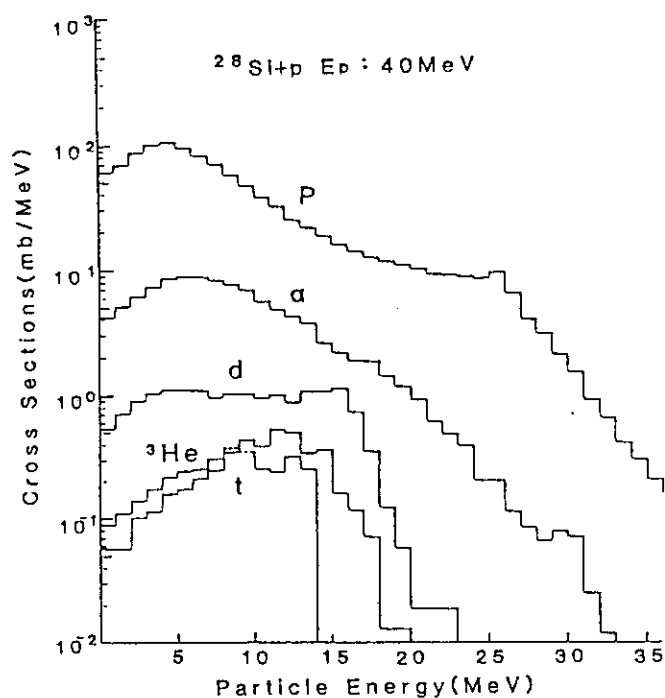


Fig. 1. Calculated energy spectra of emitted particles from $^{28}\text{Si}+p$ reactions, by an exciton model. For 40-MeV protons.

to a two dimensional pulse height analyzer, and simultaneously measured two dimensional pulse height distributions were analyzed and accumulated in the two dimensional memory. This measuring system, as shown schematically in Fig. 2, was also effective to discriminate pile-up proton signals from proton-Si nuclear reaction particles.

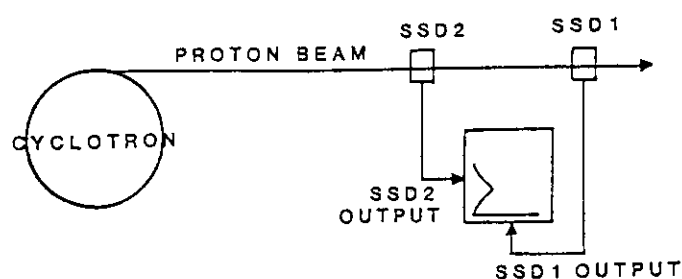


Fig. 2. Schematic representation of two dimensional measuring system. Only coincident output pulses from SSD1 and SSD2 are accumulated and analyzed. SSD2 output is fed to Y channels, and SSD1 to X channels.

Fig.3 shows two dimensional display of a measured spectrum for 45 MeV protons. The measurement was made in the Proton Irradiation Facility for Semiconductor Testing at LD-1. Doglegged parts are proton signals of degraded energies. p+Si nuclear events extend along X-axis.

FILE NAME : P2D32312.

ADC1, ADC2 = 1023, 63

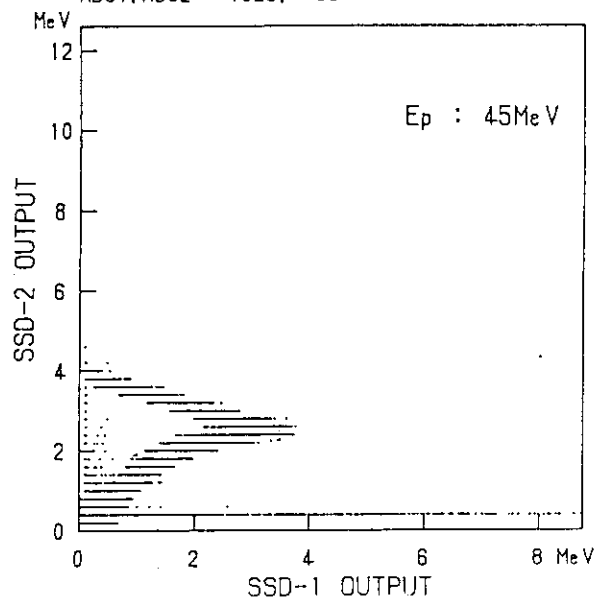


Fig.3 Two dimensional display of a measured spectrum for 45 MeV protons. Doglegged part is proton signals of degraded energies. p+Si nuclear events extend along and near X-axis.

Recoil energy spectrum for 40 MeV protons is illustrated in Fig. 4. Open circles are experimental values, while a stepwise solid line is computed values for whole non-elastic recoil events, and a smooth solid line is those for elastic recoil events.

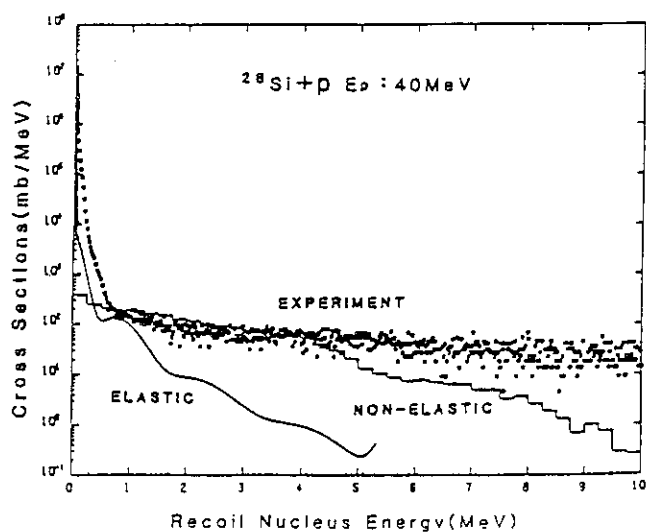


Fig. 4. Recoil energy spectra for 40-MeV protons. Open circles are experimental values, and solid lines are computed values.

Our computed SEU cross section values and experimental values by Shimano et al. for 40-, 30-, 20-, and 10-MeV protons are tabulated in Table 1. Shimano's SEU cross sections for 93L422(AMD) disagree with Bion's data with a factor of three⁵⁾. We presume even if their performances are identical, the sensitive volume differ by manufacturers.

Table 1. Experimental and Computed SEU Cross Sections in cm^2/bit .

$E_p(\text{MeV})$	Experimental values by Shimano et al.[16]	Computed values by our model
40	1.05×10^{-10}	0.77×10^{-10}
30	0.73×10^{-10}	0.80×10^{-10}
20	0.37×10^{-10}	0.69×10^{-10}
10	0.05×10^{-10}	0.12×10^{-10}

For 30-MeV protons the agreement is excellent. For 40 MeV computed values is about 25 percent less. This difference is likely to come from the optical model potential selected for 40-MeV proton reactions, which gives smaller total reaction cross section for 40-MeV than 30 MeV- protons. The discrepancy for 20 and 10 MeV protons, a factor of 2, is not well understood.

References

- 1) M.Blann, "Preequilibrium Decay", Ann. Rev. Nucl. Sci., Vol. 25, pp.123-166(1975)
- 2) K.Gudima et al., "Model for Preequilibrium Decay of Excited Nuclei", Sov. J. Nucl. Phys., Vol.21, No.2, pp.138-143(1975)
- 3) N.Kishida et al., "On the Validity of the Internuclear Cascade and Evaporation Model for High Energy Proton Induced Reactions", Proc. Int. Conf on Nuclear Data for Science and Technology, Mito, May 1988, pp 1209-1211
- 4) Y.Shimano et al., "The Measurement and Prediction of Proton Upset", IEEE Trans Nucl Sci Vol.36 No.6, pp 2344-2348(1989)
- 5) T Bion et al., "A Model for Proton Induced SEU", IEEE Trans Nucl. Sci., Vol. 36, No 6 pp.2281-2286(1989)

2. Biotechnology

2.1	Ion Beam Apparatus for Biological Samples(II)	
	Y.Kobayashi, M.Kikuchi, A.Tanaka, T.Shimizu and H.Watanabe	27
2.2	Cellular Proteins of <u>Deinococcus radiodurans</u> R ₁ Irradiated by Ion Beams	
	A.Tanaka, T.Shimizu and H.Watanabe	31
2.3	DNA Double-strand Breaks and the Repair in Radioresistant Bacterium, <u>Deinococcus radiodurans</u> , Irradiated by Ion Beams	
	M.Kikuchi, Y.Kobayashi, A.Tanaka, T.Shimizu and H.Watanabe	34
2.4	Morphology of <u>Deinococcus radiodurans</u> Irradiated by Heavy Ion Beams	
	S.Inaba, T.Shimizu and H.Watanabe	38
2.5	Repair of Transforming Capacity of Cells Irradiated with High-LET Ions in a Radiation Resistant Bacterium, <u>Deinococcus</u> <u>radiodurans</u>	
	T.Kikuchi, N.Mizuma, H.Watanabe, A.Tanaka, Y.Kobayashi and M.Kikuchi	42
2.6	Resistance to Heavy Ion Particles on Radioresistant Bacterium, <u>Deinococcus radiodurans</u> Dry Cells Packed in Gelatin	
	K.Harada, R.Kimura, T.Nakano, H.Watanabe, A.Tanaka and M.Kikuchi	46
2.7	The Use of Pollen Irradiated with Helium Ion Beam for Interspecific Hybridization in <u>Nicotiana</u>	
	M.Inoue, H.Watanabe, A.Tanaka and A.Nakamura	50
2.8	Studies on Induced Mutations by Ion Beam in Plants	
	H.Nakai, H.Watanabe, A.Tanaka, S.Kitayama, T.Asai and K.Shindoh	54
2.9	Optical Spectra of Rabbit Red Blood Cells Irradiated with Heavy Ion Beams	
	T.Fujimura, N.Ishihara, H.Watanabe, H.Ohmichi, H.Kobayashi and M.Tamura	57
2.10	Effect of Ion Beam Irradiation on Seed Germination and Growth of <u>Phalaenopsis</u>	
	T.Ohara, N.Fuwa, T.Harada and H.Watanabe	59

2.11 Radiation Sensitivities of Protoplasts of Cabbage (<u>Brassica</u> <u>Oleracea</u>) Irradiated by Ion Beams or X-rays	
H.Watanabe, A.Tanaka, S.Mochizuki and T.Nishihira	61

2.1 ION BEAM APPARATUS FOR BIOLOGICAL SAMPLES (II)

Yasuhiko KOBAYASHI, Masahiro KIKUCHI, Atsushi TANAKA,
Takashi SHIMIZU and Hiroshi WATANABE

Department of Radiation Research for Environment and
Resources, JAERI

I. INTRODUCTION

Densely ionizing radiations like protons or heavy charged particles are different in their biological effectiveness compared to sparsely ionizing radiation like γ -rays or electrons. These differences have been attributed to the different quality and energy density of radiation. It has been assumed that the quality of radiation can be characterized by "Linear Energy Transfer"(LET) to the biological target, however, LET is not a good parameter to describe the radiobiological effects with heavy charged particles because many biological experiments showed that different particles cause disparate results at the same LET. Although the LETs are equal, the microscopical pattern of energy deposition may differ drastically. The same is true for other parameters related to LET like "dose" or "Relative Biological Effectiveness"(RBE); they may sometimes be useful but the limitations have to be kept in mind.

It is necessary to obtain more data to understand the basic principles underlying the interaction of radiations with living matter. Experimental research should be focussed not only just on lethality but also on analyzing molecular damage, repair and genetic effects arising in damaged but not inactivated survivors. For the biological measurement with living materials like bacteria, yeast, pollen, seeds, roots, cells in vitro and somatic tissues, biological samples have to be irradiated in adequate conditions, essentially in the atmosphere. For this purpose we have installed two irradiation apparatuses in TIARA. One is "Irradiation Apparatus for Cell"(IAC) installed on a horizontal beam line of 3 MV tandem electrostatic accelerator, the other is "Irradiation Apparatus for Seed"(IAS) installed at HY1 port which is a vertical beam line of AVF cyclotron. Design concepts of these apparatuses were previously described in TIARA Annual Report vol.1 (1992). The present paper is focussed on the dose uniformity and the method of dosimetry.

II. OUTLINES OF "IAC" AND "IAS"

IAC is an apparatus to irradiate relatively small biological samples like bacteria, pollen, and cells *in vitro*. Ion beams, ranging from He to C, are accelerated by 3 MV tandem electrostatic accelerator and taken out through a Kapton film of 8.5 μm thickness from vacuum to atmosphere. This particle spectrum covers an LET range of 100 to 800 $\text{keV}/\mu\text{m}$. Choosing appropriate ion species and energy, only the surface of biological samples can be irradiated.

IAS is an apparatus to irradiate relatively large biological samples like seeds, seedlings and tissues. As it is installed under a vertical beam port of AVF cyclotron, various biological samples can be exposed to downward ion beams. The exit window for the beams from vacuum to atmospheric pressure consists of a 30 μm thick Ti-foil of 80 mm in diameter. The particle spectrum, ranging from He to Ar, covers an LET range of 14.0 to 2200 $\text{keV}/\mu\text{m}$.

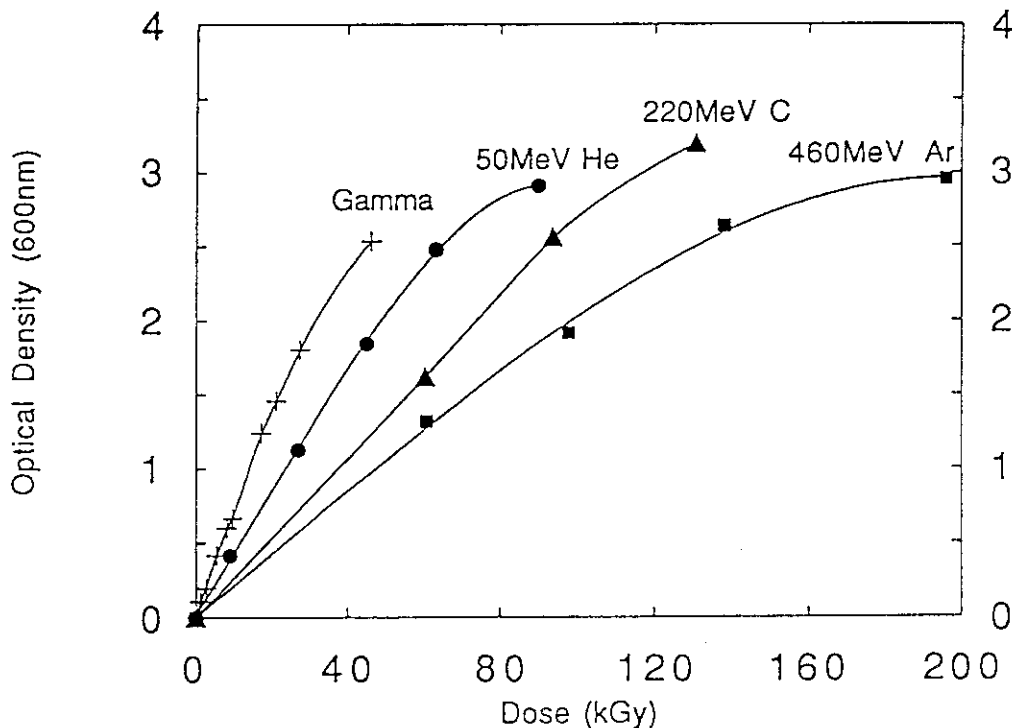


Figure 1. Dose responses of OD_{600} of RCD exposed to ^{60}Co gamma-rays or different heavy ions.

III. DOSE UNIFORMITY

Dose uniformity was checked by using a radiochromic dosimeter(RCD) with thickness of 50 μ m. The dosimetry is based on a linear dose response of radiation-induced optical densities at 600 nm. Figure 1 illustrates the dose responses of radiation-induced optical densities of RCD after exposed to ^{60}Co gamma-rays, He ions, C ions and Ar ions. Measurement of optical density of RCD was carried out with a scanning spectromicrophotometer(NML-301) developed by JAERI.

Dose distribution of $^4\text{He}^{2+}$ ions with energy of 1.5 MeV/u in IAC is shown in figure 2. The RCD was attached on the hexagonal sample column and moved across one-dimensionally scanned beams from the Kapton window.

Figure 3 shows a dose distribution of $^4\text{He}^{2+}$ ions with energy of 12.5 MeV/u in IAS, obtained by two-dimensional scanning of the beams. The dose uniformity in the edges was a little lower than in center, however, it is possible to improve the dose uniformity by over-scanning and trimming of the edges of scanned beams by slits. After all, the dose uniformity was dominated by the performance of power source of the scanner, although the homogeneity was dependent on the beam spot size.

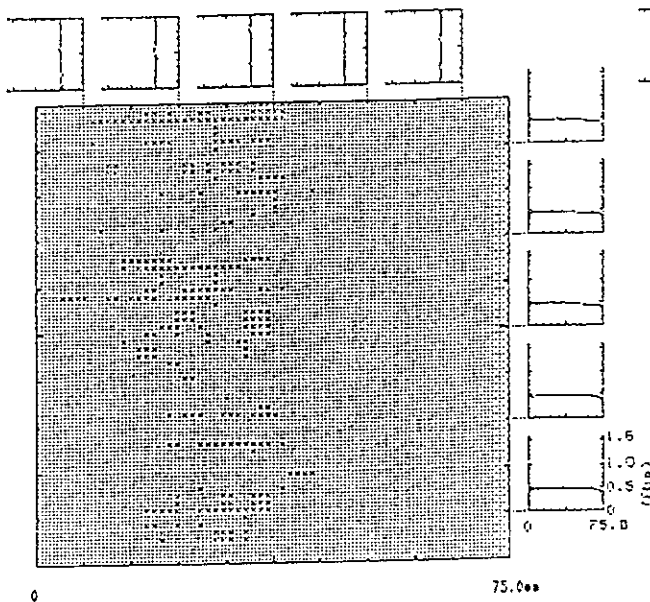


Figure 2. Dose distribution of 1.5 MeV/u $^4\text{He}^{2+}$ ions in IAC.

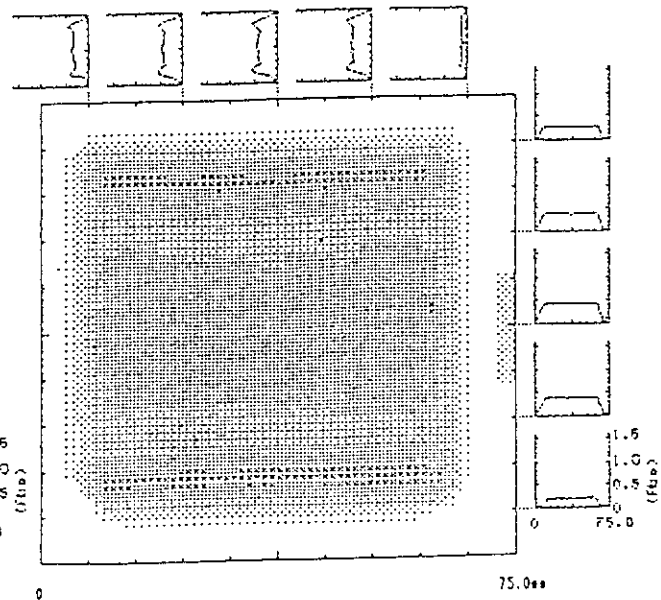


Figure 3. Dose distribution of 12.5 MeV/u $^4\text{He}^{2+}$ ions in IAS.

IV. DOSIMETRY

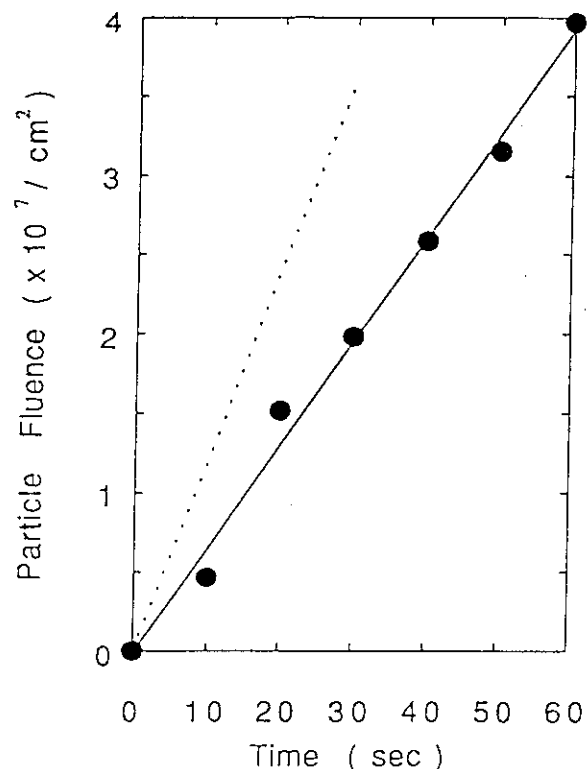
The beam intensity was measured by exposing suitable track detectors like CR-39 instead of the biological samples and counting the individual tracks. To convert particle fluence to dose in Gy the following relationship was used:

$$\text{Dose[Gy]} = 1.6 \times 10^{-9} \times \text{LET[keV/\mu m]} \times \text{Fluence[particles/cm}^2\text{]}$$

As the intensity of the beams and its homogeneity can not be monitored during exposure of the biological samples, irradiation doses have to be controlled by the times of exposure under such condition that the beam intensity is as stable as possible.

In figure 4 dotted line indicates a planned particle fluence on the target in IAS that is calculated from the beam intensity measured with a Faraday cup and the dose distribution detected with RCD. Solid line indicates particle fluences of 10.9 MeV/u $^{40}\text{Ar}^{13+}$ ions detected with CR-39 versus exposure times. Because of the fluctuation and the drift of the beam intensity doses on the target can not be controlled exactly, and it is difficult to check the particle fluence simultaneously with CR-39 at high dose irradiation. It is planned to install a beam monitoring system in IAS to estimate the beam intensity during the exposure of biological samples by monitoring the emission of secondary electrons of a thin foil like a carbon foil.

Figure 4. Particle fluences of 10.9 MeV/u $^{40}\text{Ar}^{13+}$ ions versus exposure times in IAS.
Dotted line: Calculation from the beam intensity measured with a Faraday cup and the dose distribution detected with RCD.
Solid line: Detected with CR-39.



2.2 CELLULAR PROTEINS OF *DEINOCOCCUS RADIODURANS* R₁ IRRADIATED BY ION BEAMS

Atsushi TANAKA, Takashi SHIMIZU* and Hiroshi WATANABE

Department of Radiation Research for Environment and Resources,

*Department of Advanced Radiation Technology, JAERI

I. INTRODUCTION

Deinococcus radiodurans R₁ is a representative strain of radiation resistant bacteria. This bacterium is not killed by γ -irradiation with doses up to 6kGy. In the dose range, it has been demonstrated that *D. radiodurans* can rejoin all strand breakages of DNA including double strand breaks (1). In addition, it has been suggested that cellular protein(s) induced after irradiation would play an important role for rejoining the strand breaks of DNA (2).

From investigation on the inducible cellular proteins, we found that γ -irradiation with a dose of 6kGy induced six major proteins in the cells of *D. radiodurans* R₁. Among these radiation induced proteins (RIPs) whose molecular weight is in a range of 31,000 to 190,000 dalton, two proteins, RIP60 and RIP46, were abundantly induced in the extremely resistant wild type strain (R₁) and a moderately resistant mutant (rec1), but not in a radiosensitive mutant (rec30) (3). Since *D. radiodurans* R₁ is also resistant to ion beam irradiation (4), these RIPs are expected to be induced in the cells by ion beams. Therefore, we examined the RIPs in the cellular proteins of R₁ cells after irradiation. A preliminary result is presented in this paper.

II. MATERIALS AND METHODS

(1) Strain and Cultivation

D. radiodurans R₁ strain was cultivated in TGY liquid medium at 30°C with shaking. The cells at stationary phase were harvested by centrifugation, washed twice with 0.1M phosphate buffer (pH 7.0), and resuspended in the same buffer. The cells (c.a. 3×10^9) were then filtrated by membrane filter (50mm ϕ) and lyophilized.

(2) Irradiation and Incubation

The membrane filter with lyophilized cells was irradiated by Ar ions scanned with square of more than 50mm from cyclotron using Irradiation Apparatus for Seed (IAC). Dosimetry was determined from fluences using CR-39 film track detector and LET which was calculated with ELOSS code developed in JAERI. The irradiated cells were harvested from filter and incubated in TGY liquid medium at 30°C for 60min with shaking in order to induce proteins after irradiation.

(3) Protein analysis

The cells incubated after irradiation were washed twice, cooled in ice water, and disrupted by sonication. The cell extracts were treated with DNase and RNase (0.01mg/ml at final concentration, respectively) at 37 °C for 2h. The supernatants recovered by centrifugation at 8,000×g for 30min were used for analysis of cellular proteins. The cellular proteins(50µg) were separated by two dimensional gel electrophoresis, and detected with a silver staining. The radiation induced proteins were determined by comparing the proteins of unirradiated cells with those of irradiated cells.

III. RESULTS AND DISCUSSION

As shown in Table 1, in the case of Ar ion irradiation, two kinds of proteins (No.1 and No.8) were increased, while another two proteins (No.7 and No.9) were decreased with increasing dose. Fig.1 shows the protein maps of two dimensional gel electrophoresis when the cells were irradiated by Ar ions. Arrows in the figure indicate the protein No.1 and No.8. These proteins were also induced by He ion irradiation (data not shown), indicating the existence of proteins commonly induced by different ion beams. Since a protein No.8 can be also induced by γ -rays, protein No.1 seems to be a novel protein induced specifically by ion beams.

On the other hand, in the case of γ -ray irradiation, the induction of protein No.2 to No.5 was observed as shown in Table, although these were not induced by Ar ions. Protein

Table 1 Changes in cellular proteins of R1 strain irradiated with γ -rays and Ar ions

Protein spot No.	γ -rays (kGy)			Ar ions (kGy)		
	0	4.5	6	0	3	6
1	+	—	—	+	++	++
2	+	++	++	+	+	+
3	—	++	++	+	+	+
4	—	+	+	—	—	—
5(RIP46)	±	±	+	+	+	+
6	+	—	—	+	+	+
7	±	—	—	+	±	—
8	±	±	+	—	+	+
9	+	+	+	+	+	—
10(RIP60)	+	+	+	+	+	+

— : undetected ± : slightly detected + : detected ++ : much stained

No.6 and No.7 were decreased, and protein No.9 and No.10 were not affected by irradiation. In a previous study, RIP60 and RIP46 were abundantly induced by γ -irradiation in phosphate buffer. However, the induction of RIP60 and RIP46 (protein No.10 and No.5 in Table 1, respectively) was not observed prominently by Ar ion irradiation. It should be noted that both RIPs in the unirradiated cells were little detected in suspension as shown in the previous experiments(3), but clearly detected on membrane filter as shown in Table. It is therefore assumed that any other stress without irradiation might influence the induction of these two proteins.

This preliminary experiments suggest that RIP60 and RIP46 are easily induced by any stress other than radiation, and might be responsible for the repair of DNA damages induced by ion beams. In addition it is suggested that ion beams would induce a specific protein which is not induced by γ -rays. Further analyses are in progress to elucidate the properties of radiation induced proteins.

REFERENCES

- (1) S.Kitayama and A.Matsuyama: Biochem. Biophys. Res. Commun., 33, 418-422 (1968).
- (2) S.Kitayama and A.Matsuyama: Agri. Biol. Chem., 35, 644-652 (1971).
- (3) A.Tanaka, H.Watanabe, R.Nozaawa, Q.Hu and S.Kitayama: Proc. Int. Conf. Radiat. Effect Prot., p.160-165, (1992).
- (4) YKobayashi, M.Kikuchi, H.Watanabe and G.Taucher-Scholz: GSI Sci. Rep., p.286 (1991).

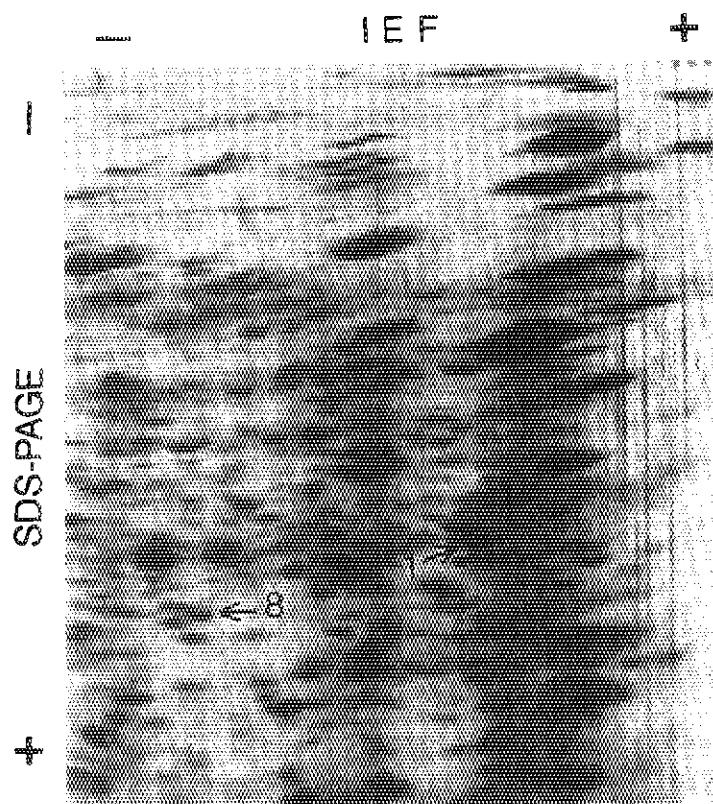


Fig.1 Two-dimensional gel electrophoresis of cellular proteins obtained from irradiated cells at the dose of 3kGy by Ar ions. Two induced proteins were indicated by arrows and numbers.

2.3 DNA DOUBLE-STRAND BREAKS AND THE REPAIR IN RADIORESISTANT BACTERIUM, *Deinococcus radiodurans*, IRRADIATED BY ION BEAMS

Masahiro KIKUCHI, Yasuhiko KOBAYASHI, Atsushi TANAKA, Takashi SHIMIZU and Hiroshi WATANABE

Biotechnology Laboratory, Department of Radiation Research for Environment and Resources, JAERI.

I. INTRODUCTION

Deinococcus radiodurans known as a radioresistant bacterium does not decrease its viability after gamma-ray irradiation with 5kGy. It is known that the high viability comes from efficient repair of not only single-strand breaks but also double-strand breaks. Because ion beams are high linear energy transfer (LET), they are expected to make some different effects such as induction of double-strand breaks and deletions at high efficiency in comparison to gamma-rays. This bacterium is also resistant to ion beam-irradiation, and the survival curve has a shoulder until 3kGy after irradiation of helium ions, suggesting that the bacterium is able to repair DNA breaks caused by ion beams. This paper describes on the result of the repair of DNA double-strand breaks (DNAdsbs), which is analyzed using pulse field gel electrophoresis (PFGE).

II. MATERIALS AND METHODS

D. radiodurans MR1 was cultivated in TGY medium at 30 °C for 24hrs to 48hrs with shaking. The cells of 4×10^9 (corresponding to 710 μ l of TGY medium at A₆₆₀=1) were harvested at stationary phase, settled on a membrane filter (Millipore Co.; type GS, pore size 0.22 μ m), washed twice with 10mM phosphate buffer (PB) and put on PB agar.

The cells were irradiated with gamma-rays of Co-60 or ion beams (He, C, Ar) at several doses. To irradiate with ion beams, we used Irradiation Apparatus for Seed (IAS), which is attached to a vertical beam line of AVF cyclotron. Dose uniformity of scanned ion beams was measured with radiochromic dosimeter (F.W.T.60-20) and fluence of ion beams was determined with CR-39 by counting the number of ion tracks with scanning electron microscope after the etching with alkali. Doses of ion beams were calculated from both the fluence and the LET estimated with ELOSS code.

For the repair of DNA the irradiated cells were transferred onto TGY agar and kept in

an incubator at 30°C for several hours.

To prepare genomic DNA the cells on the filter were washed with butanol-saturated PB, washed with Multibuffer (50mM sucrose, 10mM Tris, 40mM EDTA, 0.1% Triton X-100) and suspended into 80µl Multibuffer except of Triton X-100. The same volume of 2% low melting point agarose was mixed with the cell suspension, and plugs were made in a sample mold. After solidification the plugs were incubated in Multibuffer containing 1mg/ml of lysozyme for more than 12hrs at 37°C and then further in 1mg/ml of proteinase K for 2days at 50°C. For the inactivation of protease the plugs were incubated in TE (10mM Tris, 1mM EDTA) containing 1mM PMSF (phenylmethane-sulfonyl fluoride) for 2hrs and washed three times with TE. Genomic DNA in the plugs was digested with NotI for 6hrs at 37°C. PFGE was performed using 1% agarose in TAFE buffer for 16hrs (pulse time; 20sec) with GeneLine (Beckman)

III. RESULTS AND DISCUSSION

When *D. radiodurans* MR1 was irradiated with gamma-rays, almost fragments of genomic DNA vanished at 1kGy where its viability did not decrease (Fig.1). The fragments of higher molecular size disappear easier than those of low molecular size. Fig.2 shows DNA dsb induced at 3kGy with gamma-rays and the repair during post-irradiation incubation.

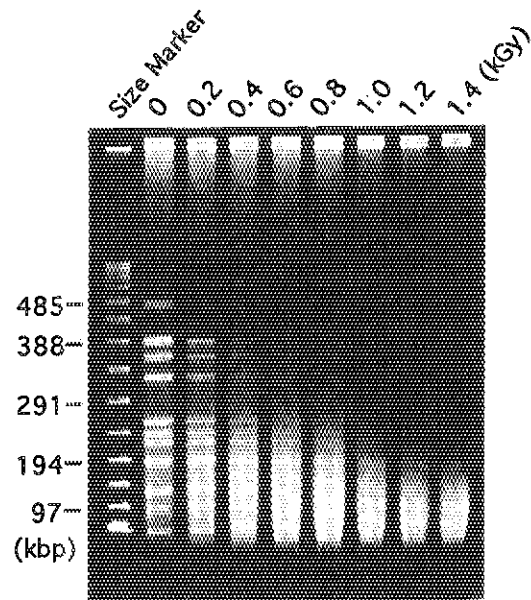


Fig.1 Genomic DNA digested with NotI after exposed to gamma-rays

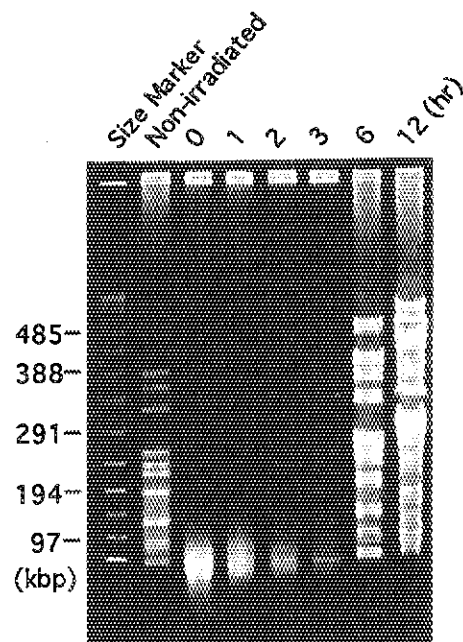


Fig.2 Genomic DNA digested with NotI after exposed to gamma-rays at 3kGy followed by incubation at 30°C for several hours

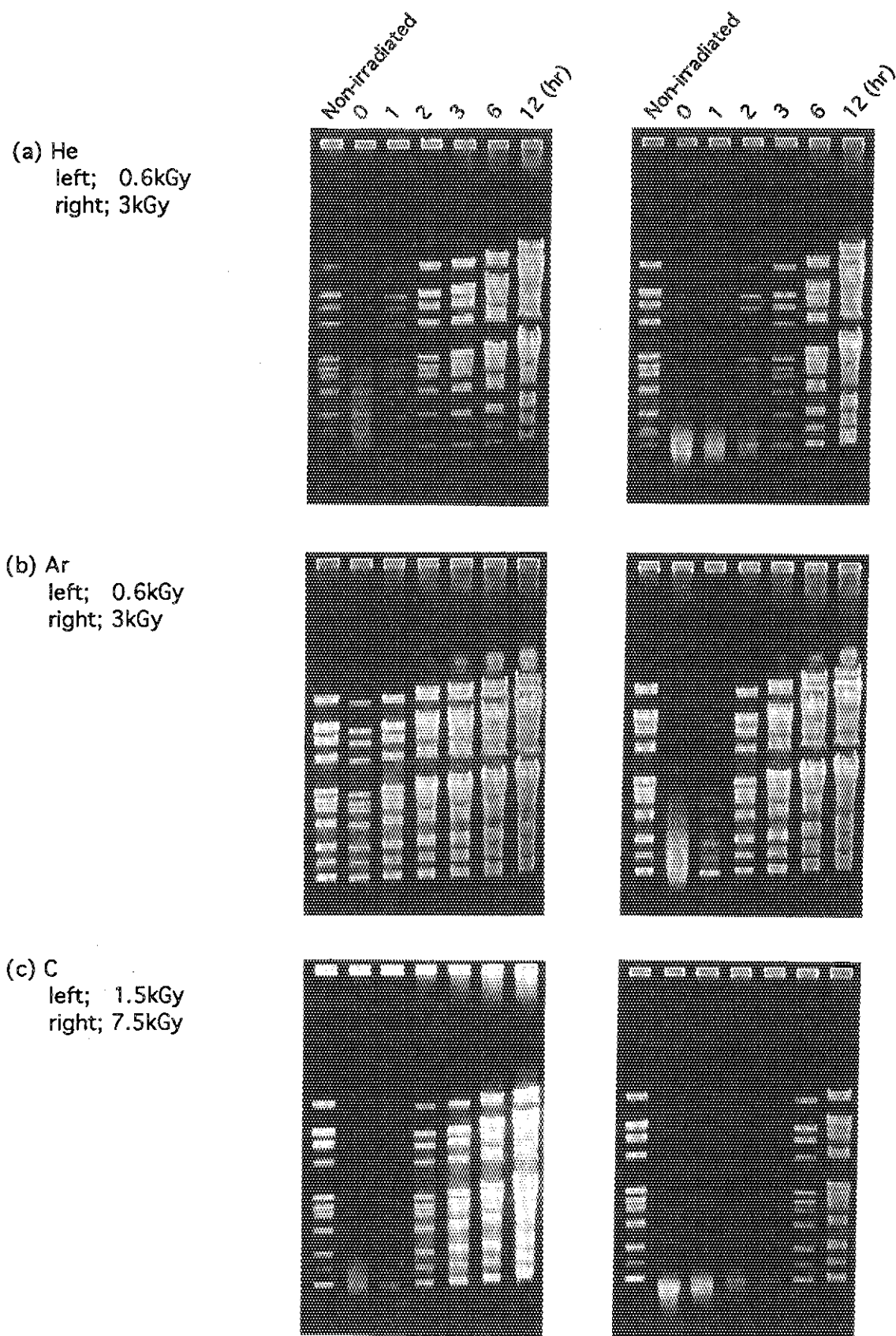


Fig.3 Genomic DNA digested with NotI after irradiated with ion beams followed by incubation at 30°C for several hours

The irradiation at 3kGy caused complete disappearance of DNA pattern on PFGE, and produced a fragment of small size below 97kbp. However, during post-irradiation incubation, the DNA pattern appeared again at 3hrs, while the small size fragment disappeared. Fig.3 also shows DNA dsb and the repair after the irradiation with helium, carbon and argon. After the irradiation at 3kGy with ion beams, the DNA pattern still remained (Fig.3a, right lane 3 and Fig.3b, right lane 3). This means that gamma-rays is more effective to induce double-strand breaks than ion beams. It is thought that gamma-rays give the energy to genomic DNA uniformly, but ion beams give the energy locally.

As shown in Fig.3, DNA exposed at 0.6kGy and 3kGy with helium ion was repaired to control level for about 1hr and 3hrs, respectively. The same repair process was observed in the cells irradiated with Ar and C. The repair time of DNA damaged by radiation was summarized in Fig.4. There was not observed any difference between gamma-rays and ion beams on the repair time. However, because gamma-rays cause more strand breaks than ion beams at the same dose, it is suggested that a breakage of DNA caused by ion beam would take more time for its repair.

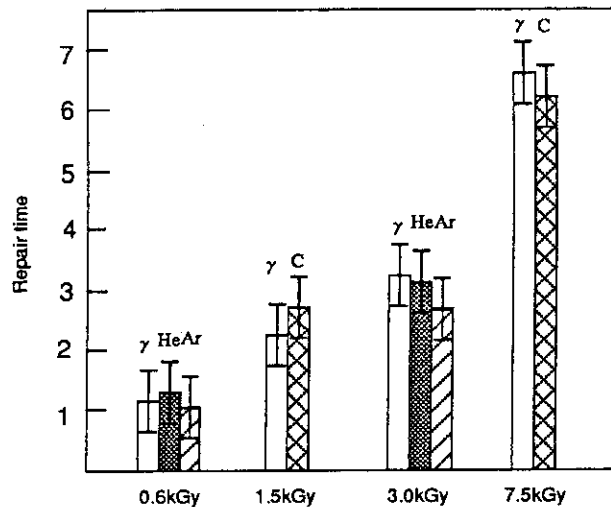


Fig.4 Comparison of repair time among gamma-rays and ionbeams

2 . 4 MORPHOLOGY OF *DEINOCOCCUS RADIODURANS* IRRADIATED BY HEAVY ION BEAMS

Shigeru INABA, Atsushi TANAKA* and Hiroshi WATANABE*

Radioisotope Center, Tokyo University of Agriculture, *Department of Radiation Research for Environment and Resources, JAERI

I. INTRODUCTION

Deinococcus radiodurans R1 is a extremely radiation resistant bacterium. The survival of this bacterium does not decrease even after γ -irradiation at about 6kGy. Such radiation resistance of R1 strain is attributable to the repair of all DNA damages induced with doses up to 6kGy(1). For ion beam irradiation, Dewey(2) and Kitayama et al.(3) examined the effects of He to Ar ions on the wet cells of R1 strain. Recently, Schafer et al.(4) also measured the radiosensitivities using Ti and U ions. From these studies, it was found that the survival curve of R1 strain was sigmoidal, indicating that the DNA damages induced by ion beams are also repaired.

It is thought that high LET radiation takes place heavy damages not only in DNA but also in cell structure which gives an environment desirable for DNA repair. However, little has been studied the change of cell structure after ion beam irradiation. Therefore, we have examined the effects of Ar and He ion beams on the wet and dry cells of *D. radiodurans* R1 strain. The changes in cell structure after direct or indirect action of ion beams were observed using transmission electron microscope (TEM).

II. MATERIALS AND METHODS

(1) Strain, Cultivation and Preparation of Sample

D. radiodurans R1 strain was cultivated in TGY medium with shaking at 30°C for 24h. The cells at the stationary phase were harvested by centrifugation, washed twice with 0.1M phosphate buffer(pH7.0), and resuspended in the same buffer. The cells (c.a. 3×10^9) were filtrated by Millipore filter(0.22 μ m), lyophilized and irradiated under dry condition. In case of irradiation under wet condition, the lyophilized cells on Millipore filter were put on the TGY-2% Agar in a petri dish (50mm ϕ), and irradiated.

(2) Irradiation

Irradiation Apparatus for Seed (IAS) which is connected to a vertical beam line of

AVF cyclotron was used for ion beam irradiation of cells. The cells on a filter were irradiated by Ar or He ion beams scanned with a square of 50mm. The doses were 2.7 and 5.4kGy with 460MeV $^{40}\text{Ar}^{13+}$ (LET:1800 keV/ μm), and 5.0 and 10.0kGy with 50MeV $^4\text{He}^{2+}$ (LET:14 keV/ μm). Ion fluence was counted by CR-39 film track detector and the dose was calculated from the fluence and LET calculated with ELOSS code developed in JAERI.

(3) Preparation of TEM-Specimens

Whole dry or wet cells irradiated were fixed in 0.1M phosphate buffer containing 2%(v/v) glutaraldehyde, mounted in 2%-agar, and then washed with 0.1M phosphate buffer. The cells were further fixed with 0.1M phosphate buffer containing 2%(v/v) osmium(VIII)oxide and washed with the buffer. After dehydration in ethyl alcohol, the specimens were embedded in Epon 812 and sectioned with glass knives mounted on LKB microtome. The specimens were double stained in uranyl acetate and lead acetate.

III. RESULTS AND DISCUSSION

(1) Radiosensitivity

The cells of *D. radiodurans* were irradiated under both dry and wet conditions. Figure 1 shows the survival curves of *D. radiodurans* R1 irradiated with Ar^{13+} and He^{2+} ion beams. Significant change of survival of dry cells was not observed between irradiations at 2.7kGy and 5.4kGy of Ar^{13+} ion beams, though slight decrease of survival at 5.4kGy was observed in wet cells. On the other hand, there was also a slight decrease in the survival of dry cells after irradiation of He^{2+} ion beams at 5.0kGy and 10.0kGy, while wet cells did not survive at 10.0kGy.

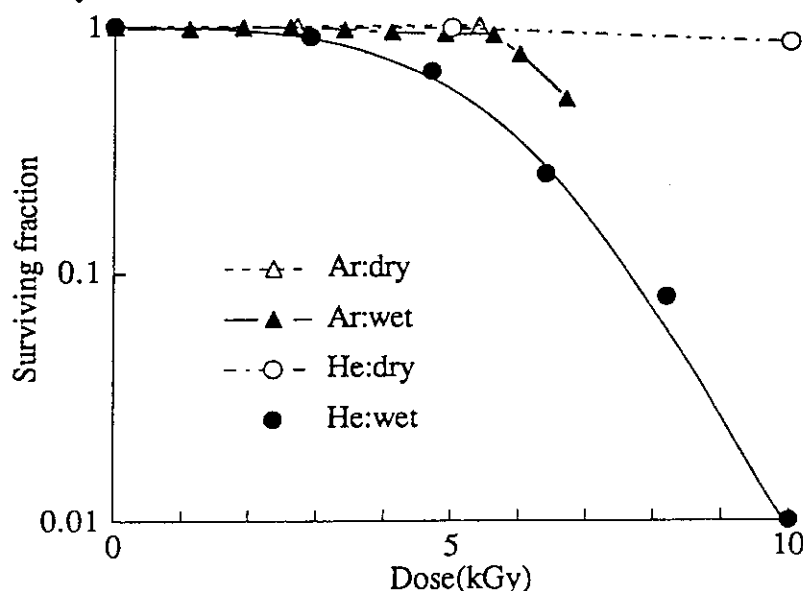


Fig.1 Survival curves of *D. radiodurans* R1 cells irradiated with Ar and He ions under both dry and wet conditions.

(2) Observation through TEM

Changes in the cell structure after irradiations were examined with a transmission electron microscope in order to clarify the remarkable difference of survival as observed

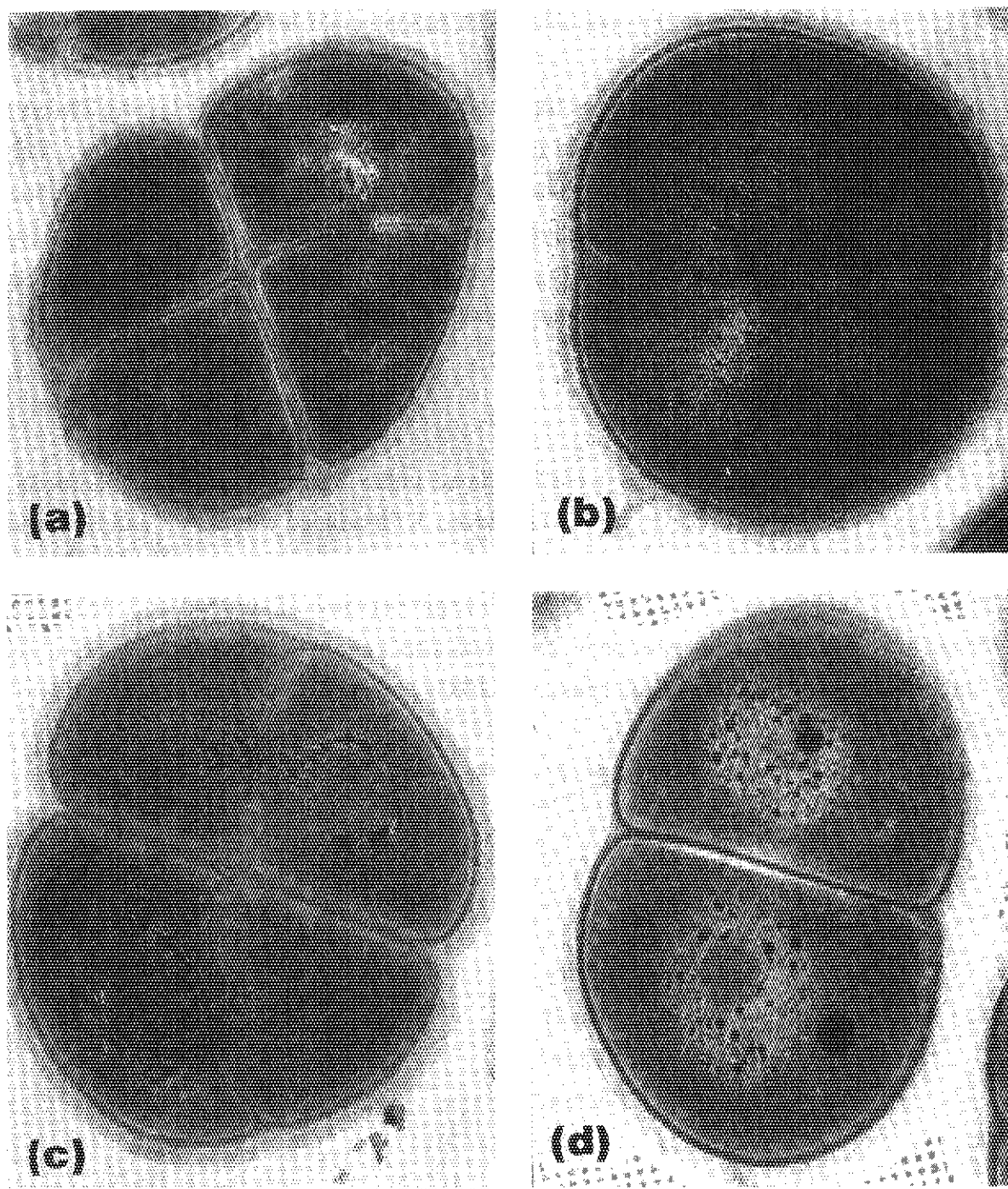


Fig.2 Thin sections of irradiated cells: (a) dry cells irradiated with 5.4kGy of Ar ions, (b) wet cells irradiated with 5.4kGy of Ar ions, (c) dry cells irradiated with 5.0kGy of He ions, (d) wet cells irradiated with 5.0kGy of He ions.

above. The TEM picture of thin sections prepared from unirradiated dry and wet cells resembled to those shown by Work et al.(5) who examined the morphology of *D. radiodurans*.

(i) Cell envelope

Slime layer: Electron density was more dense in wet cells than in dry cells. Significant damages were observed in wet cells (Fig.2).

Cell wall: Significant damages of morphological structure were observed in the wet cells. In particular, the large deformations of walls were caused by both ion beams, especially by He^{2+} ion beams at 10.0kGy.

(ii) Cytoplasmic-granules

Cytoplasmic-granules were also destroyed by He^{2+} ion irradiation, consequently the size of granules became about half. The effect of irradiation on the decrease of size was more significant in wet cells than in dry cells. Significant destroys of cytoplasmic-granules were not observed after Ar^{13+} ion irradiation on both wet and dry cells.

(iii) Cell nucleus

Photographs (a) to (d) of Fig.2 show thin sections prepared from irradiated cells. No significant differences of morphological structures were observed between the unirradiated cells and dry cells irradiated with 5.4kGy of Ar^{13+} ion beams, while the partially broken cell nucleus was observed in the wet cells irradiated with 5.4kGy of Ar^{13+} ions. Compared with cell survival, these decomposition of nucleus would be recovered during the incubation of post-irradiation. On the other hand, irradiation of dry cells with 5.0kGy of He^{2+} ions did not cause any significant change in the nucleus as shown in photography (c). However, when the wet cells were irradiated with the same dose, as shown in photography (d), the broken nucleus was observed.

These results indicate that partially broken nucleus could be recovered, but heavy broken nucleus could not, and further indicate that the increased sensitivities and decomposition of cell nucleus under the wet condition would be due to indirect action of water radicals.

REFERENCES

- (1) S. Kitayama and A. Matsuyama, Biochem. Biophys. Res. Commun., 33, 418 (1968).
- (2) D. L. Dewey, Int. J. Radiat. Biol., 16, 583 (1969).
- (3) S.Kitayama, K. Igarashi, T. Karasawa and M. Matsuyama, Agri. Biol. Chem., 41, 2297 (1977).
- (4) M.Schafer and H.Bucker, GSI Scientific Report, p.223 (1987).
- (5) E. Work and H. Griffiths, J. Bacteriol., 95, 641 (1968).

2.5 REPAIR OF TRANSFORMING CAPACITY OF CELLS IRRADIATED WITH HIGH-LET IONS IN A RADIATION RESISTANT BACTERIUM, *Deinococcus radiodurans*

Tadatoshi KIKUCHI, Nagayo MIZUMA, Hiroshi WATANABE*, Atsushi TANAKA*, Yasuhiko KOBAYASHI*, Masahiro KIKUCHI*

Research Reactor Institute, Kyoto University, *Biotechnology Laboratory, JAERI (Takasaki)

I. INTRODUCTION

Deinococcus radiodurans R₁ is exceptional radiation-resistant bacterium which was originally isolated in 1965¹⁾.

From the sedimentation analyses after γ -rays irradiation, it has been demonstrated that *D. radiodurans* was able to repair double-strand break in DNA²⁾. It was proposed that the exceptional resistance of *D. radiodurans* to killing induced by ionizing radiation must be due to the high efficiency of its recombination repair system, but the detailed mechanisms of this resistance induction remain obscure. The present study was performed using the method of transformation to know the ability of recombination repair after the postirradiation incubation of dry cells irradiated with ion beams ($^4\text{He}^{2+}$ and $^{40}\text{Ar}^{13+}$), and also the results obtained were compared with those found in the previous work which conducted using wet cells irradiated with γ -rays or high-LET radiations (BNCB) produced by the nuclear reaction $^{10}\text{B}(n, \alpha)^7\text{Li}^{3+}$.

II. MATERIALS AND METHODS

(1) Strain, Cultivation and preparation of cell samples for irradiation

D. radiodurans R₁ strain was cultured to the late-logarithmic growth phase in TGY medium at 30°C with shaking. The harvested cells were washed in phosphate buffer (0.1M, pH 7.0), then suspended in the same buffer. For the preparation of gelatin-mixed dry cells, 20 % gelatin-containing phosphate buffer was heated at 40°C and mixed with an equal volume of cell suspension to make finally 10 % gelatin. The small amount of cell-gelatin mixture prepared as above was put on a millipore membrane filter, and dried under sterilized-air flow in a clean bench. For the lyophilized cells, 5 ml of cell suspension was filtrated through a millipore membrane filter (47 mm

Φ), then the harvested cells together with a membrane filter were transferred into a deep freezer. The frozen cells were lyophilized in a freeze-drying apparatus (~0.03 TOR). The lyophilized cells were preserved in a refrigerator till irradiation, measurement of surviving fraction and assay of transforming activity, respectively.

(2) Irradiation

For irradiation with ${}^4\text{He}^{2+}$ ions (50 MeV, LET; 14 keV/μm) produced by AVF cyclotron (JAERI, Takasaki Establishment), the membrane filters with the gelatin-mixed dry cells were exposed with the dose rate of 1.74 kGy/min (beam current; 0.02 μA) or 4.56 kGy/min (beam current; 0.05 μA). For exposure with ${}^{40}\text{Ar}^{13+}$ ions (460 MeV, LET; 1800 keV/μm) produced by AVF cyclotron, the membrane filters with lyophilized cells were irradiated with the dose rate of 20.7 kGy/min (beam current; 10 μA). Both the irradiations were performed under helium-gas flow to suppress the radiation activation of sample in an automatic-sample-exchanging apparatus with remote control system.

(3) Assay of transforming activity

For the assay of transforming activity^{3),4)}, the recipient cells irradiated with ions were mixed with DNA, which isolated from the rifampicin resistant strain (rif^r)⁵⁾, in TGY medium supplemented with Ca^{++} and incubated for 30 min at 30°C with shaking, and then DNase I solution was added into the

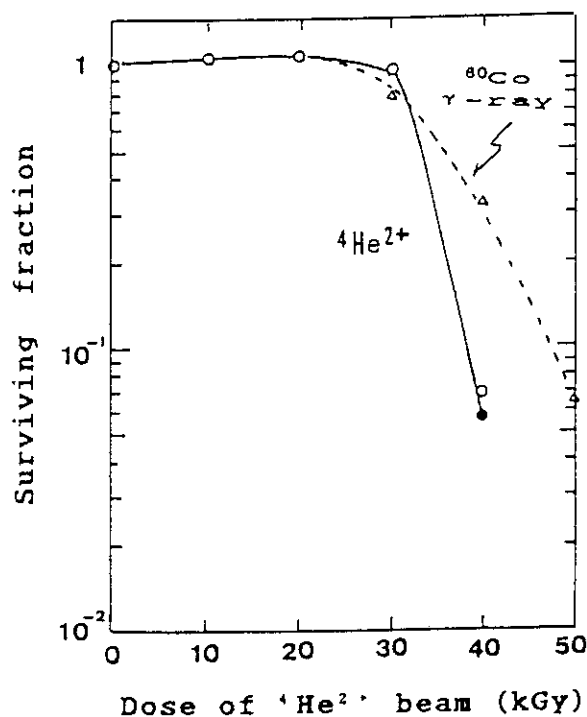


Fig.1 Survival Curves of 10 % Gelatin-Mixed Dry Cells of *D. radiodurans* R₁ Irradiated with 50 MeV ${}^4\text{He}^{2+}$ Ions and γ -rays

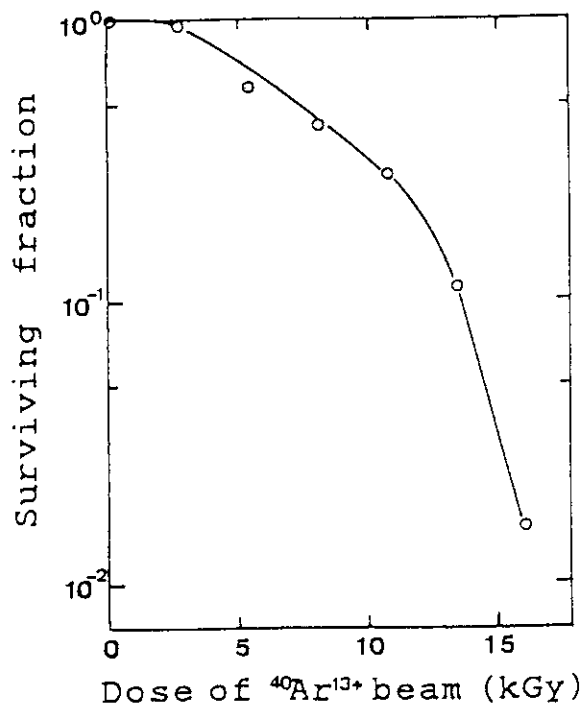


Fig.2 Survival Curve of Lyophilized Cells of *D. radiodurans* R₁ Irradiated with 460 MeV ${}^{40}\text{Ar}^{13+}$ Ions

cell suspension to stop transforming reaction. Melted-TGY-agar medium(10 ml, 47°C) was mixed with diluted cell suspension in a petri dish, and incubated for 3 hr at 30 °C after solidification, and then overlaid with the same melted-agar medium (10 ml) containing rifampicin (8 µg/ml). The colonies derived from rifampicin-resistant transformants were scored as the indication of transformed cells after 3-4 days incubation at 30 °C. And then the frequency of transformants were calculated from cell number obtained thus and the total number of recipient cells appeared on agar medium without rifampicin. For the repair assay of the transforming capacity in the recipient cells irradiated with ions, the irradiated cells were treated with chloramphenicol(100µg/ml) for 10 min intermittently during postirradiation incubation in TGY medium at 30 °C to recover the damaged cells and a part of cell suspension was taken off to determine transforming activity at various times during the incubation.

III. RESULTS AND DISCUSSION

(1) Sensitivity to the ion beams

When the gelatin-mixed dry cells were irradiated with ${}^4\text{He}^{2+}$ ions, the survival did not decrease even after exposure with about 30 kGy but declined exponentially at the dose of more than 30 kGy. For the γ -rays irradiated

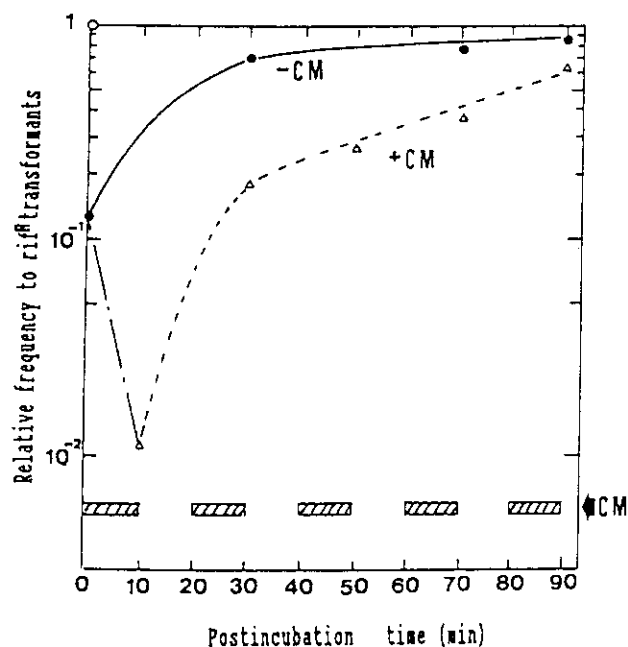


Fig.3 Transformation Frequency of *D. radiodurans* R₁ Irradiated with ${}^4\text{He}^{2+}$ Ions (9.6 kGy) after Short-Period Treatment with Chloramphenicol(+CM)

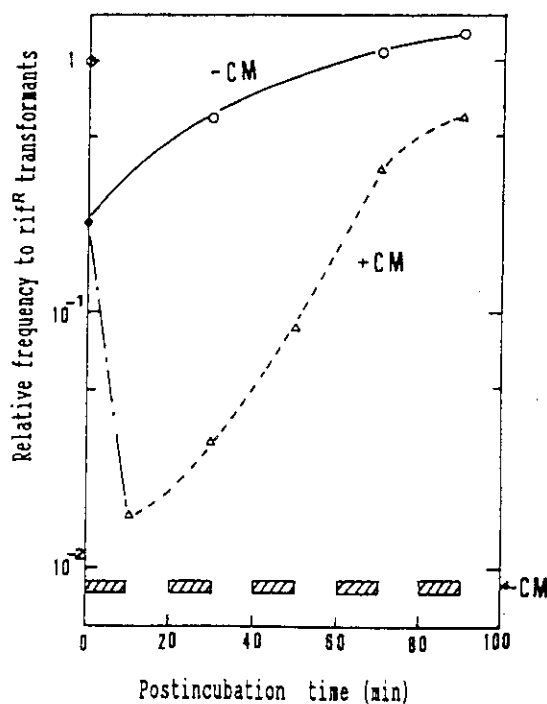


Fig.4 Transformation Frequency of *D. radiodurans* R₁ Irradiated with ${}^{40}\text{Ar}^{13+}$ Ions (3.3 kGy) after Short-Period Treatment with Chloramphenicol (+CM)

ion of the same cell sample, at the dose of more than 30 kGy the survival curve showed slower decline than that for the exposure to He^{2+} ions (Fig.1). Addition of 10 % gelatin into the cell sample showed the protection effect against irradiation for both the cases. For the irradiation with Ar^{13+} ions, lyophilized cells were used in connection with the track distance ($<50 \mu\text{m}$) of ions. As shown in Fig.2, the cell survival decreased gradually with doses up to about 10 kGy and showed remarkable decrease at more than about 10 kGy. The slower decrease in the survival of lyophilized cells at the lower doses seems to be due to partly instability at a room temperature.

(2) Repair of damage in transforming ability

When the dry cells irradiated with He^{2+} or Ar^{13+} ions were incubated in TGY medium at 30°C , the transforming activity lowered with irradiation was increased with the time course of incubation. For the repair of cells irradiated with He^{2+} ions, transforming activity markedly increased for initial 30-min incubation and then enhanced gradually (+CM in Fig.3). On the other hand, for the irradiation with Ar^{13+} ions it took more than 60 min for the initial increase of transforming activity (+CM in Fig.4). The pattern of initial increase in transforming activity of the cells irradiated with He^{2+} ions is similar to that in the repair process of transforming activity of the cells irradiated with γ -rays³⁾, but for γ -ray irradiation the inhibitory effect of chloramphenicol to the expression of transforming activity was abolished after about 30-min postirradiation incubation. For the cells irradiated with Ar^{13+} ions, there was more than 1 hr time lag for the recovery of transforming activity (Fig.3 and 4). From the results noted above, *de novo* protein synthesis seems to be required for the recovery of transforming activity in the cells irradiated with high-LET ions and it is suggested that there are some qualitative differences between γ -rays and high-LET-ion beam irradiations for the newly synthesized proteins involving in recombination repair for double-strand breaks in cellular DNA.

REFERENCES

- 1) A.W.Anderson, H.C.Nordan, R.F.Cain, G.Parrish and D.Duggan, Food Technol. 10 (1956) 575.
- 2) S.Kitayama and A.Matsuyama, Biochem.Biophys.Res.Comm. 33 (1968) 418.
- 3) N.Mizuma and T.Kikuchi, Abstracts of Report. at Scientific Meeting of the Research Reactor Institute. Kyoto Univ., 27 (1993) 61.
- 4) S.Tigari and B.E.B.Moseley, J.gen.Microbiol. 119 (1980) 287.
- 5) J.Marmur, J.Mol.Biol. 3 (1961) 208.

2. 6 RESISTANCE TO HEAVY ION PARTICLES ON RADIORESISTANT BACTERIUM *DEINOCOCCUS RADIODURANS* DRY CELLS PACKED IN GELATIN

Kazuki HARADA, Rika KIMURA, Tatsuo NAKANO, Hiroshi WATANABE*,
Atsushi TANAKA* and Masahiro KIKUCHI*

PL Botanical Institute, PL Gakuen Women's Junior College, *Takasaki
Radiation Chemistry Research Establishment, JAERI

I. INTRODUCTION

Extremely radioresistant bacterium *Deinococcus radiodurans* is described in the Guinness Book of Records as the "toughest bacterium in the world". It was asporogenous one that formed a tetracoccus of 1.5 to 3.0 μm in diameter from the observation of scanning electron microscope (SEM) (Fig. 1), had multiple carotenoids, and formed a red-pigmented and smooth colony on agar. It was reported that DNA repair capability in the cells contributed to the resistance against ionizing radiation¹⁾. We reported that it was resistant to ultraviolet radiation, chemical agents and hyperthermia besides ionizing radiation²⁻⁴⁾. Also, we reported that the DNA repair capability and the absence of inflection point in Arrhenius plot of this organism contributed to hyperthermia resistance⁵⁻⁷⁾.

In this study, we examined the survival response of *D. radiodurans* gelatin-packed dry cells exposed to low LET (linear energy transfer) radiation (γ -irradiation) or high LET radiations (heavy ion particles). These dry cells packed in gelatin will be used at the space experiment as the biological monitor researching the influence of high energy cosmic radiation (HZE particles) on the lethality in human beings.

II. MATERIALS AND METHODS

(1) Strain and Cell Preparation

D. radiodurans wild type strain MR1 was used throughout this study. The dry cells of *D. radiodurans* were prepared as follows⁸⁾. The cultivation was done at 30°C in TGY medium²⁾ containing 0.5 % Bactotryptone (Difco), 0.1 % glucose and 0.3 % yeast extract (Difco), adjusted to pH 7.0. Growth was followed by measuring the optical density at 660 nm using a recording spectrophotometer (Shimadzu UV-240). Cell growth was stopped at the late logarithmic growth phase that was equivalent to approximately 1×10^8 colony-forming units/ml. The cell suspension in TGY medium was added with the equivalent quantity of 20 % Bacto-Gelatin (Difco), and then the cells in TGY medium including gelatin were put on the membrane filter (pore size; 0.45 μm , Advantec). The wet cells on the membrane filter were dried in desiccator including silica gel *in vacuo* using air pump. The dried cells on the filter were irradiated with various radiations.

(2) Irradiation

Gamma(γ)-irradiation was carried out with a ^{60}Co source (3.7×10^{14} Bq) using facilities of

Research Reactor Institute, Kyoto university (KURRI)⁹⁾.

Heavy ion beam exposure was carried out at AVF (Azimuthally Varying Field) cyclotron of Takasaki Ion Accelerator for Radiation Application (TIARA) in Japan Atomic Energy Research Institute (JAERI). The high LET radiations employed were ${}^4\text{He}^{2+}$ ions of 14 keV/ μm LET, ${}^{12}\text{C}^{5+}$ ions of 121 keV/ μm LET and ${}^{40}\text{Ar}^{13+}$ ions of 1800 keV/ μm LET.

(3) Survival Criterion

After irradiation, the dry cells were immersed in TGY medium and were diluted with the same medium. The diluted samples were spread on TGY agar plates that were made by solidifying a TGY medium with 1.5 % Bacto-agar. Colonies were counted after incubation at 30°C for 5 days. As a total of six plates diluted at three different steps were used for each survival point, each data point represented the mean of six plates.

III. RESULTS AND DISCUSSION

The dose-survival curves with respect to colony-forming ability of *D. radiodurans* dry cells irradiated with various radiations are shown in Fig. 2. From this figure, we found that *D. radiodurans* dry cells were more resistant to low LET radiation than high LET radiations, and that D_{10} value for γ -irradiation was 48 kGy.

Also, the dry cells of *D. radiodurans* were generally resistant to low and high LET radiation compared with the suspension cells (data not shown).

From Fig. 2, though the cells showed tendency to be easily killed by high LET radiations and the order of decreasing lethality was ${}^{40}\text{Ar}^{13+}$, ${}^4\text{He}^{2+}$ and ${}^{12}\text{C}^{5+}$, we considered that the effect of ${}^4\text{He}^{2+}$ on the lethality of the cells was similar to that of ${}^{12}\text{C}^{5+}$.

It is generally said that RBE (relative biological effectiveness) value for cell inactivation becomes gradually small according to the increasing of LET for procaryote and phage. Then, the sequence of sensitivity against heavy ions must be ${}^4\text{He}^{2+} > {}^{12}\text{C}^{5+} > {}^{40}\text{Ar}^{13+}$. However, it was reported that on *D. radiodurans* dry cells the plots of RBE versus LET showed two peaks¹⁰⁾, and assumed that one of the peaks was located to about 5000 keV/ μm LET (personal communication with Dr. Y. Kobayashi, JAERI-Takasaki). Whether the no correspondence between this result and RBE versus LET general law is caused by RBE values of many organisms not being researched above 1000 keV/ μm LET in detail or by the characteristics of radioresistant bacterium *D. radiodurans* itself, the reason is yet obscure.

From these results and further study, the relation between RBE value and LET on *D. radiodurans* dry cells might be made clear.

On the other hand, it was decided that we would perform the space experiment using Space Shuttle at the 2nd International Microgravity Laboratory Mission (IML-2) in 1994 by National Aeronautics and Space Administration (NASA) of USA and National Space Development Agency of Japan (NASDA). There are three distinct source of radiation in space, differing in their location: galactic cosmic ray, trapped particle radiation and solar particle radiation. Especially, galactic cosmic ray consists of heavy ions (HZE particles) that has been accelerated to high energy somewhere in our galaxy. Then we intend to perform the research titled "Effect of Cosmic Radiation on *D. radiodurans*" in order to develop protection technology for human

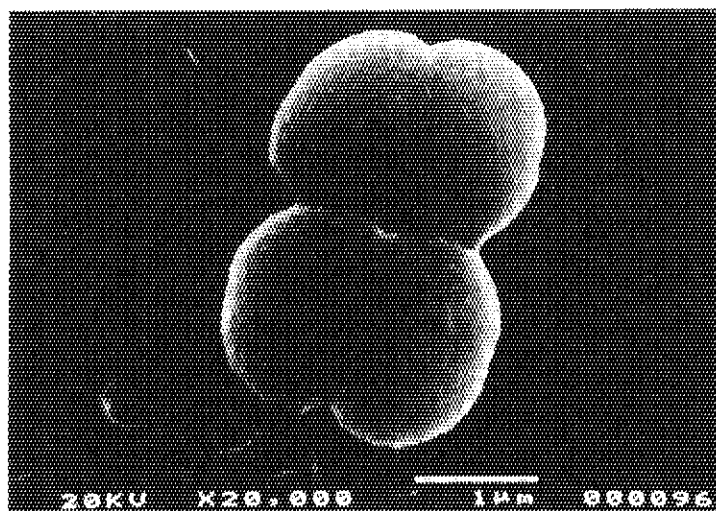


Fig. 1 Scanning Electron Micrograph of the Cell of *D. radiodurans* Wild Type Strain MR1.

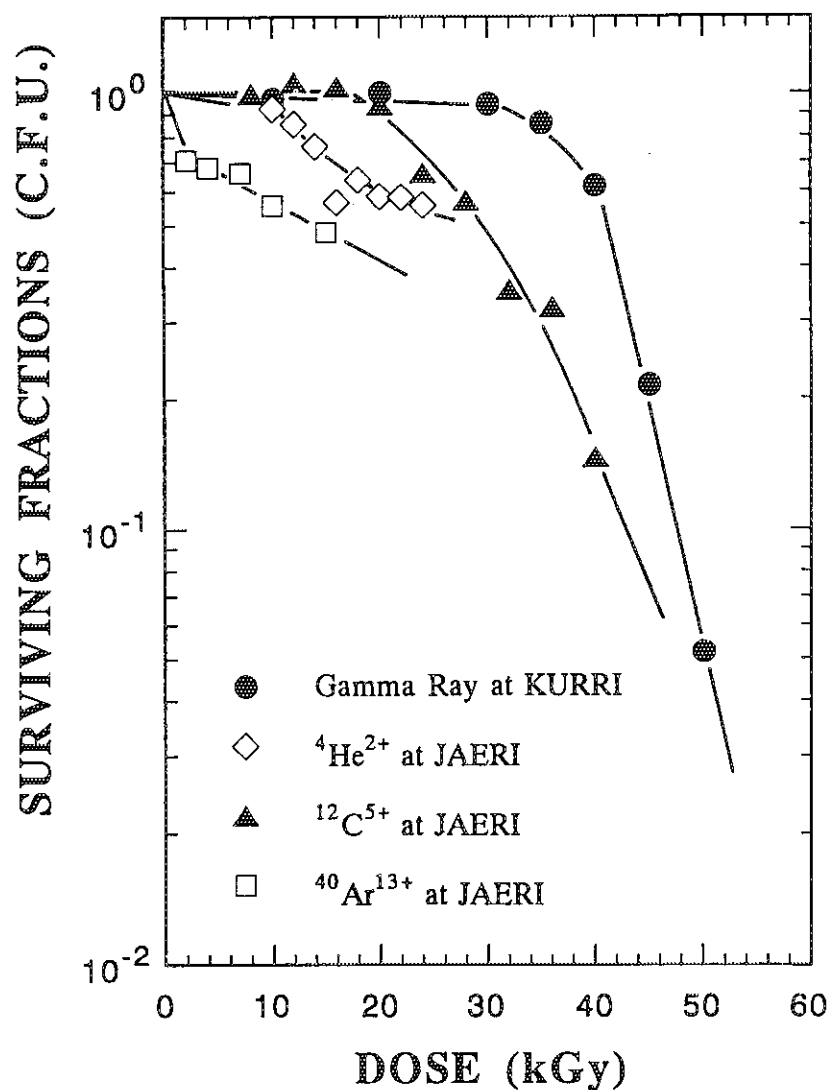


Fig. 2 Dose-Survival Curves of *D. radiodurans* Gelatin-Packed Dry Cells Irradiated with Various Radiations.

against space radiations inside the Shuttle. Though the total absorbed doses from cosmic radiations were very few during Shuttle flight for short period, we cannot neglect the highly localized cell damage by energy deposition along single HZE particle's trajectory.

These results indicated that *D. radiodurans* cells can tolerate the effect of low LET radiation up to 35 kGy, and that the cells would be useful as a biological monitor of only high LET cosmic ray.

A further study will contribute to development of cancer therapy using heavy ion beam and hyperthermia, and of manned space activities protecting astronauts from cosmic radiation.

We are grateful to Dr. Shigeru Kitayama (The Institute of Physical and Chemical Research) for providing us with *Deinococcus radiodurans* wild type strain MR₁, and to Dr. Nagayo Mizuma (Research Reactor Institute, Kyoto University) for her technical teaching of γ -irradiation. We are also grateful to Professor Shigeru Oda (Director of PL Botanical Institute), President Michisuke Kawashima (PL Gakuen Women's Junior College) and Patriarch Takahito Miki (Church of perfect Liberty) for constant kind guidance and encouragement during this work.

REFERENCES

- 1) S.Kitayama and A.Matsuyama, Biochem. Biophys. Res. Commun., **33** (1968) 418.
- 2) K.Harada and S.Oda, PL G. W. J. C. Bull., **12** (1985) 60.
- 3) K.Harada and S.Oda, Agric. Biol. Chem., **52** (1988) 2391.
- 4) K.Harada, PL G. W. J. C. Bull., **17** (1990) 17.
- 5) K.Harada, S.Oda and T.Miki, Radiation Research, Proc. of the 8th Int. Congress of Radiation Research, Vol. 1, Taylor & Francis Ltd., London (1987) p.345.
- 6) K.Harada, M.Moriwaki and S.Oda, J. Gen. Appl. Microbiol., **34** (1988) 209.
- 7) K.Harada, R.Kimura, S.Oda, M.Kawashima, T.Miki, N.Mizuma, H.Maki, M.Saito, H.Watanabe and S.Tano, Proc. Int. Conference on Evolution in Beam Applications, Radiation Application Development Association (1992) p.593.
- 8) R.Kimura and K.Harada, PL G. W. J. C. Bull. (in Japanese), **19** (1992) 57.
- 9) R.Kimura, K.Harada and S.Oda, PL G. W. J. C. Bull. (in Japanese), **17** (1990) 1.
- 10) Y.Kobayashi, M.Kikuchi and H.Watanabe, J. Radiat. Res., **34** (1993) 77.

2.7 THE USE OF POLLEN IRRADIATED WITH HELIUM ION BEAM FOR INTERSPECIFIC HYBRIDIZATION IN *NICOTIANA*

Masayoshi INOUE, Hiroshi WATANABE*,
Atsushi TANAKA*, Akio NAKAMURA**

Department of Agriculture, Kyoto Prefectural University,
*Department of Radiation Research for Environmental and
Resources, JAERI, **Department of Agriculture, University
of Osaka Prefecture

I. INTRODUCTION

The introduction of desirable genes from wild plants to crops is important in plant breeding, particularly, in relation to disease and/or insect resistance. In this connection, many attempts to get interspecific and intergeneric hybrid have been made. However, it is very difficult to obtain a viable hybrid in the case of wide cross, because of cross incompatibility and/or hybrid inviability. For overcoming these barriers, pollen irradiation^{2),3)}, ovule irradiation⁷⁾, ovule culture^{4),5)} and hormone treatment⁶⁾ were reported.

We have been searching for an effective procedure of interspecific hybridization in *Nicotiana*, and have already obtained viable hybrid between distantly related species, e.g. between *N.gosseii* and *N.tabacum*, by using gamma-ray-irradiated pollen¹⁾. The purpose of the present study was to investigate the effect of helium ion beam on pollen viability and the possibility of producing interspecific hybrid by using the irradiated pollen.

II. MATERIALS AND METHODS

(1) Plant materials

N.tabacum L., cv Bright Yellow 4 (BY-4) as cultivar, and *N.gosseii* Domin, *N.rustica* L., *N.repanda* Willd. and *N.glutinosa* L. as wild species, were used in the experiments.

(2) Pollen irradiation and pollination

Mature pollen of BY-4 was collected immediately before anthesis and stored in a desiccator. After 1 day, the collected pollen was held between kapton films (8.5 μ m thickness, Toray-Dupont Co.LTD.) and divided to several groups. A portion of them were irradiated with helium ion beam ($^4\text{He}^{2+}$) of 6MeV

and 60 ~ 65 nA (3MV Tandem Electrostatic Accelerator, Takasaki Establishment, JAERI). The rest was irradiated with ^{60}Co gamma-ray at the dose rate of 200Gy/hr (Institute for Advanced Science and Technology , University of Osaka Prefecture). The dose of helium ion beam was calculated as the gamma-ray-equilibrated, on the basis of the data performed by radiochronic dosimetry.

The flowers of the wild species were emasculated before anthesis and pollinated with the irradiated pollen.

(3) Pollen viability after irradiation

Pollen viability was determined in two ways: germination rate after 24hr-setting in agar plate (20% sucrose, 100ppm boric acid and 1% agar) under 25°C-dark condition and morphological change in pollen grains stained with aceto-carmin solution.

III. RESULTS AND DISCUSSION

After helium ion beam irradiation, pollen germination was reduced with the range over 1000Gy, and the degree of reduction was in proportion to the irradiation dose (Fig.1). Gamma-ray-irradiation over 2000Gy, also reduced

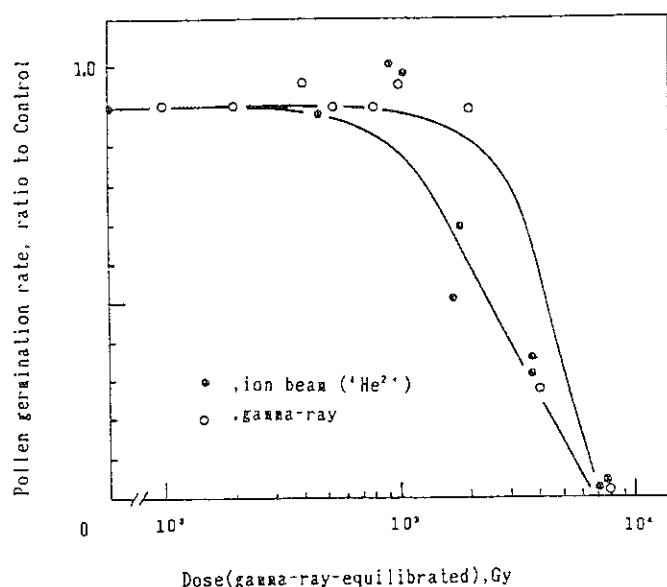


Fig.1 Changes of pollen germination after irradiation with helium ion beam or gamma-ray.



Fig.2 "Leaky"(center)pollen observed in pollen irradiated with helium ion beam

pollen germination drastically. In both regimens of helium ion beam and gamma-ray, most of the irradiated pollen could not germinate with around 8000Gy. From these results, it appears that pollen germination is a little more sensitive to helium ion beam than to gamma-ray.

When the irradiated pollen was stained with aceto-carmin, a different

feature was detected between helium ion beam and gamma-ray regimen. In the regimen of helium ion beam, there was "leaky pollen" (Fig.2), in which

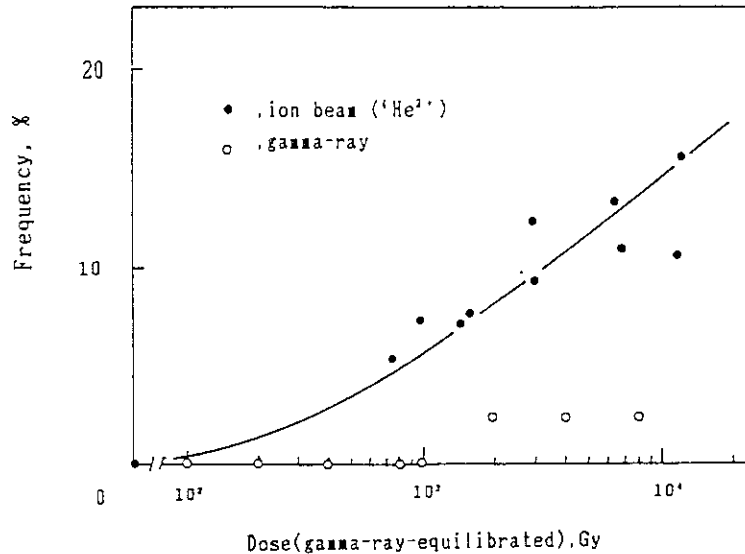


Fig.3 Frequency of leaky pollen

internal substance leaked through an opening in outer membrane of the pollen grain. After leakage, outer membrane remained open or closed. The frequency of leaky pollen significantly increased as the irradiation dose increased (Fig.3). On the other hand, such phenomenon was not observed in the gamma-ray regimen. Leaky

pollen seemed to result from physical lesion induced in outer membrane of pollen grain by helium ion beam. However, it is still too early to evaluate that the induction of leaky pollen is specific for ion beam. Further investigation using other kinds of ion, will be necessary before this effect can be evaluated.

Table 1 Effect of irradiation to pollen on seed formation

Combination	Irradiation *	Number of crosses	Number of capsules developed	Number of capsules fertilized
<i>N.gosseii</i> × BY-4	G	10	2	2
	I	44	30	1
<i>N.rustica</i> × BY-4	G	6	6	0
	I	30	26	5
<i>N.repanda</i> × BY-4	G	19	3	0
	I	44	12	10
<i>N.glutinosa</i> × BY-4	G	11	2	0
	I	35	0	0

* G; gamma-ray, 1×10^3 Gy.

I; helium ion beam, $9-17 \times 10^2$ Gy (gamma-ray-equilibrated).

Table 1 shows the results on seed formation in interspecific crosses between the wild species and the cultivar, using pollen irradiated with gamma-ray or helium ion beam. Pollen of the cultivar (*N. tabacum*, cv BY-4) was irradiated and used as the male parent in all crosses. In the cross of BY-4 × BY-4 (data not shown), about 50% of flowers crossed, yielded fertile seeds, and about 90% of them was viable to the mature stage, in both regimens of gamma-ray and helium ion beam. With regard to interspecific hybridization, it is almost impossible to obtain a viable hybrid by conventional cross, in the combination of *N. gossei*, *N. rustica* and *N. repanda* with *N. tabacum*. In these combinations, the irradiated pollen made seeds developed to germinate, and some of the resulting seedlings grew up to flowering. Reversely, in the combination of *N. glutinosa* × *N. tabacum*, where viable hybrid can be obtained through *in situ* cross, no seed was obtained with application of the irradiated pollen.

In conclusion, it is perhaps possible to say that effect of helium ion beam to pollen is different from that of gamma-ray, and also that cross incompatibility and hybrid inviability can be overcome to a certain extent by using pollen irradiated with ion beam.

REFERENCES

- 1) H. Yakushiji, M. Inoue and A. Nakamura, Jpn. J. Breed. 40 (Suppl.2) (1992) 444.
- 2) J.L. Jinks, P.D.S. Caligari and N.R. Ingram, Nature. 291 (1981) 586.
- 3) K.K. Pandey, Nature 256 (1975) 310.
- 4) N. Shizukuda and T. Nakajima, Jpn. J. Breed. 32 (1982) 371.
- 5) S.M. Reed and G.B. Collins, J. Hered. 69 (1978) 311.
- 6) W.M. Zhou, K. Yoshida, Y. Shintaku and G. Takeda, Theor. Appl. Genet. 82 (1991) 657.
- 7) Y. Shintaku, K. Yamamoto and T. Nakajima, Theor. Appl. Genet. 76 (1988) 293.

2.8 STUDIES ON INDUCED MUTATIONS BY ION BEAM IN PLANTS

Hirokazu NAKAI, Hiroshi WATANABE, Atsushi
TANAKA*, Shigeru KITAYAMA**, Tatsuo ASAI and
Kennichi SHINDOH

Shizuoka University, *JAERI, **RIKEN

High LET radiations, of which radiobiological actions are different from that of low LET radiations, could be specific mutagens for efficiently inducing mutations useful to plant breeding^{1, 2)}. The present studies were initiated aiming at application of various ion beams to plant mutation breeding.

In the studies, some preliminary experiments are required for accumulating basic data on radiobiological effects of the ion beams on plants, since there is little data previously obtained on this matter. This paper pertains to effects of an ion beam, He^{+2} , on the growth of rice plants in the first generation after irradiation (M_1).

In 1992, dry seed lots of rice, *Oryza sativa* L., c.v. Koshihikari, were irradiated by the ion beam (He^{+2}) from the AVF Cyclotron in JAERI operating at about 50 MeV. On the other hand, for comparison, the seeds were exposed to thermal neutrons with a flux of 2.5×10^9 Nth/cm²/sec for 0-6 hr in the heavy water facility of Kyoto University Reactor operated at 5000 KW, and exposed to gamma-rays of 0-600 Gy from a ⁶⁰Co source. After irradiation with the three mutagens, the seeds were brought back to Shizuoka University to grow in a condition of hydroponic culture at 25° C indoors. The plants were measured for root length and plant height 9 days after sowing.

The effects of gamma-rays, the ion beam (He^{+2}) and thermal neutrons on root length and seedling height are presented in Fig. 1 and Fig. 2. In the figures, the dose-response curves were drawn by the equation, $S = e(-\alpha \times D - \beta \times D^2)$, where S and D means degree of radiation damage relative to control and absorbed dose, respectively, and α and β are a constant to be calculated by experimental data. As seen

in Fig. 1 and Fig. 2, the dose-response curves of gamma-rays and the ion beams (He^{+2}) on both the traits were sigmoidal or somewhat sigmoidal, whereas those of thermal neutrons were rather exponential. The M_1 damage per unit of dose caused by thermal neutrons appeared to be larger than that by the ion beams (He^{+2}).

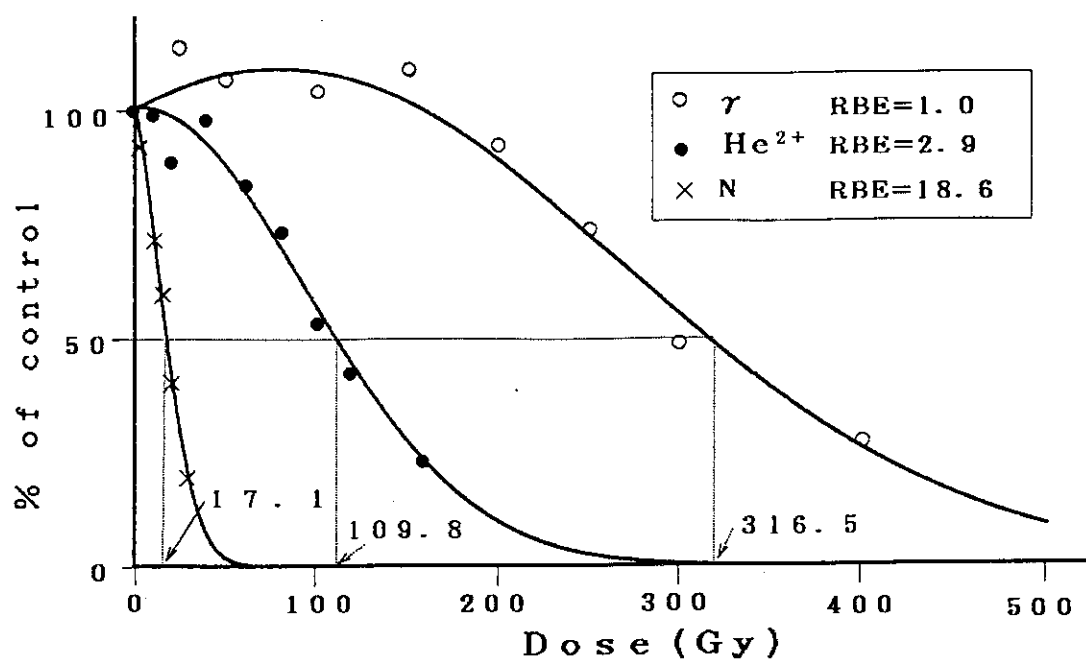


Fig. 1. Dose-response of gamma-rays, ion beams(He^{2+}) and thermal neutrons on root length in rice 9 days after sowing in M_1 generation

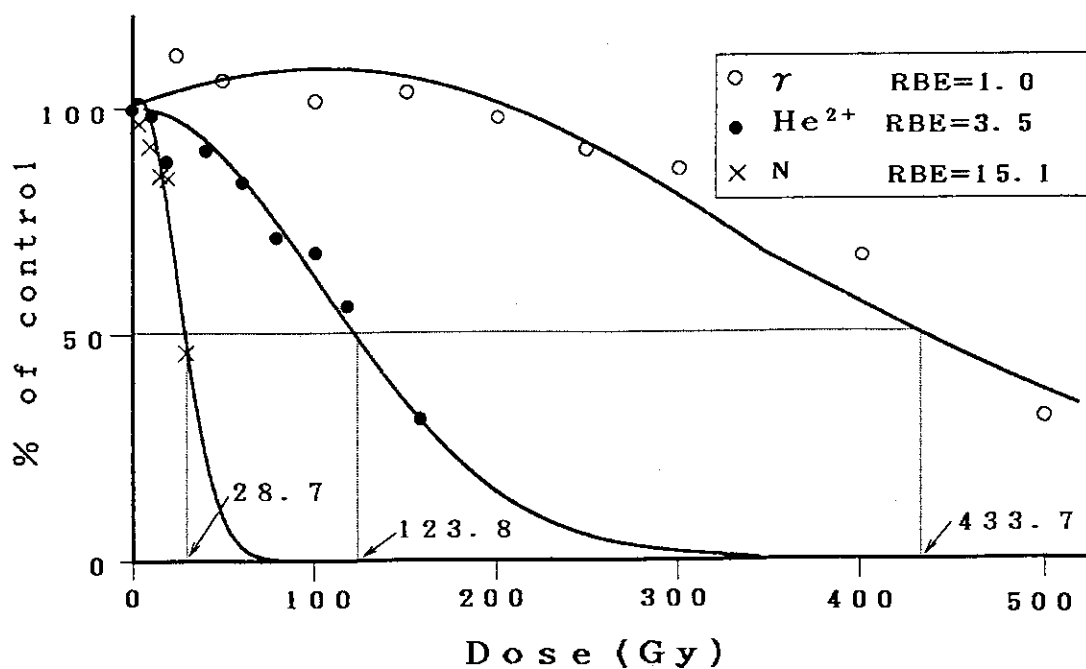


Fig. 2. Dose-response of gamma-rays, ion beams(He^{2+}) and thermal neutrons on seedling height in rice 9 days after sowing in M_1 generation

*) RBE(relative biological effectiveness) values of the ion beams and thermal neutrons relative to gamma-rays were calculated by the formula, D_{50} of relevant radiation / D_{50} of gamma-rays, where D_{50} means a dose which reduces the average values of root length and plant height to 50 % of control. The RBE values of the ion beams(He^{+2}) on root length and seedling height were 2.2 and 1.8, respectively. The RBE values of both radiations on root length were significantly higher than those on seedling height, supporting the previously reported data on RBE of thermal neutrons. This result is explained on the basis that the damage on root length was caused mainly by some chromosome aberration used, whereas that on seedling height mainly by some physiological event⁴⁾. The RBE values of the ion beam(He^{2+}) calculated in the present experiment were significantly higher than those of another ion beam, e.g. $^{14}\text{N}^+$, previously calculated in the studies using the Ring Cyclotron of RIKEN ; RBE values of $^{14}\text{N}^+$ on root length and seedling height were 2.2 and 1.8, respectively. This indicates that the biological effects of ion beams in plants may be different from one ion beam to another. Further experiments in detail on the biological effects of ion beams are in progress.

REFERENCES

- 1) H. Nakai, M. Saito and H. Yamagata, *Env. and Exp. Bot.* 20(1980)191.
- 2) H. Nakai and M. Saito, *ibid.* 25(1985)385.
- 3) A.M. Kellerer and H.H. Rossi, *Radiat. Res.* 47(1971)15.
- 4) Y. Kowayama, M. Saito and T. Kawase, *Japan. J. Breed.* 37(1987)299.

2.9 OPTICAL SPECTRA OF RABBIT RED BLOOD CELLS IRRADIATED WITH HEAVY ION BEAMS

Takashi FUJIMURA, Noriyuki ISHIHARA, Hiroshi WATANABE,
Hideki OHMICH, *Harumichi KOBASHI, **Mamoru TAMURA

JAERI, *Gunma University, **Hokkaido University

I. INTRODUCTION

Several investigations were carried out for the gamma-ray irradiation effect of purely isolated hemoglobin solution¹⁾, and it was established that methemoglobin is formed from hemoglobin by radiation oxidation. There have been little data of spectrophotometric study of irradiation effect on red blood cells containing hemoglobin. We have reported optical absorption spectra of red blood cell suspension irradiated by gamma-ray²⁾. In that study, an absorption band due to methemoglobin was observed for red blood cells irradiated by gamma-ray. During ion-beam irradiation, optical detection technique could follow reactions induced by irradiation inside organism. For the first step of the studies along this line, optical absorption spectra were measured for rabbit blood cells after heavy ion-beam irradiation in the present work.

II. MATERIALS AND METHODS

Red blood cells were separated from fresh blood taken from rabbits in the morning of the experimental day. Phosphate buffer (pH 7.3) containing 1% heparin was added to the fresh blood and centrifuged at 2500 r.p.m. for 5min. This treatment was successively cyclized three times. Thus obtained condensed red blood cell suspension was coated on the inside bottom of an optical cell. Sample was irradiated in air by $^{40}\text{Ar}^{3+}$ heavy ion-beam from AVF cyclotron. The heavy ion-beam was ejected from beam line to atmosphere through thin polymer film³⁾. Just after irradiation, the buffer was added to the sample at the bottom of the optical cell, and thus red blood cell suspension subject to optical measurement was prepared.

The Yunisoku USP 410 spectrophotometer was used for photometrical study. Light source was 100-W halogen lamp. Light shorter than 500 nm from source was eliminated with a cut-off filter, then monochromated with a diffraction grating, and the monochromatic light was introduced to the

suspension containing red blood cells irradiated with the ion-beam. The transmitted light was detected with photomultiplier by photon counting method.

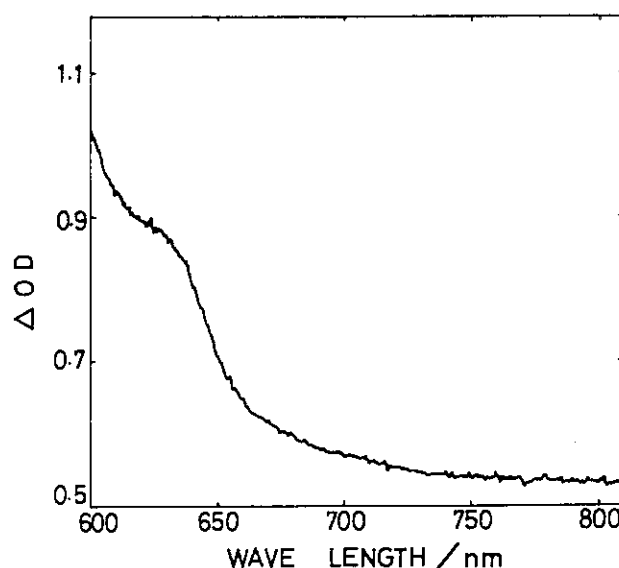
III. RESULTS AND DISCUSSION

Fig. 1 shows the spectrum of rabbit red blood cells dissolved in the buffer after irradiation with the $^{40}\text{Ar}^{13+}$ heavy ion. This spectrum is the difference of irradiated one and nonirradiated one. Increment of absorption band around 630 nm can be seen clearly.

It has been established that methemoglobin is formed by radiation oxidation with gamma-ray in purely isolated hemoglobin solution and methemoglobin have an absorption band at 630 nm. We have reported optical absorption spectra of rabbit red blood cell suspension irradiated by gamma-ray from $^{60}\text{Co}^{2)}$. At 630 nm, a clear absorption band due to methemoglobin was observed. In the present work, the shoulder of absorption band at 630 nm is almost the same as that in rabbit red blood cell suspension irradiated by gamma-ray. Therefore, this absorption band in Fig.1 is attributable to methemoglobin formed from hemoglobin in red blood cells by radiation oxidation induced by the irradiation with the $^{40}\text{Ar}^{13+}$ beam.

Fig.1

Optical absorption spectrum of rabbit red blood cells dissolved in the phosphate buffer after irradiation with $^{40}\text{Ar}^{13+}$ heavy ion-beam. The difference spectrum of irradiated one and nonirradiated one.



- 1) Z. Szweda-Lewandowska, M. Puchala, and P. A. Osmulski, *Radiat. Environ. Biophys.* 28, 39 (1989)
- 2) T. Fujimura, N. Ishihara, M. Kouno, T. Watanabe, H. Ohmichi, H. Kobashi, and M. Tamura, Abstract of 35-th Symposium on Radiation Chemistry, Abst. No. 3016 (1992) and submitted for publication.
- 3) H. Watanabe et al., private communication

2.10 EFFECT OF ION BEAM IRRADIATION ON SEED GERMINATION AND GROWTH OF PHALAEENOPSIS

Takayoshi OHARA, Noritoshi FUWA, Tatsuya HARADA and Hiroshi WATANABE*

Biological Engineering Laboratory, Asahi Industries Co., Ltd., *Department of Research, JAERI

I. INTRODUCTION

Up to now, usually gamma-rays or X-rays have been used for mutation breeding of plants. Generally ion beams irradiation can give higher mutation rates than gamma- or X-rays because ion beams have higher LET, and there is a possibility that it will become an effective method for plant breeding.

In these days, Phalaenopsis has become one of the most important orchids from a horticultural view point. We had investigated effects of gamma-irradiation on germination of Phalaenopsis seeds in the previous experiment. To find out suitable ions, LET and dose for mutagenesis of Phalaenopsis, we investigated effects of ion beams on seed germination of Phalaenopsis in this study.

II. MATERIALS AND METHODS

(1) Plant material

Seeds of Phal. amabilis var. formosana (No. AM36 x AM37) were used. These seeds were almost mature (25 weeks after crossing).

(2) Sterile seeding

Seeds were taken out sterilely from capsule and suspended in liquid medium consisting of 3,500 mg/l Hyponex (N:P:K=7:6:19), 100 mg/l myo-inositol, 1 mg/l nicotinic acid, 1 mg/l thiamine-HCl, 20 g/l sucrose (pH 5.7). The density of seeds was adjusted to 200 seeds/ml. 0.5 ml of the suspension was plated onto 5 ml of the solidified medium consisting of 3,500 mg/l Hyponex (N:P:K=7:6:19), 100 mg/l myo-Inositol, 1 mg/l nicotinic acid, 1 mg/l thiamine-HCl, 20 g/l sucrose, 2 g/l activated charcoal, 4 g/l Gellan gum (pH 5.7) in plastic Petri dish (35 mm x 10 mm). The plates were covered with a piece of Saran Wrap previously sterilized with UV.

(3) Irradiation and Incubation

The seeds on Petri dishes were irradiated by 50 MeV He^{2+} with 1 nA using Irradiation Apparatus for Seed at TIARA. Total radiation dose was set at 0, 6, 18, 30, 54, 102 and 210 Gy. After 24 hours of cooling, the seeds were incubated at 25 °C with 16-h light(1,000 lux) and observed periodically.

(4) Observation

Each 100 seeds (50 seeds x 2 Petri dishes) were observed by stereoscopic microscope, and then germination rate and greening of embryo after germination were examined. Germination was defined that the seed coat was broken by enlarged embryo.

III. RESULT AND DISCUSSION

Changes of germination rate were shown in Fig.1. Irradiation at 210 Gy caused delay of the germination while irradiation at 0 to 102 Gy did not have any effect on germination rate of Phalaenopsis seed. It suggests that minimum irradiation dosage to affect germination of Phal. amabilis was approximately 210 Gy. Unfortunately greening of embryo was scarcely observed in this study though usually most of embryo become green. It was supposed that it would be due to a problem of medium composition. In the previous experiment, it has been showed that gamma-irradiation up to 1 kGy had no effects on the germination rate of Phalaenopsis. Therefore He^{2+} ions appear to be more effective on inhibition of germination than gamma-rays.

To find out suitable dose of ion beams, it is necessary to investigate the effect of irradiation at more than 210 Gy on germination of Phalaenopsis seeds and development of those seedlings.

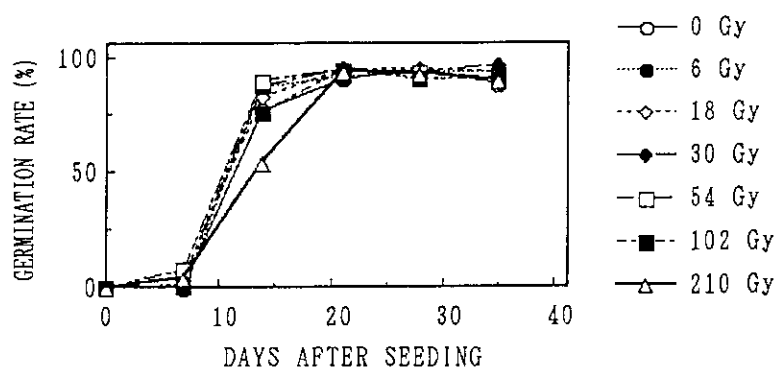


Fig.1. Effect of He^{2+} ions on germination rate of Phalaenopsis

2 . 1 1 RADIATION SENSITIVITIES OF PROTOPLASTS OF CABBAGE (*BRASSICA OLERACEA*) IRRADIATED BY ION BEAMS OR X-RAYS

Hiroshi WATANABE, Atsushi TANAKA, Seiji MOCHIZUKI* and
Takayoshi NISHIHARA*

Department of Radiation Research for Environment and Resources, JAERI

*Hashie Institute for Biological Sciences, Kaneko Seeds Co., LTD.

I. INTRODUCTION

Plant protoplasts are one of the most important vehicles for crop improvement through mutation, somatic hybridization and genetic modification by uptake of foreign genome. In recent years an asymmetric protoplast fusion is a useful tool not only for hybridization between distantly related species but also for cybrid formation. By the fusion, nuclei and cytoplasm from both parents can be mixed into a new nucleus-cytoplasm combination through the process of plant regeneration. A male sterility controlled by cytoplasmic genome has been transferred from one nuclear genotype to another in several plant species. In the process of fusion, X-rays, UV light or iodoacetate treatments have so far been used in order to inactivate the nucleus of cytoplasm donor parent and subsequently to obtain more efficiently the desired combination. However, these treatments are not enough to inactivate only the nucleus, because a recovery of the damaged nucleus takes place and heavy treatment causes the damages of cytoplasm.

Many studies have demonstrated that ion beams cause more efficiently the inactivation of nucleus than other radiations, since the charged particles such as He, C, and Ar deposit locally the energy to cells. However, there have been no studies on the effect of ion beams on protoplasts of plant. Therefore, we conducted to measure the radiation sensitivity of protoplasts of cabbage which was chosen as a sample for the fusion with radish. In the present paper, comparison of effects between ion beams and X-rays is described.

II. MATERIALS AND METHODS

(1) Protoplast Isolation

Leaf tissue was sliced into 1 mm wide strips, and incubated in enzyme solution at 25°C for 3.5hr with shaking at 30rpm. The enzyme solution at pH5.8 consisted of Cellulase Onozuka RS (0.5%), Pectryase Y-23 (0.1%), mannitol (0.5M) and CPW solution (KH_2PO_4 27.2mg, KNO_3 101mg, $\text{CaCl}_2 \cdot 2\text{H}_2\text{O}$ 1480mg, $\text{MgSO}_4 \cdot 7\text{H}_2\text{O}$ 246mg, KI 0.16mg and $\text{CuSO}_4 \cdot 5\text{H}_2\text{O}$ 0.025mg per liter). The protoplasts were washed 3-4 times with mannitol-

CPW solution by centrifugation at 500rpm for 3min. The density of protoplast suspension was adjusted to about 1×10^5 per ml for the following experiments.

(2) Irradiation

One ml of protoplast suspension was put into a petri dish of 3.5mm ϕ , and irradiated by 50MeV $^4\text{He}^{2+}$ ions scanned with square of more than 50mm from cyclotron using Irradiation Apparatus for Seed (IAC) in TIARA. Ion fluences were determined by CR-39 film track detector. The doses were calculated from the fluence and LET calculated with ELOSS code. X-ray irradiation was performed using 60KV X-ray generator (OM-60R) in Hashie Institute.

(3) Protoplast Culture

The protoplasts of about $10^5/\text{ml}$ were incubated in basic medium which contained 1/2 MS medium enriched with 2,4-D (1ppm), BA (0.5ppm), sucrose (1%) and mannitol (0.4M). The cultures were incubated at 25°C in the dark for 7 days, then exposed to light for differentiation. One ml of flesh basic medium was added to the culture every 10 days.

III. RESULTS AND DISCUSSION

Table shows the radiation sensitivities of protoplasts irradiated with He ions or X-rays. In the unirradiated protoplasts, calli of 2mm size were formed after incubation for about one month. In the case of He ion irradiation, the protoplasts were irradiated with doses up to 9 Gy, but no calli were formed even at 0.5 Gy. At the dose, any proliferation of protoplasts was not observed during the cultivation. On the other hand, X-ray irradiation at 100 Gy also prevented the formation of calli, but at the dose the protoplasts could divide cells several times. These results indicate that He ions induce more efficiently the inhibition of cell division than X-rays. It is further clear that the protoplasts of cabbage are very sensitive to ion beams. The detailed determination of radiation sensitivity is in progress.

Table Radiation Sensitivity of Protoplasts Irradiated with He Ions or X-Rays

Dose (Gy)	Number of calli	
	He ions	X-rays
0	30	30
0.5	0	—
1.0	0	—
1.6	0	—
100	—	0*

* The protoplasts can divide several times, but not form callus.

3. Radiation Chemistry

3.1	Characteristics of Various Film Dosimeters for Ion Beams	
	T.Kojima, H.Sunaga, H.Takizawa and J.Okamoto	65
3.2	Microdosimetry with Heavy Ions	
	H.Namba, M.Taguchi, K.Furukawa, S.Ohno and Y.Aoki	69
3.3	The Study of Chemical Processes Induced by Heavy Ions	
	H.Namba, M.Taguchi, H.Koizumi, H.Hiratsuka and H.Yoshida	72

3.1 CHARACTERISTICS OF VARIOUS FILM DOSIMETERS FOR ION BEAMS

Takuji KOJIMA, Hiromi SUNAGA, Haruki TAKIZAWA,
Jiro OKAMOTO

Department of Materials Development, JAERI

I. INTRODUCTION

Dosimetry for high-energy ion beams has been studied on the basis of measurement of particle fluence so far. However, dose measurement as a function of depth of penetration in materials is indispensable to interpret radiation effects on organic materials and biological samples, because of dose ununiformity within the depth of materials of interest.

The authors have been developing precise dosimetry techniques for both gamma rays and electron beams of energies from 0.15 to 3 MeV. Preliminary studies on fluence measurement of ion beams and dose-response characteristics of film dosimeters were done using cyclotrons at RIKEN¹⁾ and Institute for Nuclear Study/University of Tokyo²⁾. The knowledge and techniques on fluence monitoring, characterization of irradiation field, and on irradiation of dosimeters obtained through these studies may lead us to settle the base of dosimetry and irradiation techniques at TIARA. As a starting point of ion beam dosimetry study, dose-responses of various film dosimeters were studied using proton and helium beams, in parallel with characterization of the irradiation field of cyclotron beams.

II. EXPERIMENTAL

(1) Film dosimeters

Alanine -PE³⁾, GAF(GAF Chemicals Corporation), RCD(FWT-60, Far West Technology), and CTA(FTR-125, Fuji Photo Film Co., Ltd.), were used as film dosimeters with a thickness range of 50 to 220 μm , because these are well characterized for gamma rays and electron beams and can be applied to high-energy ion beams with short penetration range. Table 1 lists composition of dosimeter

Table 1 Properties of film dosimeters

dosimeter		Alanine-PE* ¹	GAF* ²	RCD* ³	CTA* ⁴
composition ratio		C ₁₂ H ₂₅ O ₅ N ₃	C ₁₀ H ₈ O ₄	C ₁₂ H ₂₂ O ₃ N ₂	C ₆ H ₄₉ O ₄₂ P ₂
density	g/cm ³	0.81	1.20	1.08	1.29
thickness	μm	223	100	50	125
ST* ⁵	20MeV H(+)	25.7	24.3	26.1	24.3
ST	50MeV He(2+)	153.3	144.5	155.2	143.7
ST	20MeV He(2+)	324.3	305.3	329.3	300.8

*1 Alanine-PE: DL-α-alanine 60wt%, Polyethylen 40wt%

*2 GAF: Polyester based dye film *3 RCD(FWT-60): Nylon polyamido

*4 CTA(FTR-125): Cellulose-triacetate 85wt%, Triphenyl-phosphate 15wt%

*5 mass stopping power(initial), MeV/g/cm²

materials, physical properties, and mass stopping power values calculated using OSCAR code.

(2) Irradiation

Film dosimeters were irradiated using 100 x 100 mm² scanning beams of 20-MeV proton and 20-MeV and 50-MeV helium ions from the AVF cyclotron in the evacuated "wide-area ion irradiation chamber"⁴⁾. Beam currents were 200 nA for CTA and 20 nA for others. Five pieces of dosimeter films were arranged side by side on 125 μm-thick kapton film mounted on the graphite absorber, and were positioned in an limited irradiation zone of two-dimensional scanned beams to avoid non-uniform local areas such as the edge and center region⁵⁾. Fluence uniformity on dosimeters is expected within ±3%. Dosimeters were irradiated to four different doses in the linear dose-response region: 2, 4, 6, 8 kGy for alanine-PE, RCD and GAF, and 40, 60, 80, 100 kGy for CTA. Beam fluence was monitored in terms of charge collected in a backing absorber after passing in the dosimeters.

(3) Readout system

Alanine-PE dosimeters were analyzed by an ESR dosimetry system (modified JEOL JES-3000) in terms of ESR signal amplitude per unit mass. Dosimeters of RCD, GAF and CTA were analyzed in terms of optical density change per unit thickness at specified wavelengths of 600 nm, 400 nm and 280 nm, respectively, by using a UV-spectrophotometer. Nominal doses in films were calculated

in the product of measured integrated charge and mass stopping power.

III. RESULT AND DISCUSSION

Dose-responses of film dosimeters are defined as ESR signal amplitude or optical density change per unit dose. These values were evaluated from the slope of linear dose-response relations. Dose-responses normalized to those for 20-MeV proton ("relative effectiveness"), were plotted in Fig.1 as a function of initial mass stopping power of the irradiated particles in linear scale. Variation in dose-responses among five dosimeters replicates irradiated simultaneously was within $\pm 5\%$. Data on CTA obtained at RIKEN (solid line) and data on RCD reported by J.W.Hansen⁶⁾ are also plotted in Fig.1 for comparison. Relative effectiveness decreases with increasing stopping power for four kinds of film dosimeters even though they have different compositions and dose-responses. This tendency roughly agrees with previous results at RIKEN and those of RCD reported by Hansen, except for the case of GAF. However, the result was obtained from only one trial at each beam condition. Reproducibility check of experiments is necessary for further discussion.

Through these experiments, the followings arose as items which should be examined in the next experiments: stability of

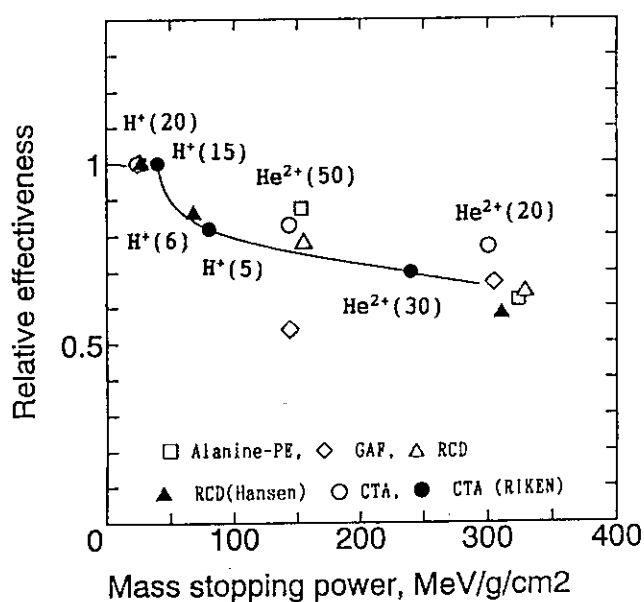


Fig.1 Dose-response normalized to those for 20-MeV proton ("Relative effectiveness"), plotted as a function of initial stopping power of the irradiated particles in linear scale. () shows energy(MeV) of the incident particles.

beam-spot size , stability of fluence profile in radiation zone, precision of integrated charge measurement at a very low current, estimation of the contribution of back-scattered secondary electrons escaped from the backing absorber surface to integrated charge measurement.

IV. SUMMARY

Dose-response characteristics of four kinds of film dosimeters were studied preliminarily for 20-MeV protons, and for 20-MeV and 50-MeV helium beams. Relative effectiveness as a function of stopping power was roughly estimated for four kinds of film dosimeters. The reproducibility of these results, and the reliability of monitoring system for integrated charge measurement will be examined in the next experiments.

For systematic dosimetry study, we have a plan to design and develop an irradiation chamber with well-characterized irradiation field, a precise online beam monitoring system without intervention by target samples, mechanical arrangement for uniform irradiation of film dosimeters, and precise dosimetry system.

ACKNOWLEDGEMENT

The authors express their appreciation to Sasuga T. and Kudo H. of JAERI for their technical assistance in handling of the wide-area ion irradiation chamber.

REFERENCES

- 1) H. Sunaga, R. Tanaka, K. Yoshida, and I. Kohno: RIKEN Accel. Prog. Rep. 22 (1988) 130
- 2) T. Kojima, R. Tanaka and Y. Uwamino: Annual Report of Institute for Nuclear Study, University of Tokyo (1987) 43
- 3) T. Kojima, A. Ranjith H.L., Y. Haruyama, S. Kashiwazaki and R. Tanaka : Appl. Radiat. Isot. 44, (1993) 41
- 4) T. Sasuga, H. Kudo, T. Seguchi: TIARA Annual Report Vol.1 (JAERI-M93-047), (1992) 117
- 5) K. Arakawa et al.: TIARA Annual Report Vol.1 (JAERI-M93-047), (1992) 31
- 6) J. W. Hansen: Risø R-507 (1984)

3.2 MICRODOSIMETRY WITH HEAVY IONS

Hideki NAMBA, Mitsumasa TAGUCHI, Katsutoshi FURUKAWA*,
Shin-ichi OHNO and Yasushi AOKI

Department of Radiation Research for Environment and Resources,
JAERI, *Department of Chemistry, JAERI

I. INTRODUCTION

It is well known that the radiation effect (e.g., lethal effect in biology) of high energy ion or neutron beam is different from that of γ -ray or electron beam. Usual LET effect did not explain the biological effect of radiation, the concept of microdosimetry was established¹⁾. The ion beam energy deposited to materials is not uniform, and has some spatial distribution that is so-called "track" structure.

We have installed a new experimental apparatus for basic study on radiation chemistry with heavy ions (EA-BRACHI) at HX1 port of AVF cyclotron in TIARA last year²⁾. In this year with EA-BRACHI, we have started to measure the spatial distribution of energy deposition to gaseous Ar from high energy Ar ion beam.

II. EXPERIMENTAL

EA-BRACHI is connected to a vertical beam port of AVF cyclotron in Second Heavy Ion Irradiation Room. EA-BRACHI has three stage differential pumping system that consists of three sets of pumps, three tantalum collimators (5mm, 0.5mm and 0.1mm) and pressure control system. It is possible to control the pressure in the third chamber with this system during ion beam irradiation.

Gaseous Ar is introduced to the third chamber with controlling its flow rate by mass flow controller (MKS 147B). The pressure of the gas is measured with pressure sensors (MKS Baratron 122A and 127A), and controlled with pressure controller (MKS113A) by pumping through throttling valve (MKS 253A-2-4CF-2) connected to the turbo-molecular pump (Osaka Vacuum TG1000M) in the third chamber.

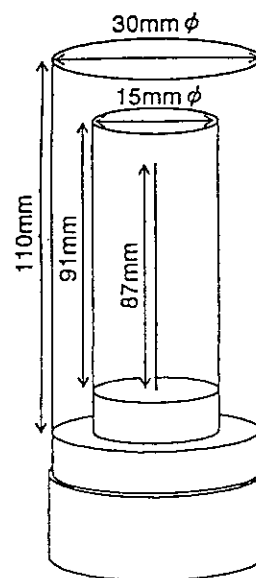


Fig. 1. Scheme of ionization chamber.

Heavy Ar ion beam (175MeV) from the cyclotron are introduced to the EA-BRACHI through a bending magnet of HX1 port. The beam monitoring and position setting were done as described before²⁾.

Two small ionization chambers, as shown in Fig. 1, were set on a stage, which are possible to move all directions with an accuracy of $5\mu\text{m}$. The ionization chamber has three electrodes, namely; meshed guard electrode, meshed high voltage electrode and wired collecting electrode. The distance from the center of ion beam was changed with moving the stage. Ionization current induced by Ar ion beam was measured by two electrometers (Keithley 617) connected to the collecting electrodes of ionization chambers. D.C. voltage was supplied to the high voltage electrode from high voltage power supplies (Hamamatsu C3350). After amplifying the measured ionization current, the signals were transferred to the neighboring operation room named Heavy Ion Preparation Room that is 25m apart from the Second Heavy Ion Irradiation Room. The signals were digitized with two electrometers (Advantest 8651, R8240) and accumulated with a computer (HP85).

III. RESULTS AND DISCUSSION

Fig. 2 shows the applied voltage dependence of induced ionization current measured at different distance from Ar beam in 0.95 torr Ar irradiated with 175MeV Ar beam. According with the distance from the center of ion beam, ionization current is decreased. The applied voltage region between 20 to 40V, the current seems to be saturated. While more than the saturation region, the ionization current is increasing rapidly.

The saturation current at different distance from the center of ion beam is shown in Fig. 3. The current is corresponds to the amount of ions produced inside of the ionization chamber. The amounts of produced ions are predicted³⁾ to be proportional to reciprocal square of the distance (R).

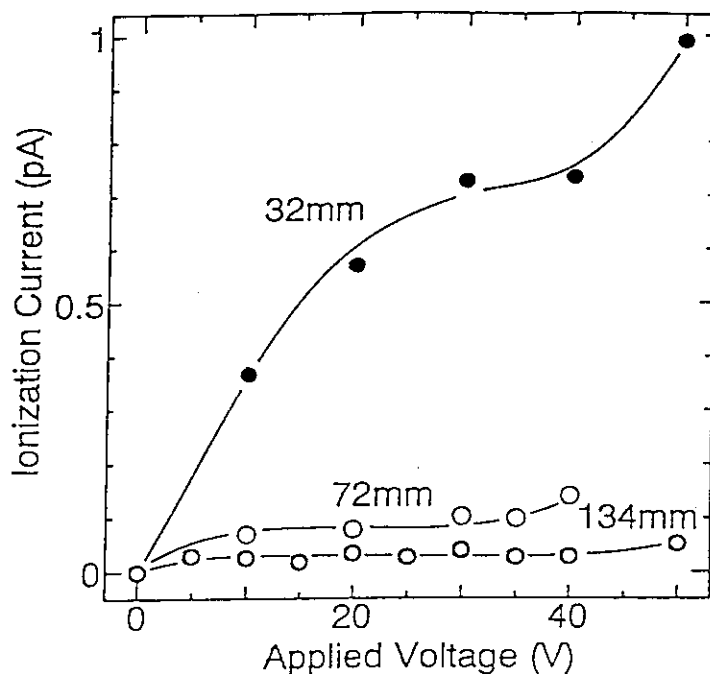


Fig. 2. Applied voltage dependence of induced ionization current.

The solid line in the figure indicates the reciprocal of R^2 . The line and the experimental results correspond well.

The radial distance in water [R (nm)] is possible to evaluate using the radial distance in gas with density ρ [R_p (nm)] as follows;

$$R = R_p \cdot \rho_g / \rho_{H_2O}.$$

Where ρ_g is the density of gas (g/cm^3) and ρ_{H_2O} is the density of water (g/cm^3).

The radial distances in gas that we have measured in this study, 32 to 134 mm, are corresponding to the distances 66 to 278 nm in water.

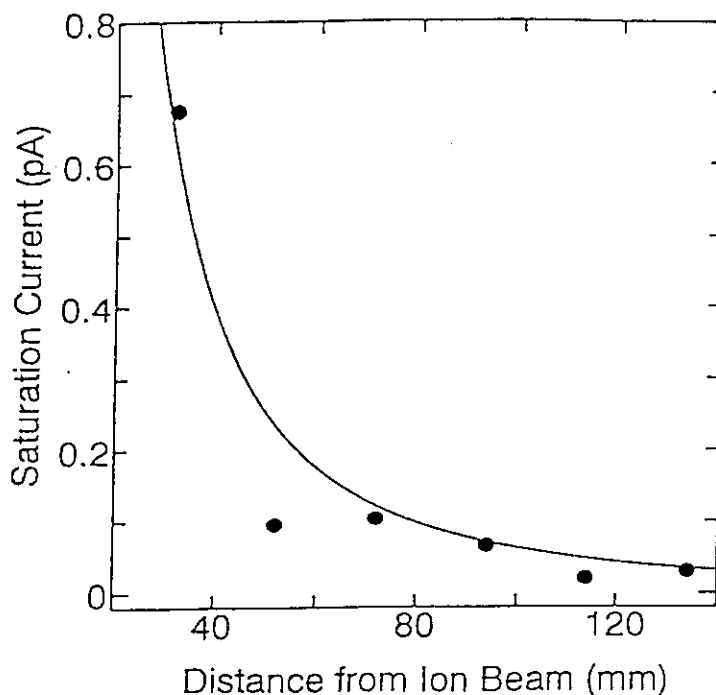


Fig. 3. Saturation current at different distance from the center of ion beam.

REFERENCES

- 1) ICRU, "Microdosimetry", **ICRU Report 36** (1983).
- 2) H. Namba, Y. Aoki, M. Taguchi and K. Furukawa, Experimental Apparatus for Basic Radiation Chemistry with Heavy Ion Beams, **JAERI TIARA Annual Report 1**, 163 (1992).
- 3) R. Katz, B. Ackerson, M. Homayoonfor and S. C. Sharma, Inactivation of Cells by Heavy Ion Bombardment, **Radiat. Res.**, 47, 402 (1971).

3 . 3 THE STUDY OF CHEMICAL PROCESSES INDUCED BY HEAVY IONS

Hideki NAMBA, Mitsumasa TAGUCHI, Hitoshi KOIZUMI*,
Hiroshi HIRATSUKA** and Hiroshi YOSHIDA*

Dept. of Radiation Research for Environment and Resources, JAERI,

*Faculty of Engineering, Hokkaido University,

**Faculty of Engineering, Gunma University

I. INTRODUCTION

It is well known that the radiation effect (e.g., lethal effect in biology) of high energy ion or neutron beam is different from that of γ -ray or electron beam. The biological or chemical effects induced by radiation occur through the energy deposition or energy transfer (physical process), formation of unstable components (e.g., radicals and ions) and the reaction of them with matters (chemical process), and finally they appear as "radiation effects". The importance of chemical process is very clear for radiation chemists, however, few research works have been done both theoretically and experimentally.

In this study, we will report about two items related to chemical process induced by ion beams. The first item is the investigation of radical formation itself. Radicals are produced in organic compounds with irradiation of ion beams. A few kinds of radicals are rather stable even at room temperature. We can measure these radicals with optical absorption, fluorescence and/or ESR measurements. The second item is a research of micro-regional energy deposition through the measurement of radicals produced in alanine dosimeter. In both experiments, ion beam irradiation were done with EA-BRACHI¹⁾ that was installed at HX1 port of AVF cyclotron in TIARA, and so-called "Off-line" measurements were done.

II. ION BEAM IRRADIATION

Heavy ion beams (175MeV and 460MeV) from cyclotron were introduced to the EA-BRACHI through a bending magnet of HX1 port. Irradiated position and shape of the beam were monitored by a MgO beam monitor. A tantalum collimator with 5mm ϕ aperture was set on a remote-controlled XY-stage (Ozak XYG) with an accuracy of 5 μ m. An 300mm ϕ rotatable stage was installed in the chamber for sample irradiation. The stage had twenty irradiation ports for 10mm ϕ samples, three beam monitors and a Faraday cup. The chamber was evacuated by a turbo-molecular pump (Osaka Vacuum TG600M) and a

rotary pump. The beam monitoring and beam alignment were done as described before¹⁾. The samples were set on the irradiation ports of rotating stage. The irradiated beam currents were measured by the Faraday cup on the stage just before and after the irradiation.

III. SAMPLES AND MEASUREMENTS

(1) Film Dosimeters

Film dosimeters are used for dosimetry of γ -ray and electron. Among them, RCD and CTA are commonly used. The research to use these dosimeters for the dosimetry of ion beam has recently started. RCD (Far West Technology: FWT-60-00) film dosimeter, which contains hexahydroxyethyl aminotriphenylnitrile in nylon film, has a thickness of $50\mu\text{m}$ and its size is $10\text{mm} \times 10\text{mm}$. CTA (Fuji Film: FTR-125) film dosimeter, which contains triphenylphosphate in cellulose triacetate, has a thickness of $125\mu\text{m}$. The samples were cut $8\text{mm} \times 12\text{mm}$.

The difference of optical absorption before and after the irradiation was measured with each sample using a spectrophotometer (Beckman: DU-65) and two-dimensional scanning micro-spectrophotometer (NALMI: NLM-301) in JAERI Takasaki.

(2) Acridine in PVA

There are not so many organic compounds that produce long-lived radicals at room temperature. Radical from acridine in film is one of the rare stable ones. Acridine was doped in PVA (Polyvinylalcohol) film with a thickness of $100\mu\text{m}$. The radical formation was measured by optical absorption by the spectrophotometer.

(3) Alanine

Alanine is famous for its stable radical formation by irradiation. Rod type of alanine dosimeter (Amino Gray) is used as standard dosimeter for γ -ray. However, it need to use film type²⁾ for ion beam irradiation. Two different type of alanine film dosimeter were used. One contains 60wt% alanine and 40wt% polyethylene, the other contains 50wt% alanine and 50wt% polyethylene. The radicals produced in the alanine dosimeter were measured using ESR spectrometer(Varian E109) in Hokkaido University.

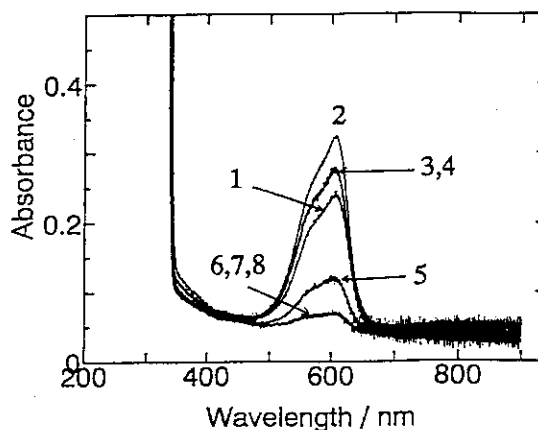


Fig. 1. The absorption spectra of RCD films after the irradiation of Ar^{13+} (460MeV, 5.5pA, 550s). The numbers corresponds to the number of layers.

IV. RANGE OF ION BEAMS

Fig. 1 shows the absorption spectra of RCD films after the irradiation of Ar^{13+} (460MeV, 5.5pA, 550s). Eight RCD films with a thickness of $50\mu\text{m}$ were set in layers. The number in the figure indicates the number of layers that ion beam have passed through. The figure clearly indicates that the energy deposition from ion beam was terminated in the 5th layer. The range 200 – $250\mu\text{m}$ obtained from this result is close to the calculated range $260\mu\text{m}$.

The two-dimensional absorption spectra of two RCD films at 510nm after the irradiation of Ar^{8+} (175MeV, 6.6nA, 300s) are shown in Fig. 2, where (1) and (2) indicate first and second layers. Fig. 3 shows the spectra of CTA films at 280nm after the irradiation of Ar^{8+} (175MeV, 1.0nA, 60s). Ar^{8+} ion reached second layer of RCD, however, did not reach second layer of CTA. That corresponds to the range of Ar^{8+} ($70\mu\text{m}$) that is calculated by TRIM code.

V. RADICAL FORMATION IN ACRIDINE

Fig. 4 shows the absorption spectra of acridine radicals produced by the irradiation of Ar^{13+} . The peaks near 490nm and 520nm increases with increasing dose. This is the first stable radical that was produced by heavy ion beams and was detected by optical measurement at room temperature.

VI. MICRO-REGIONAL ENERGY DEPOSITION

The ion beam energy deposited to materials is not uniform, and has some spatial

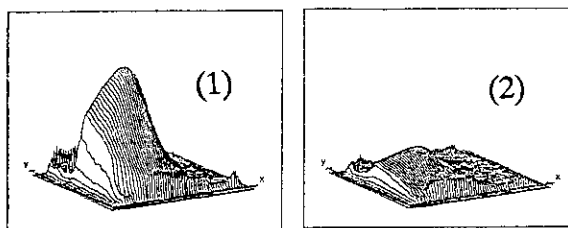


Fig. 2. The two-dimensional absorption spectra of two RCD films at 510nm after the irradiation of Ar^{8+} (175MeV, 6.6nA, 300s). (1): first layer, (2): second layer. Scanning area is 12mm X 12mm.

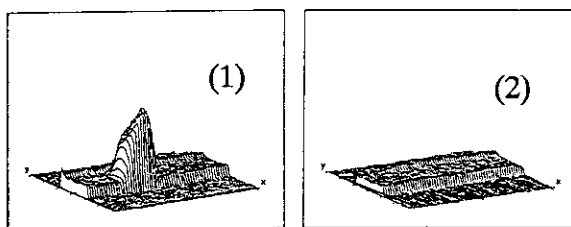


Fig. 3. The two-dimensional absorption spectra of two CTA films at 280nm after the irradiation of Ar^{8+} (175MeV, 1.0nA, 60s). (1): first layer, (2): second layer. Scanning area is 24mm X 24mm.

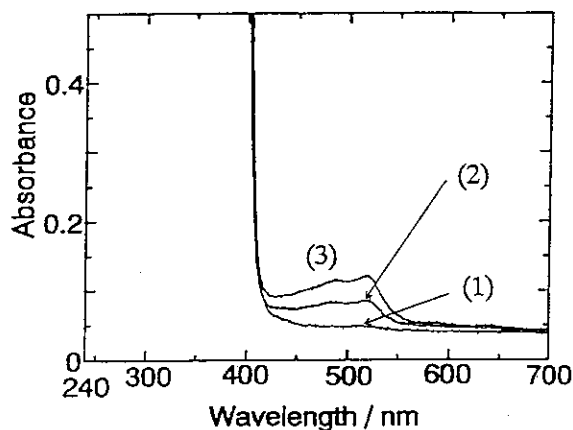


Fig. 4. The absorption spectra of acridine radical produced by the irradiation of Ar^{13+} (460MeV). (1): 6.4pA, 93s, (2): 6.9pA, 493s, (3): 5.7pA, 1060s.

distribution that is so-called "track" structure. The distribution of radicals produced by the ion beam irradiation is not uniform according with the track. The distribution of radicals is affected by diffusion and recombination of the radicals and their precursors as well as the original track structure. Then finally it will reach some equilibrium. The distribution is called "chemical core".

In case of light ion beams (H, He), yield of radical (amount of produced radical per ion) was constant at low incident ion density (number of incident ions per area) region and was decreased at more than 10^{12} ions/cm². This indicates chemical core radius produced in alanine by light ion beams is about 5nm.

Fig. 5 shows the relationship between radical yield and incident ion density by irradiation of Ar¹³⁺ (460MeV) and Ar⁸⁺ (175MeV). The radical yield decreases as increasing incident ion density and has no constant region more than 10^9 ions/cm². It will correspond to the radius of more than 100nm. There is some difference in the feature of chemical core produced by high energy heavy ion beams and light ion beams. It is known that dose response curve of CTA film dosimeter has great discrepancy between light beams (e⁻, H, He) and heavy ion beams (C, O etc.,)³⁾. It needs more precise knowledge of energy deposition and chemical reactions in ion beam irradiated matters to clarify the discrepancy.

ACKNOWLEDGEMENT

The authors wish to express their thanks to Mr. Takuji Kojima of JAERI for his kind offer to use alanine film dosimeters that is under development.

REFERENCES

- 1) H. Namba, Y. Aoki, M. Taguchi and K. Furukawa, **JAERI TIARA Annual Report I**, 163 (1992).
- 2) T. Kojima, Y. Haruyama, R. Tanaka H.L.A. Ranjith and S.Kashiwazaki, **Appl. Radiat. Isotopes**, 44 41(1993).
- 3) H. Sunaga, R. Tanaka, K. Yoshida and I. Kohno, **RIKEN Accel. Prog. Rep.**, 22, 130 (1988).

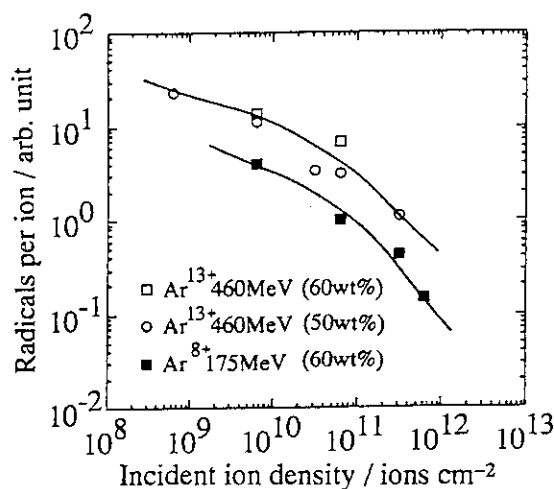


Fig. 5. The relationship between radical yield and incident ion density by irradiation of Ar¹³⁺ (460MeV) and Ar⁸⁺ (175MeV). 50wt%: alanine 50wt%, 60wt%: alanine 60wt%.

4. Organic Materials

4.1	High Energy Ion Irradiation Effects on Polymers(I) Changes in Mechanical Properties Induced by 10 MeV Protons	
	H.Kudoh, T.Sasuga and T.Seguchi	79
4.2	Uniformity of Beam Fluence Distribution Obtained by the Multiple Coulomb Scattering Using Thin Metal Foils	
	M.Asano, M.Yoshida, M.Tamada, H.Omichi, M.Fukuda, T.Agematsu, S.Okumura and K.Arakawa	83
4.3	Irradiation Effects on Mechanical Properties of CFRP for Spacecraft	
	K.Yudate, Y.Morino, T.Sasuga, A.Udagawa and T.Seguchi	87

4.1 High Energy Ion Irradiation Effects on Polymers (I) Changes in Mechanical Properties Induced by 10 MeV Protons

Hisaaki KUDOH, Tsuneo SASUGA and Tadao Seguchi
Department of Material Development, JAERI Takasaki

Introduction

For selection and application of materials used in space environment the knowledge about deterioration behavior of mechanical properties induced by ion irradiation is required. It is known in the studies on organic materials and several polymers¹⁻³⁾ that radiation effects altered by energy deposition per track length ($-dE/dx$) of radiation source. The $-dE/dx$ is called as linear energy transfer (LET). Since the LET of charged particles are extremely large compared with that of electrons and they deposit energy in local area in high density, deterioration behavior would be affected by LET of radiation sources.

To measure reasonable radiation-induced changes in mechanical properties, uniform irradiation on wide area is essential. The chamber which allows polymeric materials to irradiate uniformly on wide area has been reported previously⁴⁾. In this work, the radiation deterioration induced by 10 MeV protons for several polymers were studied and compared with those induced by 2 MeV electrons.

Experimental

Polymers used were a medium density polyethylene and a polytetrafluoroethylene (PTFE), polyethersulphone (PES), and bisphenol-A type polysulphone (U-PS). These polymers were the film with about 0.1 mm thickness.

Proton irradiation was carried out by scanning the 10 MeV spot beam (about 10 mm diameter) to 100 mm x 100 mm area. The current of the spot beam was 500 nA for PE, PES and U-PS, and 50 nA for PTFE. Since the projectile range of 10 MeV proton is 112 mg cm⁻² for PE, the 10 MeV protons pass through the polymer films. Electron irradiation was carried out by scanning 2 MeV electron beam from a Dynamitron type accelerator. PE, PES and U-PS were irradiated in air and PTFE was irradiated in vacuum. The electron fluence rates are 0.28 micro C cm⁻²s⁻¹ for PE, PES and U-PS and 0.056 micro C cm⁻²s⁻¹ for PTFE. The dose rate measured by a cellulose tri-acetate (CTA) film dosimeter was 0.5

and 0.1 kGy s^{-1} , respectively.

Radiation effects were evaluated by measuring tensile properties, heat of melting, glass transition temperature, molecular weight, and gel fraction.

Absorbed dose (D) in the irradiation of high energy charged particle is given by;

$$D = S \times Q \quad (1)$$

where S is the mass stopping power of material and Q is the fluence. The stopping power for protons was calculated using Bethe's equation⁵⁾ and the one for electron was calculated from Seltzer and Berger method⁶⁾. The stopping power calculated are summarized in Table 1 for the polymers used in this work. The stopping powers of 10 MeV protons is 21 to 25 time lager than those of 2 MeV electrons, in other words, LET of 10 MeV protons is 21 to 25 times larger than that of 2 MeV electrons.

Table 1. Mass stopping powers for materials used

Materials	Stopping power (MeV cm ² /g)		ratio of p/e ⁻
	10 MeV Proton	2 MeV electron	
PE	43.96	1.772	24.81
PTFE	37.38	1.720	21.73
PES	40.66	1.783	22.80
U-PS	41.44	1.778	23.31
CTA	41.01	1.773	23.13

Results and discussion

Figures 1 and 2 show the elongation at break for the four polymers as a function of the proton and electron doses. In the case of PE and PTFE, no clear difference is observed between the proton and electron irradiations, but in PES and U-PS, the decrement of elongation per dose becomes moderate in the proton irradiation.

Gel fraction of U-PS is shown as a function of dose in Figure 3. Gelation does not occur in the electron irradiation up to 2 MGy, but is observed at 0.8 MGy proton irradiation. The gel fraction increases with higher dose, which indicates that radiation crosslinking is predominant in the high LET irradiation.

The glass transition of PES and U-PS shifts to lower temperature by electron and proton irradiation. The lower temperature shift of the glass transition by irradiation is known owing to

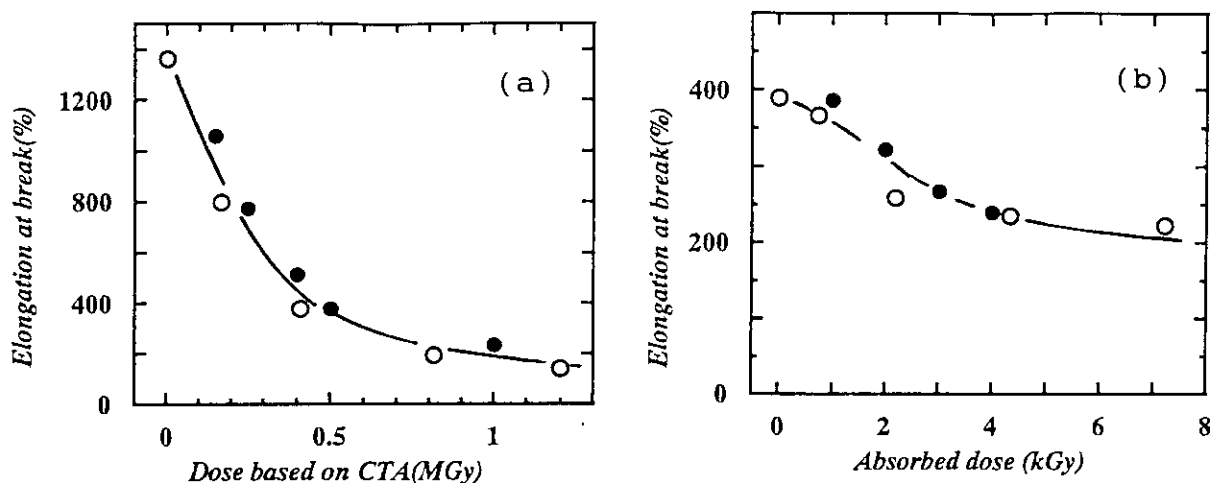


Figure 1. Dose dependence of elongation for PE(a) and PTFE(b),
(○):10 MeV protons and (●) 2 MeV electrons.

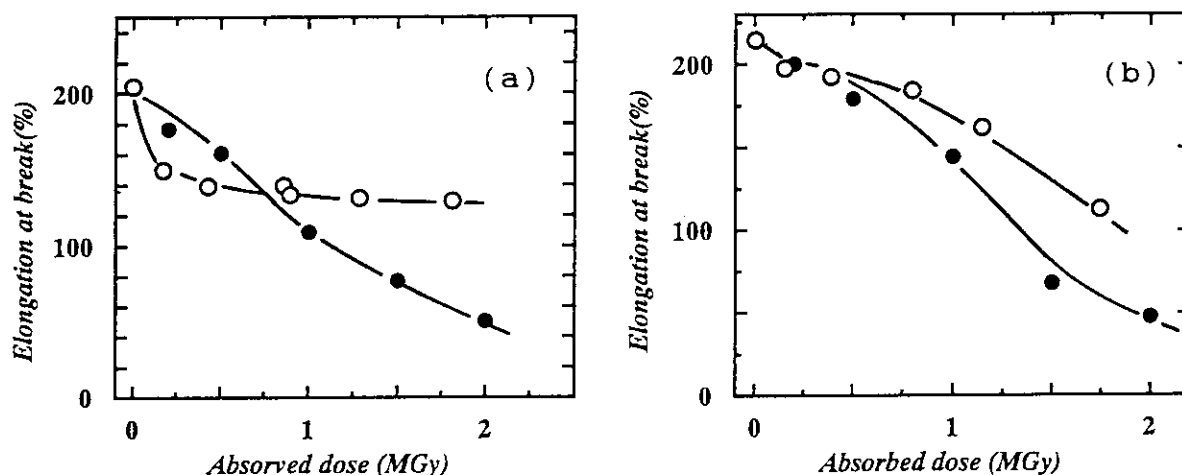


Figure 2. Dose dependence of elongation for PES(a) and U-PS(b),
(○):10 MeV protons and (●) 2 MeV electrons.

decrease in the molecular weight by main chain scission. In the proton irradiation the lower temperature shift of glass transition of PES and U-PS is markedly depressed. Therefore the probability of chain scission should be decreased by high LET irradiation.

The changes in mechanical properties induced by 8 MeV protons⁷⁾ have been studied for several polymers. In that experiments, clear LET effects was scarcely observed in the aliphatic polymers such as PE and polypropylene. On the contrary, the radiation deterioration of the aromatic polymers of PES, bisphenol-A based polyester(U-polymer) and U-PS was reduced in the 8 MeV proton irradiation. It was concluded from the results that appearance or not of LET effects on the changes in mechanical

properties is owing to aromaticity of polymers.

The temperature rise during proton irradiation was not actively controlled in the previous experiments and it was estimated to be 60°C. The results in PE, PES and U-PS obtained under controlled temperature in this work well accords with previous observations and existing of LET effects in aromatic polymers is confirmed. Furthermore, the result on PTFE adds a new evidence which aliphatic polymer dose not shows the clear LET effects.

The characteristics in high LET radiation effects on organic materials is formation of active species with a high density in a local area, so that the probability of recombination of the active species would increase. It was reported that formation of dimer increases in benzene with LET, but the dimer does not form in cyclohexane by high LET irradiation¹. This phenomena are interpreted by the recombination of excited molecule formed in aromatic compound. The LET effect observed in aromatic polymers of PES and U-PS would be induced by the reaction of excited molecules. The experiments in other aromatic polymers like polyimides and poly-ether-ether-keton are being planned.

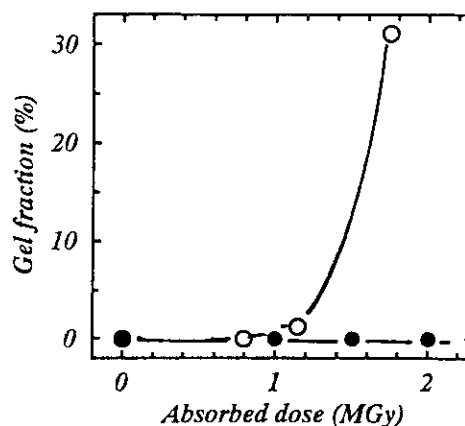


Figure 3. Gel fraction as a function of dose for U-PS, (○) 10 MeV protons, (●) 2 MeV electrons.

References

- (1) W.G. Burns and J.R. Parry, *Nature* 201, 814(1964).
- (2) A. Licciardello, O. Puglisi, L. Calcagno and G. Foti, *Nucl. Instrum. Meth. Phys. Res.(B)*, 32, 131(1988).
- (3) Y. Aoki, N. Kouchi, H. Shibata, S. Tagawa and Y. Tabata, *ibid.*, 33, 799(1988).
- (4) T. Sasuga, H. Kudoh and T. Seguchi, *JAERI TIARA Annual Report*, 177(1992).
- (5) H.A. Bethe and J. Ashkin, "Experimental Nuclear Physic", Wiley, New York, (1953).
- (6) S.M. Selzer and M.J. Berger, *J. Radat. Phys. Chem.* 33, 1189(1982).
- (7) T. Sasuga, S. Kawanishi, T. Seguchi and I. Kohno, *Polymer*, 30, 2054(1989).

4.2 UNIFORMITY OF BEAM FLUENCE DISTRIBUTION OBTAINED BY THE MULTIPLE COULOMB SCATTERING USING THIN METAL FOILS

Masaharu ASANO*, Masaru YOSHIDA*, Masao TAMADA*, Hideki OMICHI*, Mitsuhiro FUKUDA**, Takashi AGEMATSU**, Susumu OKUMURA**, and Kazuo ARAKAWA**

* Department of Materials Development, Takasaki radiation Chemistry Research Establishment, JAERI

** Department of Advanced Radiation Technology, Takasaki Radiation Chemistry Research Establishment, JAERI

1. INTRODUCTION

This year the irradiation apparatus for the preparation of ion track pores¹⁾ was transferred from HY-1 port to HD-2 in order to avoid an elaborate procedure - attaching and detaching the apparatus at every beam time, because the HY-1 was used for two different apparatus. The new port, however, required some technical improvements to obtain a uniform distribution of beam fluence on a flat sample, since this port has no beam-scanning system. We combined two different techniques to realize the uniformity. One is to defocus the beam and enlarge its diameter. The other is to utilize a phenomenon of multiple Coulomb scattering of ions penetrating into metal foils. In the present study, we investigated the efficiency of these techniques to realize a uniform distribution of the beam.

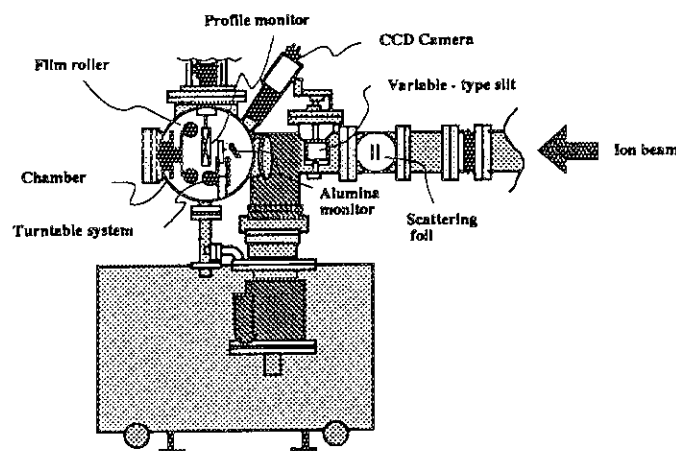
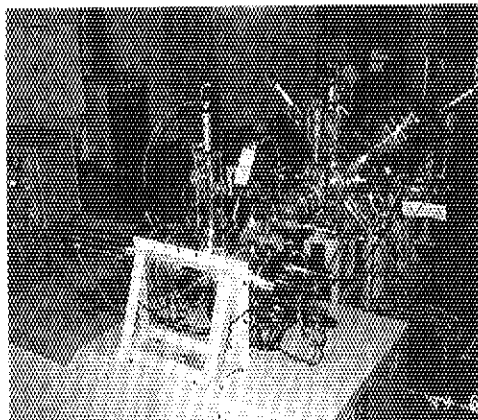


Figure1 Modified apparatus for preparation of ion track pores.

2. RECONSTRUCTION OF THE IRRADIATION APPARATUS

The irradiation apparatus was modified from the vertical irradiation system of HY-1 to the horizontal one of HD-2. Figure 1 shows the irradiation apparatus having a multiple Coulomb scattering system.

3. MULTIPLE COULOMB SCATTERING

When ion beams are collided with a matter, ions change the forward direction in term of probability with the influence of elastic Coulomb scattering. The angular distribution of the multiple Coulomb scattering is approximately expressed by Gaussian distribution in the region of a small scattering angle as follows:²⁾

$$\frac{1}{\sqrt{2\pi}\theta_0} \exp\left[-\frac{\theta_{plane}^2}{2\theta_0^2}\right] d\theta_{plane}$$

where θ_{plane} is the projected deflection angle which is expressed by

$$\theta_0 = \frac{13.6(\text{MeV})}{p(\text{MeV}/c)\beta c} Z\sqrt{X/X_0} [1 + 0.088 \log(X/X_0)] (\text{rad})$$

and P is the momentum, βc the particle velocity, Z the charge of the ion, X the thickness of the scattering foil, X_0 the radiation length of the scattering foil.

4. EXPERIMENTAL

Figure 2 shows the arrangement for the target and the scattering foils in the apparatus attached to HD-2 port of AVF cyclotron. The metal foils for scattering are introduced in the beam line in front of the target which is located in the distance of 60 cm. The shape of the controlled beam with both metal foils and a quadruple electromagnet is monitored with a quartz monitor and with a profile monitor having three lines (Irie Co., Ltd.). The distribution of beam fluence was measured by using CTA (cellulose triacetate) film dosimeter and CR-39 (diethyleneglycol-bis-allylcarbonate polymer) solid state nuclear track detector.

Generally the effect of mul-

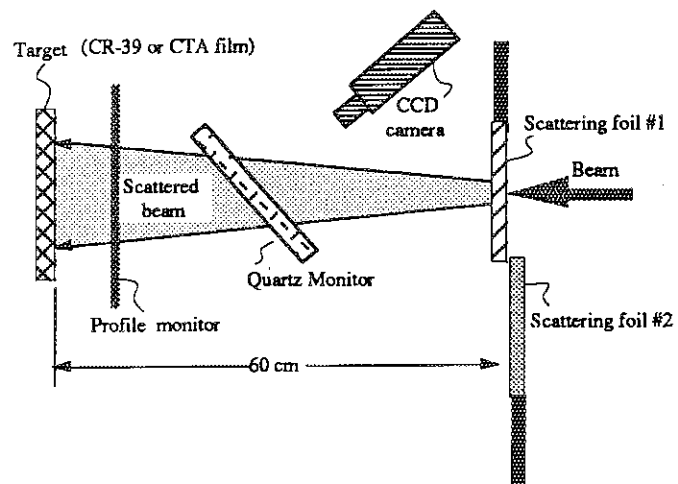


Figure 2 Arrangement for target and scattering foils.

Table 1 Kind of scattering foil with the multiple Coulomb scattering.

Kind	Atomic number	Thickness (mg/cm ²)	Radiation length (cm)	θ_0^{**} (mrad)	FWHH*** (mm)
Cu	29	4.48	1.43	2.5	1.8
Cu	29	8.96	1.43	3.7	2.6
Al	13	8.10	8.9	2.5	1.8
Ta	73	11.6	0.35*	6.6	4.7

* The value of W.

** Width of the angular distribution of the multiple Coulomb scattering for $^{40}\text{Ar}^{13+}$ (460MeV).*** Full Width of Half Maximum (FWHM) of Gaussian distribution on target for $^{40}\text{Ar}^{13+}$ (460MeV).

multiple scattering is larger for the material with a high atomic number and a thick foil. In the case of heavy ion irradiation, therefore, the energy loss is serious in thicker foils. Table 1 lists the kinds of metal foils (Rare metallic Co., Ltd.), their thicknesses, radiation length, width of the angular distribution of the multiple Coulomb scattering, and full width of half maximum (FWHM) of Gaussian distribution on target. We intend to realize the irradiation condition of 10^7 ions/cm² of heavy ions (10MeV/u) with a uniformity of ca. $\pm 20\%$ in the whole area of 4 cm x 4 cm.

5. RESULTS AND DISCUSSION

The original transparent CR-39 changes to an opaque state when it is irradiated with ion beams and then etched with alkaline solution. Figure 3 shows the CR-39 films of 4 cm x 4 cm etched for 1h with 6 N NaOH solution at 60 °C after irradiation with $^{40}\text{Ar}^{13+}$ of 460 MeV. The area of the opaque part of the film irradiated through the scattering metal foil (Figure 3-a) was apparently larger than that of the irradiated film without scattering foil

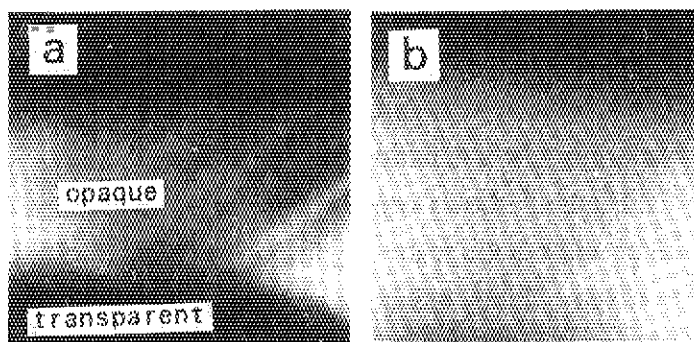


Figure 3 Etched CR-39 films irradiated with Ar^{13+} (460 MeV). (a) without scattering foil and (b) with scattering foil of 7 μm Ta.

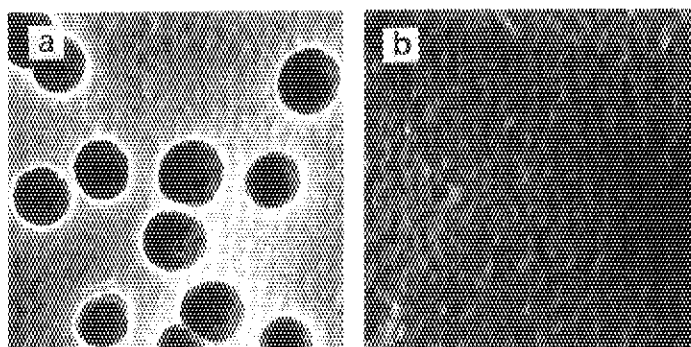


Figure 4 SEM photograph of etched CR-39 films irradiated with Ar^{13+} (460 MeV) in Figure 3. (a) opaque part and (b) transparent part.

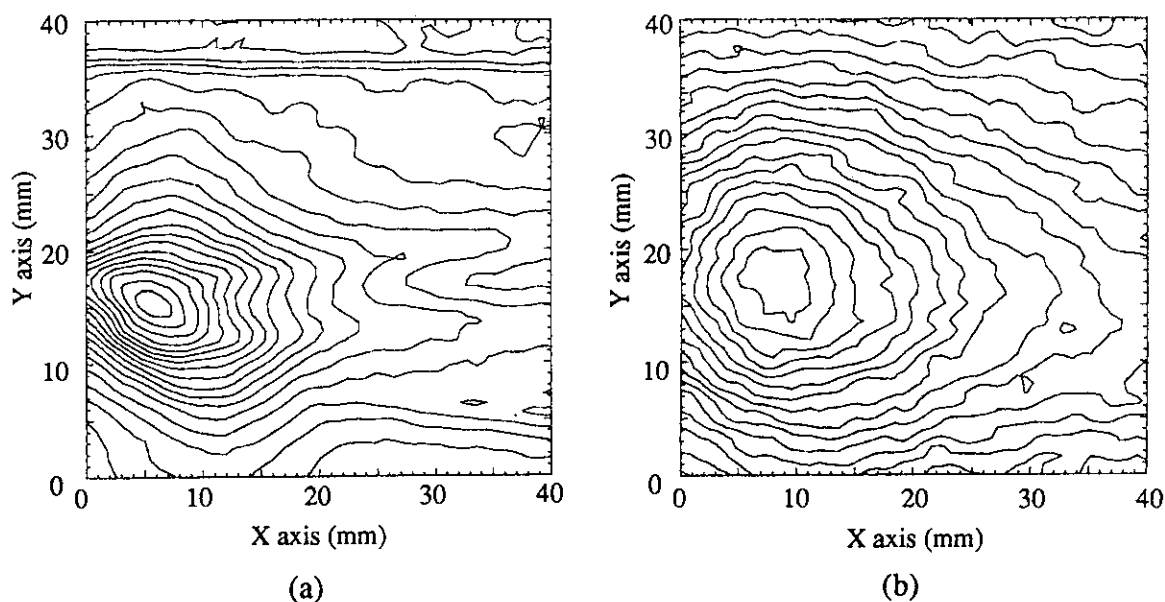


Figure 5 Contour lines of beam fluence distribution in the condition of Ar^{11+} (330 MeV). (a) without scattering foil and (b) with scattering foil of $7 \mu\text{m}$ Ta.

(Figure 3-b). The electron microscope was used to confirm the irradiation of ions on the films. Results are shown in Figure 4. The etched pores only existed in the opaque part in both films, while no pore was observed in the transparent part. This indicates that Ar^{13+} ions penetrated only the opaque parts and the introduction of scattering foil into ion beam course was capable of enlarging the irradiation area at the target point.

Figure 5 shows contour lines of beam fluence distribution of Ar^{11+} ion of 330 MeV with or without the scattering foil of Ta ($7 \mu\text{m}$ thick). It is clear that the beam fluence distribution became flat by using the scattering foil. Uniformity were calculated in the area of $1 \text{ cm} \times 1 \text{ cm}$ near the maximum strength of beam fluence. The values were $+33 \%$ and -50% without scattering foil and $+13 \%$ and -18% with scattering foil.

As a result, we concluded that introducing the metal scattering foil into the beam line could improve the uniformity of the distribution of beam fluence. The uniformity within $\pm 20 \%$ was obtained in the area of $1 \text{ cm} \times 1 \text{ cm}$ near the maximum strength of beam fluence. For the next step, we intend to defocus the beam to enlarge the size of beam and realize the flat distribution of both fluence and energy.

REFERENCES

- 1) M. Asano, M. Yoshida, M. Tamada, H. Omichi, and R. Katakai, JAERI TIARA Annual Report 1 (1992) p.109
- 2) G. R. Lynch and O. I. Dahl, Nucl. Instr. and Meth. B58 (1991) p.6

4.3 IRRADIATION EFFECTS ON MECHANICAL PROPERTIES OF CFRP FOR SPACECRAFT

Kozo YUDATE *, Yoshiki MORINO *

Tsuneo SASUGA **, Akira UDAGAWA ** and Tadao SEGUCHI **

*Office of Research and Development; National Space Development Agency of Japan.

** Department of Material Development; Takasaki Radiation Chemistry Research Establishment, Japan Atomic Energy Research Institute

I. INTRODUCTION

Composite materials, particularly Carbon Fiber Reinforced Plastic(CFRP), offer substantial advantages for large space system applications, because of their superior specific strength, specific stiffness and low coefficient of thermal expansion. CF/Epoxy resin composite (CF/Ep) is being increasingly utilized as a structural material for space use.

NASDA is now conducting R&D efforts on reentry winged vehicle "HOPE". CF/Polyimide resin composite is expected as the first candidate material for the primary structure of this "HOPE". CF/Polyimide composite (CF/Pi) resists higher temperature than CF/Ep composite. These superior characteristics of CF/Pi would contribute to weight saving of HOPE structure.

Resistance to space environmental effect such as electron and proton radiation as well as mechanical properties of CFRP is the most important characterization to apply to structural material for space use. Irradiation effects (electron, proton) on mechanical properties were studied for CF/Ep and CF/Pi composites.

II. EXPERIMENTAL PROCEDURE

(i) Materials

The UD (Uni-directional) preimpregnated sheets were laminated and cured. 20 plies of sheet for CF/Ep and 16 plies of sheet for CF/Pi were laminated, the laminated direction was 0/90°, and the thickness of the CFRP was 2 mm. Table -1 shows the carbon fiber and resin properties.

Table 1. Carbon Fiber and Resin Properties

CFRP	Carbon Fiber				Resin (cured)			
	Type	Tensile Strength	Tensile Modulus	Strain	Type	Tensile Strength	Tensile Modulus	Strain
CF/Ep	M-50J(Toray)	4020 MPa	475 GPa	0.8 %	Epoxy	90 MPa	3.7 GPa	4.0 %
CF/Pi	T-800H (Toray)	5490	294	1.9	Polyimide	69	3.9	2.5

(ii) Effects of electron irradiation on mechanical properties of CFRP
CF/Ep composite

Fig 1 shows flexural strength and modulus at room temperature for CF/Ep as a function of dose of electron, and Fig 2 shows those at 77 K. The degradation of mechanical properties was not observed at room temperature measurement, on the other hand the flexural strength decreased steeply above 15 MGy of electron dose at 77 K measurement. It seems that the damages in epoxy resin induced by electron irradiation was not observed as degradation in measurement at R.T.

The original (no irradiation) CF/Ep composite had the T_g of 145°C. The T_g decreased to 119°C by 30 MGy irradiated, resulting that Epoxy resin was classified as a chain-scission type resin under electron irradiation.

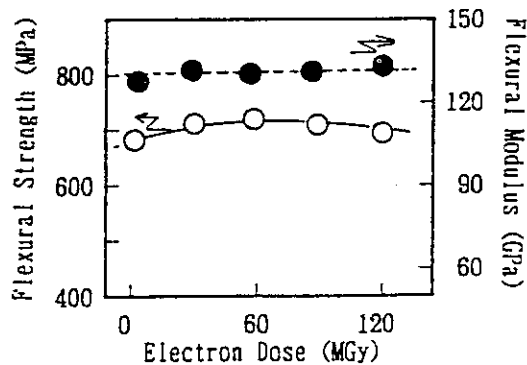


Fig 1. Flexural Strength and Modulus vs. electron dose for CF/Ep at R.T

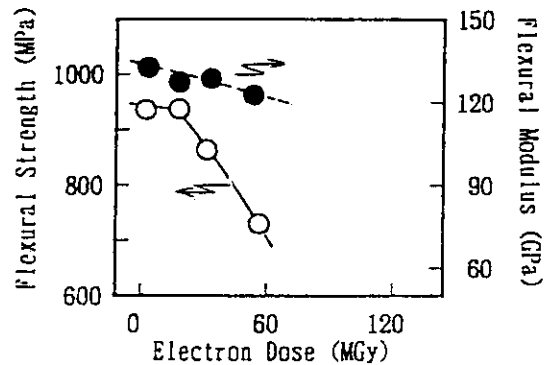


Fig 2. Flexural Strength and Modulus vs. electron dose for CF/Ep at 77 K

CF/Pi(PMR-15) composite

Fig 3 shows flexural strength and modulus for CF/PMR-15 as a function of dose of electron. The flexural strength increased slightly with dose, and modulus showed a maximum at 90 MGy. Fig 4 shows the same results measured at 77 K. No degradation was not observed at 77 K up to 120 MGy electron irradiation. From these results it is concluded that CF/PMR-15 composite is excellently stable to electron irradiation.

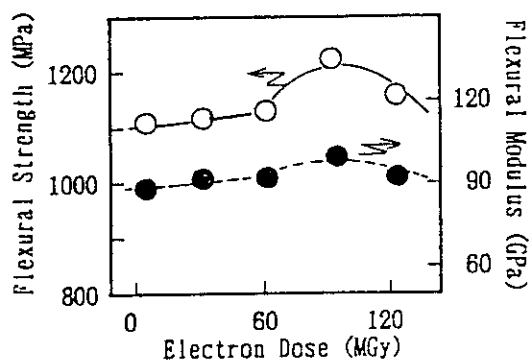


Fig 3. Flexural strength and Modulus vs. electron dose for CF/Pi at R.T

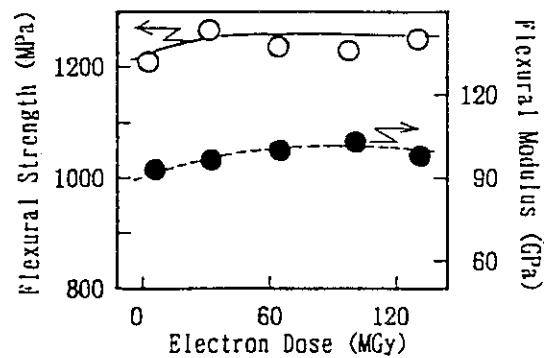


Fig 4. Flexural strength and Modulus vs. electron dose for CF/Pi at 77 K

(ii) Irradiation

Irradiation was performed by 45 MeV protons from a AVF cyclotron and 2 MeV electrons from an electron accelerator installed in the JAERI Takasaki Radiation Chemistry Research Establishment. The proton fluence rate was 2.5×10^9 p/cm²/s and the total adsorbed dose (D) was 736 KGy. The electron fluence rate was 1.16×10^{13} e/cm²/s and absorbed dose (D) was 30 ~120MGy. To avoid rising temperature during the electron irradiation, the sample were rapped by aluminum foil and stuck on the irradiation table with cooling jacket.

(iii) Measurement of mechanical properties

3 point flexural test was carried out at room temperature and 77K with a cross-head speed of 5 mm/min, the size of sample was 102 mm (L) X 10 mm (W) X 2 mm (T) and span length was 80mm (span ratio = 40).

Visco-elastic measurement was carried out by torsion pendulum type visco-elastmer at temperatures of 160 to 450 °C to measure the glass transition temperature (T_g) of sample ⁽¹⁾. The frequency was 0.2 to 2 Hz.

III. RESULTS AND DISCUSSION(i) Mechanical properties of CFRP

The thermosetting polyimide, PMR-15, is the leading matrix resin for high temperature resistant polymer composites. NASA Lewis Research Center developed the polyimide resin, which is prepared by the polymerization of monomer reactants ⁽²⁾ (PMR). The monomers are essentially unreactive at room temperature, but undergo sequential in situ condensation and ring-opening addition crosslinking reactions at elevated temperatures to form a thermo-oxidatively stable polyimide matrix resin.

Table-2 shows the mechanical propeties of CFRP. CF/Pi has a high T_g, indicating that high temperature resistant composite.

Table 2. Mechanical Properties of CFRP

CFRP	Flexural Strngth(MPa)	Flexural Modulus(GPa)	ILSS (MPa)	T _g (°C)
CF/Ep	684	133.3	47.6	145
CF/Pi	1051	87.8	74.6	354

Fig 5 shows T_g of CF/PMR-15 composite as a function of dose of electron. T_g increased with dose, indicating that PMR-15 resin is classified as a crosslinking-type polymer under electron irradiation.

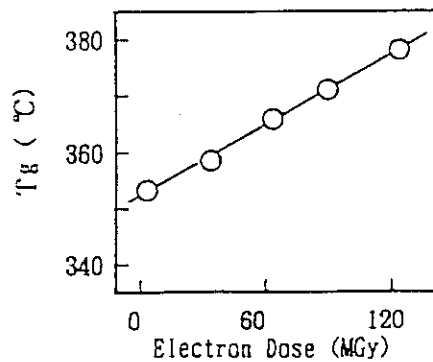


Fig 5. T_g vs. electron dose for PMR-15

(iii) Effects of proton irradiation on mechanical properties of CFRP

CF/Ep and CF/PMR-15 composites were irradiated by scanning 45 MeV proton from a AVF cyclotron over an area of 80 X 80 mm, and dose was 736 KGy. The range of 45 MeV proton in the CFRP is 12.1 mm, therefore it was confirmed that proton passed completely through the CFRP with 2 mm thickness, and sample could be irradiated uniformly.

The mechanical properties of proton-irradiated CFRP is now measuring. The effect of proton irradiation on mechanical properties of CFRP would be comparable with the effect of electron irradiation from the observations in several polymers ⁽³⁾.

(iv) Evaluation of CFRP for space use

It is estimated that spacecraft surface in the geostationary orbit with altitudes of 36000 km is irradiated by electron upper limit 100 MGy for 10 years, and in the low earth orbit(LEO) with altitudes of 500 km is irradiated by proton and electron upper limit 100 MGy for 30 years. It is verified that CF/Ep composite was degraded by electron irradiation (above 15 MGy), therefore this degradation must be considered for space use.

IV. CONCLUSION

- (i) CF/Ep composite has low electron-radiation resistance. The degradation was observed above 15 MGy electron irradiation. Epoxy resin is a bond-scission type polymer under electron irradiation.
- (i) CF/PMR-15 Composite has high electron-radiation resistance. PMR-15 resin is a crosslinking type polymer under electron irradiation.

REFERENCES

- (1) T. Sasuga, M. Hagiwara; Polymer, 26, 501 (1985)
- (2) R.W. Lauver; Journal of Polymer Science, Polymer Chemistry Edition, Vol.17, 2529-2539 (1979)
- (3) T. Sasuga et al; Polymer, 30, 2054. (1992)

5. Inorganic Materials

5.1	Metastable Phase Formation by Ion Implantation	
	H.Takeshita, S.Yamamoto, Y.Aoki and H.Naramoto	93
5.2	Irradiation Effects on Electrical Resistivity of Ceramic Materials	
	K.Noda, T.Nakazawa, T.Tanifuji and Y.Ishii	96
5.3	Effects of Helium on Microstructures and Mechanical Properties of Stainless Steels	
	S.Hamada, T.Nakazawa and T.Tanifuji	98
5.4	Electrical Properties of Ion-beam-irradiated Semi-insulating GaAs	
	K.Kurihama, Y.Takahashi, K.Tomizawa, T.Kato, H.Takeshita, S.Yamamoto and H.Naramoto	101
5.5	High Energy Ni Ion Implantation and Thermal Annealing for α -SiC Single Crystal	
	K.Kawatsura, N.Shimatani, T.Nakae, S.Arai, T.Shiono, H.Horino, Y.Mokuno, K.Fujii, H.Takeshita, S.Yamamoto, Y.Aoki and H.Naramoto	105
5.6	PKA Energy Spectrum Dependence of Defect Cluster Formation in Gold by High Energy Self-ion Irradiation	
	N.Sekimura, Y.Kanzaki, S.Okada, T.Masuda, S.Ishino and R.Tanaka.	109
5.7	Molybdenum Silicide Formation by Means of Ion Mixing	
	S.Ohnuki, T.Hatakeyama, S.Watanabe, H.Takahashi, S.Yamamoto, H.Takeshita and H.Naramoto	113

5 . 1 METASTABLE PHASE FORMATION BY ION IMPLANTATION

Hidefumi TAKESHITA, Syunya YAMAMOTO, Yasushi AOKI
and Hiroshi NARAMOTO

Department of Materials Development, JAERI

1. INTRODUCTION

Ion implantation has proved to be valuable both for new material development and the understanding of basic principles underlying metastable phase formation. Ion implantation has enabled extension of equilibrium solid solubility in a large number of systems. Extension of solid solubility is not only limited to substitutional solutions but also to interstitial solutions. These metastable solid solutions have formed the basis of alloy development through ion implantation. Ion implantation has been also used to make metastable crystalline intermediate phases. Some of metastable intermediate phases(e.g., Nb₃Ge) exhibited a superconducting transition temperature of 17K by conforming to the stoichiometry. The corresponding equilibrium nonstoichiometric phase has a transition temperature of only 7K. An understanding of metastable phase formation on ion implantation can thus be scientifically challenging and technologically useful.

As a first step we investigate the metastable silicide formation of the Si-Au, Si-Ag and Si-Cu systems. In the Si-Au system mutual solubilities are quite small and there are no equilibrium intermediate phases reported in the phase diagram. This is also the case for the Si-Ag system. The mutual solubilities of Si and Ag in the solid state are negligible. Thus interest for these systems is the metastable phase formation in the Si-Au and Si-Ag systems as well as extended solid solubilities. In contrast with the Si-Au and Si-Ag systems, there exist several intermetallic compounds in the phase diagram for the Si-Cu system. The equilibrium solubility of Cu in the terminal solid solution, (Si), is negligible.

2. EXPERIMENTAL

Ion implantation was carried out using the 3MV tandem accelerator in a vacuum better than 1×10^{-6} torr. Si wafers were implanted at room temperature with Au, Ag and Cu ions, respectively. The beam energy and current were 0.8-1.2 MeV and 20-600 nA/cm², respectively. A 5° incident angle was used to avoid channeling. The concentration profiles resulting from implantation were measured using Rutherford backscattering spectroscopy(RBS). The RBS spectra were recorded with 2.0 MeV alpha particles, a 165° scattering angle and a detector with 14 keV resolution.

3. RESULTS

The concentration profiles of Au, Ag and Cu for the as implanted samples are shown in fig.1-3. The beam energies and fluences were 1.2MeV and $2.8 \times 10^{16} \text{ Au/cm}^2$; 0.8MeV and $7.5 \times 10^{15} \text{ Ag/cm}^2$; and 0.8MeV and $1.0 \times 10^{17} \text{ Cu/cm}^2$. The profiles for the former two elements can be roughly described as gaussian, while that for Cu deviates significantly from gaussian.

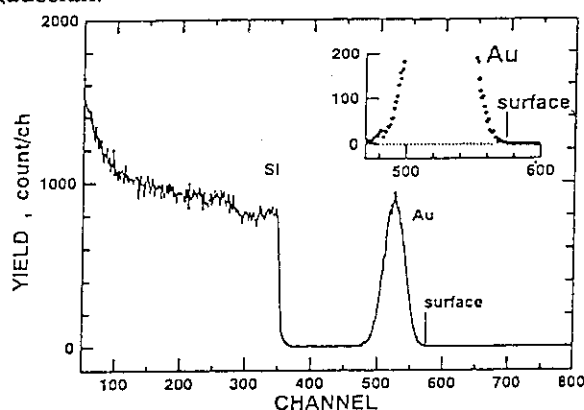


Fig.1 2MeV $^4\text{He}^+$ backscattering spectrum of Si implanted at 1.2MeV to $2.8 \times 10^{16} \text{ Au/cm}^2$.

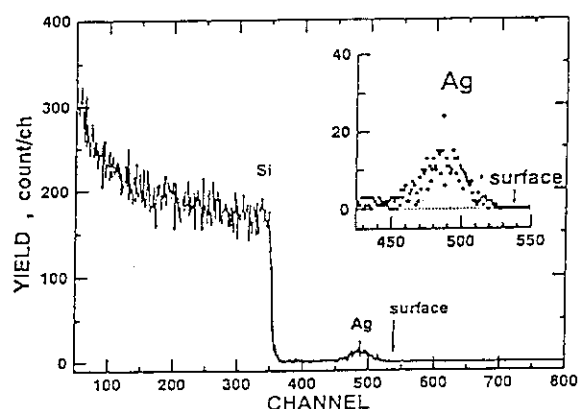


Fig.2 2MeV $^4\text{He}^+$ backscattering spectrum of Si implanted at 0.8MeV to $7.5 \times 10^{15} \text{ Ag/cm}^2$.

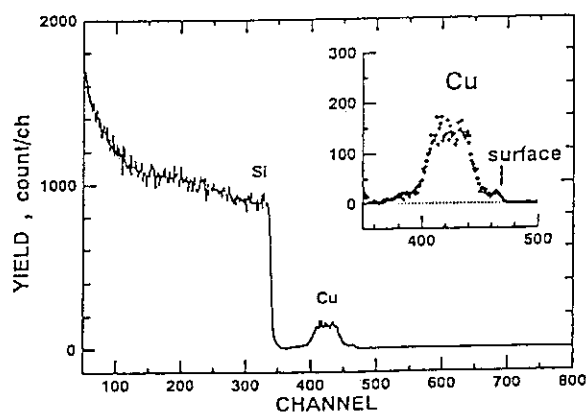


Fig.3 2MeV $^4\text{He}^+$ backscattering spectrum of Si implanted at 0.8MeV to $1.0 \times 10^{17} \text{ Cu/cm}^2$.

The profile for Cu may be characterized by the "plateau concentrations". The equilibrium phases of the Si-Cu system are the terminal solid solution, (Si), with negligible solubility of Cu; three intermediate phases at room temperature and the terminal solid solubility, (Cu), with a maximum solubility of 11.25at.% at the peritectoid temperature. Cu dissolves interstitially in Si with a maximum solubility of 0.002at.% Cu between 1200 and 1300°C[1]. Since there are several intermediate compounds in the equilibrium phase diagram of the Si-Cu system, it is probable that the observed plateau concentrations may correspond to the formation of such compounds. The x-ray diffraction analysis for the as-implanted sample will be made to identify the structure of the "plateau" compounds.

On the other hand, there are observed no compound formation for Au and Ag, which is consistent with the respective equilibrium phase diagrams[1]. The equilibrium phase diagram of the Si-Au system has the SiC(diamond)-type cubic terminal solid solution, (Si), with negligible solubility of Au ($\sim 2 \times 10^{-4} \text{ at\% Au}$). The maximum solubility of Ag is about $4 \times 10^{-4} \text{ at\% Ag}$.

around 1350°C. Fig.4 shows RBS spectra for Au-implanted Si. It is clearly seen that Si matrix within the projected range of implanted Au was completely amorphized due to ion implantation. Amorphous phases have been observed in a wide composition range (-9 to 91 at%Si) by such means as laser pulse heating and quenching. Metastable crystalline structures can be obtained either through annealing of amorphous alloys above the amorphous-crystalline transition temperature[2]. Thus it is expected that annealing of our Si-Au amorphous mixture may yield a metastable intermediate phase.

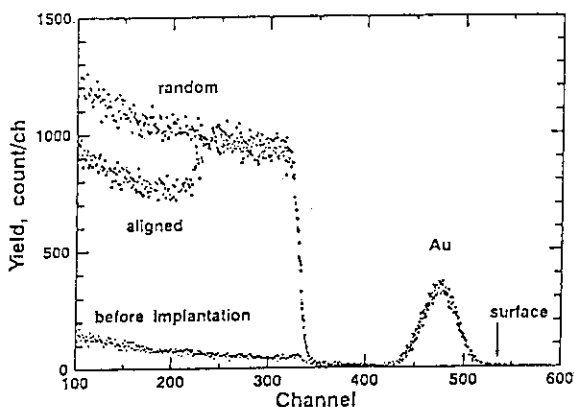


Fig.4 2MeV $^4\text{He}^+$ backscattering spectra of pure Si and Si implanted at 1.46MeV to 1.0×10^{16} Au/cm 2 .

REFERENCES

- 1) T.B.Massalski, H.Okamoto, P.R.Subramanian and L.Kacprzak Ed., Binary Alloy Phase Diagrams, 2nd Ed., ASM International(1990)
- 2) B.-X.Liu, L.S.Wieluński, M.Mäenpää and M.-A.Nicolet in: Metastable Materials Formation by Ion Implantation, S.T.Picraux and W.J.Choyke, Eds., Elsevier Science Publishing Company(1982)133-138.

5.2 IRRADIATION EFFECTS ON ELECTRICAL RESISTIVITY OF CERAMIC MATERIALS

Kenji NODA, Tetsuya NAKAZAWA, Takaaki TANIFUJI
and Yoshinobu ISHII

Department of Fuels and Materials Research, JAERI

Many ceramic insulator materials will be used in D-T fusion reactors. During operation of the fusion reactors, the ceramic materials will be exposed to high energy neutrons with energies up to 14 MeV and gamma rays. Radiation-induced conductivity (RIC) is induced in the ceramic materials by electronic excitation during various kinds of irradiation: Electrons in valence bands are excited to conduction band due to the irradiation, and therefore the electrical conductivity of the ceramic materials increases only during the irradiation¹⁾. An energy released for electronic excitation in the materials by a 14 MeV neutron is larger than that by a fission neutron. Thus, evaluation of degradation of electrical resistivity due to RIC is one of R&D issues for ceramic insulator materials for the fusion reactors.

Recently, it was found that the electrical conductivity during irradiation increased substantially with the fluence above certain fluence level for some ceramic materials (e.g., Al_2O_3 , MgO) irradiated with applied electric fields²⁻³⁾. The electrical conductivity during irradiation is given by $\sigma = \sigma_0 + KR^d$, where σ_0 is the conductivity in the absence of irradiation, R is ionization dose rate, K is constant depending on materials and d is generally between 0.5 to 1.0. The second term is contribution due to RIC. The above-mentioned fluence dependence of electrical conductivity arises from change of the first term, σ_0 due to the irradiation, and this increase of conductivity, i.e., decrease of electrical resistivity, remains after irradiation. Such decrease of electrical resistivity is called "radiation-induced electrical degradation (RIED)".

The influence of RIED on electrical insulation performance of ceramic materials is considered to be much larger than that due to RIC especially at high fluence. Thus, studies on RIED for various ceramic materials are required to obtain materials database for fusion reactor designs and development of radiation resistant materials for fusion reactors.

In this standpoint, we started an investigation of RIED for various ceramic materials by high energy helium ion irradiation using a cyclotron at Takasaki establishment of Japan Atomic Energy Research Institute. In this fiscal year, Al_2O_3 , AlN and MgO specimens were irradiated with 50 MeV helium ions in the fluence range 4.5 to 5.5×10^{19} ions/ m^2 without applied electric field to obtain reference data for RIED. The measurements of electrical resistivity at various temperatures are being carried out.

The fluence of irradiation carried out so far was limited to low level because of lack of approval for handling of radioactive specimens. The procedure to obtain the approval is now under way. The helium ion irradiation at high fluence level is expected to be able to be carried out in the next fiscal year for various ceramic materials with and without applied electric field.

REFERENCES

- 1) R.W.Kraffky, B.H.Rose, A.N.Goland and G.J.Dienes, Phys. Rev. B21(1980)3610.
- 2) E.R.Hodgson, J. Nucl. Mater. 191-194 (1992)552.
- 3) S.J.Zinkle and E.R.Hodgson, J. Nucl. Mater. 191-194 (1992)58.

5 . 3 EFFECTS OF HELIUM ON MICROSTRUCTURES AND MECHANICAL PROPERTIES OF STAINLESS STEELS

Shozo HAMADA, Tetsuya NAKAZAWA and Takaaki TANIFUJI

Department of Material Research, JAERI,

I. INTRODUCTION

Structural materials for water-cooled components in a fusion reactor are required to possess excellent resistance to stress corrosion cracking (SCC) in pressurized water at elevated temperature. Ferritic stainless steels are known to have better SCC resistance as compared to austenitic stainless steels. Toughness loss, however, of ferritic stainless steel is greater than that of austenitic stainless steel under irradiation. Ferrite/austenite duplex stainless steel consisted of both ferritic and austenitic phase possess mixed characteristics of these both steels. Previous papers on the radiation study of ferrite/austenite duplex stainless steels are a few¹⁻³⁾. They have focussed on void swelling at heavy damage levels. Helium, however, which produces by nuclear transmutation reaction in a fusion reactor environment, also as well as displacement damage will affect other characteristics of the materials as well as swelling behavior under irradiation.

The objective of this study is to clear the effects of helium on the microstructures and mechanical properties of the ferritic and the austenitic phase of duplex stainless steel.

This experiment was preliminarily performed to evaluate availability of the apparatus attached to the LD1 port in the third light ion target room for radiation study of metallic materials.

II. EXPERIMENTAL PROCEDURE

The chemical composition of the material used in this study is as follows: 0.019C - 0.49Si - 1.01Mn - 0.02P - 0.003S - 9.0Ni - 21.3 Cr - 2.5Mo - 0.013N - Fe balance, all in weight per cent. The material is composed of both ferritic and austenitic phases, and contains alpha-ferrite of 36% in volume fraction. An ingot was made using a vacuum induction furnace. The ingot was hot-rolled to a 10 mm thickness plate. Water-quenching of the plate followed heat-treatment for 30 min at 1050 C. Rods 3 mm in diameter parallel to rolling direction were cut out of the plate. Discs 0.25 mm in thickness were sliced from a rod and the surface of discs to be ion-irradiated were mechanically polished with aluminum oxide

powders. Two TEM discs superposed were set in a specimen holder. The wide area ion irradiation chamber for polymeric materials attached to the LD1 port in the third light ion target room was employed for irradiation and discs were irradiated in the cyclotron of Takasaki Research Establishment of JAERI using 50 MeV He^{2+} at room temperature. Discs were irradiated for about 11 hours with beam current of $2.8 \times 10^{-2} \mu\text{A}/\text{cm}^2$ ($1 \mu\text{A}/6\text{cm} \times 6\text{cm}$). Depth profiles of displacement damage and deposited helium ions in pure iron were calculated using the E-DEP-1 code. After irradiation, the irradiated TEM discs were cooled in the atmosphere for about three months. The activities of them were measured and the nuclides produced in them were unidentified using a Ge(Li) semiconductor detector.

II. RESULTS

The depth profiles of damage level and deposited helium ions were calculated using the E-DEP-1 code in a stainless steel. The projected range of 50 MeV helium ions is evaluated to be about $370 \mu\text{m}$. So that, only damage nearly uniformly produced in the front disc, and the average damage level was evaluated to be about 4×10^{-3} dpa. On the other hand, helium ions deposited and the maximum damage level formed in the middle region of the second disc. Their values were 80 at.ppm and 10^{-2} dpa respectively. The activity of every disc was about $1 - 2 \mu\text{Sv/h}$.

The nuclides and their activities produced in one TEM disc were shown in table 1 in comparison with those calculated using the IRAC code. The measured and calculated activities indicated good agreement excluding ^{54}Mn and ^{51}Cr .

Hereafter, transmission electron microscopy (TEM) observation was carried out for the irradiated TEM discs.

Table 1 Nuclides and activities in the stainless steel cooled for 30 days after irradiation of 50 MeV helium ions

Nuclide	Activity	
	Measured	Calculated
^{56}Co	3.9×10^2	1.1×10^3
^{57}Co	5.9×10^3	3.9×10^3
^{58}Co	2×10^3	3.6×10^3
^{54}Mn	3.8×10^2	NG
^{51}Cr	9.8×10	NG

NG means negligible small
These values are for one TEM disc.

III. CONCLUSION

Stainless steels were irradiated by 50 MeV helium ions with a beam current of 2.8×10^{-2}

$\mu\text{ A/cm}^2$. The maximum damage level was calculated to be about 10^{-2} dpa. These irradiation conditions are not adequate for irradiation experiment of stainless steels. And it is impossible to inject uniformly helium ions into materials. In order to increase damage levels, it is required increasing of beam current such as focussing of beam and decreasing of scanning width. Under consideration of regular irradiation for structural materials, considerable modification of the present apparatus such as installation of a degrader and a temperature controller, or a new chamber to another beam line will need in the future.

Acknowledgement

We would like thank to Dr. T. Sasuga and Mr. H. Kudo of JAERI for their help in irradiation experiment.

References

- 1) D. Blasl, H. Tsunakawa, K. Miyahara and N. Igata, J. Nucl. Mater. 133 & 134 (1985)517.
- 2) W.G. Johnston, J.H. Rosolowski, A.M. Turkalo and T. Lauritzen, J. Nucl. Mater. 54(1974)24.
- 3) S.D. Harkness, B.J. Kestel and P. Okamoto, Radiation-Induced Voids in Metals, J.W. Corbett and L.C. Inniello, Eds. (U.S. Energy Commission, Oak Ridge, Tn. 1972) CONF-71060, p.334

5.4 ELECTRICAL PROPERTIES OF ION-BEAM-IRRADIATED SEMI-INSULATING GaAs

K. Kuriyama , Yukimi Takahashi ,
K. Tomizawa , Takashi Kato ,
H. Takeshita *, S. Yamamoto* , and H. Naramoto *

*College of Engineering and Research Center of Ion Beam
Technology, Hosei University*

** Department of Materials Development, JAERI / Takasaki*

1. INTRODUCTION

GaAs has been widely used as a functional material to form high speed devices such as n-p-n bipolar transistors. The traditional p-type elements such as Be, Mg, Zn and Cd have been employed as p-type dopants. However, it is difficult to realize heavy doping and to fabricate a shallow p-type base layer because of their larger diffusion coefficients. Recently, the fabrication of p-type layer¹⁾ due to carbon doping has been investigated because of its lower diffusion coefficient. In this work, we report the electrical activation process in carbon implanted semi-insulating GaAs.

2. MATERIALS AND IRRADIATIONS

The samples used here were obtained from undoped (100) -oriented semi-insulating GaAs ($\rho \approx 10^7 \Omega\text{-cm}$) grown by As pressure Czochralski (PCZ) technique. 1.0-MeV carbon ions were irradiated around 270 K with nitrogen-gas cooling. The carbon dose was $1 \times 10^{14} \text{ cm}^{-2}$. In order to avoid the ion-channeling effects, irradiations were carried out in the 7° - off $\langle 100 \rangle$ direction. The irradiated samples were confirmed to be crystalline by Rutherford Backscattering channeling experiments. A carbon depth profile in GaAs evaluated by TRIM simulation has a peak at about $1.2 \mu\text{m}$. Irradiated samples were isochronally annealed for 15 min at 400, 500, 550 and 600 $^\circ\text{C}$, respectively.

3. EXPERIMENTS

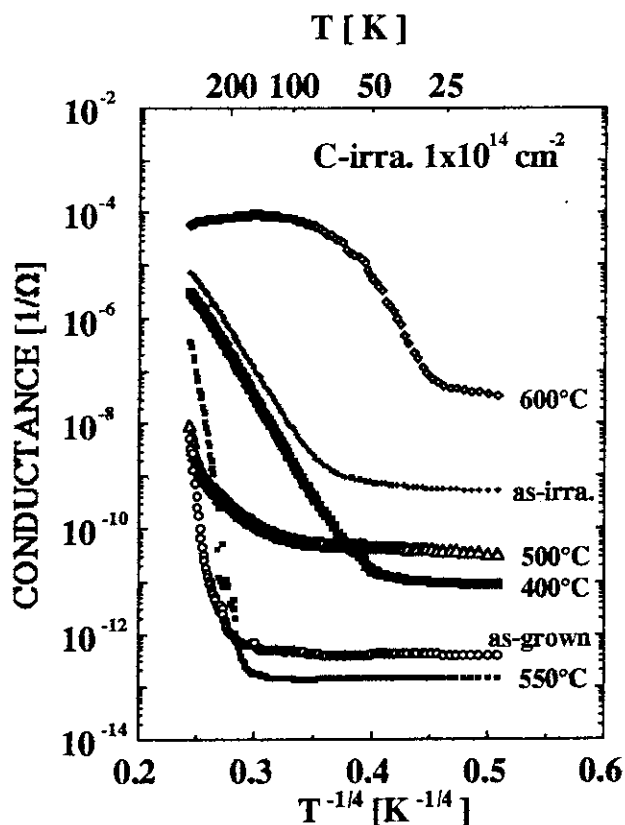


Fig.1 Temperature dependence of conductance for carbon irradiated semi-insulating GaAs. The carbon dose is $1 \times 10^{14} \text{ cm}^{-2}$.

Figure 1 shows the temperature dependence of conductance at various anneal temperatures. After irradiation, unannealed and 400 °C annealed samples showed a hopping conduction [$G \propto T^{-1/4}$] at the temperature ranging from 50 to 300 K. This behavior is known as *variable range hopping*²⁾ that electrons hop between defect levels introduced by irradiation. This kind hopping conduction has been observed in neutron irradiated GaAs³⁾. The defect concentration associated with the hopping conduction was estimated to be $\sim 10^{18} \text{ cm}^{-3}$ by Mott's theory²⁾. It is considered that the defect levels relating to hopping conduction contain not only EL2 center, but also As antisites (As_{Ga}), whose traps are located at the 0.77 eV below the conduction band⁴⁾. In the case

of carbon irradiation, however, defect levels produced have not been identified yet. On the other hand, the conductances of 500 and 550 °C annealed samples did not show the $T^{-1/4}$ - law. This indicates that defects associated with the hopping conduction were partially annealed out above 500 °C. Consequently, in these annealing temperatures, the band conduction is predominantly rather than the hopping conduction. In the temperature ranging

from 200 to 300 K, the activation energies were 285 and 355 meV, respectively. Since these values correspond to those of complex defects such as $\text{As}_{\text{Ga}} + \text{V}_{\text{As}}$ ⁵⁾, the conduction would arise from $\text{As}_{\text{Ga}} + \text{V}_{\text{As}}$ defects. Furthermore, we observed the metallic impurity conduction⁶⁾ that activation energies are little or about 1 meV in the range from 15 to 50 K. 600 °C annealed samples showed the electrical activation of carbon, accompanying by a conductance increase. In the temperature ranging from 30 to 60 K, an activation energy was 22 meV, which corresponds to that of carbon acceptor reported in GaAs⁷⁾.

Table.1 Electrical transport properties for as-grown , 600 , and 800°C annealed samples.

sample	Sheet Resistance [Ω]	Sheet Carrier Concentration [cm^{-2}]	Mobility [cm^2/Vs]	Conduction type
as-grown	2.0×10^8	4.6×10^6	6900	N
C : $1 \times 10^{14} \text{cm}^{-2}$ 600°C anneal.	1.7×10^3	1.0×10^{12}	350	P
C : $1 \times 10^{14} \text{cm}^{-2}$ 800°C anneal.	2.4×10^3	1.2×10^{13}	220	P

In order to evaluate the electrical activation processes of implanted carbon atoms , we measured the Hall effect with Van der Pauw technique. Table 1 shows the results for 600 and 800 °C annealed samples. In samples indicating the electrical activation of carbon, the conduction was p-type. Sheet carrier concentrations of these samples were 1.0×10^{12} and $1.0 \times 10^{13} \text{cm}^{-2}$ at room temperature, respectively. However, the electrical activation rates that irradiated carbons act efficiently as acceptors were ~ 1 and $\sim 10\%$, respectively.

It is well known that the midgap electron trap (EL2 defect) in GaAs is transferred from normal to metastable state by photoillumination below 125 K . In order to survey the relationship between EL2 defect and hopping sites, the conductance after photoillumination ($\lambda=890\text{nm}$) was measured for 400 °C

annealed samples . However, the conduction variation was not observed after photoillumination. It is concluded that the defect concentration associated with hopping conduction is two orders of magnitude larger than EL2 concentration ($\sim 10^{16} \text{ cm}^{-3}$) or defect levels relating to the hopping conduction are apart from the EL2 defect level.

4. CONCLUSION

Carbon irradiated GaAs showed the variable range hopping conduction, indicating the temperature dependence of $T^{-1/4}$. In samples annealed above 500 °C , the hopping conduction vanished with decreasing hopping sites. The electrical activation of implanted carbon ions were observed for samples annealed above 600 °C .

This work was performed under the JAERI / TIARA Collaboration Program #22008.

REFERENCES

- 1) P. M. Enquist , Appl. Phys. Lett. 57 , 2348 (1990).
- 2) N. F. Mott , J. Noncryst. Solid 1 , 1 (1968).
- 3) K. Kuriyama , K. Yokoyama , and K. Taniguchi , Phys. Rev. B45 , 6251 (1992).
- 4) M. Satoh , and K. Kuriyama , Phys. Rev. B40 , 3473 (1989).
- 5) J. C. Bourgoin , and H. J. von Bardeleben , J. Appl. Phys. 64 , R65 (1988).
- 6) D. A. Woodbury , and J. S. Blakemore , Phys. Rev. B8 , 3803 (1973).
- 7) S. M. Sze , in *Physics of Semiconductor Devices* (John Wily & Sons, New York , 1981) , p-21.

5.5 HIGH ENERGY Ni ION IMPLANTATION AND THERMAL ANNEALING FOR α -SiC SINGLE CRYSTAL

Kiyoshi KAWATSURA, Narutoshi SHIMATANI, Takanori NAKAE, Shigeyoshi ARAI, Takeshi SHIONO, Yuji HORINO*, Yoshiaki MOKUNO*, Kanenaga FUJII*, Hidefumi TAKESHITA**, Shunya YAMAMOTO**, Yasushi AOKI** and Hiroshi NARAMOTO**

Department of Chemistry, Kyoto Institute of Technology,

*Government Industrial Research Institute, Osaka,

**Department of Materials Development, JAERI, Takasaki

I. Introduction

Because of the extreme hardness, high temperature stability, high thermal conductivity, chemical inertness and high temperature semiconducting properties, silicon carbide (SiC) crystals are very potent as electronic devices which operate even in a harsh environment.

Since the late 1960's, implantations and annealing behaviors for SiC single crystals have been studied^{1, 2)}. It is found for the annealing behavior that the recrystallization temperature increases with the radiation-induced damage. However, the annealing mechanism has not been revealed because of its complexity.

Gettering of impurities in silicon^{3, 4)} is a widely used technique to increase the purity of materials in the active regions of devices. However, such a gettering effect has not been studied for SiC regardless of a great deal of interest at SiC devices.

Here, we preliminarily demonstrate the results of experiments aimed at a gettering layer introduction into a α -SiC single crystal using ion implantations and thermal annealings⁵⁾.

II. Experimental

The α -SiC single crystals employed in the present study were obtained from Taiheiyo-rundum Co.. They were synthesized by the Acheson method. The polytype was predominantly 6H form. Each crystal surface was parallel to the (0001) basal plane.

The 1.0 MeV $^{58}\text{Ni}^+$ implantation was carried onto 5 mm ϕ of the surface of α -SiC samples at RT at the angle 27.5° to the (0001) axis, using a 3 MV

tandem accelerator in Japan Atomic Energy Research Institute, Takasaki (JAERI, TIARA facilities). The fluence was 1×10^{15} and $1 \times 10^{17}/\text{cm}^2$, and the dose rate was $0.5 \mu\text{A}$. The implantation was carried in a vacuum chamber with 1×10^{-5} Pa.

Post-implantation annealings were done in a gas flow of 1 atm argon. Thermal annealings were carried at 500, 1000 and 1500°C for two hours.

Rutherford backscattering spectroscopy with channeling (RBS-C) was performed using 1.8 and 1.6 MeV He^+ ions from a 2 MV Van de Graaff accelerator in Government Industrial Research Institute, Osaka. The probe beam size was $1 \times 1 \text{ mm}^2$. A solid state detector with 15 keV resolution was mounted at 165° for the incident in a vacuum chamber with 5×10^{-4} Pa. The probe beam current was 8-15 nA. RBS-C measurements were carried on samples after each annealing.

III. RESULTS AND DISCUSSION

Figs. 1a-1d show RBS spectra at the random and the aligned orientations for the unimplanted region of a 1.0 MeV Ni^+ implanted $\alpha\text{-SiC}(0001)$ sample with a fluence $1 \times 10^{17}/\text{cm}^2$ at RT at 27.5° to the (0001) axis, and for the implanted region of the as-implanted, and the 1000 and 1500°C annealed samples, respectively. The spectra for the 500°C annealed sample are almost the same as those in fig. 1b. The spectra in fig. 1d were measured using 1.6 MeV He^+ , and the others using 1.8 MeV He^+ . Similarly, the RBS-C measurements were carried for the $1 \times 10^{15} \text{ Ni}^+/\text{cm}^2$ sample.

The larger aligned yield in fig. 1b than that in fig. 1a is due to the radiation-induced damage. Here, to discuss the depth distribution of the

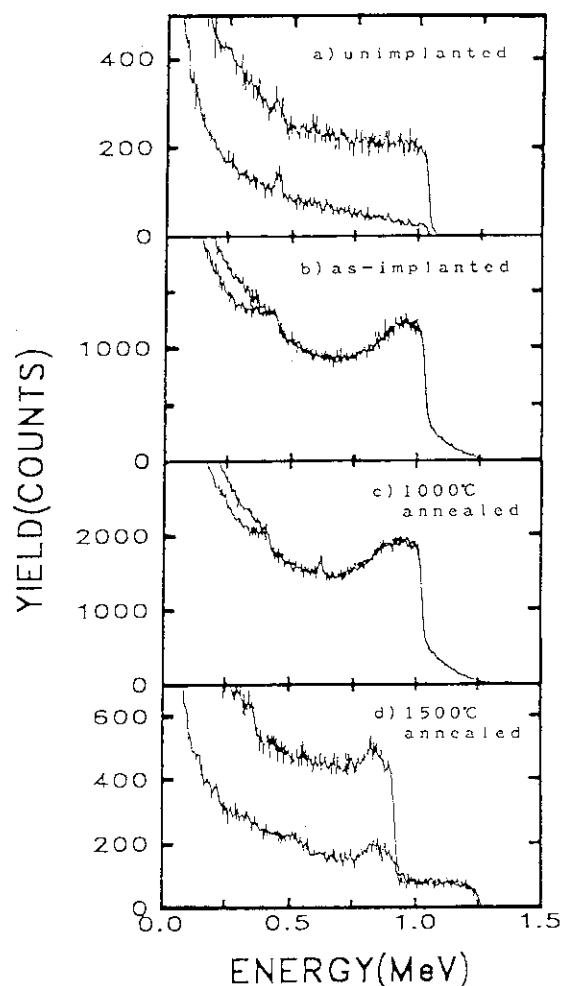


Fig. 1 RBS-C spectra for random and aligned orientations for the $1 \times 10^{17} \text{ Ni}^+/\text{cm}^2$ implanted $\alpha\text{-SiC}(0001)$ sample. Spectra in fig. 1d were analyzed using 1.6 MeV He^+ , and the others using 1.8 MeV He^+ .

damage, χ_{\min} is introduced. χ_{\min} is defined as the ratio of the minimum (0001) aligned yield to the random yield. In this paper, a layer whose χ_{\min} is unity is defined as an amorphous layer. The depth dependence of χ_{\min} for the 1×10^{15} and 1×10^{17} Ni^+/cm^2 samples is shown in figs. 2a and 2b, respectively. In fig. 2b, χ_{\min} of the as-implanted sample is unity from the surface to the depth $0.80 \mu\text{m}$. The thickness, T_A , of the amorphous layer is estimated at $0.80 \pm 0.08 \mu\text{m}$ for the 1×10^{17} Ni^+/cm^2 sample, and similarly $0.65 \pm 0.07 \mu\text{m}$ for the 1×10^{15} Ni^+/cm^2 one (See fig. 2a).

T_A of both samples did not change during the 500°C annealing. Even during the 1000°C annealing, T_A decreased only a little from $0.65 \pm 0.07 \mu\text{m}$ to $0.52 \pm 0.05 \mu\text{m}$ for the 1×10^{15} Ni^+/cm^2 sample, and not for the 1×10^{17} Ni^+/cm^2 . The recrystallization temperature seems to increase with the fluence.

The initial stage of the recrystallization is found during the 1000°C annealing for the 1×10^{15} Ni^+/cm^2 sample (See fig. 2a). In the depth region from $0.52 \mu\text{m}$ to $0.7 \mu\text{m}$, the χ_{\min} of the 1000°C annealed sample is smaller than that of the as-implanted one. This indicates that the recrystallization starts epitaxially²⁾ from the crystal layer. On the other hand, in the deeper region than $0.7 \mu\text{m}$, the χ_{\min} of the 1000°C annealed sample is larger than that of the as-implanted one.

The explosive recrystallization of the whole amorphous layer during the 1500°C annealing is found for both the samples. This is recognized from the decrease of the aligned yield and the χ_{\min} (See figs. 1c and 1d, and figs. 2a and 2b).

On the other hand, in the χ_{\min} curve for the 1×10^{17} Ni^+/cm^2 sample,

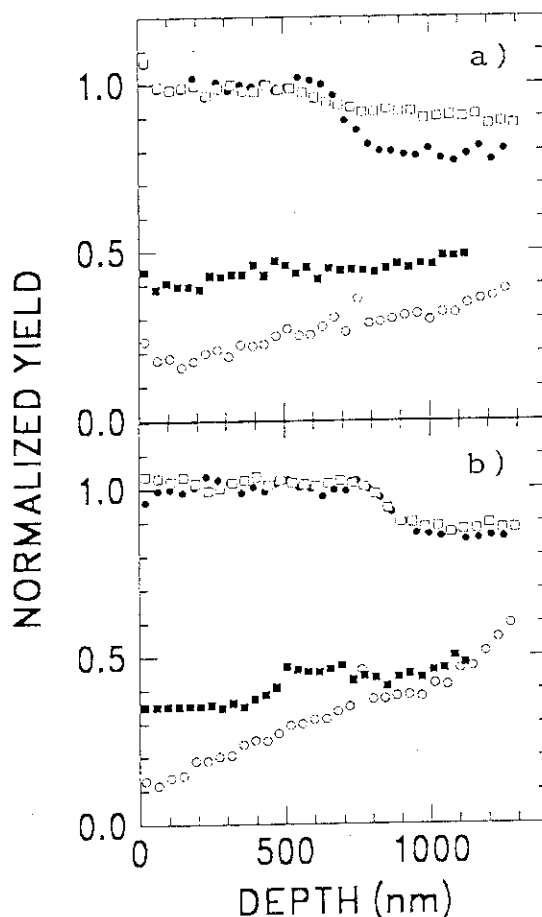


Fig. 2 Depth dependence of χ_{\min} for (a) 1×10^{15} Ni^+/cm^2 and (b) 1×10^{17} Ni^+/cm^2 samples. Unimplanted (\circ), as-implanted (\bullet) and 1000°C (\square) and 1500°C (\blacksquare) annealed.

a plateau region is found in the depth region from $0.5 \mu\text{m}$ to $0.7 \mu\text{m}$ (See fig. 2b). This indicates a layer with a high defect concentration in the recrystallized layer. The discussion for the depth of this layer is given below.

Here, the implanted Ni atom is discussed. The separation of the Ni spectrum is carried by the subtraction of the SiC spectrum from the SiC(Ni) spectrum. The spectrum of the as-implanted Ni atoms is like a gaussian distribution. The peak depth, P, is $0.54 \pm 0.05 \mu\text{m}$ and the full width at half maximum (FWHM), W, is $0.31 \pm 0.03 \mu\text{m}$.

During the 1500°C annealing, the Ni profile dramatically changed from the gaussian-like distribution to a trapezoid. This is due to the extensive Ni diffusion to the surface during the 1500°C annealing. The Ni profile expands from the surface to the depth $0.5 \mu\text{m}$ with $W(1500^\circ\text{C})$ of $0.58 \pm 0.06 \mu\text{m}$.

The depth $0.5 \mu\text{m}$ corresponds to the depth of the plateau region mentioned above. The precipitation of defects seems to occur beneath the Ni distribution. The lattice sites which are occupied by the Ni atoms before the 1500°C annealing, after the Ni atoms leave them, may behave as trap sites for the diffusing defects. Also, the trapped defects may be blocked by the Ni distribution.

The aligned Ni yield is the same as the random. This means that the implanted Ni atoms in the recrystallized layer do not occupy the substitutional lattice sites. This is different from the case of Sb ions¹⁾. About 50 per cent of implanted Sb atoms are located along the $\langle 0001 \rangle$ atomic rows after the 1500°C annealing. The difference seems to arise from that Sb atom is a dopant for SiC but Ni atom is not.

REFERENCES

- 1) R.R. Hart, H.L. Dunlap and O.J. Marsh, Radiat. Eff. 9 (1971) 261.
- 2) H.G. Bohn, J.M. Williams, C.J. McHargue and G.M. Begun, J. Mater. Res. 2 (1987) 107.
- 3) T.M. Buck, K.A. Pickar, J.M. Poate and C-M. Hsieh, Appl. Phys. Lett. 21 (1972) 485.
- 4) H. Wong, N.W. Cheung, P.K. Chu, J. Liu and J.W. Mayer, Appl. Phys. Lett. 52 (1988) 1023.
- 5) N. Shimatani et al., Int. Conf. for the Radiation effect in insulator-7, Nagoya (Sep. 1993).

5 . 6 PKA Energy Spectrum Dependence of Defect Cluster Formation in Gold by High Energy Self-Ion Irradiation

Naoto SEKIMURA, Yurugi KANZAKI*, Seiji OKADA*,
Takahiro MASUDA*, Shiori ISHINO* and Ryuichi TANAKA**

Nuclear Engineering Research Laboratory,

* Department of Quantum Engineering and Systems Science,
Faculty of Engineering, University of Tokyo

**Department of Advanced Radiation Technology, JAERI

I. Introduction

The structure of cascade damage in metals produced by high energy particles is dependent on energy of PKA (Primary Knock-on Atoms). To establish correlations between various irradiation data, microstructural changes in irradiated materials should be analyzed based on the PKA energy spectrum¹⁻²⁾. In the present study, thin foils of gold were irradiated with high energy self-ions to examine PKA energy spectrum dependence of defect cluster formation and cascade damage structure.

II. Experimental

Irradiations with 21 MeV and higher energy self-ions were carried out at room temperature using the 3 MV tandem accelerator in TIARA facilities. By placing gold foils of several thicknesses in front of the TEM specimens, we can change the PKA energy spectrum in the specimens.

Figure 1 shows the example of PKA energy spectrum calculated by the TRIM 89 code. PKA production cross section decreases monotonically with PKA energy in all the cases. Total PKA production cross section and high energy component of PKA increase with the thickness of gold foils up to the ion range of self-ions which is $6.5 \mu\text{m}$ from the ion incident surface. Ion fluence was 1.0×10^{14} and 1.0×10^{15} ions/m² to avoid cascade overlapping. Irradiated samples were observed by a 200 keV transmission electron microscope at the University of Tokyo.

Irradiation experiments using a 400 keV accelerator in the University of Tokyo were also performed to compare the cascade damage structure produced by the single energy cascade damage.

III. Results and Discussion

Groups of defect clusters which reflect subcascade structure produced by PKA are observed in the TEM foils of gold. All the clusters are found to be of vacancy type because of the high mobility of interstitials. Number of defect clusters in the group and their sizes are shown in Figures 2 and 3, respectively. In all the specimens, density of cluster groups monotonically decreases with the number of defect clusters in a group.

These results are compared with the data from 20-400 keV self-ion irradiation experiments, in which injected ions are regarded as monoenergetic PKA. Density of defect groups per incident ion is estimated as functions of number of clusters in the group and ion energy. Figure 4 shows fraction of defect groups which consist of n clusters as a function of PKA energy, E_P . Using this function, $P(n, E_P)$, and the PKA energy spectrum, $W(E_P)$, we can evaluate distribution of defect clusters under the high energy particle irradiation conditions by the following equation.

$$\int_0^{\infty} W(E_P) P(n, E_P) dE_P \quad (n = 1, 2, 3, \dots)$$

Figure 5 compares measured and predicted number of clusters in a groups. From this results, it is quantitatively shown that small fraction of high energy component of PKA

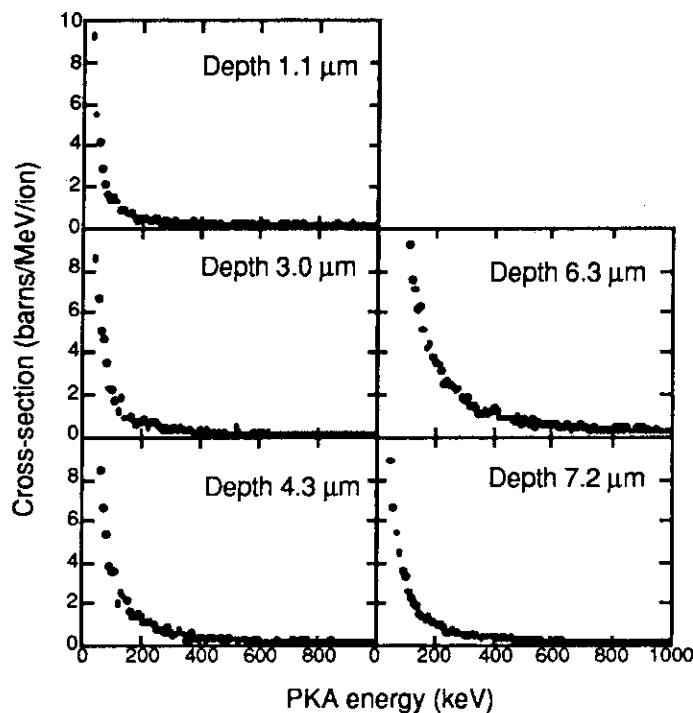


Fig. 1 Example of calculated PKA energy spectrum in gold irradiated with 170 MeV self-ions.

affects the formation of cluster groups which have large number of clusters. A model to predict defect cluster formation under any PKA spectrum is being proposed from the extrapolation of defect cluster formation by PKA over 400 keV.

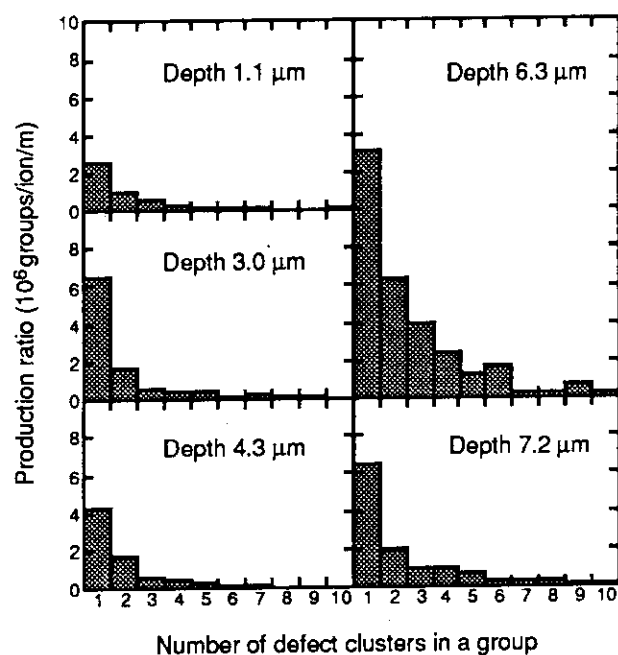


Fig. 2 Number of defect clusters in defect groups in irradiated gold to 1.0×10^{14} ions/m² at room temperature.

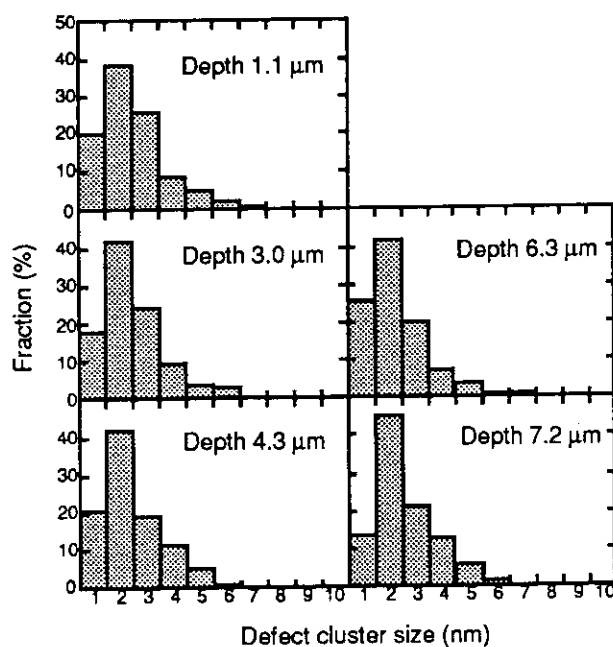


Fig. 3 Size of defect clusters in defect groups in irradiated gold to 1.0×10^{14} ions/m² at room temperature.

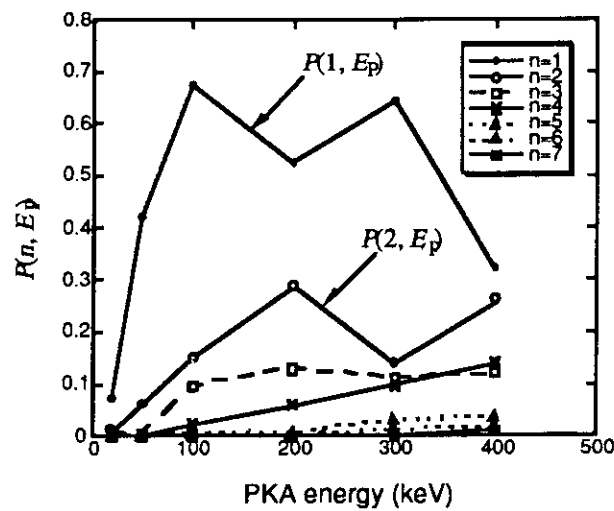


Fig. 4 Fraction of defect groups which contain n clusters as a function of PKA energy determined by 20 - 400 keV self-ion irradiation.

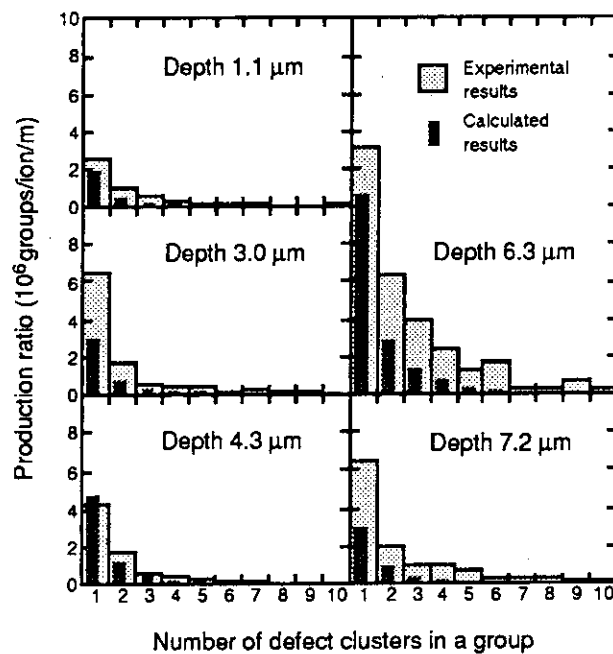


Fig. 5 Comparison of measured and estimated distribution of number of defect clusters in a group.

References

- 1) S. Ishino and N. Sekimura, Annales de Chemie, Science des Materiaux, 16 (1991) pp.341-350.
- 2) M. Kiritani, T. Yoshiie, S. Kojima and Y. Satoh, Radiation Effects and Defects in Solids 113 (1990) pp.75-96.

5.7 MOLYBDENUM SILICIDE FORMATION BY MEANS OF ION MIXING

Somei OHNUKI, Tsuyoshi HATAKEYAMA, Seiichi WATANABE,
Heishichiro TAKAHASHI, Shunya YAMAMOTO*,
Hidefumi TAKESHITA*, Hiroshi NARAMOTO*

Faculty of Engineering, Hokkaido University

*Takasaki Institute, JAERI

I. INTRODUCTION

Ion-mixing method can contribute to modify the material properties through two processes; one is production of large amount of point defects, which enhances lattice diffusion, and the other is the direct atomistic collision, which causes atom movement even at low temperature. For the formation of silicides during fabricating LSI, heat-treatment at relatively high temperature has been needed. Therefore, ion-mixing has currently application as a method of silicide formation at low temperature. The objectives of this study are to clarify the condition of silicide formation by means of ion-mixing, to identify microstructures of formed phases and to evaluate diffusion constant during irradiation.

II. EXPERIMENTAL PROCEDURE

Si wafer of single crystal with (100) was used for experiment, after Mo vapor deposition with thickness of 600 Å. Irradiation with Ar^+ ion of 180 keV was carried out in 300 kV accelerator of Hokkaido University, at where the temperature were -100 - 300 C, and irradiation doses were 1×10^{16} - 1×10^{17} ion/cm². Si^+ ion irradiation of 1000 keV was carried out in TIARA at only ambient temperature. After irradiation, specimens for transmission electron microscopy (TEM) were prepared by the cross-cut method, which means the observed direction was $\langle 110 \rangle$, perpendicular to irradiation beams. Depth distribution of concentration of Mo and Si was determined by using a energy dispersive X-ray spectroscopy (EDS) equipped with 200 kV TEM.

3. RESULT AND DISCUSSION

3.1 180 keV Ar^+ ion Irradiation

Figure 1 shows crosssectional micrographs and diffraction patterns from ion-mixed layer of Mo coating on Si wafer irradiated by 180 keV Ar^+ ion at room temperature to several ion doses. At lower irradiation dose, 1×10^{16} /cm², the irradiation affected to the thickness of 200 nm of Si substrate, and the middle of the layer turned to amorphous. Crystalline Mo remained, and a layer between Mo and amorphous Si was confirmed as amorphous stricture. With increasing of dose, the amorphous of mixture of Mo and Si was increased in thickness, which means that ion-mixing process occurred clearly in this condition. In the case of higher dose, 1×10^{17} /cm², gas

bubbles were observed at amorphous layer.

Figure 2 shows crosssectional view of ion-mixing layers after Ar^+ irradiation to $1 \times 10^{17} / \text{cm}^2$ at various temperature. At lower temperature, -100°C , almost all of mixed layer was crystalline, and Mo rich layer can be defined as a dark contrast. After the irradiation at 100°C , crystalline MoSi_2 was formed between amorphous Mo/Si mixture and amorphous Si layers. At 200°C , the thickness of MoSi_2 increased, and amorphous Si layer turned to crystalline Si layer which included large amount of irradiation-produced damages. At higher temperature, 300°C ,

only MoSi_2 and damaged Si layers were observed. This results indicate that by ion-mixing method crystalline MoSi_2 can be formed over 100°C , which temperature is quite lower comparing to thermal treatment. It can be suggested that the stability of each amorphous layers is the order of $\text{MoSi}_2 < \text{Mo/Si mixture} < \text{Si}$. It has been reported that amorphous Si is stable under 200°C .

Figure 3 shows the concentration profiles of Si in specimens irradiated to $1 \times 10^{17} / \text{cm}^2$ at various temperatures. At lower temperatures, Si diffused to the direction of the surface and formed concentration gradient, though data points have large scattering. At higher temperatures, the gradient of Si concentration became to flat, which can suggest to occur more progressive diffusion.

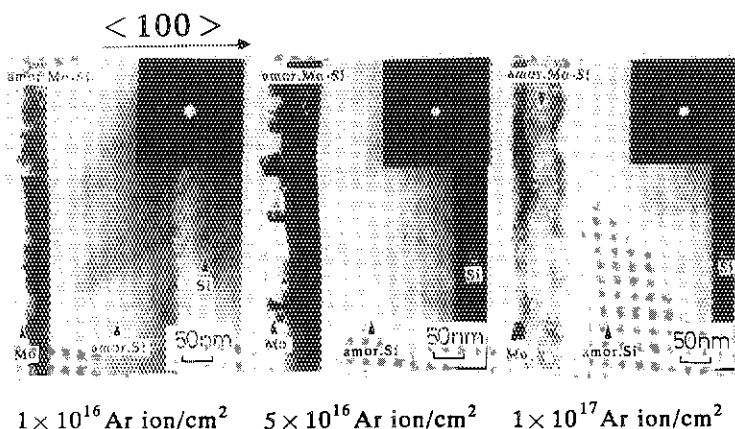


Fig.1

Cross-section and electron diffraction patterns in Mo/Si(Mo=60nm)system irradiated by 180 keV Si ion at R.T

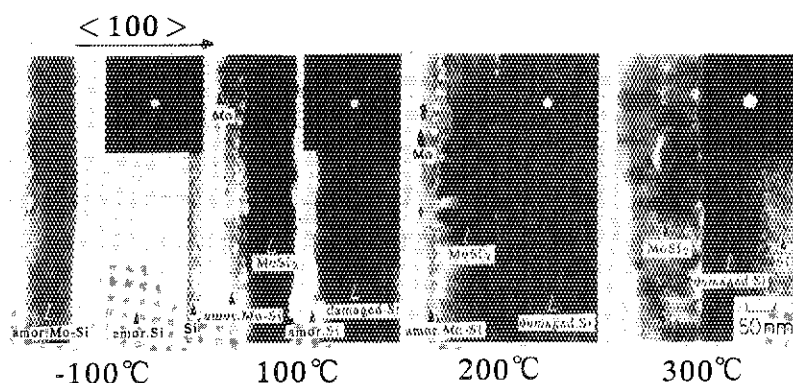


Fig.2

Cross-section and electron diffraction patterns in Mo/Si(Mo=60nm)system irradiated by 180 keV Si ion at various temperature

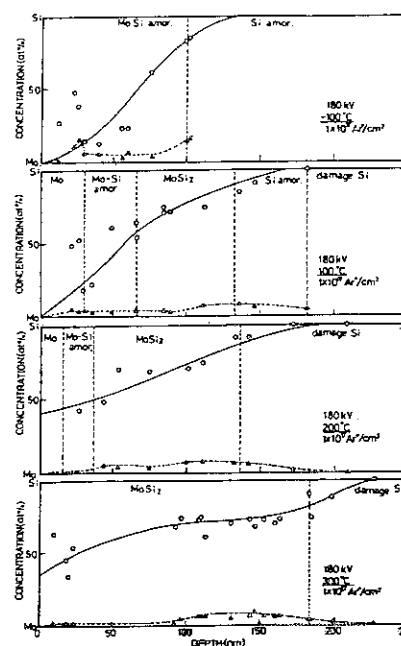


Fig.3 Depth profile of Si after Ar^+ mixing.

3.2 1000 keV Si⁺ ion Irradiation

Figure 4 shows crosssectional

microstructures and electron diffraction patterns from ion-mixed layer irradiated by 1000 keV Si⁺ ion at room temperature to different ion doses. At lower irradiation dose, 1×10^{16} /cm², the irradiation affected to the thickness of 200 nm of Si substrate, and Si layer until 1000 nm in thickness turned to be amorphous. Crystalline Mo remained, and a layer between Mo and amorphous Si was confirmed as amorphous stricture. With increasing of dose, the amorphous of mixture of Mo and Si was increased in thickness, which means that ion-mixing process occurred clearly in this condition. In the case of higher dose, 5×10^{16} /cm², gas bubbles were not confirmed at this irradiation condition.

Figure 5 shows the concentration profiles of Si in specimens irradiated by 1000 keV Si⁺ ions to 1 and 5×10^{16} /cm². The result of lower dose, Si diffused clearly to the direction of the surface and formed concentration gradient, though data points have large scattering. At higher dose, the gradient of Si concentration became to flat, which showed that a enough diffusion occurred at this condition.

3.3 Estimated Diffusion Constant

Figure 6 shows the temperature dependence of diffusion constant which was estimated from the experimental data by using Matano's method, and it includes thermal diffusion data of Mo in Si. In this case, the concentration profiles are assumed to be smooth curves, though there are large scattering and constant concentration for each layers. The diffusion constant is almost constant under 200 C, which means that this is controlled by athermally ion-mixing process. The dose dependence of

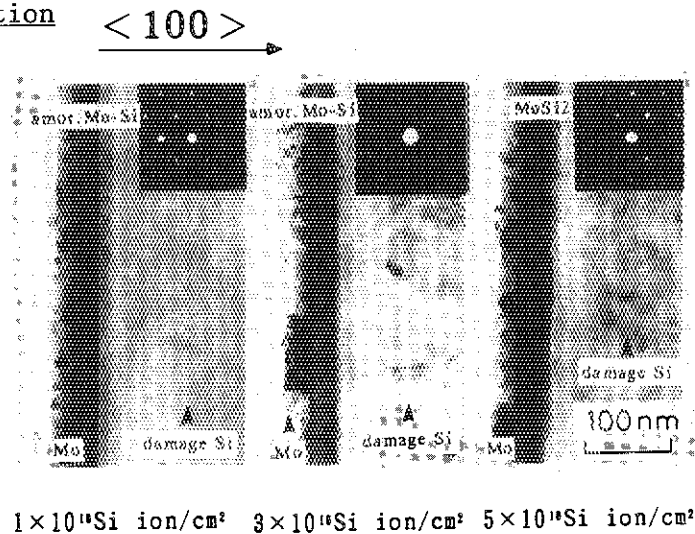


Fig.4 Cross-section and electron diffraction patterns in Mo/Si(Mo=60nm)system irradiated by 1MeV Si ion at R.T.

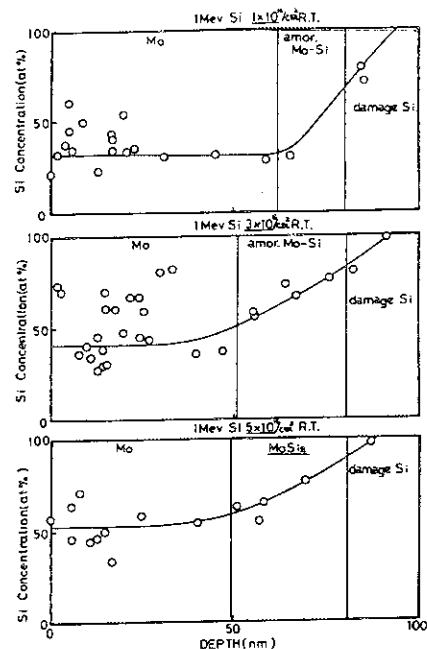
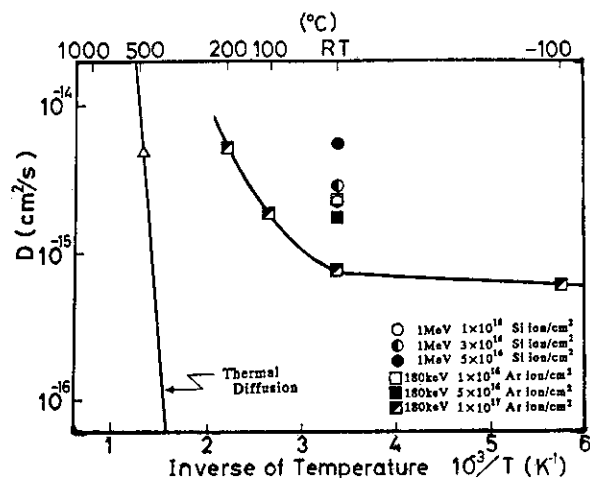


Fig.5 Depth profile of Si after Si⁺ mixing.

diffusion constant at room temperature shows interesting behavior; the diffusion constant decreased with increasing of irradiation dose. This suggests the presence of a saturation of diffusion process during irradiation, because the diffusion constant has been decided under assuming constant rate process. This saturation process was confirmed to checking the diffusion distance is not changed over the dose of $5 \times 10^{16} / \text{cm}^2$. This



saturation of diffusion may come

from the cavity formation on layer surfaces, which cause a reduction of contacted area and stated in microstructures irradiated to higher doses. To confirm the effect of reducing areal fraction, the dose dependence of diffusion constant has been checked by using Si^+ irradiation; diffusion constant increased with increasing of Si^+ ion dose. These results indicate that gas bubbles formed on the interfaces could cause to suppress the silicide formation during ion-mixing.

4. SUMMARY

To clarify the condition of silicide formation by means of ion-mixing, 180 keV Ar^+ and 1000 keV Si^+ ion irradiation was performed to Mo/Si system. The objective silicide MoSi_2 was formed by the irradiation relatively low temperatures, over 100 C. The estimation of diffusion constant indicates that atomistic collision and radiation enhanced diffusion processes are predominate in this phenomenon. The ion-mixing is strongly dependent on ion species, especially gaseous elements has a possibility to reduce the amount of ion-mixing during gas bubble formation.

6. Materials Analysis

6.1	Ion Beam Analysis on Sapphire Implanted with Vanadium Ions H.Naramoto, H.Takeshita, Y.Aoki and S.Yamamoto	119
6.2	Light Elements Analysis in Thin Films by RBS S.Yamamoto, Y.Aoki, H.Takeshita and H.Naramoto	123
6.3	High-energy Shadowing Effect Studied with Ion-induced Secondary Electron Spectroscopy H.Kudoh, H.Takeshita, Y.Aoki, S.Yamamoto, H.Naramoto and S.Kuwabara	126
6.4	Application of Heavy Ions to Rutherford Backscattering S.Nagata, K.Takahiro, S.Yamaguchi, S.Yamamoto, H.Takeshita, Y.Aoki and H.Naramoto	130
6.5	Optical Measurement System for Study of Electron-hole Pairs Induced in Semiconductors by High-energy Ion Irradiation H.Itoh, T.Hirao and I.Nashiyama	134
6.6	Positron Annihilation Study of Defects in Si: An Internal Source Method M.Hasegawa, S.Okada, A.Kawasuso and M.Suezawa	138
6.7	Time-resolved X-ray Absorption Spectroscopy of Laser Ablated Silicon and Carbon Particles O.Yoda, A.Miyashita, T.Ohyanagi and K.Murakami	143
6.8	In-situ Measurement of Secondary Ions During Hydrocarbon Ion Beam Deposition H.Ohno, Y.Aoki and S.Nagai	145
6.9	XPS Studies on the Charge States of Cr and Cu Atoms Implanted into α -Al ₂ O ₃ and MgO Single Crystals T.Futagami, Y.Aoki, O.Yoda, S.Nagai and D.M.Rück	149
6.10	In-situ Observation of Effect of Hydrogen and Helium Dual-ion Irradiation in Aluminum S.Furuno, K.Hojou, H.Otsu, K.Izui, N.Kamigaki, K.Ono and T.Kino	153

6.1 ION BEAM ANALYSIS ON SAPPHIRE IMPLANTED WITH VANADIUM IONS

Hiroshi NARAMOTO, Hidefumi TAKESHITA, Yasushi AOKI
and Shunya YAMAMOTO

Department of Materials Development, JAERI/Takasaki

1. Introduction

Ion implantation is a violent method to introduce different species in a matrix, but it is still attractive because one can control the materials properties in a way far from the thermal equilibrium¹⁾. Sapphire is expected to become excellent insulators as substrates for the growth of electronic functional materials because of its high crystal perfection and its high purity. Some oxides of vanadium experience the phase transition by cooling or by applying high pressure. Thus, these oxides are promising functional materials. Especially on sapphire substrates, the formation of $\alpha\text{-V}_2\text{O}_3$ is reasonably expected because of its same crystal symmetry. But it is still needed to perform the systematic study about the interaction of implanted species with the radiation-induced defects by changing the implantation temperature.

In the present report, the preliminary results are shown about the RBS/NRA/channeling analysis on $\alpha\text{-Al}_2\text{O}_3$ implanted with V ions. The recovery process of each sublattice under oxygen circumstance is compared, and the occupation of V on the Al sublattice is concluded through the formation of the crystalline mixed oxide.

2. Experimental

(0001) $\alpha\text{-Al}_2\text{O}_3$ plates were used as substrates for the ion implantation. Typical size of these specimen were $10 \times 10 \times 0.3 \text{ mm}^3$ and the surface strains were removed away by chemical etching using concentrated phosphoric acid at high temperature before ion implantation. The implantation was performed by impinging 1 MeV ^{51}V ions onto Sapphire surface in a glancing angle of 30

degrees to assure the shallow penetration depth for the ion beam analysis. The specimen surface was partly covered for the later crystal orientation after each thermal annealing. This process gives us a chance of checking the crystal quality change even in the unimplanted region after thermal annealing. The implantation dose was monitored precisely to be about 3×10^{16} /cm² by adjusting a secondary electron suppressing system. 2 MeV ⁴He ions were employed for a standard ion beam analysis because the choice of higher energy ⁴He ions will induce the non-Rutherford backscattering. The axially aligned spectra were obtained along a <0001> crystallographic axis. Thermal annealings were made in open air for a hour at 600, 800 and 1000°C. The special cares were paid to avoid the charging problem by putting a metallic plate close to a probing beam. This was assured by comparing the shifts of surface peaks among the aligned spectra.

3. Results and discussion

Fig. 1 shows three kinds of RBS spectra from α -Al₂O₃ crystal implanted with 1 MeV ⁵¹V ions up to 3×10^{16} /cm². The spectrum with highest yield is taken under a random orientation, and other two are <0001> aligned spectra for implanted (higher yield) and unimplanted (lower yield) area. The increase in a aligned spectrum after the ion implantation reflects the distribution of radiation-induced defects along depth. One can see some difference in the yield increase in Al and O sublattice in a aligned spectrum from the implanted region (50 and 70% of the random level for Al and O sublattice, respectively). This difference implies the selective displacement of O sublattice. The depth-distribution of implanted V is not symmetric between the aligned and random spectrum. It is difficult to find out an exact answer to this problem at this stage but this phenomenon is possibly related to the difference of the charge states of implanted species associated with radiation-induced defects along depth.

The distributions of induced defects and implanted species show a dramatic change by thermal annealing. This change starts from 800°C, and the most of induced defects recovers after 1000°C annealing as can be observed in Fig. 2. The loss of implanted V atoms is also observed with the recovery of symmetrical distribution between the aligned spectra. In accordance with

this recovery, the substitutionality of implanted V increases. In this temperature region, it is difficult to assume the self-diffusion²⁾ of oxygen atoms, and it was needed to employ a combined analysis of RBS/NRA by utilizing $^{16}\text{O}(\text{d}, \text{p})^{17}\text{O}$ nuclear reactions in order to distinguish the contribution from each sublattice clearly. It is almost impossible to derive the information of O sublattice from the standard RBS measurements. The angular scans were made around the $\langle 0001 \rangle$ crystallographic axis for V, Al and O components in a sample after annealing at 1000°C in open air. The data from O sublattice was recorded directly through the integration of proton signal from the nuclear reactions. The random values among three kinds of spectra were assured to be the same by employing a fully automated goniometer system where the random orientation can be always set at the same position without rotating a sample around its normal. In insulating specimens like the present case, a metallic plate and probing beam should be kept to be close enough, and a true random spectrum can not realised by rotating a specimen around the crystal axis. The angular widths at the half maximum for Al, V and O atoms 1.25, 1.08 and 0.49 degrees, respectively. Thus, it is simply concluded from the close values of angular widths that implanted V atoms occupy the Al sublattice. The value of V atoms should be larger than the value for Al if V atoms form precipitated V_2O_3 . Thus, it is clear from the present study that implanted V atoms form mixed oxide by the occupation of Al sublattice after 1000°C annealing.

The present study will be expanded into the low temperature ones by using a dual beam analysis system installed in TIARA of JAERI/Takasaki. This system will make it possible to do the on-site analysis during ion implantation at low temperature down to around 15K. The microstructure of implants associated with induced defects is expected to be sensitive to the implantation temperature.

References:

- 1) C. W. White, C. J. McHargue, P. S. Sklad, L. A. Boatner and G. C. Farlow, Materials Science Reports 4, Nos.2/3(1989).
- 2) H. Naramoto, C. W. White, J. M. Williams, C. J. McHargue, O. W. Holland, M. M. Abraham and B. R. Appleton, J. Appl. Phys. 54(1984)683.

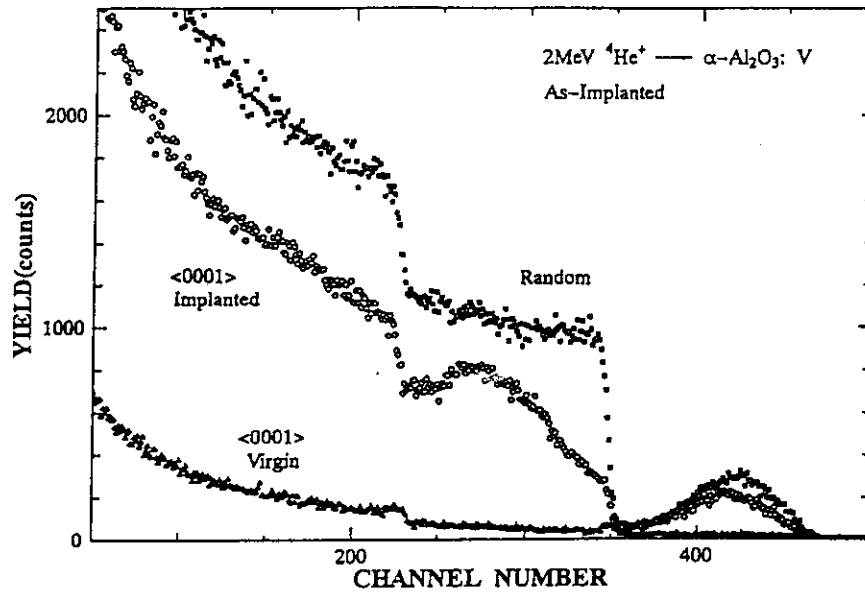


Fig.1: RBS spectra of 2MeV He ions from $\alpha\text{-Al}_2\text{O}_3$ as-implanted with 1MeV ^{51}V ions. Squares:random spectrum; open circle:<0001> aligned one in implanted region; open triangle:<0001> aligned one in unimplanted region.

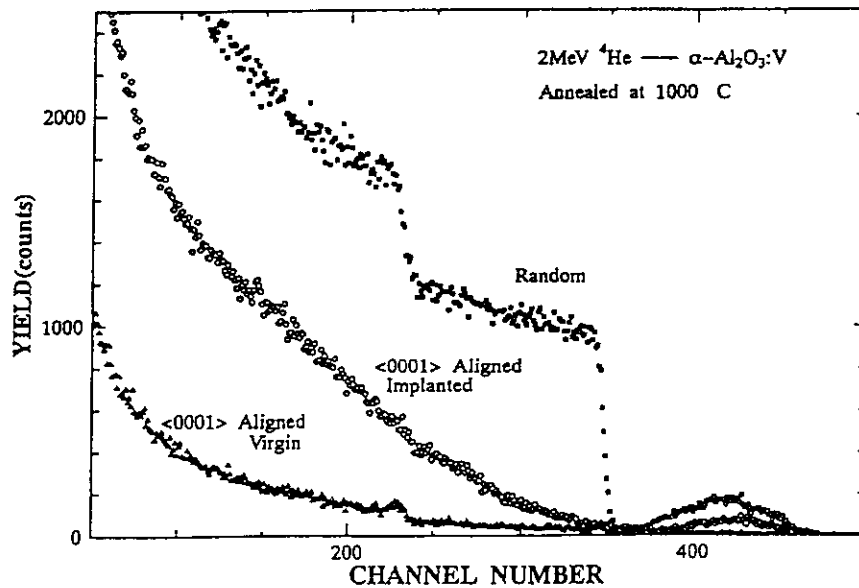


Fig.2: RBS spectra of 2MeV He ions from the same specimen as in Fig. 1 after annealing at 1000°C. Each spectrum corresponds to the same symbol as above.

6.2 LIGHT ELEMENTS ANALYSIS IN THIN FILMS BY RBS

Shunya YAMAMOTO, Hidefumi TAKESHITA, Yasushi AOKI
and Hiroshi NARAMOTO

Department of Material Development, JAERI/Takasaki

I. INTRODUCTION

Ion beam analysis using Rutherford backscattering process has been demonstrated to be a powerful technique for sensitive and reliable measurements of material composition and structure at surface/interface of thin layers.¹⁾ The characterization of thin films and multilayers are increasingly important to design the new functional materials in an atomic scale.

Nb-Cu metallic multilayers prepared by sputtering method have been studied about such as superconducting²⁾, structure³⁾ and elastic⁴⁾ various properties. It is known that the oxidation and the hydrogenation of Nb films have effect on both the electrical resistivity and the superconducting transition temperature. In this report, the results of ion beam analysis on Nb-Cu multilayers are described. we have prepared Nb,Cu and Nb-Cu multilayers films by electron beam evaporation method, and measured the sharpness of interface, the depth profile of compositional elements and the contaminated light elements.

II. SAMPLE PREPARATION

The Nb, Cu and Nb-Cu multilayers films were prepared by electron beam(EB) evaporation on silicon(110), glassy carbon(G.C) and MgO(001) substrates at room temperature. Our system is equipped with three EB guns and a Kundsens cell and can be evacuated down to about 10^{-10} Torr. Liquid nitrogen shrouds covering the heated place keep a good vacuum even under evaporation, and the pressure during the evaporation was in the mid 10^{-8} Torr range. The deposition rates and deposition thicknesses were controlled by quartz monitors located near the substrate and shutters on each hearth. The deposition rates of Cu and Nb were controlled so as to be about 0.2nm/s.

III. EXPERIMENTAL

Structural analysis was carried out using a 3MV tandem accelerator, NEC

9SDH2, in TIARA. 2MeV ^4He ions were chosen for the analysis not induce the non Rutherford scattering. The size of the beam was about 1mm in diameter and the beam current was about 5nA, typically. Backscattered particles were energy-analysed by a standard surface-barrier detector(ORTEC) placed 120mm from the target at 165 degrees to the incident beam. In order to suppress secondary electrons, the negative potential of 350V was applied to a copper ring in front of a target. During the measurement the pressure in the analysis chamber was of order 10^{-7} Torr.

IV. RESULTS AND DISCUSSION

In order to correlate the layer thickness to the values from quartz thickness monitor located near the substrates, RBS measurements were carried out for Nb and Cu films on Si(110) substrates in the thickness range of 10nm to 150nm. The thickness was estimated from the area under a backscattered signal in the surface energy approximation method. Layer thickness by RBS measurements were proportional to the monitored values and their calibration factor of Cu and Nb were 0.57 and 0.56, respectively.

Fig.1 shows RBS spectra for Nb layer deposited on G.C substrate. Because G.C is composed of low Z element, existence of oxygen in Nb layer is detected easily at the lower energy region. The areal atomic density was estimated directly from each area of the signals of Nb and O, and the ratio of the O in Nb film was obtained to be 0.61. The areal atomic densities in Nb and O atoms were 3.1×10^{17} (atoms/cm²) and 1.9×10^{17} (atoms/cm²), respectively. The oxygen content in Cu film was less than background.

Fig.2 shows RBS spectra for a multilayers film with four layers of Cu and Nb on G.C. The period of compositional modulation which has sharp interfaces is clearly observed, which reflects

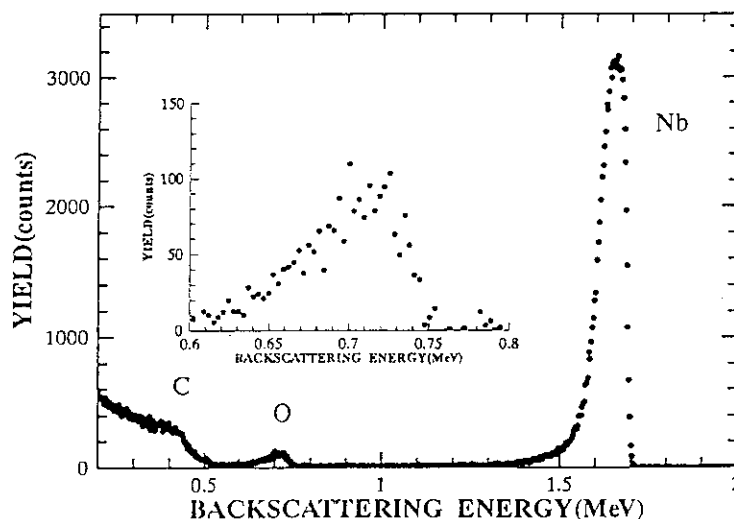


Fig.1. Backscattering spectrum for 2.0MeV ^4He ions incident on a thin Nb film.

the immiscible property between Nb and Cu. The spectrum attributed to oxygen atoms is obtained through the surface energy approximation method, and is shown in the inset. One can find that this oxygen peak is from the 1st Nb layer. The present results also indicate that the 2nd Nb layer is protected from oxygen contamination because of the inserted Cu layer. The oxidation of the Nb film found in Fig.1 is due to the exposure in air.

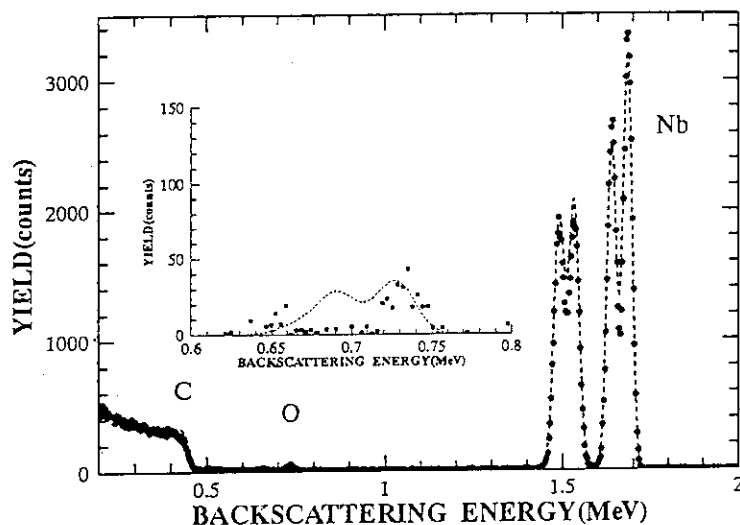


Fig.2. Backscattering spectrum for 2.0MeV ^4He ion incident on a film with four layers of Nb and Cu. The dash curve is a RUMP simulated spectrum.

Another samples with the increased number of layers deposited on MgO were analysed by RBS, but the structure of compositional modulation are not resolved clearly, because the contributions from Nb and Cu layers overlaps with each other. Thus, it is necessary to compare the experimental spectrum with the simulated one to obtain the information about multilayered structure.

- 1) W.K.Chu, J.W.Mayer and M.A.Nicolet, Backscattering Spectrometry, (Academic Press, New York, 1978).
- 2) I.Banerjee, Q.S.Yang, C.M.Falco, and I.K.Schuller, Phys.Rev.B28, 5037(1983).
- 3) W.P.Lowe, T.W.Barbee, Jr., T.H.Geballe, and D.B.McWhan, Phys.Rev.B24, 6193 (1981).
- 4) J.A.Bell, R.J.Zanoni, C.T.Seaton, G.I.Stegeman, W.R.Bennett and C.M.Falco, Appl.Phys.Lett.51, 652(1978).

6.3 HIGH-ENERGY SHADOWING EFFECT STUDIED WITH ION-INDUCED SECONDARY ELECTRON SPECTROSCOPY

Hiroshi KUDO, Hidefumi TAKESHITA*, Yasushi AOKI*,
Shunya YAMAMOTO*, Hiroshi NARAMOTO* and Susumu KUWABARA**

Institute of Applied Physics, University of Tsukuba,

*Department of Materials Development, JAERI, **Isobe
R&D Center, SEH Co.

I. INTRODUCTION

When a parallel beam of energetic ions is incident on a surface of solid, each of the surface atoms casts a coneshaped shadow where no ion can enter.¹⁾ For keV ions, the cone is wide enough to shadow the neighbouring atom completely. This phenomenon, i.e., the shadowing effect for keV ions has been commonly used for structure analysis of solid surfaces.

For MeV/u ions, the width of shadow cone behind a surface atom is very narrow. Actually, the radius of the shadow cone at a distance of a few Å behind the surface atom is typically less than the thermal vibration amplitudes (~ 0.1 Å) of atoms in solids, so that the atoms near the surface cannot be fully shadowed. Under such high-energy conditions, the effective "shadow" develops only along atomic rows or planes in a crystal as a result of small-angle multiple scatterings of ions by the aligned atoms. Essentially, the high-energy shadowing effect is an initial stage of ion channeling phenomena.²⁾

The high-energy shadowing effect is determined by the well known parameter, i.e., the shadow cone radius R given by

$$R = (8Z_1 Z_2 e^2 d / M_1 v)^{1/2}, \quad (1)$$

where Z_1 and Z_2 are the atomic numbers of ion and target atom, respectively, e is the electronic charge, d is the interatomic distance along the axial direction, M_1 is the mass of ion, and v is the ion velocity.^{1,3)} It should be noted that the shadowing effect for high-energy ions cannot be directly related to the actual shadow cone of an isolated atom, unlike in the case of keV ions.

2. BINARY-ENCOUNTER ELECTRONS

The high-energy shadowing effect for MeV/u ions can be observed by using high-energy (\sim keV) secondary electrons emitted from the surface,³⁻⁶⁾ rather than by use of backscattered ions.¹⁾ When the atoms are shadowed, the electron yield decreases since the secondary electrons are predominantly produced from the atoms near the surface, that are well exposed to the beam. It is notable that the electron measurement is useful even when the ion backscattering method is difficult to apply. In fact, the electron measurement is applicable to the case when the projectile ion is heavier than the target atom, or when non-Rutherford backscattering of high-energy ions occurs.³⁻⁶⁾

The high-energy secondary electrons are originally produced by hard recoil of target electrons by the ions in a forward direction and can be measured if they are backscattered and emitted from the surface. Such hard recoils in solids can be well treated by the binary encounter approximation model which predicts that the recoil cross section for equal-velocity ions is proportional to Z_1^2 .^{2,4,5)} Therefore, the observed electron yield that results from the binary encounter processes has the same parameter dependence, i.e., the Z_1^2 -scaling behavior. Actually, such pure binary-encounter electrons can be observed in the electron spectrum at energies higher than the "loss-peak energy", $E_L = mv^2/2$, where m is the mass of electron. For electron yields below E_L , the Z_1^2 -scaling cannot be anticipated since they partly originate from the loss electrons which have been previously accompanied by the incident ions, or from convoy electrons produced by the ions. It should be noted that an intense Auger peak superposed on the spectra sometimes disturbs the analysis of the binary-encounter yield. In this case, it is better to measure the pure binary-encounter yield above the Auger emission energy.

3. SHADOWING EFFECT FOR ALL ELECTRONS IN THE TARGET CRYSTAL

Since orbital velocities of outer-shell or valence electrons are much less than the velocities of MeV/u ions, the maximum energy transferable from the ion to the electrons (by head-on collision), E_B , is approximately given by $E_B = 2mv^2$. Inner-shell electrons, however, have orbital velocities comparable to v . In this case, a recoiled inner-shell electron can have

kinetic energy greater than E_B .

Therefore, the electron yield above E_B stems from scattered inner-shell electrons only, and therefore, under channeling incidence conditions the decrease in the yield is due to the shadowing effect on inner-shell electrons of aligned atoms. Since scattered outer-shell or valence electrons, as well as inner-shell electrons contribute to the electron yield below E_B , shadowing on all electrons can be observed with binary-encounter electron yields between E_L and E_B .

4. RESULTS AND DISCUSSION

Details of the electron measurements in a backward direction (at 180° with respect to the ion beam) under channeling incidence conditions have been described elsewhere. The method to determine the effective nuclear charges of fast ions in a crystal, Z_{eff} , has been discussed and demonstrated previously.⁵⁾ Z_{eff} can be determined from a comparison of the shadowing effect for heavy ions and for equal-velocity light ions that are fully stripped in the crystal. In the analysis, unshadowed electrons, such as valence electrons which are not localized near the nuclei in the crystals, must be carefully taken into account since those electrons should suffer no shadowing effect. By using the values of W measured for H^+ , average numbers of unshadowed target electrons can be determined experimentally.

Figure 1 shows the values of W measured at 4.4 keV for 3.5-MeV/u $^1H^+$, $^4He^{2+}$, $^{10}B^{5+}$, $^{12}C^{4+}$, $^{12}C^{6+}$, $^{16}O^{5+}$, $^{16}O^{8+}$, $^{28}Si^{8+}$, $^{28}Si^{13+}$, $^{32}S^{10+}$, and $^{32}S^{15+}$ under $Si\langle 110 \rangle$ incidence conditions. The electron energy is roughly in the middle of $E_L=1.9$ keV and $E_B=7.6$ keV. In Fig. 1, the numbers near the plots indicate the incident charges of the ions. We see that for each ion species the value of W for lower incident charge is greater than for higher incident charge. It is clear from this result that the ions are in non-equilibrium charge states. It is also seen in Fig. 1 that for the fully-stripped He, B, C, and O ions the values of W are the same (the averaged value is 0.396). This indicates that the shadow cone radius for those ions are the same, implying that the ions are still fully stripped in the crystal. For H^+ , the value of W is smaller than the fully-stripped level, 0.396, because the shadow cone radius for H^+ is a factor of $\sqrt{2}$

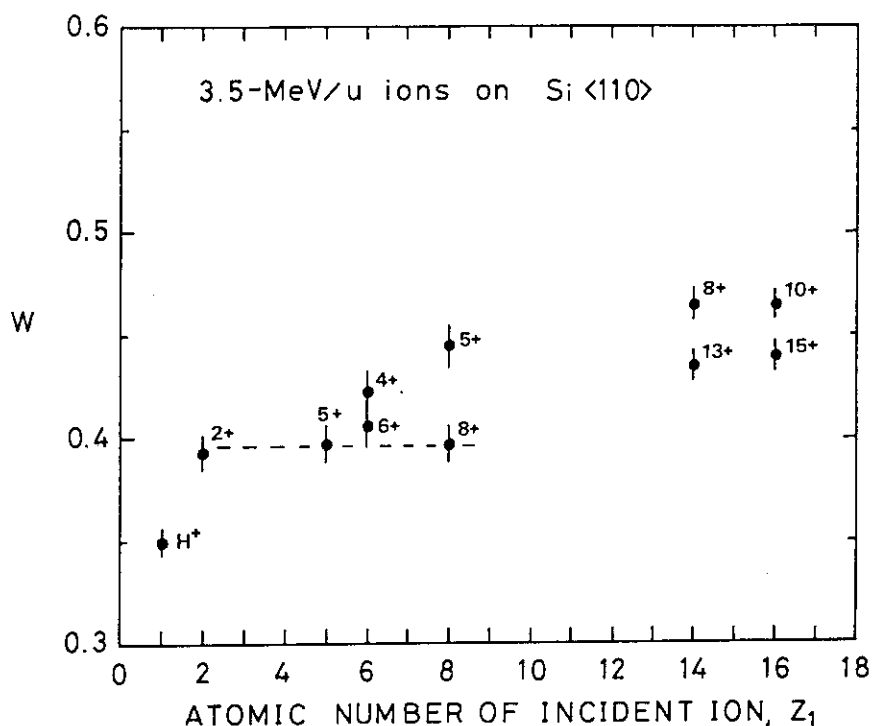


Fig.1. Ratio of channeling to random electron yield, W , at 4.4 keV, induced by 3.5-MeV/u various ions under Si <110> channeling conditions. The incident charge states of ions are indicated near the plots. $W=0.396$ shown by the dashed line is the assumed level for the fully stripped case.

greater than the fully stripped ions. The W values for the other heavy ions are greater than the fully-stripped level. This results from screening of the nuclear charges of the ions by captured inner-shell electrons. Detailed analysis of the data is now under way.

This work was performed under the JAERI/TIARA Collaboration Program #22017.

References:

- 1) L.C.Feldman, J.W.Mayer, and S.T.Picraux, *Material Analysis by Ion Channeling* (Academic, New York, 1982), Chap.1.
- 2) D.S.Gemmell, Rev. Mod. Phys. **46** (1974)129.
- 3) H.Kudo et al, Phys. Rev. B**38** (1988)44.
- 4) H.Kudo et al, Phys. Rev. B**43** (1991)12729.
- 5) H.Kudo et al, Phys. Rev. B**43**(1991)12736.
- 6) H.Kudo et al, Phys. Rev. B**47** (1993) 27.

6.4 APPLICATION OF HEAVY IONS TO RUTHERFORD BACKSCATTERING

Shinji NAGATA, Katsumi TAKAHIRO, Sadae YAMAGUCHI,
Shunya YAMAMOTO*, Hidefumi TAKESHITA*, Yasushi AOKI* and
Hiroshi NARAMOTO*

Institute for Materials Research, Tohoku University,

*Department of Material Development, JAERI/Takasaki

I. Introduction

It has been recognized that Rutherford backscattering spectrometry (RBS) with massive incident ions has several advantage over the conventional RBS using hydrogen and helium. In this paper, we will briefly review the basic concept of RBS, noting the advantages associated with heavy ion use. Limitations of the techniques will be also discussed and we will consider experimental techniques for which these limitations are minimized.

II. Advantage of heavy ion RBS (HIRBS)

The principal advantage of HIRBS is that the mass resolution and sensitivity can be improved appreciably for heavy target isotopes. Let us assume that the projectile which has mass M_1 and nuclear charge Z_1 scatters from a target atom of mass M_2 and charge Z_2 . The scattering angle, measured with respect to the original direction of the projectile, is θ . The energy, E_b , of the scattered from elementary kinematics:

$$E_b = KE_0 \quad \text{where } K = \left(\frac{M_1 \cos \theta + \sqrt{M_2^2 - (M_1 \sin \theta)^2}}{M_1 + M_2} \right)^2. \quad (1)$$

Equation 1 predicts an enhanced mass resolution for more massive projectiles. Figure 1 shows the separation in backscattered energy ($\theta=180^\circ$) between adjacent masses for three choices of projectile. Except for the lowest masses, the energy separation is seen to be greater for heavy ions.

The differential cross section for Rutherford scattering is also well known from basic physical concept. In the laboratory reference frame, the differential cross section, $d\sigma/d\Omega$, is given as

$$\frac{d\sigma}{d\Omega} = \left(\frac{Z_1 Z_2 e^2}{4 E_0} \right)^2 \frac{4}{\sin^4 \theta} \frac{\left\{ M_2 \cos \theta + \sqrt{M_2^2 - M_1^2 \sin^2 \theta} \right\}^2}{M_2 \sqrt{M_2^2 - M_1^2 \sin^2 \theta}}. \quad (2)$$

This cross section suggests that the backscattering technique improves with increasing ion mass since a large charge is also implied. Figure 2 shows the laboratory cross section for 8 MeV ^{16}O and 17 MeV ^{35}Cl ions relative to that for 2 MeV α ions at a scattering angle of 179.5° . The cross sections are equal only for large target masses, but cross sections for light elements decrease with increasing incident mass, falling to zero as expected when the mass of the target atom is less than that of the incident ions. This decrease in sensitivity for light elements is often beneficial for application where a light substrate is not of primary interest.

Rutherford scattering is also a powerful tool for depth profiling. In a thick target, the energy E_d , of the detected particle depend on the depth, x , at which it was scattered. For an ion incident on the target at an angle θ_{in} with respect to the surface normal and exiting at angle θ_{out} ,

$$E_d(x) = K \left(E_0 - \frac{x}{\cos \theta_{in}} \left. \frac{dE}{dx} \right|_{in} \right) - \frac{x}{\cos \theta_{out}} \left. \frac{dE}{dx} \right|_{out} = K E_0 - [S] x \quad (3)$$

$$\text{where } [S] = \frac{K}{\cos \theta_{in}} \left. \frac{dE}{dx} \right|_{in} - \frac{1}{\cos \theta_{out}} \left. \frac{dE}{dx} \right|_{out}$$

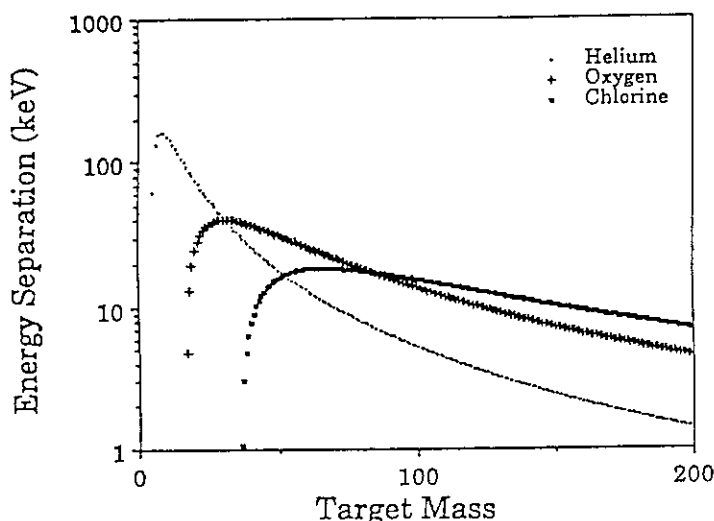


Figure 1: Backscattered energy separation for scattering from adjacent masses for 4 MeV Helium, Oxygen and Chlorine incident beams. A scattering angle of 180° is assumed.

The quantities $(dE/dx)_{in}$ and $(dE/dx)_{out}$ refer to the average rate of energy loss for an ion scattered at a depth x before and after scattering, respectively. Equation 3 is linear in x and provides a convenient relationship between energy of a detected particle and the depth at which is scattered, provided the quantity $[S]$ is known. A concentration profile may then be obtained if the energy is known for the detected particle at the scattering location. Because of the larger stopping

powers associated with heavy ions at all energies relative to those for α particles, [S] is larger for HIRBS and the depth resolution of the technique should exceed that of the conventional technique.

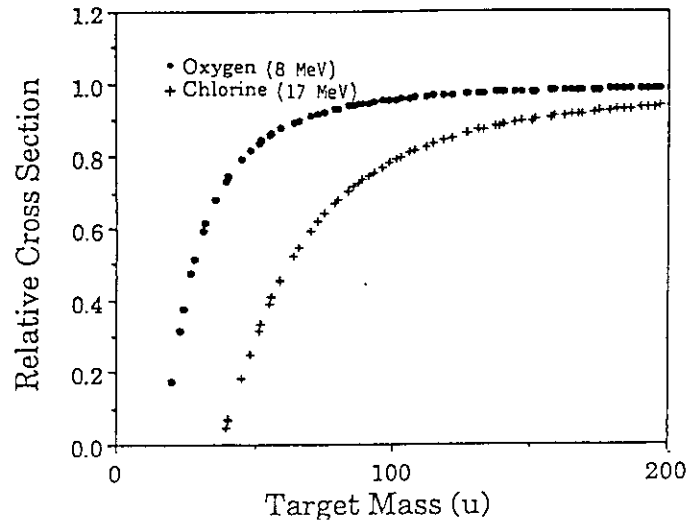


Figure 2: Rutherford scattering cross sections as a function of target mass for 8 MeV Oxygen, and 17 MeV Chlorine incident beams relative to that for a 2 MeV Helium beam. A scattering angle of 179.5° is assumed.

III. Disadvantage of HIRBS

The disadvantage of HIRBS is the damage caused by heavy ions to the silicon surface barrier detectors (SSBD) which severely limits their useful lifetime, also the heavier mass ions induce greater damage in the target during analysis.

In addition, the energy resolution using SSBD is significantly poorer when using heavy projectiles. The energy resolution for SSBD is a function of Z_1 , and detection energy [1] i.e.

$$\delta E_D(Z_1, E_D) = A + BE_D^{1/3} \quad (4)$$

where E is in keV, and A and B are constant which depend on the incident ions as shown in Table 1.

Table 1

Ion	A[keV]	B
^1H	7.0	0.0
^4He	15.0	0.0
^{12}C	12.4	2.50
^{14}N	17.3	2.64
^{16}O	24.4	2.92

IV. Experimental

The scattering of 18 MeV ^{16}O from GaAs samples has been used to evaluate the energy resolution for SSBD. A new Ortec SSB detector type BF-18-100-60 was mounted at 170° .

Figure 3 shows an example of the use of oxygen HIBS on a thick GaAs sample. The mass resolution between Ga and As is considerably better than that which would be expected for a backscattering. While energy resolutions are generally better than 20 keV for the detection of α particles, the resolution of SSBD for oxygen ions is at best only 100 keV. For heavier incident beams, the energy resolution is even worse, ultimately resulting in a loss of mass resolution for heavier ions. In addition, the energies of scattered particles as determined by SSBD detection are invariably less than those expected on the basis of equation 1 due to "pulse height defect".

In cases where the target constituents are not known prior to analysis, this may lead to difficulties in identification of the element responsible for a given spectrum.

V. Improvement of detection technique

As described above, HIRBS offers significant advantage over the conventional technique, but it also has limitations. Many of these limitations are not intrinsic to HIRBS. Rather, they are by-product of the heavy-ion detection process. To realize the real benefit of HIRBS, other forms of energy analysis such as time-of-flight (TOF) or magnetic and electrostatic spectrometers need to be used. Usefulness of HIRBS using TOF detector and magnetic spectrometer are demonstrated by Chevavier et al. [2] and Yang et al. [3], respectively.

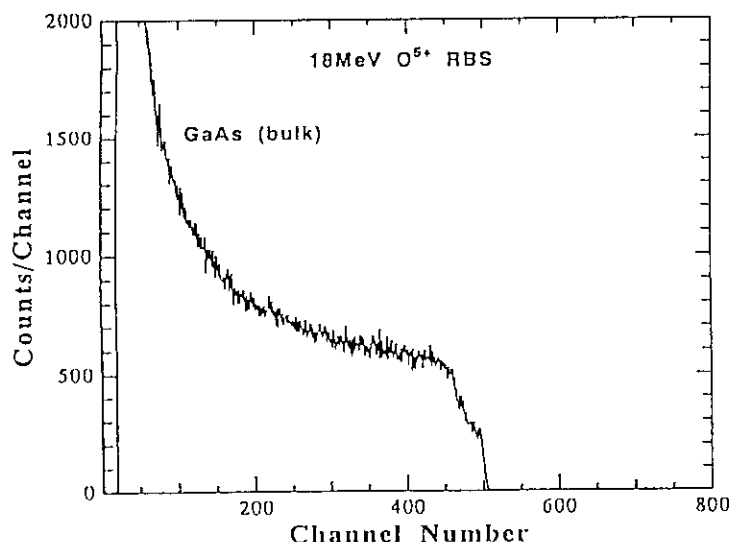


Figure 3 RBS spectrum from GaAs (bulk)

References

- [1] G. Amsel, C. Cohen and A. L'Hoir, Ion Beam Surface Layer Analysis, Vol. 2 eds. O. Meyer, G. Linker and F. Kappeler (Plenum, New York, 1976).
- [2] A. Chevavier and N. Chevavier, Nucl. Instr. and Meth. 218 (1983)1.
- [3] Q. Yang and D. J. O'Connor, Nucl. Instr. and Meth. B67 (1992)98.

6.5 OPTICAL MEASUREMENT SYSTEM FOR STUDY OF ELECTRON-HOLE PAIRS INDUCED IN SEMICONDUCTORS BY HIGH-ENERGY ION IRRADIATION

Hisayoshi ITOH, Toshio HIRAO, and Isamu NASHIYAMA

Department of Materials Development, JAERI

I. INTRODUCTION

The impingement of a single high-energy ion on semiconductors generates dense electron-hole pairs along the ion track. These electron-hole pairs give rise to single-event phenomena such as soft-error, latch up, and burn-out of semiconductor devices.^{1,2)} The study of electronic excitation and relaxation caused by ion irradiation in semiconductors is essential to understand the fundamental processes of those single-event phenomena. It is well known that highly excited carriers accompany with the change in optical properties like reflectance and transmittance of semiconductors³⁾ and that recombination of excited electron-hole pairs induces a photon emission (luminescence) from them. Thus the time-resolved optical measurements of semiconductors in ion irradiation give us an information about irradiation induced electron-hole pairs. Then we have constructed an optical measurement system which consists of a streak camera mainly in order to investigate dynamics of electron-hole pairs generated by irradiation. In this paper, we report this measurement system and the results of irradiation induced luminescence in alumina, which were obtained for the preliminary test of the optical measurement system.

II. MEASUREMENT SYSTEM

Figure 1 shows a schematic illustration of our optical measurement system. Temperature of samples is controllable in a range between $\approx 20\text{K}$ and room temperature (RT) by using a cryostat (Iwatani Cryo-Mini D310/CW303) on a two-axes goniometer installed in a chamber HE1. Details of the vacuum chamber HE1 have been described in a previous paper.⁴⁾ Reflectance and transmittance are obtained by detecting photons reflected on samples and those transmitted from samples, respectively, when a pulsed or cw laser (Hamamatsu PLP-01) is incident on samples for a probe beam. Ion irradiation induced luminescence is also obtained by measuring photons emitted from samples due to irradiation. Transient photon intensity is acquired by a streak camera system (Hamamatsu C1587/C3140) which has a maximum time-resolution of 2ps. An energy profile of photons is also obtained by using a monochromator (Jovin Yvon HR250). In these time-resolved measurements, trigger signals of the AVF cyclotron and/or the P-chopper⁵⁾ are used to start

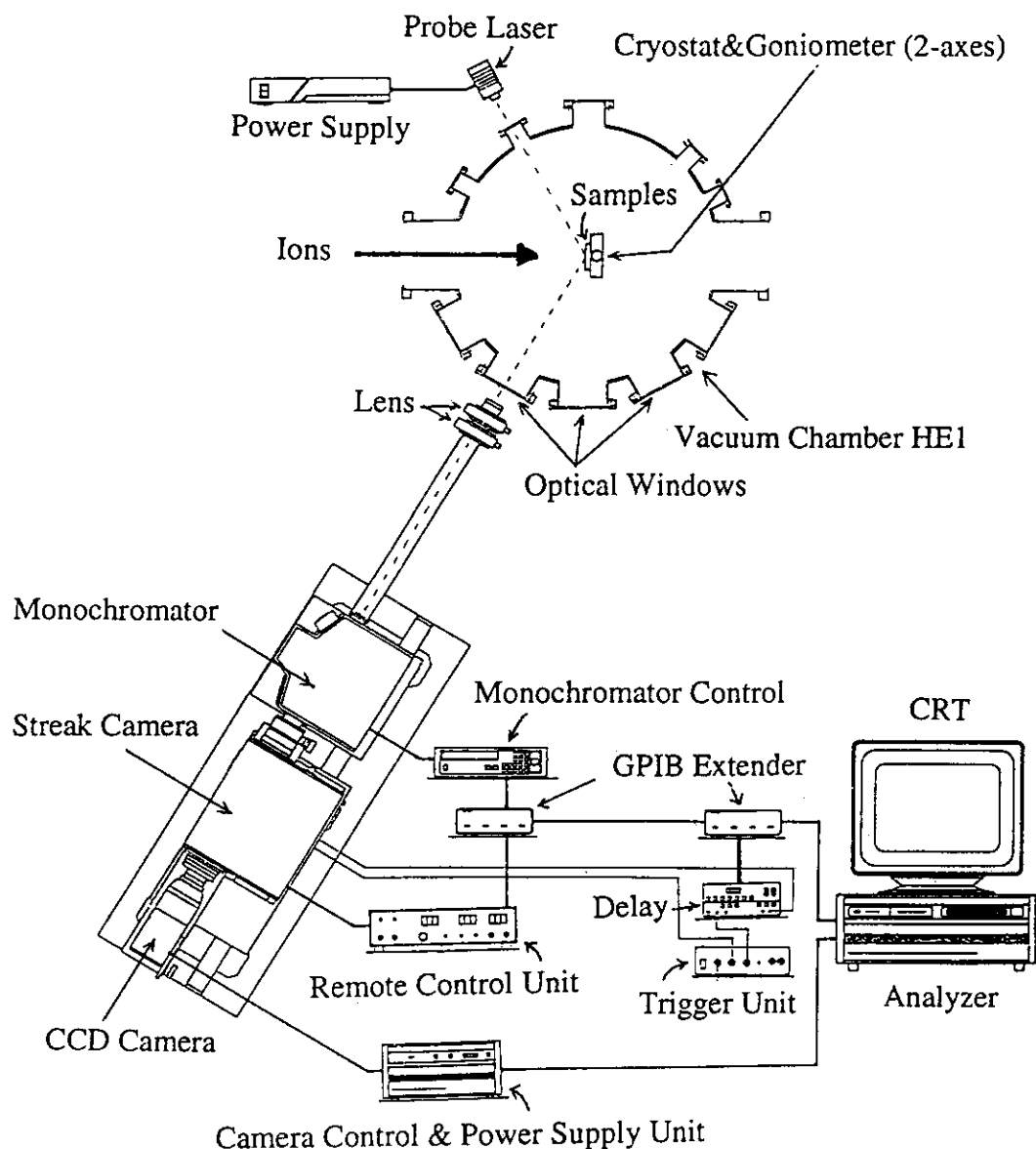


Fig.1 Optical measurement system.

acquiring data. The streak camera system and the monochromator are remotely controllable.

III. RESULTS

Figure 2 shows a typical luminescence spectrum induced at RT in alumina samples by 175MeV-Ar⁸⁺ irradiation (beam current ≈ 35 nA). In this figure, the abscissa indicates the wavelength of luminescence. The wavelength at the maximum peak of the obtained spectrum was ≈ 320 nm and the full width of half maxima was ≈ 40 nm. Similar spectra were

reported for γ -ray irradiated sapphire samples.⁶⁾ This spectrum is probably caused by the recombination of excited carriers through some defect-levels in alumina on the analogy of luminescence in irradiated sapphire⁶⁾. A time-resolved intensity of this spectrum is shown in Fig.3. Because the lifetime of excited electrons exhibiting the $\approx 320\text{nm}$ photon emission is very short⁶⁾, the obtained signal is thought to correspond to the shape of ion-pulses impinging on the samples. In fact, the interval of the obtained signals was estimated to be 67ns, which is in good agreement with that of 175MeV-Ar ion-pulses from the AVF cyclotron. In addition, the pulse width of the observed signals shows a 7ns width of the Ar

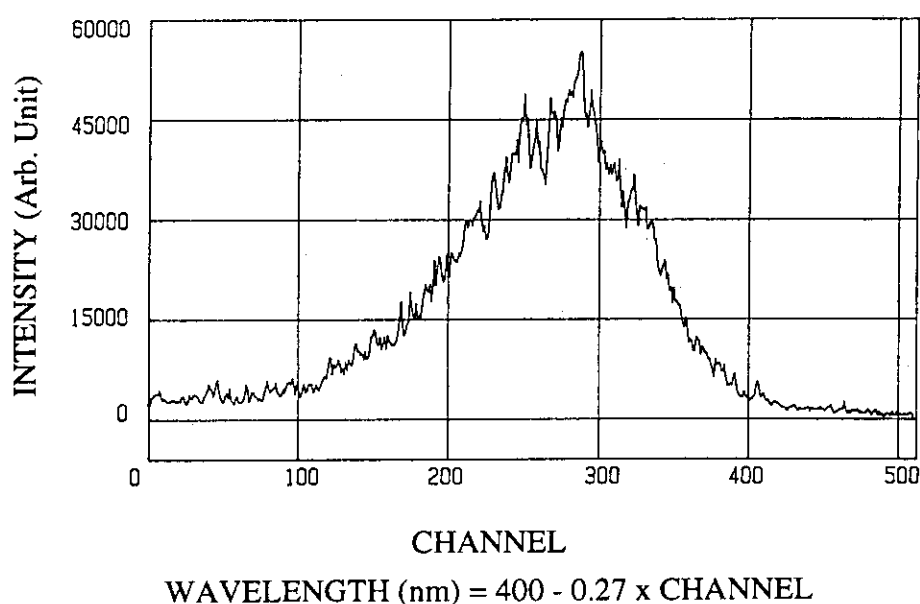


Fig.2 Ion irradiation induced luminescence spectrum of alumina.

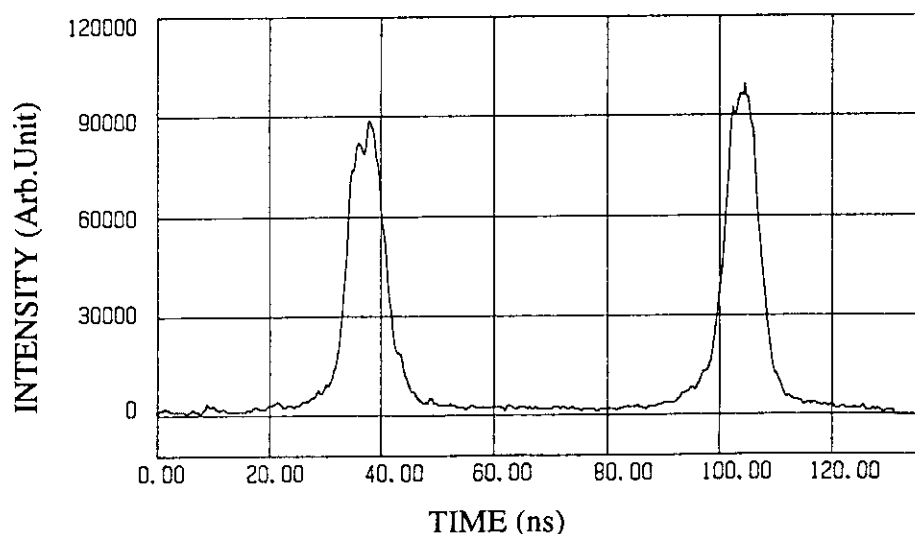


Fig.3 Time-resolved luminescence-signal induced in alumina by Ar ion irradiation.

ion-pulses. These results demonstrate that the optical measurement system works well and that it can be applied to the study of electron-hole pairs generated by ion irradiation in semiconductors.

IV. SUMMARY

We have constructed the optical measurement system for the study of dynamics of ion irradiation induced electron-hole pairs: Dynamic behavior of those electron-hole pairs can be found from the examination of the change in optical properties (reflectance, transmittance, luminescence, etc.) of semiconductors due to irradiation of high-energy ions accelerated by the AVF cyclotron. By using this system, we obtained the wavelength- and time-resolved luminescence signals induced in alumina samples by 175MeV-Ar⁸⁺ irradiation. The observed luminescence spectra agreed well with that reported previously for γ -ray irradiated sapphire⁶⁾. It was also found that the time-resolved signals of the irradiation induced luminescence represented well the characteristics of pulsed Ar ions. These show that the constructed system is useful to investigate radiation response of optical properties of materials. We will apply this measurement system to the study of dynamic behavior of dense electron-hole pairs in semiconductors.

REFERENCES

- 1) E.L.Petersen, in the Text of Tutorial Short Course in IEEE 1983 Nuclear and Space Radiation Effects Conference, held on July 17, 1983, in Gatlinburg, TN, USA.
- 2) J.C.Pickel, in the Text of Tutorial Short Course in IEEE 1983 Nuclear and Space Radiation Effects Conference, held on July 17, 1983, in Gatlinburg, TN, USA.
- 3) See, for example, J.I.Pankove, in Optical Processes in Semiconductors (Dover, New York, 1971) p.87.
- 4) H.Itoh, T.Hirao, Y.Morita, I.Nashiyama, TIARA Annual Report, 1 (1992) 97.
- 5) K.Arakawa, Y.Nakamura, W.Yokota, M.Fukuda, T.Nara, T.Agematsu, S.Okumura, I.Ishibori, T.Kamiya, R.Tanaka, T.Tachikawa, K.Hoshika, M.Tachibana, Y.Kumata, Y.Hayashi, K.Ishii, M.Sano, K.Iso, T.Torii, K.Suzuki, J.Sagawa, and T.Tonooka, TIARA Annual Report, 1 (1992) 1.
- 6) H.W.Lehmann and Hs.H.Gunthard, J.Phys.Chem.Solids, 25 (1964) 941.

6 . 6 POSITRON ANNIHILATION STUDY OF DEFECTS IN Si: AN INTERNAL SOURCE METHOD

Masayuki Hasegawa, Sohei Okada*, Atsuo Kawasuso
and Masashi Suezawa

Institute for Materials Research, Tohoku University, Sendai 980

*Takasaki Establishment, Japan Atomic Research Institute,
Takasaki 370-12

I. INTRODUCTION

Positron annihilation method has been widely used for studies of defects in metals and alloys. This method very sensitively detects vacancy-type defects and provide us useful information about the defects, such as vacancy formation and vacancy clustering process. This technique is also useful for defects in semiconductors^{1,2}. Positrons are attracted by long-range Coulombic force from negatively charged defects (vacancy, divacancy and so on). Because of this, positron annihilation is very sensitive tools for negatively-charged vacancies and vacancy clusters^{1,2}. Further, recently neutral divacancies as well as negative divacancies have been found to exhibit very large trapping ability for positrons at low temperature³. Reflecting these, positron annihilation has been extensively used for studies of defects in semiconductors.

One of fundamental properties of vacancy in semiconductors is its formation energy. It is, however, very difficult to carry out high-temperature (close to melting point) experiments to obtain the formation energy, because usual positron source, for example $^{22}\text{NaCl}$, will melt at high temperature. Two technique have been used for the high-temperature experiments; (1) internal source method^{3,4} and (2) slow positron beam method^{5,6}. Internal method uses "in situ" positron emitter. For silicon it is impossible to dope positron emitter, such as ^{22}Na , by diffusion. We can use a nuclear reaction $^{28}\text{Si}(p, ^7\text{Be})^{22}\text{Na}$ for an internal source. This reaction, however, because of a Q-value of 24 MeV, and then requires proton beam of very high energy, as available in a AVF cyclotron. It should be noted that taking advantage of internal source-samples we can also easily perform low temperature experiments for vacancy migration which occurs below liquid-nitrogen temperature.

In this study we aimed at obtaining internal-source sample of Si to do the high-temperature experiments and to study the induced irradiation-induced defects in them. We have done preliminary experiments with low dose irradiation to make sure of the irradiation-induced activity and of the defects.

II. POSITRON SOURCE PRODUCTION

To examine depth profile of "internal" positron source of ^{22}Na in silicon by nuclear reaction $^{28}\text{Si}(p, ^7\text{Be})^{22}\text{Na}$, ten slabs of silicon single crystal were stacked and then irradiated with high energy protons from the AVF cyclotron at Takasaki Establishment of JAERI. The slabs, with thickness of 1mm, were cut from an undoped-ingot grown by a floating-zone method and have specific-resistivity of about $1000\Omega\text{cm}$. We have carried out two run of irradiation:

- 1) 45MeV, 31.4nA, 8h, $7.2 \times 10^{15} \text{ H}^+/\text{cm}^2$,
- 2) 70MeV, 9.5nA, 1h, $2.7 \times 10^{14} \text{ H}^+/\text{cm}^2$.

The diameter of proton beam was about 10 mm. Gamma-ray energy spectrum, taken with a solid-state detector, of the slab sample after 45MeV-irradiation (Fig.1) clearly shows the induced nuclides, ^{22}Na and ^7Be .

The specific induced-activity of ^{22}Na in each slab is plotted in Fig.2, together with the calculated one with use of "IRAC Code" for induced activities. The activity after 70MeV-irradiation is almost constant of about $25 \text{ kBq}/\mu\text{A.h/mm}$ to depth of 6mm, followed by gradual decrease with the depth. The observed activity agrees well with the calculated one for depth less than 5mm, however, being higher than the calculation. This indicates that the induced activity at deep distance from the surface is higher than that by IRAC Code calculation.

Fig.1 Gamma-ray spectrum of the samples after 45 MeV irradiation.

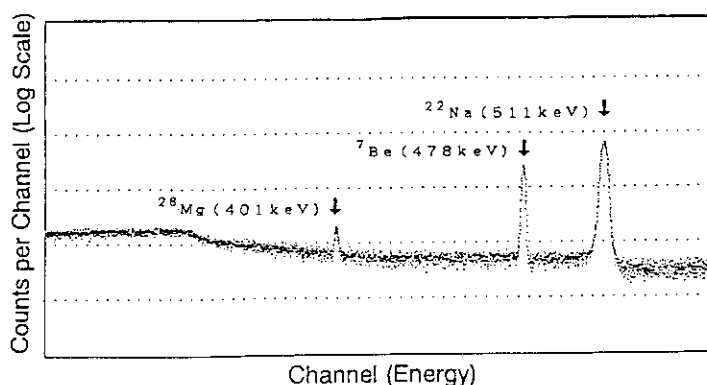
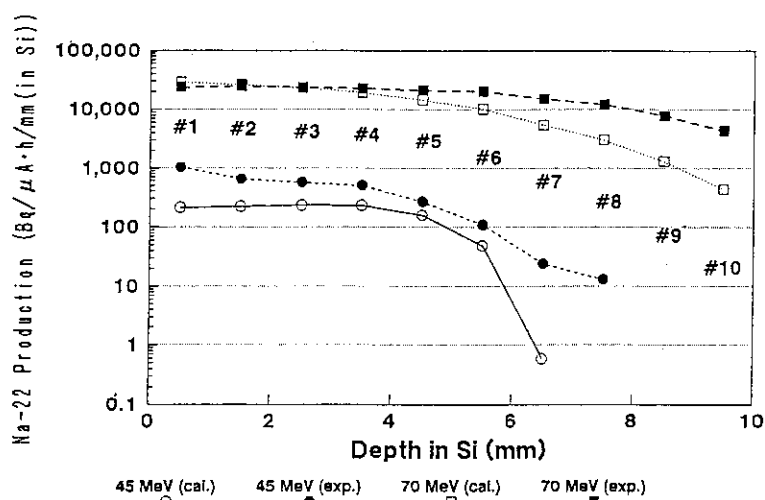


Fig.2 The induced activity of ^{22}Na in the slabs after irradiation of 45 MeV and 70 MeV protons.



The activity after 45 MeV irradiation is less than that after 70 MeV irradiation by two order of magnitude. The activity decreases rapidly with depth, which reflects the nuclear reaction of a Q-value of 24 MeV.

Now we are planning 90 MeV irradiation. High-temperature experiment with use of a chamber usually requires positron source with strength more than about 1 MBq in samples of thickness about 2 mm. Calculated activity after 90 MeV irradiation is given in Fig.3. Energy loss along proton beam is also shown. The activity at the top surface is about 600 kBq/μA·h/2mm and nearly constant up to depth of 10 mm (about 70 MeV). Within this depth we can expect enough activity of 1 MBq/2mm for our experiments after 90 MeV irradiation for about 20 hours.

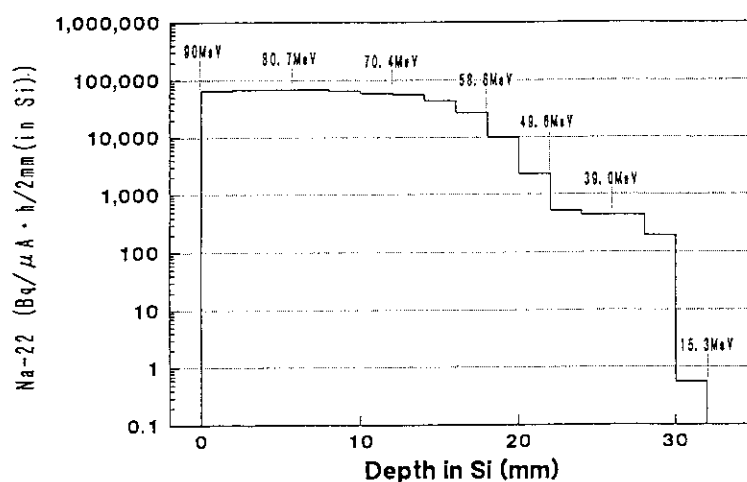


Fig.3 The calculated activity of ^{22}Na after 90 MeV irradiation.

III. IRRADIATION EFFECTS

High energy protons produce Frenkel pairs (vacancies and interstitials) and cascade damages. These irradiation-induced defects form attractive subjects of study of lattice defects in Si. During irradiation at room temperature the interstitials and vacancies are widely known to migrate. Then we can assume that main defects, in undoped Si, which trap positrons are neutral divacancies. Because of the small doses of 45MeV and 70 MeV irradiation in this study, induced activities are too low to be used as the source for lifetime and Doppler broadening measurements; after 45 MeV irradiation induced activity was about 0.3 kBq/slab. Then we employed a conventional sandwiched source (^{22}Na about 700kBq)-sample set-up to perform positron experiments after 45MeV irradiation; mean lifetime (Fig.4.) and Doppler broadening line-shape parameter (Fig.5). For Doppler broadening measurements we used two slabs, unirradiated and irradiated one, to see irradiation effects in each slab.

Fig.4 Positron mean lifetime in the slabs after 45MeV irradiation.

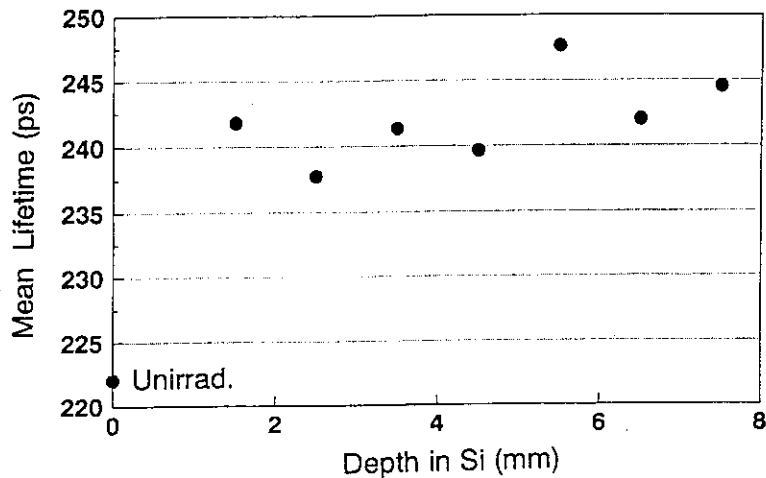
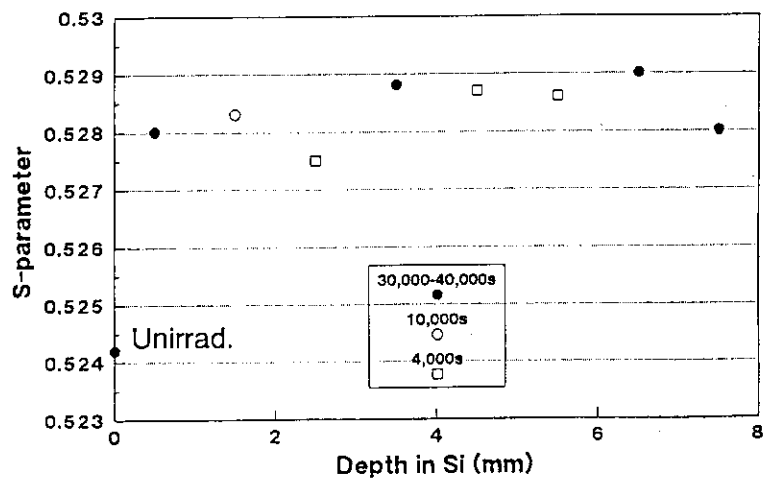


Fig.5 Doppler broadening S-parameter of the slab after 45 MeV irradiation. Measuring time is also shown.



Positron mean lifetime increases by about 30 ps after irradiation. A S-parameter of Doppler broadening, given by the area under the annihilation spectra in a narrow energy range divided by the sum the area of the tail region, shows increase of about 0.8%. These changes by irradiation are almost constant to a depth of about 8 mm; this shows that the defect productions is nearly independent of depth in these range, as usually expected.

We can estimate concentration of the divacancy from the mean lifetime, τ_m , after irradiation. According to a conventional trapping model, the positron trapping rate κ is given by

$$\kappa \tau_B = \frac{\tau_m - \tau_B}{\tau_d - \tau_m}$$

where τ_B (= 222 ps), is positron lifetime in bulk matrix (perfect crystal) and τ_d (=293ps) the lifetime in the neutral divacancy. The observed mean lifetime of 245ps leads to the trapping rate of $1.5 \times 10^6 \text{ ns}^{-1}$ and the divacancy concentration of $6 \times 10^{16} \text{ divacancies/cm}^3$. Annealing behavior of these divacancies will be interesting subject of future studies.

We thank the staff members of the AVF Cyclotron for their irradiation of the samples.

REFERENCES

- 1)S. Dannefaer, "Defect Control in Semiconductors", ed. by K. Sumino, (Elsevier, Amsterdam 1990) p1561.
- 2)M.J. Puska, Mat. Sci. Forum, 105-110 (1992) 419.
- 3)A. Kawasuso, M. Hasegawa, M. Suezawa, S. Yamaguchi and K. Sumino, Hyper fine Interactions, in press.
- 4)S. Dannefaer, P. Mascher and D. Kerr, Phys. Rev. Lett., 56 (1986) 2195.
- 5)S. Dannefaer, P. Mascher and D. Kerr, J. Appl. Phys. 73 (1993) 3740.
- 6)R.Wurschum, W. Bauer, K. Maier, A. Seeger and H.E. Schaefer, J.Phys.:Con dens. Matter 1 (1989) SA33.
- 7)J.Throwe, T.C. Leung, B. Nielsen, H. Huomo and K.G. Lynn, Phys. Rev. B40 (1989) 12037.
- 8)S. Tanaka, M. Fukuda, K. Nishimura, W. Yokota, T. Kamiya, H. Watanabe, T. Shiraishi, K. Hata and N. Yamano, JAERI TIARA Annual Report 1 (1992) p76.

6 . 7 TIME-RESOLVED X-RAY ABSORPTION SPECTROSCOPY OF LASER ABLATED SILICON AND CARBON PARTICLES

Osamu YODA, Atsumi MIYASHITA, Takasumi OHYANAGI* and
Kouichi MURAKAMI*

Department of Material Development; *University of Tsukuba

Introduction

In recent years, laser ablation has been recognized to be one of the most potential techniques to create novel materials such as carbon fullerenes and high T_c oxide superconducting thin films. The property of thin films formed by laser ablation can be believed to be strongly dependent on the physical and chemical states of fragments ejected from the solid surface. The states of fragments may include species -- whether the fragments are atoms, molecules or clusters, the electronic state -- whether they are neutral or ionized, and the kinetic energy or the velocity of them. With a view to understanding the elemental process of novel materials fabrication by laser ablation, the present authors have set-up a time-resolved soft X-ray absorption spectrometer using laser produced plasma X-rays as a pulsed X-ray source.

In this paper, we report some results on the ablation fragments of silicon (Si) and carbon (C) disclosed by means of the time-resolved X-ray absorption spectroscopy^{1,2)}.

Silicon

A bulk Si crystal has been irradiated by the second harmonic of a Nd:YAG/glass laser (532nm, 10ns) with an irradiance of $20\text{J}/\text{cm}^2$. Soon after irradiation, Si^{2+} , Si^{3+} and Si^{4+} ions are found near the crystal surface. At a delay time of 120ns, removed fragments are neutral Si atoms (Si^0), Si^+ and Si^{2+} ions close to the surface, while they are mostly Si^{2+} ions at positions far from the surface. Through the assignment of Rydberg transitions observed in the absorption spectra, energies of the $L_{II,III}$ absorption edge of the Si atom and ions have been determined within an accuracy of 1eV. These values are, to our knowledge, the first experimentally observed ones for the Si atom and ions. Table 1 summarizes the observed $L_{II,III}$ energies along with values obtained by Hartree-Fock calculations (Atom. Data & Nucl. Data Tab. 14, No. 3-4, 1974).

Carbon

Figure 1 shows absorption spectra of fragments ejected from a carbon rod for vacuum deposition. The laser irradiance and the delay time were $20\text{J}/\text{cm}^2$ and 120ns, respectively. The spectra exhibit several peaks in-between 280 and 290eV, and an intense broad absorption

beginning at around 290eV. As the probing distance increases, only two distinct peaks are seen at 284 and 288eV, and the absorption beyond 290eV decreases. These two peaks are assigned to transitions $1s$ to $2p$ of the neutral carbon atom (C^0) and C^+ ion, respectively. The peak at 281eV is tentatively assigned to the negative carbon ion (C^-).

References

1. O. Yoda, A. Miyashita, T. Ohyanagi and K. Murakami, JAERI-M 92-173 (1992).
2. K. Murakami, T. Ohyanagi, A. Miyashita and O. Yoda, Proc. 2nd Int. Conf. Laser Ablation (Oak Ridge, April 1993).

Table 1. $L_{II,III}$ edge energies for the Si atom and ions.

State	Observed Value	Calculated Value
Si^0	110 eV	114.9 eV
Si^+	121 eV	125.4 eV
Si^{2+}	132 eV	137.1 eV
Si^{3+}	148 eV	152.0 eV
Si^{4+}	166 eV	168.4 eV

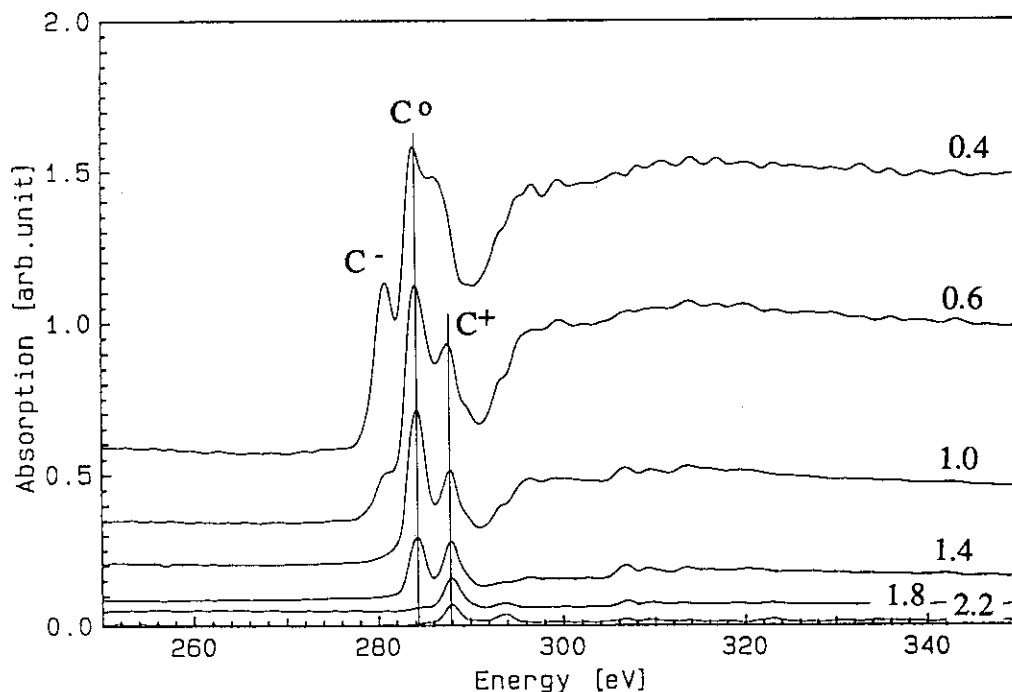


Fig. 1 Typical X-ray absorption spectra of laser-ablated C fragments measured at various distances. The figure on each spectrum indicates the probing distance from the surface of the carbon rod in mm.

6 . 8 IN-SITU MEASUREMENT OF SECONDARY IONS DURING HYDROCARBON ION BEAM DEPOSITION

Hideki OHNO*, Yasushi AOKI and Siro NAGAI

Takasaki Radiation Chemistry Research Establishment, JAERI

*Department of Physics, Meisei University

1. INTRODUCTION

Extensive studies have been carried out on thin film growth by the use of the ion beam deposition (IBD) technique employing low energy (< 1 keV) ion beams. The advantages of the IBD technique are epitaxial growth of crystalline films¹⁾ and synthesis of metastable phase materials like diamond²⁾. The IBD technique is expected to be one of the promising techniques that allow the thin film growing process to be controlled at the levels of atoms and molecules. To approach this goal, it seems most important to relate the nature and structure of the deposited thin film with the deposition parameters using a highly sophisticated beam deposition apparatus combined with in-situ surface analysis equipment. This report describes the result on measurements of secondary ions during CH_n^+ ($n = 4, 3$ and 2) and CD_3^+ ion beam deposition, using our ultra-low energy ion beam deposition apparatus installed last year³⁾.

2. EXPERIMENTS

Figure 1 shows the low-energy ion beam deposition apparatus (LEIBS11; VSW scientific instrument LTD.) which consists of a Freeman-type ion source, a mass separation magnet, and an irradiation chamber equipped with surface analysis apparatuses of Auger electron spectroscopy (AES), ion scattering spectroscopy (ISS), secondary ion mass spectrometry (SIMS), and reflection high energy electron diffraction (RHEED)³⁾. This system enables us to perform low-energy ion beam deposition with incident ion energy from 10 to 200 eV and ion current density $\sim 10 \mu\text{A}/\text{cm}^2$ under the base pressure of about 10^{-9} Pa and real-time and/or in-situ surface analysis.

SIMS spectra were continuously recorded during bombardment of a Si(111) surface with CH_4^+ , CH_3^+ , CH_2^+ and CD_3^+ ions at room temperature. The Si(111) surface was cleaned by 3 keV Ar^+ ion bombardment before the experiment. The incident ion energy studied here was in the range from 10 to 100 eV, and the current densities were from 0.1 to $1.0 \mu\text{A}/\text{cm}^2$ depending on ion species. The angle of incidence was 7° to the Si(111) surface and the angle between incident ions and the axis of quadrupole mass spectrometer was 30° which proved to give the highest S/N ratio for secondary ions.

3. RESULTS AND DISCUSSION

Figure 2 shows mass spectrum from the Si(111) surface during bombardment with 50 eV CH_3^+ ions. The spectrum indicates that various hydrocarbon ions up to C_6 hydrocarbon

ions are produced in addition to some impurity ions like Na^+ and K^+ . The most intense peak at $m/e = 15$ is due to CH_3^+ ions scattered from the $\text{Si}(111)$ surface. The C_2H_3^+ peak ($m/e = 27$) and C_3H_5^+ peak ($m/e = 41$) are most intense in the peaks due to C_2 , and C_3 hydrocarbon ions, respectively. These qualitative features of SIMS spectrum did not change with time of CH_3^+ bombardment and the energy of incident CH_3^+ ions in the range from 10 to 100 eV. Furthermore, no significant change in SIMS spectrum was observed when incident CH_4^+ or CH_2^+ ions were used in place of CH_3^+ ions.

After the bombardment with CH_n^+ ions, the $\text{Si}(111)$ surface was bombarded with 100 eV Ar^+ ions while SIMS spectrum was continuously monitored. Although the observed SIMS spectrum was similar to those by CH_n^+ ions, the peak intensities due to hydrocarbon ions decreased gradually with time of Ar^+ ion bombardment, indicating that deposited hydrocarbon films were sputtered by Ar^+ ions, giving rise to secondary hydrocarbon ions. This fact provides us with a strong evidence that CH_n^+ ion bombardment produces hydrocarbon films on the $\text{Si}(111)$ surface.

Figure 3 shows SIMS spectra in the m/e range from 26 to 31, observed during CH_3^+ and CD_3^+ bombardment. As can be seen from Figure 3(a), the intensities of three dominant ions, C_2H_3^+ ($m/e = 27$), C_2H_4^+ (28) and C_2H_5^+ (29) are in the order of $I(\text{C}_2\text{H}_3^+) > I(\text{C}_2\text{H}_5^+) > I(\text{C}_2\text{H}_4^+)$ in the incident energy range from 20 eV to 100 eV. In contrast, CD_3^+ bombardment produced SIMS spectrum dependent on the incident energy from 20 to 50 eV, as shown in figure 3(b). At and below 20 eV, $m/e = 29$ peak is most intense. At 30 eV, three peaks of $m/e = 27$, 28 and 29 are comparable in intensity. Above 40 eV, $m/e = 27$ peak becomes most intense and the SIMS spectrum at and above 50 eV of incident CD_3^+ energy resembles that by CH_3^+ bombardment and also those by CH_4^+ , CH_2^+ and Ar^+ bombardment. Therefore, the SIMS spectrum observed during high energy CD_3^+ bombardment must be arisen solely from sputtering of hydrocarbon films which contain few D atoms originating from incident CD_3^+ ions.

The change in SIMS spectrum with the change of incident CD_3^+ ion energy can be explained if CD_3^+ ion bombardment is assumed to dominantly produce C_2H_3^+ and its allotropes, $\text{C}_2\text{H}_2\text{D}^+$ ($m/e = 28$) and C_2HD_2^+ (29), their relative yields being dependent on the incident CD_3^+ energy. At low CD_3^+ energy below 20 eV, C_2HD_2^+ formation becomes predominant compared to that of $\text{C}_2\text{H}_2\text{D}^+$ and C_2H_3^+ , resulting in the SIMS spectrum shown in Figure 3(b). If this explanation is correct, the result obtained with CD_3^+ ions indicates that incident ions with energy lower than 40 eV participate in the chemical reactions to produce secondary ions.

Further study is under way on the energy distribution of the secondary ions.

REFERENCES

- 1) Kevin G. Orrman-Rossiter, Amir H. Al-Bayati, D.G. Armour and S.E. Donnelly, Nucl. Instr. Meth., B59/60, 197(1991).

- 2) Y.Lifshitz, S.R.Kasi and J.W.Rabalais, Phys. Rev., **B41**, 10468(1990).
- 3) H.Ohno and S.Nagai, Proc. Symposium on Beam Engineering of Advanced Material Syntheses, Tokyo, Nov. 24 - 26, (1992), 261.

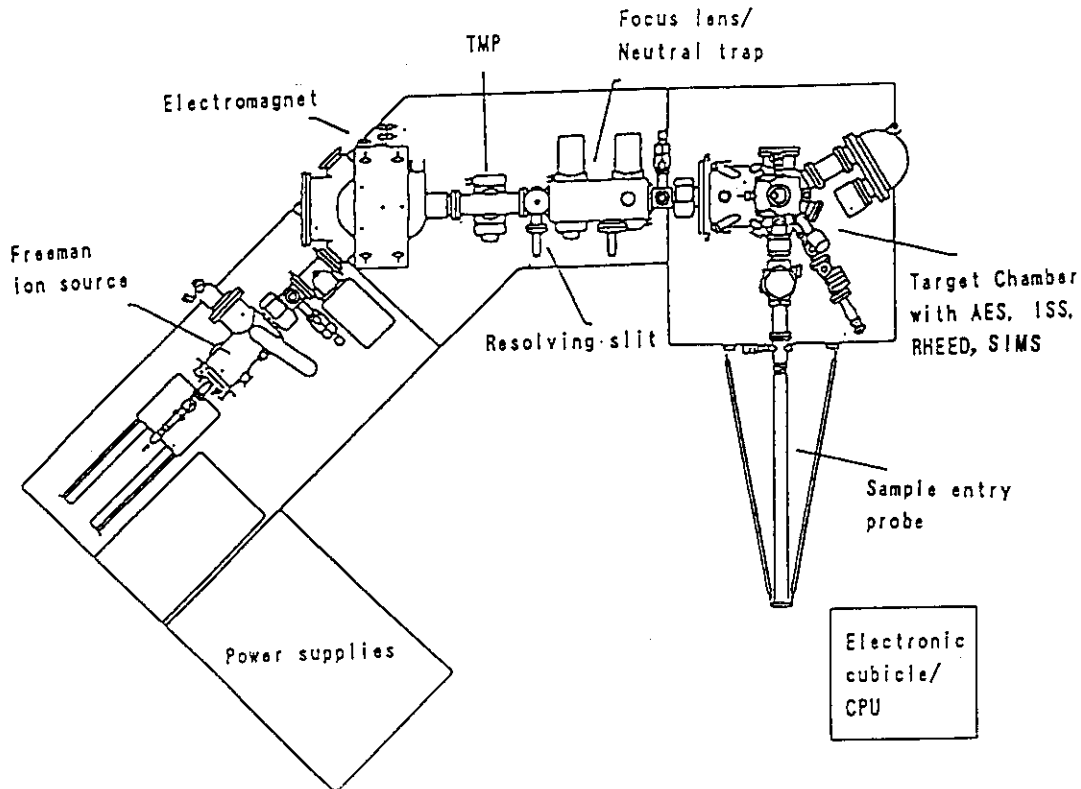


Figure 1. Plan view of the low energy ion deposition apparatus.

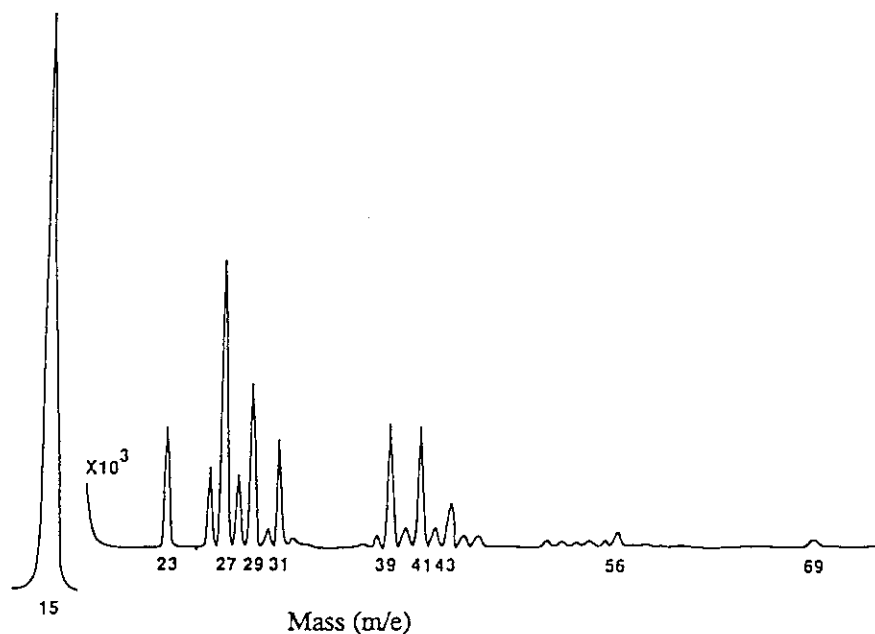


Figure 2. Mass spectrum of scattered and secondary ions during hydrocarbon film deposition by 50 eV CH_3^+ ions on Si(111).

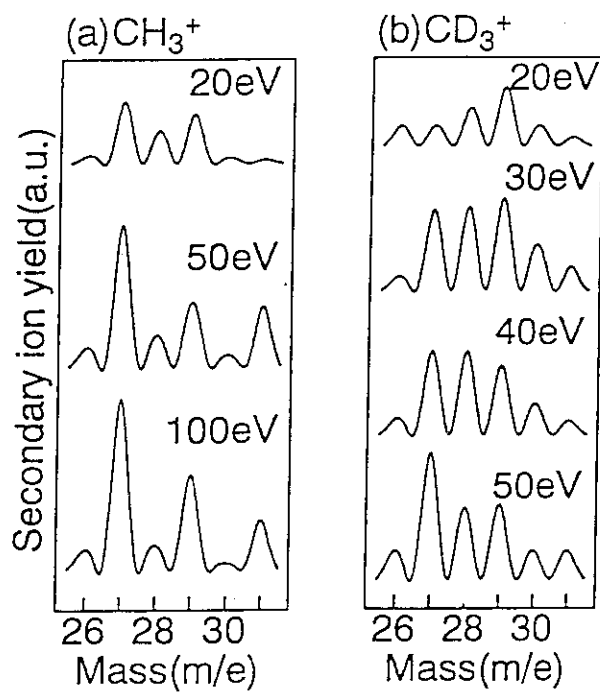


Figure 3. SIMS spectra during 20 ~ 100 eV CH_3^+ (a) and CD_3^+ (b) ion bombardment of Si(111).

6.9 XPS STUDIES ON THE CHARGE STATES OF Cr AND Cu ATOMS IMPLANTED INTO α -Al₂O₃ AND MgO SINGLE CRYSTALS.

Tsuneji FUTAGAMI, Yasushi AOKI, Osamu YODA, Siro. NAGAI
and Dorothee M. RÜCK*

Takasaki Radiation Chemistry Research Establishment, JAERI,
Watanuki-machi 1233, Takasaki, Gunma, 370-12 Japan

*GSI, D-6100 Darmstadt, Germany

I. INTRODUCTION

For ceramic materials, ion implantation has been used in order to modify near-surface physical properties such as hardness, electrical conductivity, refractive index, etc. in the recent years. Changes in surface properties are correlated with microstructure of surface layer induced by ion implantation¹⁻³⁾. In other words, structure of lattice defects and charge states of implanted atoms play an important role in these properties and these are closely associated with each other. Therefore, charge states of implanted atoms have been vigorously investigated by means of conversion electron Mossbauer spectroscopy (CEMS)⁴⁻⁸⁾ and X-ray photoelectron spectroscopy (XPS)⁹⁻¹¹⁾. In this paper, Charge states of Cu and Cr ions implanted in MgO and α -Al₂O₃ single crystals were investigated by XPS.

II. EXPERIMENTAL PROCEDURES

Single crystals of MgO(100) and α -Al₂O₃(0001) with an optical grade polish were used as implantation substrates. Implantation was performed at room temperature with ion implanters of TIBI at JAERI-TAKASAKI and Test Injector at GSI. During the implantation, the sample surface was inclined by about 5° off the normal to the beam, in order to avoid channeling effects. Ion beams were scanned to get uniform implantation doses over the sample surfaces (10mm x 5mm).

XPS measurements were performed by an ESCA LAB-MKII (VG Scientific Co.). For measuring the depth dependence of XPS spectrum an etching method with 4keV Ar ion was used under the pressure about 1×10^{-7} Torr. The charge state of Cu was determined from XPS and X-ray induced Auger electron spectra. Auger parameter, which is defined as a sum of the binding energy of a photoelectron peak and the kinetic energy of a Auger electron peak, was measured to compared with the values of 1850.4 eV (Cu⁰) and 1848.6 eV (Cu⁺). The divalent state Cu²⁺ can be recognized by the existance of shake-up satellite peaks in the 2p photoelectron

spectra. On the other hand, charge states of implanted Cr atoms were determined using the chemical shift (2.5 eV) of the Cr^{3+} 2p photoelectron.

III. RESULTS AND DISCUSSION

The XPS spectrum of Cu $2p_{3/2}$ and Cu $2p_{1/2}$ and X-ray excited Cu LMM Auger electron spectrum for MgO crystal implanted to 4×10^{16} Cu/cm² is shown in Fig. 1. The shake-up satellite peaks are clearly seen in the photoelectron spectrum so that the state of the implanted Cu should be divalent. Furthermore, there was no clear change in the spectrum shape when the measured surface was sputtered with Ar ion. Therefore, the charge state can be considered to be divalent at all depths. Similar results were obtained for MgO implanted to 8×10^{16} Cu/cm². The depth dependence of the photoelectron spectrum and X-ray excited Auger electron spectrum for MgO implanted to 2×10^{17} Cu/cm² is shown in Fig. 2. The dominant charge state was observed to change in the order of Cu^{1+} , Cu^0 and Cu^{2+} with Ar etching time. On the other hand, the Cu atoms implanted in $\alpha\text{-Al}_2\text{O}_3$ crystal to doses of 4×10^{16} and of 2×10^{17} Cu/cm² were observed to be trapped as Cu^0 .

As previously reported¹²⁾, the Cr atoms implanted in $\alpha\text{-Al}_2\text{O}_3$ and MgO crystals are trapped as Cr^0 or Cr^{3+} . The fractions of Cr^{3+} and Cr^0 at each depth in implanted samples were determined by separation of Cr $2p_{3/2}$ XPS peak areas into two peaks of Cr^0 and Cr^{3+} . In Fig. 3, concentrations of Cr^0/Al (or Cr^0/Mg) and Cr^{3+}/Al (or Cr^{3+}/Mg) are shown as a function of total Cr concentration, $(\text{Cr}^0 + \text{Cr}^{3+})/\text{Al}$ (or $(\text{Cr}^0 + \text{Cr}^{3+})/\text{Mg}$) for $\alpha\text{-Al}_2\text{O}_3$ (a) and MgO (b). In both cases, Cr^0/Al and Cr^0/Mg increases monotonically with the total concentration and Cr^{3+}/Al and Cr^{3+}/Mg tend to saturate. The saturation value and the saturation dose were measured to be 0.05 and 0.15 in $\alpha\text{-Al}_2\text{O}_3$, and 0.2 and 0.3 in MgO. In both Cu and Cr implantation, implanted Cr and Cu tend to take the cationic states in low density implanted region and to take the metallic states in highly implanted region.

Optical absorption spectra were measured for MgO crystals implanted with N, Ar, Cu, Cr and Kr ions in the spectral region of 200 – 800 nm. Absorption peaks were observed at wavelengths of 250, 330, 360, and 570 nm. It is known that the absorption peaks observed at 250 nm, 360 nm and 570 nm are attributed to the F (or F^+), the F_2 and the V^- centers, respectively. But 330nm absorbing entity has not been identified yet. As shown in Fig. 4, Cu, Cr implanted samples show clear and intense absorption peak, but the others show weak absorption. These results suggest that the structure of lattice defects produced by ion irradiation depend on the kind of ion used and it supports the concept that lattice defects are closely associated with implanted atoms.

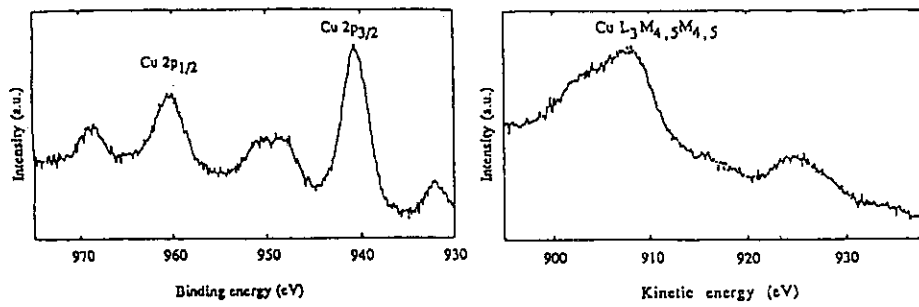


Fig. 1 XPS spectra in the Cu 2p region and X-ray excited LMM Auger electron spectra for MgO crystals implanted to 4×10^{16} Cu/cm² etching time 130min.

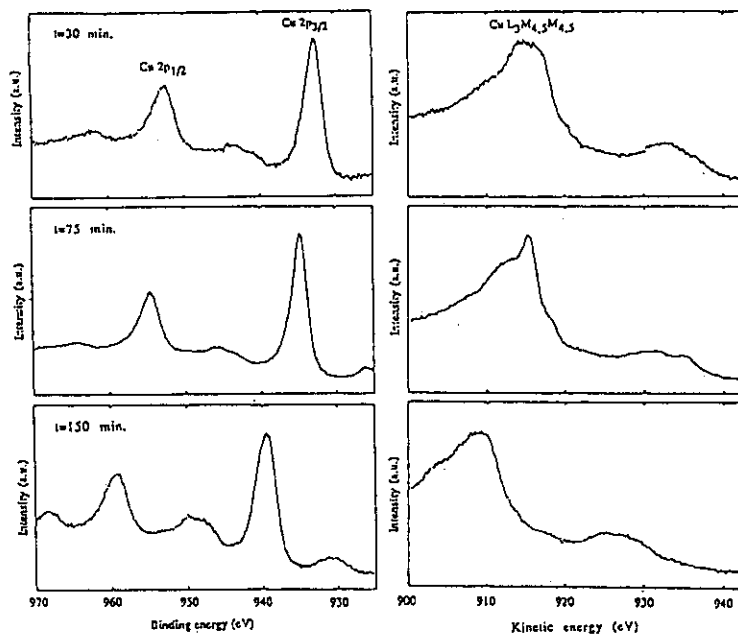


Fig. 2 XPS spectra in the Cu 2p region and X-ray excited LMM Auger electron spectra for MgO crystals implanted to 2×10^{17} Cu/cm². The XPS and Auger peaks were shifted due to charging-up during measurement for etching time 150 min.

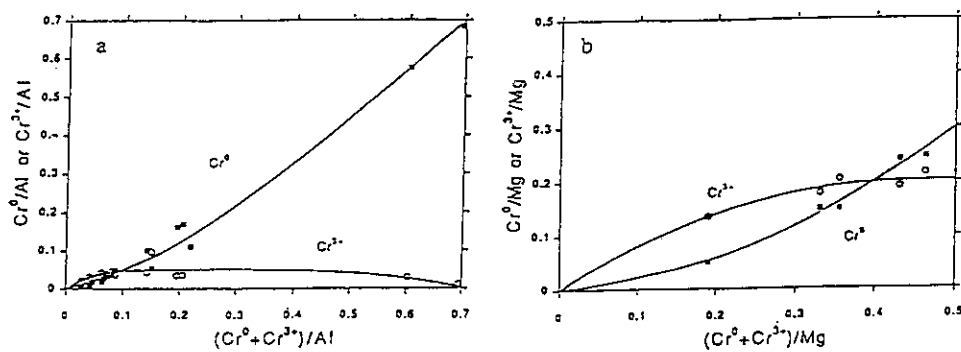


Fig. 3 (a) Relation between $(\text{Cr}^0 + \text{Cr}^{3+})/\text{Al}$ and Cr^0/Al (or Cr^{3+}/Al)
(b) Relation between $(\text{Cr}^0 + \text{Cr}^{3+})/\text{Mg}$ and Cr^0/Mg (or Cr^{3+}/Mg)

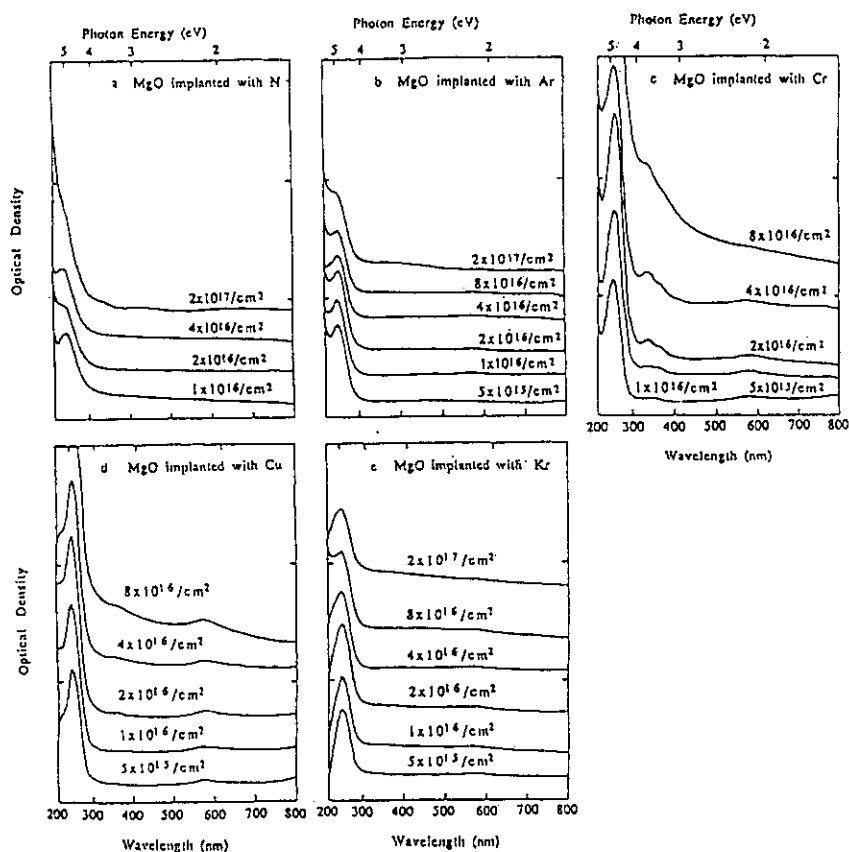


Fig. 4 Optical absorption spectra for MgO crystals implanted with N, Ar, Cr, Cu and Kr ions to doses of $5 \times 10^{15}/\text{cm}^2$ to $2 \times 10^{17}/\text{cm}^2$.

REFERENCES

- 1) H. Naramoto, C.J. McHargue, C.W. White, J.M. Williams, O.W. Holland, M.M. Abraham and B.R. Appleton, Nucl. Instr. and Meth., **209/210** (1983) 1159.
- 2) P.J. Burnett and T.F. Page, J. Mater. Sci., **19** (1984) 3524.
- 3) T. Hioki, A. Itoh, S. Noda, H. Doi, J. Kawamoto and O. Kamigaito, Nucl. Instr. and Meth., **B7/8** (1985) 521.
- 4) A. Perez, G. Marest, B.D. Sawicka, J.A. Sawicki and T. Tyliczszak, Phys. Rev., **B28** (1983) 1227.
- 5) C.J. McHargue, G.C. Farlow, P.S. Sklad, C.W. White, A. Perez, N. Kornilios and G. Marest, Nucl. Instr. and Meth., **B19/20** (1987) 813.
- 6) J.A. Sawicki, G. Marest, B. Cox and S.R. Julian, Nucl. Instr. and Meth., **B32** (1988) 79.
- 7) J. Kowalski, G. Marest, A. Perez, B.D. Sawicka, J.A. Sawicki, J. Stanek and T. Tyliczszak, Nucl. Instr. and Meth., **209/210** (1983) 1145.
- 8) C.J. McHargue, P.S. Sklad, J.C. McCallum, C.W. White, A. Perez, E. Abonneau and G. Marest, Nucl. Instr. and Meth., **B46** (1990) 74.
- 9) C. Donnet, H. Jaffrezic, N. Moncoffre, J. Tousset and G. Fuchs, Nucl. Instr. and Meth., **B46** (1990) 89.
- 10) C. Donnet, G. Marest, N. Moncoffre, J. Tousset, A. Rahioui, C. Esnouf and M. Brunel, Nucl. Instr. and Meth., **B59/60** (1991) 1205.
- 11) T. Miyamoto, T. Matumae, H. Yoko-o, Y. Andoh, Kiuchi and M. Satou, Nucl. Instr. and Meth. **B59/60** (1991) 1167.
- 12) T. Futagami, Y. Aoki, O. Yoda, S. Nagai and D.M. Ruck, Nucl. Instr. and Meth., **B80/81** (1993) 1168.

6.10 IN-SITU OBSERVATION OF EFFECT OF HYDROGEN AND HELIUM DUAL-ION IRRADIATION IN ALUMINUM

Shigemi FURUNO, Kiichi HOJOU, Hitoshi OTSU,
Kazuhiko IZUI*, Nobuo KAMIGAKI**, Kohtarou
ONO*** and Takao KINO****

Department of Materials Science and Engineering,
JAERI, *Nagasaki University, **Ehime University,
Shimane University, *Hiroshima Denki
Institute of Technology

I. INTRODUCTION

Technique of in-situ electron microscope observation during ion irradiation becomes more and more prevalent in these ten years in the fields of material science, above all in study of radiation damage.

We developed an in-situ observation system consisting of a electron microscope linked with ion accelerators¹⁾. Using this system we examined the main factors influencing the formation and growth of helium and hydrogen bubbles during He^+ and H_2^+ dual-ion irradiation²⁾.

In the present experiments, to examin the difference in irradiation effects under the various irradiation modes, three kinds of irradiations were performed at room temperature.

II. EXPERIMENTAL PROCEDURE

Specimens were zone refined aluminum of 99.9999% purity.

Dual-ion beam irradiation and in-situ observation were performed by using the system consisting of JEM-4000FX type electron microscope linked with two sets of 40 kV ion accelerators. The incident angle of ion beam is 60° to the surface of specimen.

In the present experiments, energies of He^+ and H_2^+ ions were 12 keV and 15 keV, respectively.

The following three kinds of irradiation experiments were performed at room temperature.

(1) Simultaneous He^+ and H_2^+ dual-ion irradiations with two kinds of the flux ratios: 2×10^{13} ions/cm²s and 1.5×10^{13} ions/cm²s, and 5×10^{12} ions/cm²s and 2.25×10^{13} ions/cm²s, respectively.

(2) H_2^+ ion irradiation after He^+ ion pre-irradiation for 20 minutes. The atomic fluxes of each ion were 5×10^{17} atoms/m²s.

(3) He^+ ion irradiation after H_2^+ ion pre-irradiation for 20 minutes. The atomic fluxes of each ion were 5×10^{17} atoms/m²s.

In all the above cases total atomic fluxes were maintained to be 5×10^{13} atoms/cm²s.

The electron microscope was operated at 150 kV to avoid electron beam damage.

III. RESULTS AND DISCUSSION

(1) Simultaneous dual-ion beam irradiations

Figs. 1 (b) and (c) show the results of simultaneous He^+ and H_2^+ ion irradiation for 30 minutes, where the atomic fluxes of He^+ and H_2^+ were in the ratio of 2:3 and 1:9 respectively, and the total flux of incident atoms in each case has the same value of 5×10^{17} atoms/m²s. For comparison Figs. 1 (a) and (d) show the results of irradiations for 30 minutes with He^+ and H_2^+ single ions, respectively. Remarkable features observed in these figures are that bubbles formed by the irradiations decrease in number and increase in size with increasing the proportion of the implanted hydrogen atoms to helium atoms.

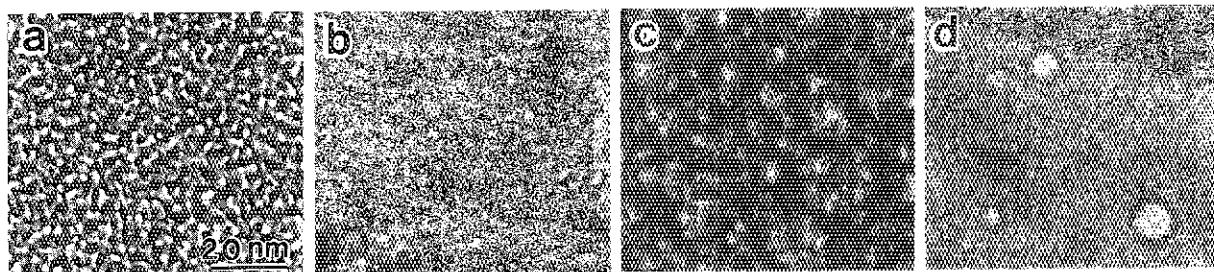


Fig. 1 Bubbles grown during single and dual-ion irradiation with He^+ and H_2^+ for 30 minutes: (a) He^+ single ion irradiation, (b) He^+ and H_2^+ dual-ion irradiation with the fluxes of 2×10^{17} ions/m²s and 1.5×10^{17} ions/m²s, respectively, (c) He^+ and H_2^+ dual-ion irradiation with the fluxes of 5×10^{16} and 2.25×10^{17} , respectively and (d) H_2^+ single ion irradiation.

The difference among the observed results is considered to

be mainly due to a difference in the production rate of point defects produced by 15 keV H_2^+ and 12 keV He^+ ion irradiations and the different mobility of hydrogen and helium atoms injected by irradiations in aluminum. The ratio of the production rate due to 12 keV He^+ ion and 7.5 keV H^+ ion was estimated to be about 10:1 from the results of TRIM-code calculations.

Since the total atomic flux of He^+ ion plus H_2^+ is kept to be constant, the increment of the implanted hydrogen atoms means the decrement of the implanted helium atoms, which means also the decrement of the number of the produced vacancies which acts as trapping sites for gas atoms. If the gas atoms trapped in vacancies migrate by vacancy mechanism and encounter with each other to form di-gas atoms trapped in vacancies, they act as stable nuclei for bubbles. The decrement of the produced vacancies results in the decrement of the number of nuclei for bubbles. The amount of gas atoms supplied for each nuclei in the process of ion irradiation increases. Consequently bubbles decrease in number density and increase in size with increasing the ratio of the implanted hydrogen atoms to the helium atoms.

(2) H_2^+ ion irradiation after He^+ ion pre-irradiation

During H_2^+ ion irradiation after He^+ ion irradiation, as shown in figs. 2 (c) and (d), the pre-formed small helium bubbles with high density act as effective trapping sites for hydrogen atoms, therefore the amount of hydrogen atoms escaping to the specimen surface is lower. Consequently the amount of hydrogen atoms supplied for bubbles become large, resulting in large growth of bubbles.

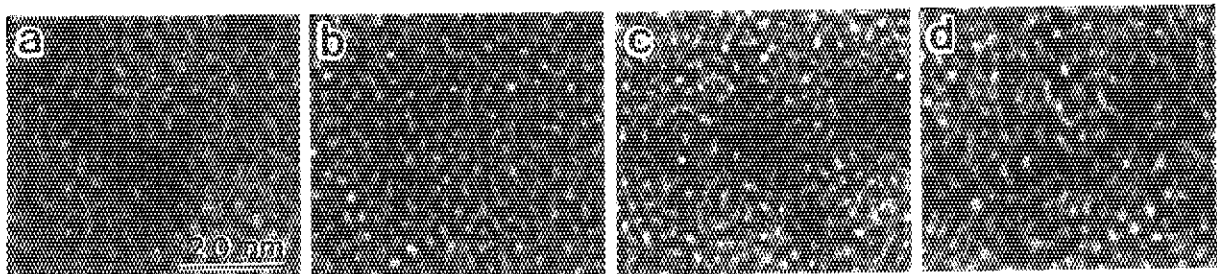


Fig. 2 Growth of bubbles during He^+ ion pre-irradiation with the flux of 5×10^{17} ions/ m^2s (a) and (b) and following H_2^+ ion irradiation with the flux of 2.5×10^{17} ions/ m^2s (c) and (d): (a) 10 minutes, (b) 20 minutes, (c) 30 minutes and (d) 40 minutes.

(3) He^+ ion irradiation after H_2^+ ion pre-irradiation

During He^+ ion irradiation after H_2^+ ion irradiation, as shown in figs. 3 (c) and (d), small bubbles are newly formed in large number due to large production rate of vacancies by He^+ ion irradiation. Only on some hydrogen bubbles formed by pre-irradiation, helium bubbles seem to increase in size by absorbing hydrogen atoms from hydrogen bubbles.

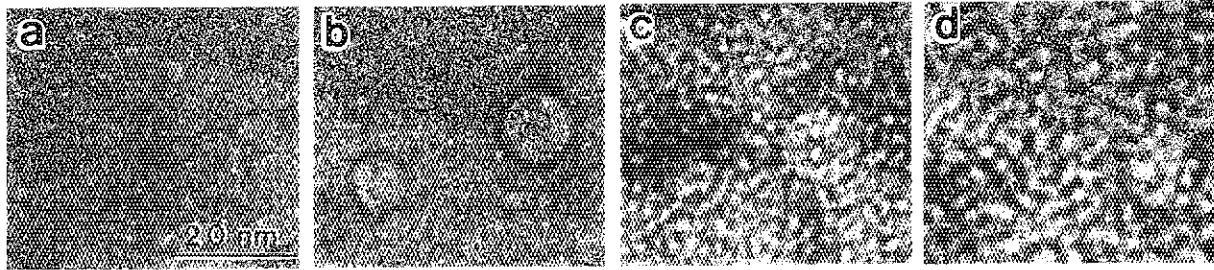


Fig. 3 Growth of bubbles during H_2^+ ion pre-irradiation with the flux of 2.5×10^{17} ions/ m^2s (a) and (b) and following He^+ ion irradiation with the flux of 5×10^{17} ions/ m^2s (c) and (d): (a) minutes, (b) 20 minutes, (c) 30 minutes and (d) 40 minutes.

IV. CONCLUSIONS

From the present experiments, the following conclusions were obtained:

- (1) Under the condition of the same injection rate of gas atoms, bubbles increase in number and decrease in size with increasing the ratio of H_2^+ ion to He^+ .
- (2) During He^+ ion pre-irradiation, small bubbles with large number density are formed, but bubbles grow large during following H_2^+ ion irradiation.
- (3) During H_2^+ ion pre-irradiation, large bubbles with extremely small number density are formed, and the small bubbles with large number density are newly formed during following He^+ ion irradiation.

REFERENCES

- 1) S. Furuno, K. Hojou, H. Otsu, K. Izui, T. A. Sasaki, T. Tsukamoto and T. Hata, J. Electron Microsc., 41(1992)273.
- 2) S. Furuno, K. Hojou, K. Izui, N. Kamigaki, K. Ono and T. Kino: J. Nucl. Mater. 191-194(1992)1219.

7. Nuclear Chemistry and Radioisotope Production

7.1	Study of Unstable Nuclei Using the TIARA-ISOL	
	T.Sekine, M.Koizumi, A.Osa, S.Ichikawa, M.Asai, H.Yamamoto and	
	K.Kawade	159
7.2	Production of Radioisotopes with Ion Beam: ^{139}Ce	
	M.Izumo, N.Shigeta, T.Sekine, H.Matsuoka, K.Kobayashi, A.Osa,	
	M.Koizumi and K.Hashimoto	161

7.1 STUDY OF UNSTABLE NUCLEI USING THE TIARA-ISOL

Toshiaki SEKINE, Mitsuo KOIZUMI, Akihiko OSA, Shin-ichi ICHIKAWA,
Masato ASAI,* Hiroshi YAMAMOTO* and Kiyoshi KAWADE*

Department of Radioisotopes, JAERI and *School of Engineering,
Nagoya University

1. INTRODUCTION

The Xe-Ba-Ce isotopes have proton numbers appreciably distant from the closed shells. These nuclei with neutron numbers off the closed shell are deformed from the sphere due to nuclear collective motion. The structure of these nuclei is the subject of nuclear collective motion.¹⁾ The present authors have studied the structure of Ba nuclei in the decay spectroscopic study of neutron-deficient La isotopes.²⁾ Using the TIARA-ISOL, this study will be extended to the structure of Ce nuclei by the decay spectroscopy of Pr isotopes.

The present paper describes the first on-line experiments on neutron-deficient Pr isotopes carried out in 1992.

2. YIELD OF Pr ISOTOPES MASS-SEPARATED IN THE REACTION $^{36}\text{Ar} + ^{nat}\text{Mo}$

The combination of an ^{36}Ar beam and a Mo target is the most adequate reaction system for the production of neutron-deficient Pr isotopes and for on-line isotope separation. It is because the ^{36}Ar isotope, which is the lightest isotope among the Ar isotopes, can produce neutron-deficient isotopes, and the Mo target keeps its shape at a high temperature in an ion source. The ^{36}Ar isotope, however, must be enriched for acceleration in a cyclotron, since its natural isotopic abundance is only 0.337%.

Table 1 On-line experiments carried out so far by using the TIARA-ISOL

Run	Beam/Energy/Current	Target	Experiment
1	$^{40}\text{Ar}^{8+}/175\text{ MeV}/10\text{ pA}$	$^{nat}\text{Mo}\ 3\text{mg}/\text{cm}^2$	First on-line mass-separation
2	$^{36}\text{Ar}^{10+}/195\text{ MeV}/7\text{ pA}$	$^{nat}\text{Mo}\ 3\text{mg}/\text{cm}^2$	Yield measurement of Pr isotopes
3	$^{36}\text{Ar}^{8+}/185\text{ MeV}/100\text{ pA}$	$^{nat}\text{Mo}\ 3\text{mg}/\text{cm}^2$	Search for ^{127}Pr

Table 2 Yield of Pr isotopes on-line mass-separated in the reaction $^{36}\text{Ar} + ^{nat}\text{Mo}$

Product	Half-life	Mass-separated yield*	
		Pr^{16}O^+	Pr^+
^{126}Pr	3.2 s	30	20
^{128}Pr	3.0 s	40	90
^{130}Pr	28 s	6700	2300
^{132}Pr	1.6 m	—	2700

*Obtained in Run 2. The ion-yield ratio between Pr^{16}O^+ and Pr^+ varied apparently with the product, because the experimental conditions were not kept constant.

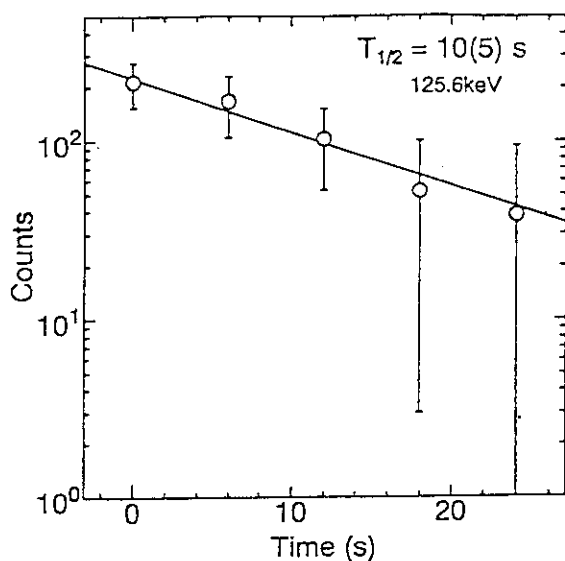


Fig. 1 The decay of the 125.6-keV peak in mass 127.

were obtained. From the spectra, the yields of even-mass Pr radioisotopes in metallic ion and monoxide ion were obtained, as shown in Table 2. In the determination of the yield, the γ -ray emission probability from the first 2^+ state to the ground state was assumed unity and a small amount of the Pr isotope growing from the Nd isobar was included. The yield was normalized at a 10 particle-nA of the ^{36}Ar beam current.

3. SEARCH FOR THE ^{127}Pr Isotopes in the Reaction $^{36}\text{Ar} + ^{\text{nat}}\text{Mo}$

Since the yield of ^{127}Pr was expected to be the same as those of ^{126}Pr and ^{128}Pr from a theoretical prediction, the isotope ^{127}Pr was searched for at the third run.

The spectroscopic measurement was carried out with an HPGe detector and a simple tape transport equipment. The tape transport equipment worked only for removing the long-lived residuals. During 32 s, the mass-separated beam was collected on the tape; after the mass-separated beam switched off by the fast high-voltage input to the electrode in the collection chamber, the γ -ray measurement continued for 32 s. The same cycle was repeated 330 times for the mass-127 monoxide ion. In the γ -ray measurement, sixteen spectra were obtained in a spectrum multiscaling mode.

From the γ -ray spectra obtained, a new γ -ray with an energy of 125.6 keV was observed. As shown in Fig.1, this γ -ray decayed with a half-life of 10 ± 5 s. The assignment of the γ -ray should be done using a ^{94}Mo enriched target; a better S/N ratio is expected in the γ -ray measurement.

REFERENCES

- 1) G. Puddi, O. Scholten and T. Otsuka, Nucl. Phys., **A348**, 109 (1980).
- 2) T. Morikawa, M. Oshima, T. Sekine, Y. Hatsukawa, S. Ichikawa, H. Iimura, A. Osa, M. Shibata and A. Taniguchi, Phys. Rev. **C46**, R6 (1992).
- 3) S. Ichikawa, T. Sekine, H. Iimura, and M. Oshima, Nucl. Instr. Methods, **A274**, 259 (1989).

Although the enriched ^{36}Ar gas is expensive, its efficient supply to the ECR ion source has been realized by the TIARA cyclotron group. As target 3 mg/cm²-thick Mo foils were used in the following experiments. This thickness is thin enough for recoiling products to escape from the target.

The experiments carried out with the TIARA-ISOL are summarized in Table 1. For ionization of the products, a surface ion source was used, which ionizes efficiently rare-earth elements with rather low ionization potentials.³⁾ In the first experiment using the 175-MeV ^{40}Ar beam, the ISOL was operated on-line for the first time. At the second experiment, γ -ray spectra of mass 126-132

7.2 PRODUCTION OF RADIOISOTOPES WITH ION BEAM: ^{139}Ce

Mishiroku IZUMO, Noriko SHIGETA, Toshiaki SEKINE,
 Hiromitsu MATSUOKA, Katsutoshi KOBAYASHI, Akihiko OSA,
 Mitsuo KOIZUMI and Kazuyuki HASHIMOTO

Department of Radioisotopes, JAERI

INTRODUCTION

At the radioisotope-production research facility¹⁾ constructed at the TIARA, the ^{139}Ce isotope was produced in the beginning. This isotope decays with a half-life of 137.2 d by electron capture, emitting a γ -ray of 165.9 keV. As shown in Fig.1, this energy point is important in the efficiency calibration of Ge detectors. In addition to the γ -ray energy, its decay mode of electron capture makes ^{139}Ce indispensable as a γ -ray source.

As preliminary to the production of ^{139}Ce , chemical separation schemes were tested following the proton irradiation of a lanthanum oxide target using the tandem accelerator in Tokai. It was found that both of a solvent extraction method and an anion exchange method can yield almost the same products in chemical purity. In the present experiment at the TIARA, the anion exchange method was adopted, because it can be much easier remotely controlled than the solvent extraction method.

EXPERIMENTAL

As target, lanthanum metal was irradiated instead of lanthanum oxide. Although lanthanum oxide is usable as a target and purer than a lanthanum metal commercially available, lanthanum metal was considered to be better from the viewpoint of safety in irradiation and transportation. It is because the

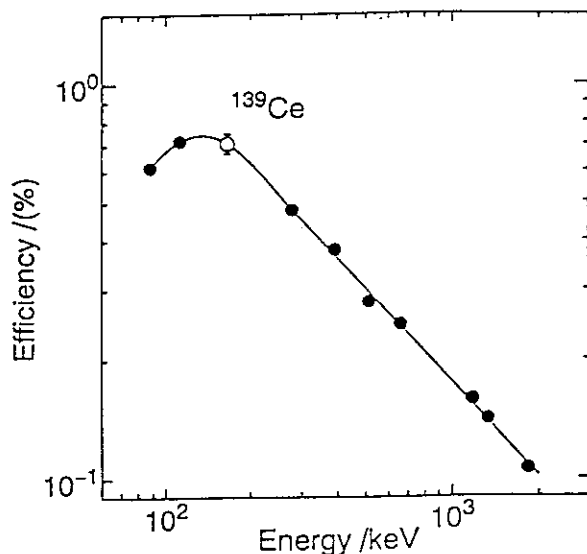


Fig.1 An example of the peak efficiency calibration curve for a Ge detector.

pellet of a lanthanum-oxide powder loses its shape on exposure to air. A powder of lanthanum metal kept in liquid paraffin was washed with *n*-hexane and was shaped in a pellet of 15 mm in diameter and 787 mg/cm² in thickness under a pressure of 650 kg/cm². The target was prepared immediately before the irradiation and fixed in a target holder.

The target assembly was transported from the shielded cell in the hot laboratory through the solid-target transfer line, which is 35 m in length, to the irradiation apparatus. The transportation to the terminal by the irradiation apparatus took about one minute and the fixing of the target assembly to the final position took about three minutes.

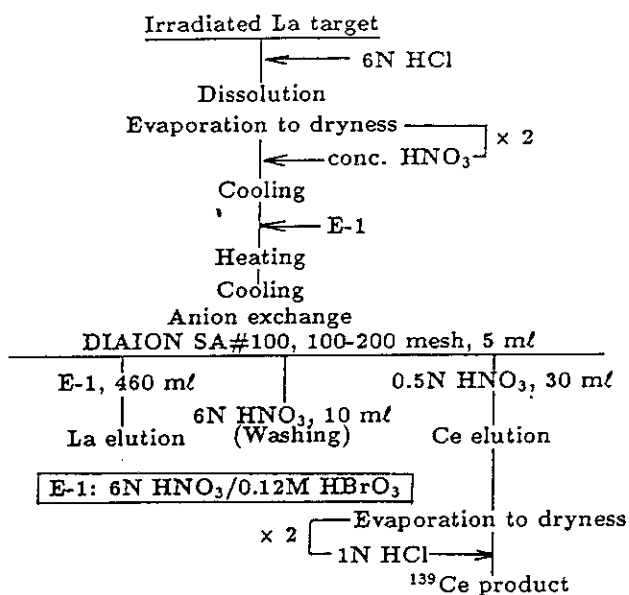


Fig.2 The scheme of the chemical separation of ^{139}Ce from a lanthanum target.

First, the target was dissolved in 6N HCl and was evaporated to dryness. The sample containing lanthanum and ^{139}Ce was redissolved in conc. HNO_3 and was evaporated to dryness; this process was repeated twice. After being cooled, the sample solution was mixed with a small amount of the E-1 solution that is 6N $\text{HNO}_3/0.12\text{M HBrO}_3$; the E-1 solution was prepared from KBrO_3 by a cation exchange method. In the foregoing process, lanthanum was prepared to take trivalent and cerium tetravalent. After being heated and then cooled, the sample solution was charged to an anion exchange column. The column was prepared by loading 5 ml of DIAION SA#100 anion exchange resin (100-200 mesh) into a glass tube. Elution curves of ^{139}Ce and ^{56}Co were plotted in Fig. 3. The lanthanum was eluted earlier than cerium, although the elution of lanthanum was not observed in this experiment. Almost all of the lan-

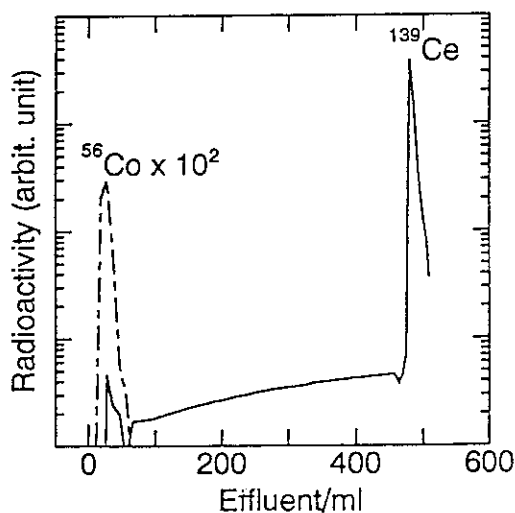


Fig. 3 Elution curves of ^{139}Ce and ^{56}Co in the anion exchange.

The target was irradiated with a 20 MeV proton beam. The irradiation continued for a period of 12.4 h. The averaged beam current was 2.8 μA .

The target was subjected to chemical processing 26 days after the irradiation. With the scheme as shown in Fig.2, the ^{139}Ce was separated from the target. The separation of cerium and lanthanum was performed with the anion exchange method proposed by Mayer *et al.*²⁾ By assembling units for chemical processing, the separation process was operated by remote control.

First, the target was dissolved in 6N HCl and was evaporated to dryness. The sample containing lanthanum and ^{139}Ce was redissolved in conc. HNO_3 and was evaporated to dryness; this process was repeated twice. After being cooled, the sample solution was mixed with a small amount of the E-1 solution that is 6N $\text{HNO}_3/0.12\text{M HBrO}_3$; the E-1 solution was prepared from KBrO_3 by a cation exchange method. In the foregoing process, lanthanum was prepared to take trivalent and cerium tetravalent. After being heated and then cooled, the sample solution was charged to an anion exchange column. The column was prepared by loading 5 ml of DIAION SA#100 anion exchange resin (100-200 mesh) into a glass tube. Elution curves of ^{139}Ce and ^{56}Co were plotted in Fig. 3. The lanthanum was eluted earlier than cerium, although the elution of lanthanum was not observed in this experiment. Almost all of the lan-

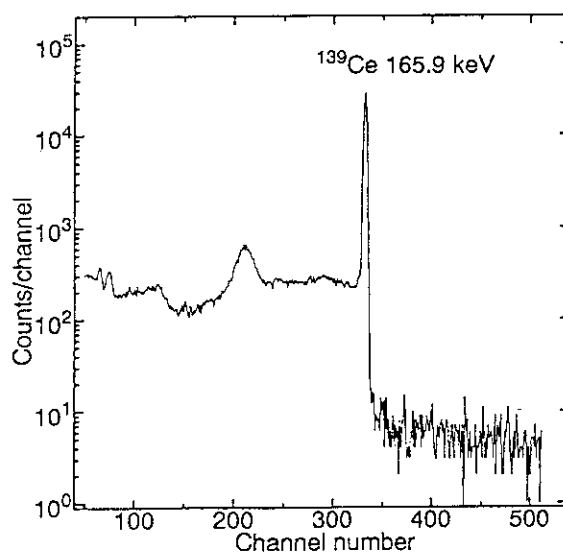


Fig. 4 The γ -ray spectrum of the ^{139}Ce product.

thorium was eluted with 460 ml of the E-1 solution. The weak radioactivity of ^{56}Co , which was eluted initially, was ascribable to the impurity iron in the target material. After the column was rinsed with 10 ml of 6N HNO_3 , the ^{139}Ce was eluted with 30 ml of 0.5N HNO_3 . After being evaporated to dryness, the solution was prepared to be 1N HCl solution.

RESULTS AND DISCUSSION

From the γ -ray spectrum of the product, as shown in Fig.4, no radioactive impurities were observed. And, when evaporated to dryness, there was no residuals observed. The radioactivity obtained was 6 MBq. The present work showed that the radioisotope-production research facility can work as expected.

References

- 1) M. Izumo, T. Sekine, S. Motoishi, H. Matsuoka, K. Kobayashi, K. Hashimoto, Y. Hatsukawa, N. Shigeta, F. Miura, T. Sorita, T. Moriya, H. Kudo, H. Umezawa and H. Watanabe, Proc. Int. Conf. on Evolution in Beam Applications (Takasaki, Nov. 5-8, 1991) p.552.
- 2) G. D. Mayer, T. N. Vander Walt, R. G. Bohmer and P. Andersen, Radiochim. Acta, **34**, 207 (1983).

8. Accelerator Technology

8.1	Heavy Ion Microbeam Apparatus for Single Event Upset Analysis T.Kamiya, T.Hirao, H.Yutoh, R.Tanaka	167
8.2	Accelerator Shielding Experiments with Monoenergetic Several Tens MeV Neutrons Y.Sakamoto, Sh.Tanaka, H.Nakashima, Y.Nakane, Su.Tanaka, T.Nakamura, M.Baba, T.Iwasaki, S.Matsuyama, M.Imamura, T.Shibata, Y.Uwamino, S.Shibata, K.Shin, H.Hirayama and S.Ban ..	171
8.3	Development of Visual Beam Adjustment Method for Cyclotron T.Agematu, K.Arakawa, S.Okumura, M.Fukuda, W.Yokota, Y.Nakamura, T.Nara, I.Ishibori, T.Okamura and T.Tachikawa	175
8.4	Design of JAERI 18GHz ECR Ion Source W.Yokota, Y.Saito, Y.Ishii, T.Nara and K.Arakawa	179
8.5	Present Status and Beam Acceleration Tests on Cyclotron K.Arakawa, Y.Nakamura, W.Yokota, M.Fukuda, T.Nara, T.Agematu, S.Okumura and I.Ishibori	183
8.6	Generation of Isochronous Fields M.Fukuda, K.Arakawa, Y.Nakamura, W.Yokota, T.Nara, T.Agematu, S.Okumura, I.Ishibori and T.Karasawa	187
8.7	Electric Fields of Deflector M.Fukuda, K.Arakawa, Y.Nakamura, W.Yokota, T.Nara, T.Agematu, S.Okumura, I.Ishibori and T.Karasawa	189
8.8	Orbit Calculation in the Central Region M.Fukuda, K.Arakawa, Y.Nakamura, W.Yokota, T.Nara, T.Agematu S.Okumura, I.Ishibori and T.Karasawa	192
8.9	Status of Ion Sources T.Nara, W.Yokota, Y.Nakamura, M.Fukuda, T.Agematu, S.Okumura, I.Ishibori and K.Arakawa	194
8.10	Development of Beam Attenuator S.Okumura, Y.Nakamura, W.Yokota, M.Fukuda, T.Nara, T.Agematu, I.Ishibori and K.Arakawa	196
8.11	Development of Parallel Plate Avalanche Counter for Fluence-rate Measurement S.Okumura, Y.Nakamura, W.Yokota, M.Fukuda, T.Nara, T.Agematu, I.Ishibori and K.Arakawa	198

8.12 Performance and Some Operation Results of the Vacuum System for the Cyclotron	
Y.Nakamura, I.Ishibori, S.Okumura, T.Nara, W.Yokota, M.Fukuda, T.Agematu, K.Arakawa and T.Yoshida	200
8.13 Radiation Resistance of Electronic Controller	
W.Yokota, Y.Nakamura, K.Arakawa and T.Agematu	204
8.14 Some Trials for Effective Operation of Negative Ion Sources for Tandem Accelerator	
Y.Saitoh, S.Tajima, I.Takada and K.Mizuhashi	207

8.1 HEAVY ION MICROBEAM APPARATUS FOR SINGLE EVENT UPSET ANALYSIS

Tomihiko KAMIYA, Toshio HIRAO*, Hidenori YUTOH
and Ryuichi TANAKA

Department of Advanced Radiation Technology and *Department of
Material Development, JAERI

I. INTRODUCTION

The development of the microbeam technique has been progressed. There are three technical means required for the study of SEUs in the heavy ion microbeam apparatus^{1,2}, i.e., (1) a microbeam focusing, (2) a beam positioning and (3) a single ion hitting. Previously, the smallest beam spot size of $0.8 \times 1.1 \mu\text{m}^2$ had already been achieved using ion beams of 15 MeV Ni and a target of Cu grid^{3,4}. More accurate measurement has been made this year using the same beam and a Si line-and-space relief pattern with sharp and straight edges^{5,6}. For the single ion hitting, The performance of a high speed beam switch was accomplished, and a new single ion detector was constructed considering compactness to fit in the microbeam lens system. Attempts to get its maximum detection efficiencies were made using both 15 MeV Ni ion from the tandem accelerator and α -ray from ^{241}Am source.

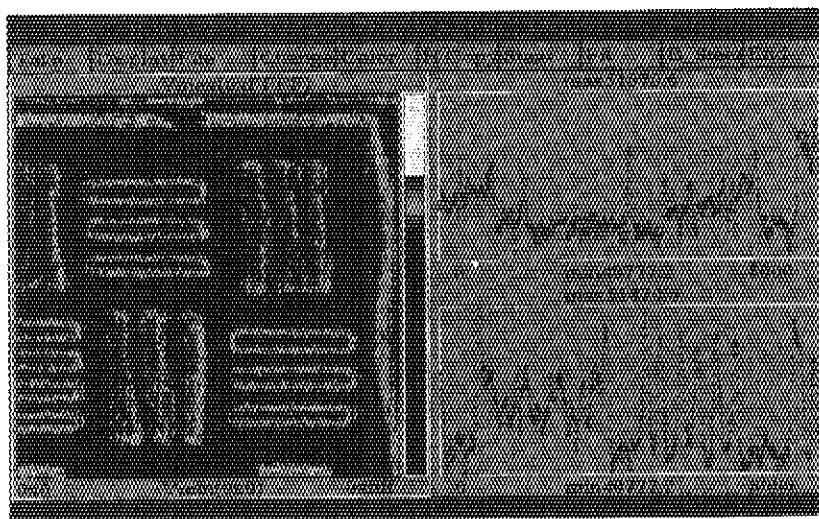


Fig. 1 The secondary electron maps of the Si relief pattern on a CRT of computer. The left picture is the two-dimensional map of about $100 \times 100 \mu\text{m}^2$ area with 150×150 pixels. And the right graphs of top and bottom represent one-dimensional secondary electron yields from 1000 successive points along two appropriate lines of the horizontal and vertical directions, respectively.

II. MICROBEAM FOCUSING

One- and two-dimensional secondary electron mapping images are displayed on a CRT screen of a microcomputer system, as shown in Fig.1. The left half of the images shows the line-and-space pattern on the silicon relief obtained microbeam scanning of 15 MeV Ni ions. The scanning area is about $100 \times 100 \mu\text{m}^2$ displayed with 150×150 pixels. The brightness of each pixel shows the intensity of the secondary electron yield. Several peaks corresponding to sharp edges of the silicon pattern appear in the right half, which represent secondary electron yield from 1000 successive scans in the horizontal (X) and the vertical (Y) directions. The beam sizes were defined by the FWHM of the peaks evaluated by least-square-fitting. The measured beam sizes are shown in Fig. 2 as a function of gaps of the microslits in the X and Y directions. The minimum beam spot size of $1.0 \times 0.8 \mu\text{m}^2$ was achieved when the object size is $4.0 \times 20 \mu\text{m}^2$ as pointed at by two arrows in Fig. 2.

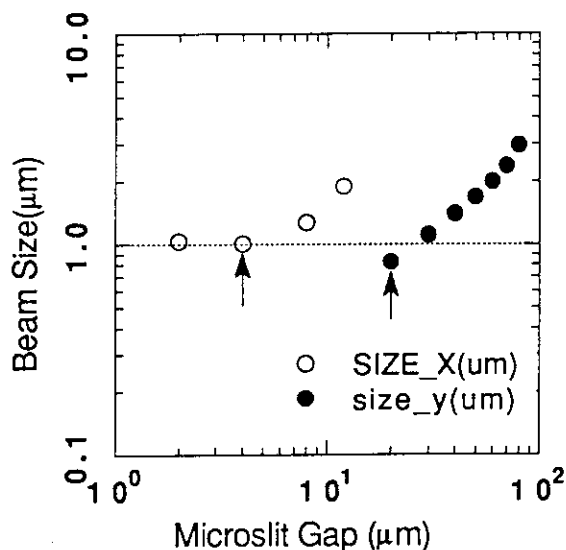


Fig.2 Beam spot sizes as a functions of gaps of the microslit (MS). Solid and empty circles indicates beam size of X and Y direction, respectively. Two small arrows point at data of the smallest beam spot size for the horizontal (X) and the vertical (Y) directions, respectively.

III. SINGLE ION HITTING

A couple of single ion detectors are used to avoid the influence of noise signals in generating trigger signals for a high-speed beam switch. One is a transmission-type detector. In the previous design of the detector, secondary electrons, generated by a single ion passing through an ultra-thin carbon foil, are transported to a microchannel plate (MCP) by magnetic and electrostatic fields. A maximum detection efficiency of 100 % could be obtained by the method using 15 MeV Ni ions. The high-speed beam switch was also tested using the transmission type detector only as a trigger source. The response time from the single ion detection was about 100 ns for generating of the 500 V deflection voltage. The beam current is required to be less than 0.1 pA to prevent farther ions from passing through the switch within the finite response time. In this test, a pulse generator was used to reset the deflection high voltages. The count rates of incident 15 MeV Ni ions were measured by a silicon

detector (SSD) and by the transmission-type detector with varying the frequency of reset pulses, as shown in Fig. 3. The count rate of MCP of the transmission-type detector is higher than that of SSD in the low frequency region because of noise from MCP. In the higher frequency, there is no significant difference between both count rates, while the count rate of SSD was not measured to avoid appreciable radiation damage of the local detector area of the SSD. This result indicates that the high-speed beam switch can provide low counting rate of incident ions in accordance with the frequency of the reset pulses up to 5×10^3 Hz. A saturation in the frequency higher than 1 kHz is identified as an asymptotic line in which all the incident ions are counted.

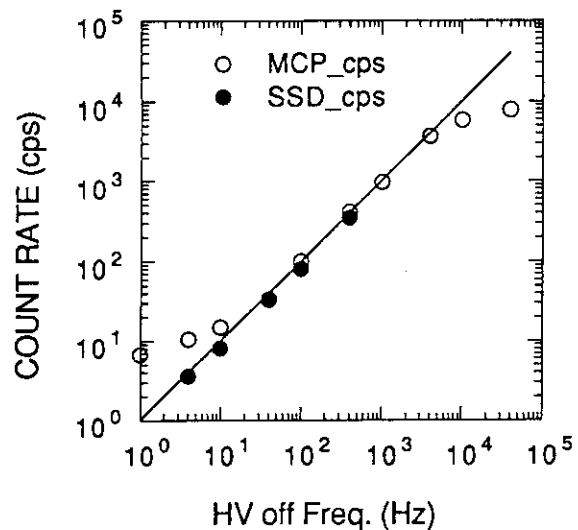


Fig.3 Counting ratio of incident 15 MeV Ni ions detected both by a SSD and by the old transmission-type detector measured with varying the frequency of reset pulses from the pulse generator. Solid and empty circles indicate counting rate of SSD and MCP, respectively.

In original design, we have another single ion detector of a channel electron multiplier installed on just side of the target to detect secondary electrons emitted by a single ion hit. However, there was not enough space to collect most of the secondary electrons for the single ion detectors, because the transmission-type detector was too big and occupied the working distance of 200 mm in the small space of the target chamber. To save the narrow space, an new type of a single ion double detecting system, a pair of the annular type MCP are mounted back to back as shown in Fig. 4. The detection efficiency of

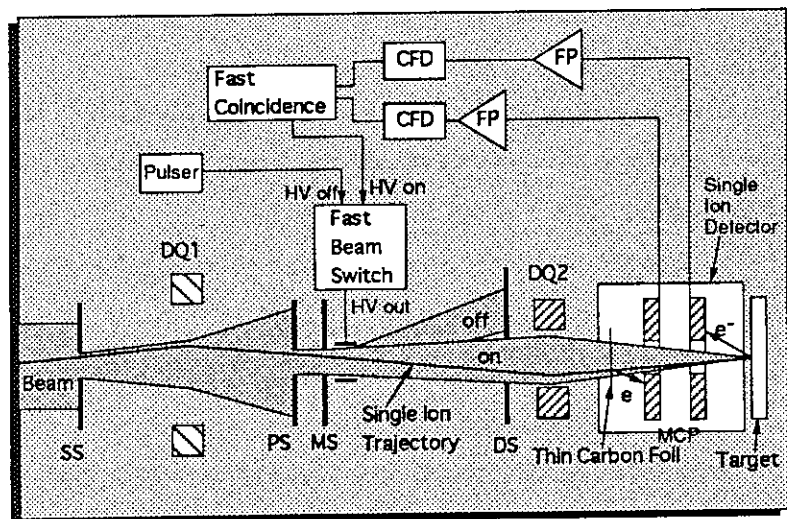


Fig. 4 Schematic diagram of single ion hit system using two sets of annular type MCP. FP: fast pre-amp, CFD: constant fraction discriminator, FCM: fast coincidence module.

an annular type MCP was also measured by using α -rays from ^{241}Am and 15 MeV Ni ion beam. The maximum detection efficiencies were 50 % for α -rays and 99 % for Ni ion. SSD was also used as a target to monitor the event number of ion hits. The efficiency values were similar to those of the transmission type detector of the original design. Although the signal to noise ratio of the annular type MCP is higher than ordinary type ones, it will be possible to eliminate noise components by using the coincidence method shown in Fig. 4.

IV. SUMMARY

The spot size of $1.0 \times 0.8 \text{ mm}^2$ was measured accurately using 15 MeV nickel ion beam and Si relief in the microbeam focusing tests. We still now have a residual low-frequency vibration of the target holder and the positioning inaccuracy of the target stages which influence high-resolution SEU analysis. We expected that they will be improved for a new target chamber exclusively for the SEU experiment, which is to be installed. The maximum detection efficiency of the originally designed transmission-type single ion detectors are 100 % for 15 MeV nickel ions. The high-speed beam switch was proved to switch off farther incident ions sufficiently in the performance test using 15 MeV nickel ions. The new compact single ion detector with annular type MCP was tested and the maximum detection efficiencies of 50 % and 99 % were measured for α -particles from ^{241}Am and 15 MeV nickel ions, respectively, to date. The characterization and the parameter optimization of it will be followed to complete the single ion detection and control system.

REFERENCES

- [1] T. Kamiya et al., Nucl. Instr. and Meth. B64 (1992) 362.
- [2] T. Kamiya et al., Proc. of 3rd Int. Conf. on Evolution in Beam Applications, Takasaki, Japan (1991) 286
- [3] T. Kamiya et al., Proc. of 1st. Meeting on The Ion Engineering Society of Japan, Tokyo, Japan, (1992) 105
- [4] T. Kamiya et al., Proc. of 3rd Symp. on Beam Engineering of Advanced Material Syntheses, Tokyo, Japan, (1992) 453
- [5] I. Ohdomari et al., Nucl. Instr. and Meth. B54 (1991) 71.
- [6] I. Ohdomari et al., Nucl. Instr. and Meth. B72 (1992) 436.

8.2 ACCELERATOR SHIELDING EXPERIMENTS WITH MONOENERGETIC SEVERAL TENS MEV NEUTRONS

Yukio SAKAMOTO, Shun-ichi TANAKA, Hiroshi NAKASHIMA,
Yoshihiro NAKANE, Susumu TANAKA ^{*1}, Takashi NAKAMURA ^{*2},
Mamoru BABA ^{*2}, Tomohiko IWASAKI ^{*2}, Shigeo
MATUYAMA ^{*2}, Mineo IMAMURA ^{*3}, Tokushi SHIBATA ^{*3},
Yoshitomo UWAMINO ^{*3}, Seiichi SHIBATA ^{*3}, Kazuo SHIN ^{*4},
Hideo HIRAYAMA ^{*5}, Syuichi BAN ^{*5}

Department of Reactor Engineering, ^{*1} Department of Advanced
Radiation Technology, JAERI, ^{*2} Tohoku University, ^{*3} University of
Tokyo, ^{*4} Kyoto University, ^{*5} High Energy Physics Research
Laboratory

I. Introduction

The project collaboration research between JAERI and universities from 1992 to 1996 has started to acquire the data for several tens MeV neutrons respect to the accelerator shielding at the AVF cyclotron in TIARA facility. In this programme ¹⁾ experiments planned using monoenergetic neutrons are (1) transmission experiments through shielding materials (concrete, iron, polyethylene), (2) double differential neutron scattering cross section measurements, (3) activation and spallation cross section measurements, and (4) charged particle production cross section measurements. These experiments are also planned, (5) streaming experiments through duct and maze using p-Cu white source neutrons from thick target, (6) neutron and gamma-ray production data measurements by charged particle from p to Ar, and (7) detection efficiency and response function measurements of neutron detectors.

II. Neutron Source Characteristics

Monoenergetic neutrons were produced by Li targets 3.5 mm and 5.2 mm thick for 43 MeV and 67 MeV protons. The neutron beam with 10 cm diameter collimated by the iron shield was injected into the shields set at the exit of the collimator 4 m apart from the target as shown in Fig.1. Proton beam current transmitted through the Li target was monitored by a Faraday cup and the source neutron intensity was monitored by two fission counters placed near the target.

Neutron spectra produced with 43 MeV and 67 MeV proton beam were measured at a position 5.5 m far from Li-targets using a proton recoil telescope detector in the energy

range over 15 MeV. The peak intensity was 1.1×10^4 n/cm² and 1.7×10^4 n/cm² per μ C at 40.5 MeV and 64.5 MeV neutrons respectively^{2, 3)}, consistent with estimated values from $^7\text{Li}(p,n)$ reaction. The FWHM of monoenergetic peak of source neutrons was about 2.0 MeV for 40.5 MeV neutrons and about 2.1 MeV for 64.5 MeV neutrons. Continuous component below 15 MeV due to break-up reaction was calculated by a phase-space model. A percentage of peak component neutrons to total neutrons was about 43% for 40.5 MeV neutrons and about 30 % for 64.5 MeV neutrons.

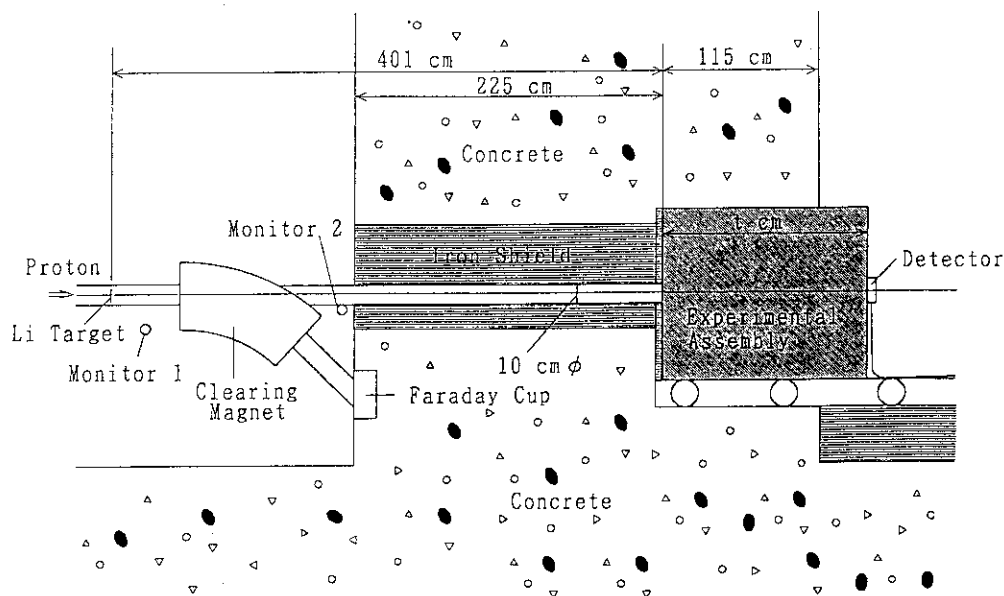


Fig.1 Layout of neutron shielding experiments.

III. Transmission Experiments

Concerning item 1 so far, transmission experiments for 40.5 MeV and 64.5 MeV monoenergetic neutrons were carried out for iron 20 – 130 cm shields and concrete 25 – 200 cm shields of which the size was 1.2 m wide x 1.2 m high.

Neutron spectra behind the shields were measured with a 5"-diameter by 5"-long organic liquid scintillator and with Bonner counters⁴⁾. Fission reaction rates and neutron dose equivalents behind the shields were measured with ^{232}Th and ^{238}U fission counters and a Rem counter. Three kinds of dosimeters were also used, solid state track detectors, thermoluminescence detectors LiF and ^7LiF , and PIN diodes. All of the data were measured at the neutron beam axis, 20 and 40 cm off the axis.

The fission reaction rates of ^{232}Th per source neutron behind iron and concrete shields on the beam axis are shown in Fig.2. Fission reaction rates on the beam line decrease exponentially over 50 cm-thickness for iron and concrete. Attenuation lengths

of ^{232}Th fission reaction rates for iron are about 8 cm and 10 cm for 40.5 MeV and 64.5 MeV neutrons respectively, and those for concrete are about 16 cm and 19 cm for 40.5 MeV and 64.5 MeV neutrons. Calculated reaction rates by the two-dimensional discrete ordinate code DOT3.5 using HILO86⁵⁾ and HILO86R⁶⁾ group cross sections agree with the measured ones within 30% on the beam line of iron and concrete.

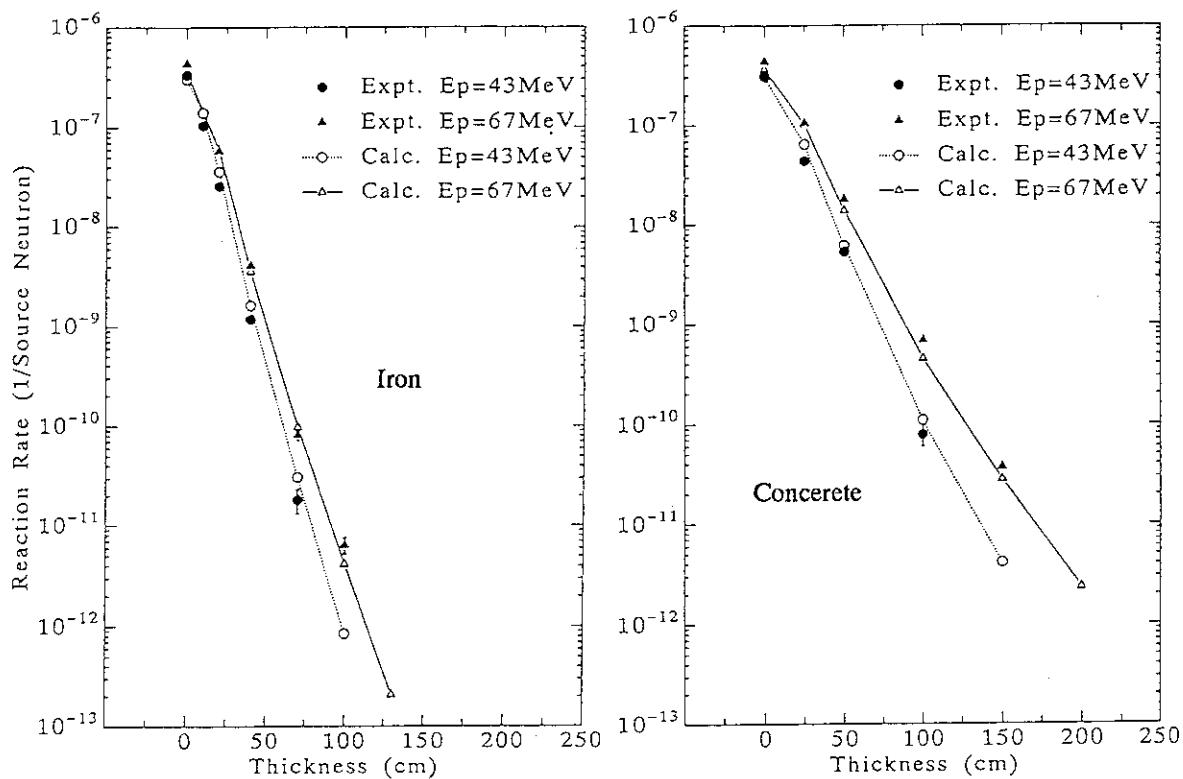


Fig.2 Attenuation of ^{232}Th fission reaction rates on the beam line behind iron and concrete.

IV. Neutron Cross Section Measurements

Activation cross sections of the important structural materials were measured by the gamma spectroscopy of irradiated samples. As an example neutron cross section for $^{12}\text{C}(n,2n)^{11}\text{C}$ is shown in Fig.3. There is a large difference between the data measured below 40 MeV. The datum measured at TIARA for 40.5 MeV monoenergetic neutrons is small than the peak near 30 – 36 MeV. Neutron cross sections of $^{209}\text{Bi}(n,xn)$ reaction to $x=5$ were also measured, which are a proposed detector with threshold energy at about 8 MeV intervals.

Production cross sections of proton, deuteron and triton from carbon atoms were measured by proton recoil telescope detector, which are necessary data in the evaluation of radiation damage and biological effects by neutrons.

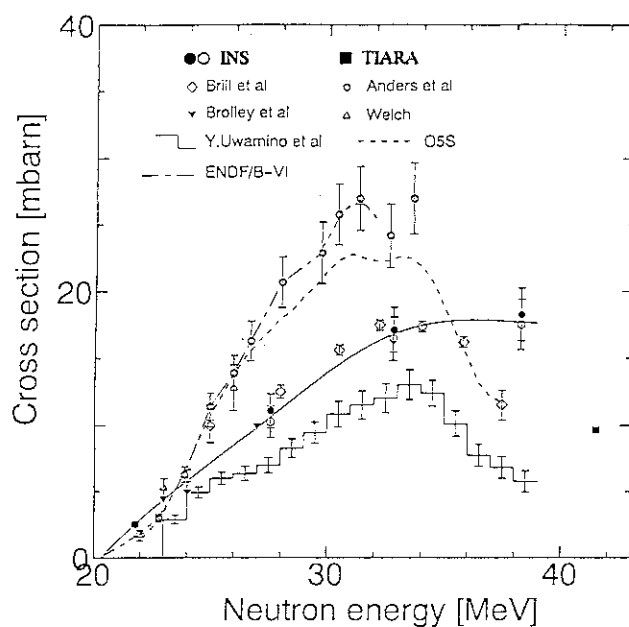


Fig.3 Neutron cross sections of $^{12}\text{C}(n,2n)^{11}\text{C}$.

References

- 1) Su.Tanaka et al., Proc. of 2nd Int. Symp. on Advanced Nuclear Energy Research(JAERI), Mito(1990) p.342.
- 2) M.Yoshioka et al., Proc. Autumn Meeting of Atomic Energy Society of Japan in Nagoya Univ.,G24(1992).
- 3) M.Baba et al., Proc. Annual Meeting of Atomic Energy Society of Japan in Kyoto Univ.,C35(1993).
- 4) N.Nakao et al., ibid,C47(1993).
- 5) R.G.Alsmiller et al.,ORNL/TM-9801(1986).
- 6) H.Kotegawa et al.,JAERI-M 93-020(1993).

8.3 DEVELOPMENT OF VISUAL BEAM ADJUSTMENT METHOD FOR CYCLOTRON

Takashi AGEMATSU, Kazuo ARAKAWA, Susumu OKUMURA,
Mitsuhiro FUKUDA, Watalu YOKOTA, Yoshiteru NAKAMURA,
Takayuki NARA, Ikuo ISHIBORI,
Tetsuya OKAMURA* and Toshiki TACHIKAWA*

Department of Advanced Radiation Technology, JAERI

* Sumitomo Heavy Industries, Ltd.

I. INTRODUCTION

In cyclotron operation, operators have to adjust the operating parameters with monitoring beam properties such as the position, the size, the shape, the divergence etc. However, obtainable information about the beam properties is so limited that operators often have to guess the beam properties. Operators also have to pay attention to the limitation of beam acceptance due to the geometry of beam condition. On the other hand, a large number of physical theories and calculation codes are required for analysis of the beam trajectory when designing a cyclotron. These codes and calculated results seem to be helpful for actual operation of cyclotrons, but have not been so far used. We have developed a computer-based visual assistance system¹⁾ for JAERI AVF cyclotron²⁾ by using the above codes and basic data.

II. A HUMAN INTERFACE

This system provides three kinds of visual human interfaces for beam parameter adjustment; (a) Beam trajectory is rapidly calculated and graphically displayed whenever the operators change the cyclotron parameters. (b) Feasible setting regions (FSR's) of the parameters which satisfy the beam acceptance condition of the cyclotron are graphically indicated. (c) Search trace, being a historical visual map of beam current values represented by various colored dots, are

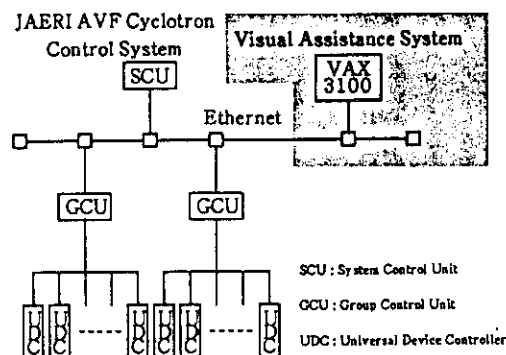


Fig.1 Architecture of the control system.

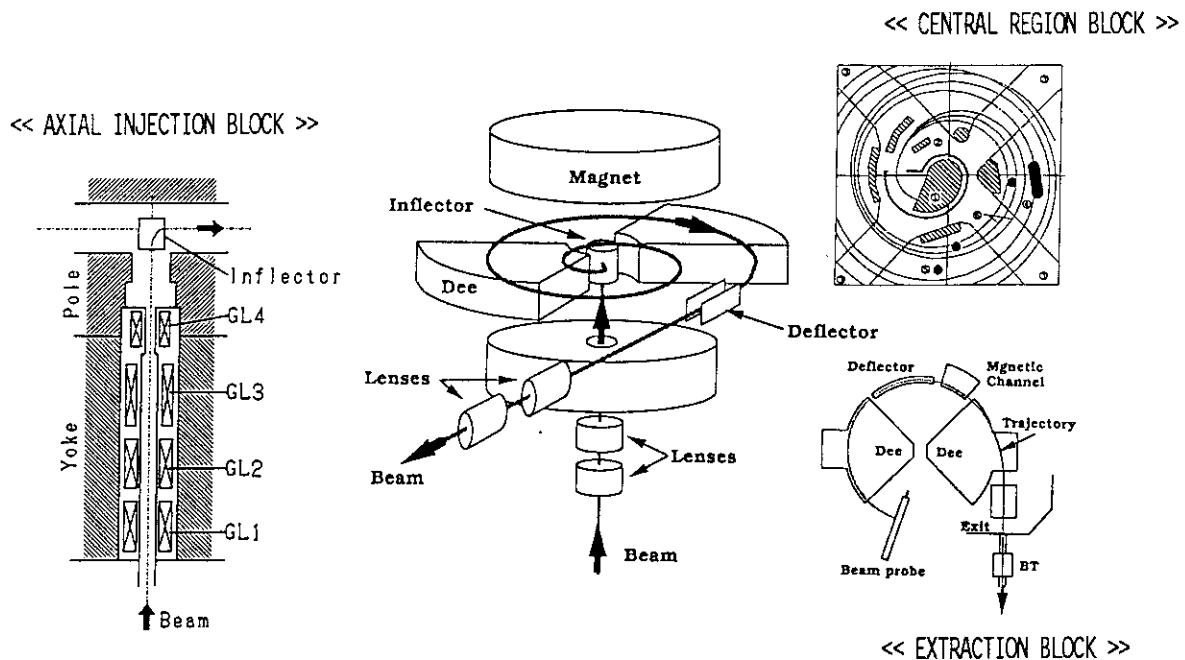


Fig.2 Schematic diagram of a cyclotron.

superimposed on the FSR's. This system is constructed by language of C and works on workstation of VAX-3100 connected through Ethernet with computers controlling³⁾ the cyclotron as shown in Fig.1.

The system treats three blocks in which the cyclotron control is divided. (1) the axial injection, (2) the central region, (3) the extraction. In this paper adjustment methods for the first two blocks are mainly reports. Both blocks are more important than the other block because the beam states of subsequent blocks are influenced by that of upstream one.

(1) Axial Injection Block

The axial injection block treats a region between the bottom of the cyclotron yoke and the inflector as shown in Fig.2. There are four Glaser lenses (GL1,2,3,4) with adjustable focal lengths. The beam is led into the cyclotron through a small gap of the inflector entrance by the parameters of adjusting these lenses. A typical beam envelope simulated is shown in Fig.3(a). The FSR's are limited mainly by the geometry of the inflector entrance. An example of FSR's are shown in Fig.3(b).

(2) Central Region Block

The central region block, which follows the axial injection block, determines the first turn of the beam trajectory after the inflector as shown in Fig.2. Figure 3(c) shows a top view of a cross section of this

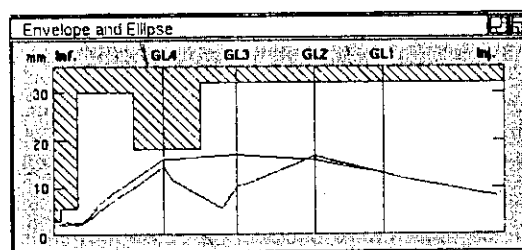
block, which is defined as a section between the exit of the inflector and the second phase slit. The parameters of the central region block is adjusted so that the beam passes through the two phase slits. Adjustable parameters in this region are dee voltages, trim coil currents and the phase of the beam buncher voltage. The beam trajectory is calculated from these parameters magnetic and electric fields. The FSR's are determined by geometrical arrangement of both phase slits. We already succeeded to make the particle beams pass through narrow channels of the slits in the system.

III. EVALUATION OF SIMULATION

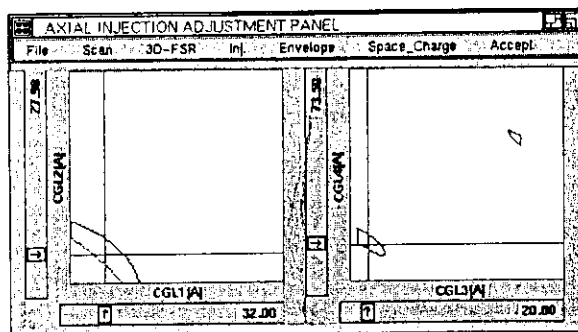
To evaluate the availability of the system, the search time required to maximize the beam current was measured for the axial injection block. Nine operators were asked to maximize the beam current by performing four lenses in two

different interface modes: Mode 1 using the existing console with four dials and a beam current indicator and mode 2 using the assistance system. Table 1 shows the search times measured in the both modes.

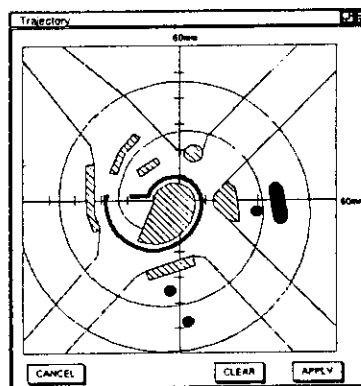
The search time was reduced by mode 1 to 65% of mode 2 on the average. This improvement in operation is attributed to the search trace display and the ability to make beam settings using a mouse. The FSR display makes the search time decrease because an operator searches a limited parametric space smaller than without the display.



(a) Envelope at the axial injection block.



(b) FSR's at the axial injection block.



(c) Beam trajectory at the central region block.

Fig.3 Typical display of simulation by the system.

IV. FUTURE ACTIVITY

Results of a system operation experiment showed that the search time to reach specific beam conditions was significantly reduced by using the displays at the axial injection block. Precise comparison of the simulated and the actual beam trajectory is planned for the three blocks of the cyclotron under various conditions.

Table 1 Summary of search time using two modes.

Operator	Level	Mode #1	Mode #2/#1
1	Expert	203 sec	0.59
2	Trainee	210 sec	0.86
3	Trainee	207 sec	0.63
4	Trainee	350 sec	0.73
5	Trainee	260 sec	0.46
6	Novice	130 sec	0.85
7	Novice	410 sec	0.80
8	Novice	605 sec	0.42
9	Novice	640 sec	0.34
Median			0.63

V. CONCLUSIONS

Three visual interfaces are developed for effective operation of the JAERI cyclotron. The results are summarized as follows;

- (1) Calculated beam trajectory was graphically displayed whenever the operator changes the cyclotron parameters.
- (2) Feasible setting regions (FSR's) of the parameters satisfying the cyclotron's beam acceptance criteria were indicated.
- (3) Search traces are superimposed on the FSR's as a historical visual map of beam current values.

The search time required to reach optimum beam current conditions was measured to evaluate the availability of the system. Results of the experiment showed that the search time to reach specific beam conditions was reduced to 65% on the average by using these interfaces.

REFERENCES

- 1) T.Okamura and T.Murakami, "An Operator Assistance System for Beam Adjustment of a Cyclotron", IEEE Trans. on Nucl. Sci., Vol.39, No.1, pp.13-20(1992).
- 2) K.Arakawa et al., "Construction and First Year's Operation of the JAERI AVF Cyclotron", Proc. 13th Int. Conf. on Cyclotron and their Applications, pp119-122(1992).
- 3) S.Okumura et al., "Control System for JAERI AVF Cyclotron", Proc. 13th Int. Conf. on Cyclotron and their Applications, pp648-651(1992).

8 . 4 DESIGN OF JAERI 18-GHz ECR ION SOURCE

W.Yokota, Y.Saitoh, Y.Ishii, T.Nara and K.Arakawa

Department of Advanced Radiation Technology, JAERI

I. INTRODUCTION

The ECR ion source of OCTOPUS type has been operated since 1991 in combination with the AVF cyclotron at JAERI. Only ions with mass to charge ratio (M/Q) less than 6.5 can be accelerated by the cyclotron, and Xe ion may be a limitation with the OCTOPUS source. The research plan requires heavier ion species and wider energy range. We designed a new ECR ion source with high performance of generating highly charged ions and metallic ions.

We chose a microwave frequency of 18 GHz because it may be the highest that is obtained by a commercially available klystron tube and applied for $2\omega_{ce}$ mode operation in use of room temperature magnets. A single stage type was adopted for high magnetic field.

The mirror field has been discussed often by its strength on the axis so far. For further understanding of ECR ion sources, however, it is important to know the shape and size of ECR shell from three dimensional field distribution including multipole fields^{1,2)}. Moreover, the geometrical condition of the ECR shell and an extraction hole should be studied to effectively extract highly charged ions in plasma through magnetic confinement.

Table 1 Design parameters of the ECR ion source.

Microwave:			
frequency	18.0	GHz	
max. power	2.5	kW	
resonance field	0.64	T	
Mirror Magnet:			
max. field on axis	1.41	T	
max. current	700	A	
length	27	cm	
outer diameter	102	cm	
inner diameter	8	cm	
Solenoid Coil:			
max. field on axis	0.7	T	
max. current	700	A	
outer diameter	82	cm	
inner diameter	18	cm	
Sextupole:			
material	NdFeB		
length	30	cm	
thickness	4	cm	
bore diameter	8	cm	
max. field on surface	1.4	T	
Plasma Chamber:			
inner diameter	7	cm	
length	100	cm	
Vacuum pump: turbo-molecular(1500l/s)			

We installed a solenoid coil between a pair of the mirror magnets to vary the shape and size of the ECR shell to study their effect on the source performance. The distance from the ECR shell to the extraction hole is variable by sliding the magnet assembly in the axial direction, and a plasma chamber is of a straight cylinder to make the slide easy. This simple chamber also allows easy replacement and modification for mounting additional attachments such as an electron gun and a rod insertion mechanism for metallic ion production. The

schematic view of the source is shown in Fig.1 and the design parameters are summarized in Table 1. The source will be completed in February, 1994, and the first ion will be extracted next spring.

II. MAGNETIC FIELD

Magnets were designed by use of ELF/MAGIC, a three-dimensional magnetic field calculation code. The most important point was to attain field strength forming a shell of $2\omega_{ce}$ resonance.

Two mirror magnets have the same structure with a soft iron yoke of 8 cm in thickness. They are magnetically separated in order to attain high mirror ratio. The distribution of the mirror fields were calculated for soft iron with saturation at 2.3 T, and the result is shown in Fig.2. The peak strength of the mirror field is about 1.4 T, higher than $2\omega_{ce}$ field of 1.28 T, and the mirror ratio is 14. The additional field of the solenoid coil enhances the minimum of the mirror field. The peak strength of the mirror field increases slightly by the solenoid field. As seen in Fig.2, there are two undesirable dips of field between the solenoid coil and the mirror magnets, but we did not find a design solution without them. By varying the solenoid field, the minimum field strength at $z=0$ ($B_z(0)$) varies from 0.1 T to 0.75 T. The length of the ECR shell for ω_{ce} varies gradually from 22 to 17 cm with $B_z(0)$ below 0.64 T. The ECR for ω_{ce} does not occur at higher field.

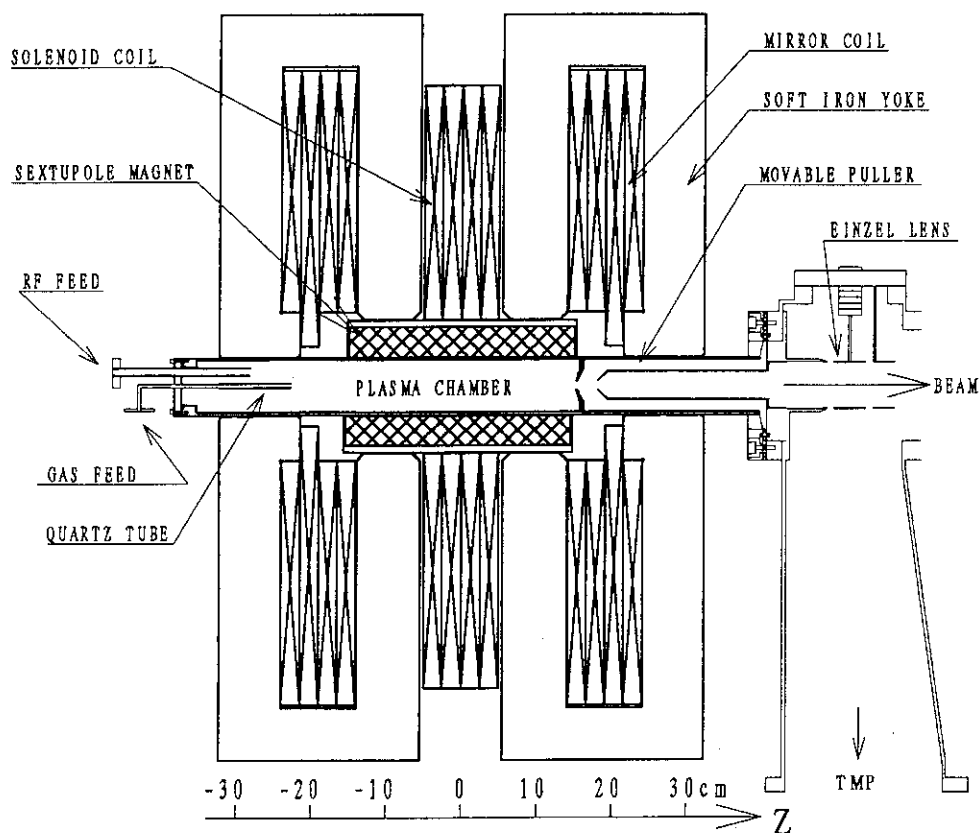


Fig. 1 Schematic drawing of the ECR ion source.

The thickness of sextupole magnets is limited by the existence of the solenoid coil, and was decided at 4 cm. In order to obtain a strong field, we examined various configuration of the shape and combinations of magnetizing direction. The final configuration is shown in Fig.3. The maximum of the calculated field is beyond 1.4 T on the surface of the magnet as shown in Fig. 3. The strength, however, is 1.1 T on the inner wall of the plasma chamber because there is a 5 mm gap between the sextupole surface and the inner wall.

The mirror and the multipole fields form a closed shell for ω_{ce} and the size is 5.6 cm in diameter and 22 cm in length without the solenoid field. With the increasing solenoid field, the length of the shell decreases down to 17 cm and the diameter to zero, and the shell disappears with $B_z(0)$ larger than 0.64 T. In the absence of the solenoid field, the resonance of $2\omega_{ce}$ is created only around the sextupole extremities. The resonance region appears along the inner wall of the chamber with the maximum solenoid field. Even in this case, however, the resonance shell is not closed in the chamber,. The area of the $2\omega_{ce}$ will be extended by reducing the gap between the magnet surface and the inner wall in the future.

III. PLASMA CHAMBER

The plasma chamber is of cylindrical shape with 7 cm inner diameter and 100 cm length, in the top of which an ion extraction system with a movable puller is mounted. Water coolant is flown through a gap of 1 mm between the inner and the outer cylinders. The chamber is fixed and connected with the beam analyzing system. The magnet assembly slides on the rails in the axial direction without touching the chamber, and the extraction hole position covers a wide range from the inside of ω_{ce} resonance to the peak of the mirror field.

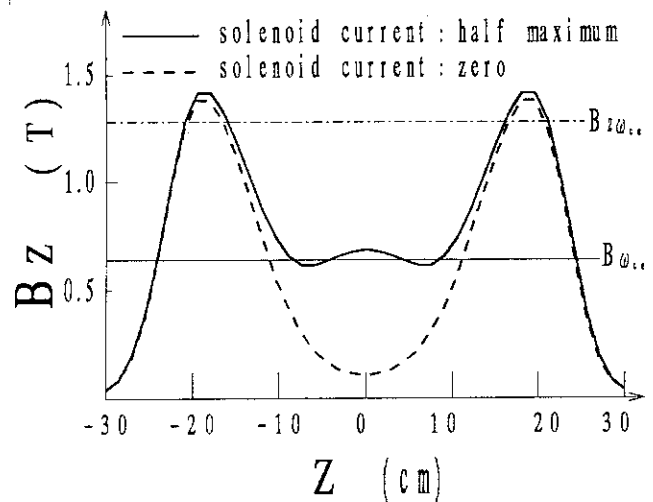


Fig. 2 Distribution of mirror and solenoid fields on the axis.

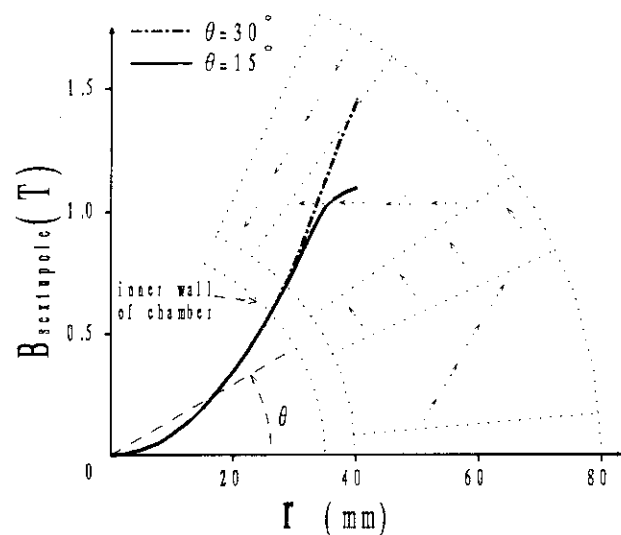


Fig. 3 Sextupole field distribution at $z=0$ cm. Dotted lines indicate configuration of the sextupole magnet and the arrows show the magnetizing direction.

In the first setting for generation of gaseous ions, a wave guide and gas feeding pipe with a quartz tube are mounted at the end flange of the chamber (Fig. 1). They will be rearranged when mounting a rod insertion mechanism for metallic ion production and mounting an electron gun in the next development phase.

REFERENCES

- [1] P. Sortais, P. Attal, L. Bex, M. Bisch, M. P. Bourgarel, Y. Bourgion, P. Leherissier and J. Y. Pacquet, Proc. of Int. Conf. on the Physics of Multiply Charged Ions and Int. Workshop on E.C.R. Ion Sources, Journal de Physique, 1989, pp. 855-866
- [2] Y. Yamashita, M. Sekiguchi, T. Hattori, Y. Ohshiro, A. Kitagawa and T. Hirata, Proc. of the 8th Symposium on Accelerator Science and Technology, Saitama, Japan, 1991, pp. 84-86

8.5 PRESENT STATUS AND BEAM ACCELERATION TESTS ON CYCLOTRON

Kazuo ARAKAWA, Yoshiteru NAKAMURA, Watalu YOKOTA,
Mitsuhiro FUKUDA, Takayuki NARA, Takashi AGEMATSU,
Susumu OKUMURA and Ikuo ISHIBORI

Department of Advanced Radiation Technology, JAERI

I. INTRODUCTION

Large AVF cyclotrons, so far, have been used mostly for fundamental nuclear physics and medical application to radiation therapy and radio-isotope production. The JAERI AVF cyclotron¹⁾ is the first one dedicated to R & D in materials science and other irradiation purposes. These applications of the cyclotron require that many kinds of light and heavy ions can be accelerated in a wide range of energies. To meet the requirement, continuing effort has been made on new beam development, improvement of beam extraction and transmission, etc.

II. GENERAL DESCRIPTION OF CYCLOTRON

(1) Cyclotron

The cyclotron is a 4-sectored variable energy AVF machine with an extraction radius of 923 mm. The acceleration electrodes consist of a couple of 86-degree dees, each connected with resonant cavity. The beam energy is variable within a magnet rigidity limit of 110 q²/A for all ions except protons. The maximum energy of protons is 90 MeV, which is limited by the vertical focusing properties and RF frequencies. The JAERI AVF cyclotron is of the model 930 of Sumitomo Heavy Industries, Ltd. The original design of the RF cavity, an inflector and the deflector were modified in order to make allowance for accelerating 90 MeV protons. A movable-panel type resonator originally proposed was replaced by a $\lambda/4$ coaxial type resonator with a movable shorting plate for generating a maximum acceleration voltage of 60 kV. A phase probe was additionally installed for measuring relative beam phases.

(2) Ion Source and Injection Line

Two types of ion sources, a multi-cusp ion source for light ions and an ECR ion source for heavy ions were installed. Both sources are located on the underground floor of the cyclotron vault. The transmission of the

ion beams is typically 85 %, and less dependent on ion species and the beam current²⁾. The beam buncher is placed at 1581.6 mm below the median plane of the cyclotron. The buncher is of two-gap klystron type with $\lambda/2$ mode. The bunching efficiency of 2.5 to 3 has been obtained for all the injected ions. The beam is axially injected into the cyclotron through several focusing lenses, and then, is inflected by 90° at the center of the cyclotron by the spiral inflector.

(3) Beam Chopper System

The beam chopping system was made to reduce the repetition of naturally bunched beam from the cyclotron (11 MHz - 22 MHz) down to a frequency range of 1 kHz to 1 MHz. A pulse voltage chopper (P-chopper) was installed in the injection line to chop DC beams from the ion sources into pulse beams with intervals of 1 μ s to 1 ms and with duration several times as long as the RF period of the cyclotron. A sinusoidal voltage chopper (S-chopper) was installed after the exit of the cyclotron to extract a single beam pulse from a train of plural beam pulses. The single pulse extraction was made for 50 MeV $^4\text{He}^{2+}$ using a couple of the choppers, with the P-chopper voltage interval of $60\tau_c$ (3.5 μ s), τ_c is RF period of the cyclotron, and 1/6 reduction rate of the S-chopper³⁾.

III. BEAM DEVELOPMENTS

(1) New Beam Acceleration

The beam acceleration tests have been conducted for H^+ (20 and 70 MeV), $^{40}\text{Ar}^{11+}$ (330 MeV), $^{36}\text{Ar}^{8+}$ (195 MeV), $^{36}\text{Ar}^{10+}$ (195 MeV), $^{20}\text{Ne}^{6+}$ (120 MeV) and $^{20}\text{Ne}^{7+}$ (260 MeV). The results of the beam acceleration test are summarized in Table 1. 99.5 percent enriched ^{36}Ar gas was fed to the ECR ion source to accelerate $^{36}\text{Ar}^{8+}$ and $^{36}\text{Ar}^{10+}$ ion beams.

(2) Extraction Current and Transmission

Particles accelerated and extracted so far are listed in Table 1. Protons and deuterons are generated by the multicusp ion source, and other ions by the ECR ion source. The extraction efficiency is defined by the ratio of the beam current measured with the main probe at $r=900$ mm to that with the Faraday cup (FC) just after cyclotron.

The overall transmission efficiency is defined by the ratio of the beam current with the FC just after analyzing magnet at the injection line to that with FC just after cyclotron. The average transmission efficiency is 8.9 %⁴⁾. Recently it increased up to 10 - 15 %. The best extraction and

overall transmission efficiency was 79 % for 45 MeV H^+ and 19 % for 260 MeV $^{20}Ne^{7+}$, respectively.

The 90 MeV protons, and 50 and 35 MeV deuterons were extracted with a beam currents of 10, 20 and 40 μA , respectively. These extracted beams are limited in the currents from the point of radiation safety because the radiation shielding of each irradiation room was designed on the basis of tolerable limit of secondary neutron generation rate, which was a set for the room. On the other hand, the extracted currents of the 10 MeV protons and 10 MeV deuterons are limited mainly by the ion source performance, because the extraction voltage of the ion source is extremely low. The constant orbit method is used as a scaling mode of cyclotron operation. In this case, the extraction voltage of the ion source should be applied according to each acceleration energy. For example, the voltage is 16 kV for 90 MeV protons and only 3.1 kV for 10 MeV. The maximum beam currents of heavy ions such as Ne, Ar and Kr mainly depend on the ability of the ion source.

IV. RECENT IMPROVEMENT

A beam attenuators were installed in the injection line to control the injected ion intensities into the cyclotron. The beam intensities at the targets can be easily controlled in an attenuation rate range of 1/2 to $1/10^3$. The details of this system is reported separately in this report.

The deflector probe consists of the differential and integral heads to measure the beam turn pattern near the extraction region in the cyclotron.

A computer-based operator assistance system was installed for the cyclotron. This system provides a CRT display for cyclotron beam trajectories, permissible setting regions of beam parameters, and searching traces designed to optimize beam parameter adjustment⁵⁾. The details of this system is reported separately in this report.

REFERENCES

- 1) K. Arakawa, Y. Nakamura, W. Yokota, M. Fukuda, T. Nara, T. Agematsu, S. Okumura, I. Ishibori, T. Karasawa, R. Tanaka, A. Shimizu, T. Tachikawa, Y. Hayashi, K. Ishii and T. Satoh, Proc. 13th Int. Conf. on Cyclotron and Their Applications, Vancouver, Canada, pp.119-122 (1992).
- 2) T. Nara, W. Yokota, Y. Nakamura, M. Fukuda, T. Agematsu, S. Okumura, I. Ishibori and K. Arakawa, Proc. 9th Sympo. on Accele. Sci. and Tech.,

Tsukuba, Japan, Aug. pp.89-91 (1993).

- 3) W. Yokota, M. Fukuda, K. Arakawa, Y. Nakamura, T. Nara, T. Agematsu, S. Okumura, I. Ishibori, Proc. 13 th Int. conf. on Cyclotron and Their applications, Vancouver, Canada, pp581-584(1992).
- 4) K. Arakawa, Y. Nakamura, W. Yokota, M. Fukuda, T. Nara, T. Agematsu, S. Okumura, I. Ishibori, Proc. 9th Sympo. on Accele. Sci. and Tech., Tsukuba, Japan, Aug. pp.202-204 (1993).
- 5) T. Agematsu, K. Arakawa, S. Okumura, Y. Nakamura, W. Yokota, T. Nara, M. Fukuda, and I. Ishibori, Proc. 9th Sympo. on Accele. sci. and Tech., Tsukuba, Japan, Aug. pp437-439 (1993).

Table 1 Results of Extracted Intensity and Transmission

Particle	Energy (MeV)	Harmonic No.	Frequency (MHz)	Extracted Intensity ($e\mu A$)	Extraction Efficiency (%)	Transmission (%)
H^+	10	2	14.97	10	68	12
	20	2	21.03	5.0	77	11
	45	1	15.46	30	79	14
	70	1	18.92	5.0	53	12
	90	1	21.14	10	39	2.0
D^+	10	2	10.63	11	29	3.7
	35	2	19.70	40	59	4.6
	50	1	11.76	20	49	7.2
$^4He^{2+}$	20	2	10.67	5.5	57	11
	50	2	16.77	20	54	15
	100	1	11.81	10	32	6.4
$^{20}Ne^{6+}$	120	3	17.70	0.30	31	2.0
$^{20}Ne^{7+}$	260	2	17.48	0.33	70	19
$^{36}Ar^{8+}$	195	3	16.82	2.4	50	10
$^{36}Ar^{10+}$	195	3	16.83	0.10	43	1.2
$^{40}Ar^{8+}$	175	3	15.14	3.0	73	9.9
$^{40}Ar^{11+}$	330	2	13.68	0.21	49	14
$^{40}Ar^{13+}$	420	2	16.24	0.03	63	13
$^{84}Kr^{20+}$	520	2	11.98	0.004	17	1.7

8.6 GENERATION OF ISOCHRONOUS FIELDS

Mitsuhiro FUKUDA, Kazuo ARAKAWA, Yoshiteru NAKAMURA,
Watalu YOKOTA, Takayuki NARA, Takashi AGEMATSU,
Susumu OKUMURA, Ikuo ISHIBORI and Takashi KARASAWA

Department of Advanced Radiation Technology, JAERI

I. INTRODUCTION

The JAERI AVF cyclotron is a variable-energy, multi-particle cyclotron which was designed to accelerate ions in a wide range of energy. An acceleration dee voltage for the cyclotron is calculated by the constant orbit method. A standard condition of the constant orbit method is 90 MeV protons for the harmonic number $h=1$ with a dee voltage of 60 kV, 460 MeV $^{40}\text{Ar}^{13+}$ for $h=2$ with 34 kV and 175 MeV $^{40}\text{Ar}^{8+}$ for $h=3$ with 34 kV. The beam phase is quite sensitive to field deviation from the isochronous condition because the turn number amounts to 550 for $h=1$, 265 for $h=2$ and 210 for $h=3$. If a base field level deviates equally by $\Delta B/B = \pm 1 \times 10^{-4}$ from the isochronous field, the beam phase drifts away by 20° in the extraction region. Thus careful fine tuning of the coil currents is required for generating the isochronous field for each ion and energy.

II. CALCULATION OF OPTIMUM COIL CURRENTS

The optimization program with a simplex method is used to calculate coil currents for generating the isochronous field. Radial distributions of the base field averaged azimuthally on equilibrium orbits are reconstructed for nine different main coil currents based on measured concentric field maps. Trim coil fields are calculated at three base field levels. The initial coil currents are obtained from the optimization calculation to fit the reconstructed field to the ideal isochronous field.

III. PHASE PROBE

Relative phases of internal beam particles are measured by a phase probe. The probe consists of ten pairs of rectangular pickup electrodes installed in the radial direction. Relative phase differences from the pickup signal of the second electrode are detected by a digital storage oscilloscope. The length variation of the signal cables is within 4 mm, so that the uncertainty of the phase measurement is negligible. The signal contains rf noise with large amplitude. Relative beam phases are measured exactly by detecting the point where the signal wave intersects the rf noise wave.

IV. CORRECTION OF COIL CURRENTS

Corrected trim coil currents are deduced from the measured phase differences. Magnetic field amplitudes to be compensated for isochronous condition are calculated with a least-square fitting code to minimize the field deviation from the isochronous field. The phase deviations can be finally reduced within $\pm 5^\circ$ after a few times iterative corrections.

V. BEAM PHASE MEASUREMENT

The isochronism of the internal beam was checked by small amounts of radio frequency shifts of $\Delta f/f = 2 \times 10^{-4}$ to 5×10^{-4} . If the isochronous field is generated ideally, the same amount of positive and negative rf shifts should result in the same amount of negative and positive phase drifts. The rf shifts are equivalent to a small change of the base field level. In case of fine tuning of the coil currents, it is difficult to estimate exactly the change of the base field for due to magnetic hysteresis. On the contrary, the radio frequency can be set precisely at a resolution of 10Hz.

Phase drifts caused by the rf change of 2.6×10^{-4} for 45 MeV protons and 2.4×10^{-4} for 50 MeV $^4\text{He}^{2+}$ are shown in Fig. 1 and 2, respectively. Phase drifts are calculated on the assumption that the isochronous field starts at a radius of 20 cm and no central field bump is concerned. The measured phases are consistent with the calculated ones. The field deviation from the isochronous condition is estimated within 1 gauss.

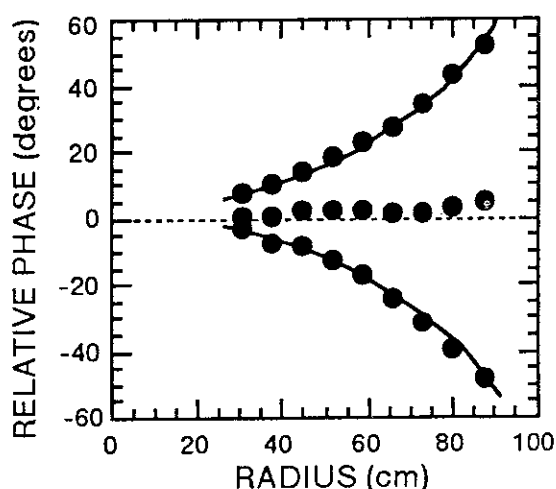


Fig. 1. Phase drifts for 45 MeV protons due to the positive and negative radio frequency change of $\Delta f/f = \pm 2.6 \times 10^{-4}$. Measured and calculated phases are indicated by circles and solid lines, respectively.

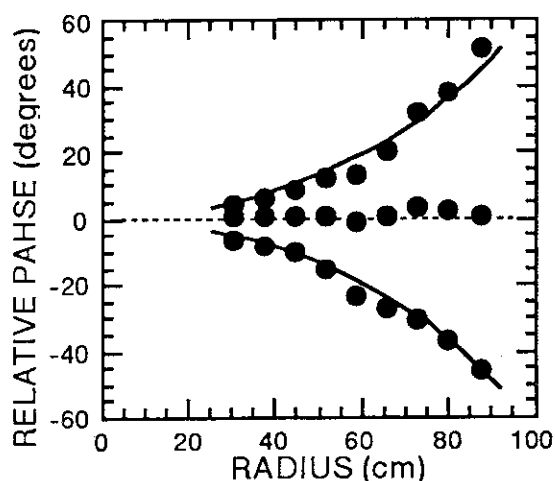


Fig. 2. Phase drifts for 50 MeV $^4\text{He}^{2+}$ due to the positive and negative radio frequency change of $\Delta f/f = \pm 2.4 \times 10^{-4}$. Measured and calculated phases are indicated by circles and solid lines, respectively.

8 . 7 ELECTRIC FIELDS OF DEFLECTOR

Mitsuhiro FUKUDA, Kazuo ARAKAWA, Yoshiteru NAKAMURA,
Watalu YOKOTA, Takayuki NARA, Takashi AGEMATSU,
Susumu OKUMURA, Ikuo ISHIBORI and Takashi KARASAWA

Department of Advanced Radiation Technology, JAERI

I. INTRODUCTION

Extraction system of the JAERI AVF cyclotron consists of an electrostatic deflector, a magnetic channel and a field gradient corrector. Analysis of beam behavior in the extraction region is much complicated because the magnetic field remarkably varies in the radial direction. Electric field distribution of the deflector is not simple due to complex change of a mechanical gap depending on the positions of septum and high voltage electrodes. Furthermore it is hard to define particle condition at the entrance of the deflector owing to difficulty of orbit computation up to the extraction. In this work we have focused on the correlation of the electric field with mv^2/q and the entrance position of the deflector.

II. ELECTRIC FIELD OF DEFLECTOR

The electric field of the deflector is represented by equivalent field reduction:

$$\Delta B = \frac{\varepsilon}{300 \times \beta}, \quad (1)$$

where ΔB is in kG, ε the electric field of the deflector in kV/cm and β v/c. The electric field is given by

$$\varepsilon = \frac{10^3}{c\rho_0} \times \frac{mv^2}{q} \times \frac{\Delta B}{B_0} \quad (2)$$

around the entrance of the deflector, where B_0 is magnetic field averaged azimuthally at a curvature of ρ_0 at the entrance of the deflector. If the field reduction ratio $\Delta B/B_0$ and the curvature are approximately constant, the electric field is proportional to mv^2/q . Figure 1 and Table 1 show dependence of the electric field at the entrance of the deflector on mv^2/q , which was obtained in practical operation. The electric fields are approximately proportional to mv^2/q . The electric fields are not corrected for positional dependence of the deflector on the magnetic field. The dashed line represents the electric field calculated by a linear fitting for the ions. There is an upper limit of the electric field in actual use in the cyclotron. The maximum electric field required for extracting 90 MeV protons is estimated around 200 kV/cm. The entrance of the deflector for 90 MeV protons should be located at an outer position in order to reduce the electric field. Actually the position for 90 MeV protons is outer than that for the

other ions. We have extracted 90 MeV protons with the electric field of 140 kV/cm which is 70 % of the predicted ones.

III. POSITION DEPENDENCE OF THE ELECTRIC FIELD

Dependence of the electric field on the entrance position of the deflector for 70 MeV protons by preliminary analysis is shown in Fig. 2. The electric fields are obtained by averaging the actual field at the entrance, mid and exit positions. The calculated electric fields are determined as follows; 1) positions and momentums at the entrance of the deflector are obtained by tracing a central particle from the exit of the inflector. 2) The gap and position of the electrodes are fixed to the actual ones. 3) The electric fields are determined so that the particle should reach the center position of the exit gap. The position dependence of the calculated electric field is consistent with the actual dependence. The calculated fields are, however, higher by around 5% than the actual ones. Precise analysis for the position dependence of the electric field is required.

Table 1. Dependence of the electric field at the entrance of the deflector on mv^2/q obtained in practical operation.

ε (kV/cm)	ion	$mv^2/2$ (MeV)	q	B(kG)	h
19	He	20	2	7	2
20	D	10	1	7	2
21	H	10	1	5	2
49	Ar	175	8	16	3
54	He	50	2	11	2
62	Kr	520	20	16	2
67	D	35	1	13	2
93	Ar	460	13	16	2
95	H	45	1	11	1
114	He	100	2	16	1
115	D	50	1	16	1
140	H	90	1	15	1
160	H	70	1	13	1

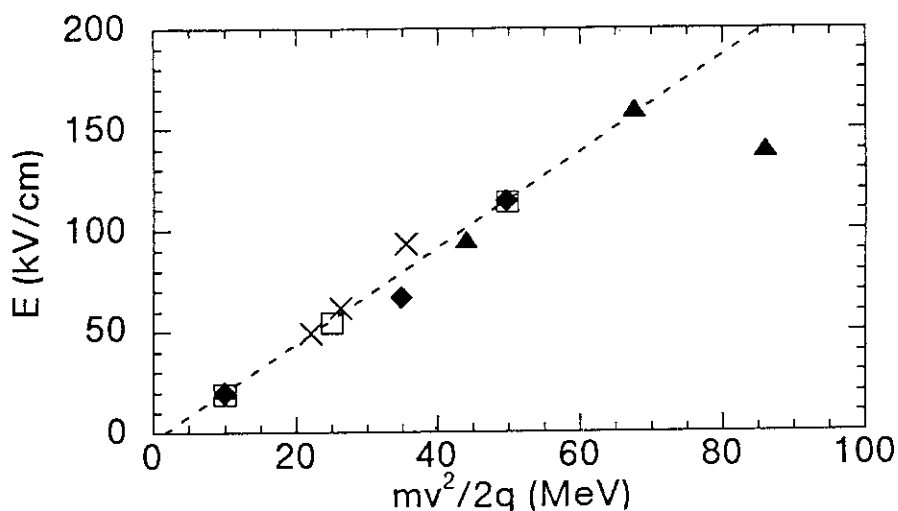


Fig. 1. Dependence of the electric field at the entrance of the deflector on mv^2/q obtained in practical operation. The measured electric fields are indicated by triangles for 10 MeV, 45 MeV, 70 MeV and 90 MeV protons, diamonds for 10 MeV, 35 MeV, and 50 MeV deuterons, squares for 20 MeV, 50 MeV and 100 MeV $^4\text{He}^{2+}$ and crosses for 175 MeV $^{40}\text{Ar}^{8+}$, 460 MeV $^{40}\text{Ar}^{13+}$ and 520 MeV $^{84}\text{Kr}^{20+}$. The electric fields obtained by a linear fitting for all but 90 MeV protons are represented by a dashed line.

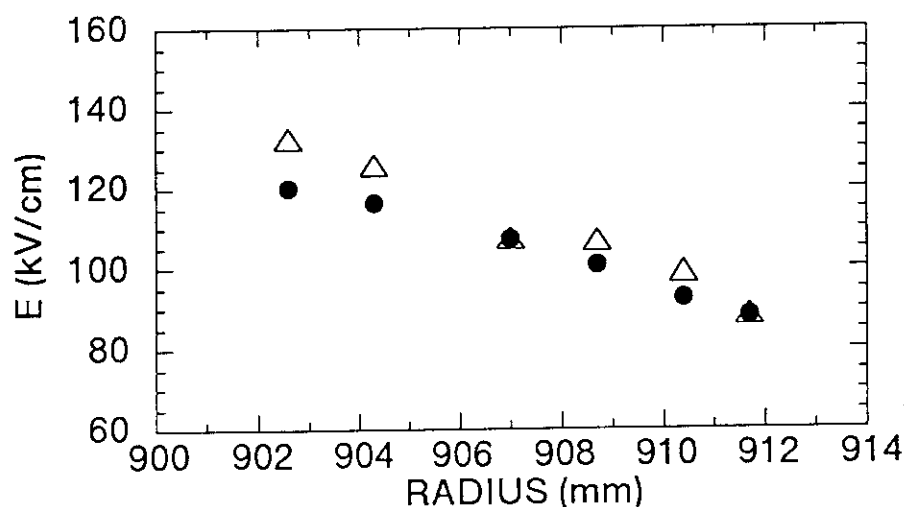


Fig. 2. Dependence of the mean electric field on the entrance position of the deflector for 70 MeV protons by preliminary analysis. The actual and calculated fields are indicated by circles and triangles, respectively.

8.8 ORBIT CALCULATION IN THE CENTRAL REGION

Mitsuhiro FUKUDA, Kazuo ARAKAWA, Yoshiteru NAKAMURA,
Watalu YOKOTA, Takayuki NARA, Takashi AGEMATSU,
Susumu OKUMURA, Ikuo ISHIBORI and Takashi KARASAWA

Department of Advanced Radiation Technology, JAERI

I. INTRODUCTION

In general orbit analysis using ideal isochronous field is carried out in designing a cyclotron. Beam behavior in practical operation, however, is less understood because actual magnetic field always does not correspond to the ideal isochronous field. Some beam diagnostics probes in an acceleration region provide us with rough information on the beam behavior. More precise analysis of beam dynamics is required for understanding the beam behavior and operating the cyclotron. In this work the orbit studies are focused on beam characteristics in the central region for 70 MeV protons.

II. BEAM TRAJECTORIES IN THE CENTRAL REGION

Harmonic numbers of 1, 2 and 3 are available for ions with mass to charge ratio up to 6.5. An inflector of the spiral type and a puller have been designed for each harmonic mode. Two sets of phase slits have been installed in the central region for defining the beam phases. Both of the slits are movable and have enough stroke to define the beam phases for the first turn. Trajectories of central particles simulated by a computer code

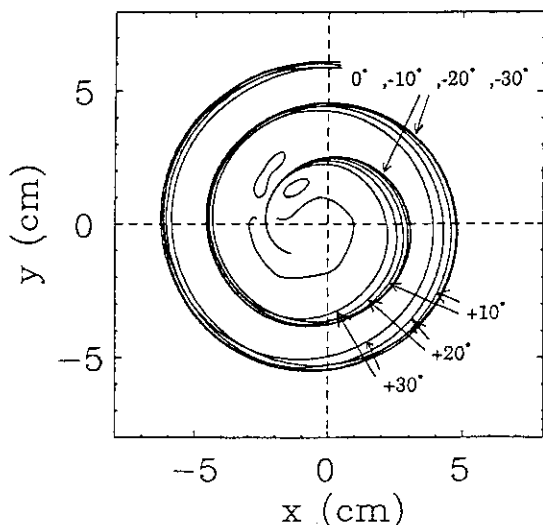


Fig. 1. Central trajectories of 70 MeV protons with injection phases of 0° , $\pm 10^\circ$, $\pm 20^\circ$ and $\pm 30^\circ$.

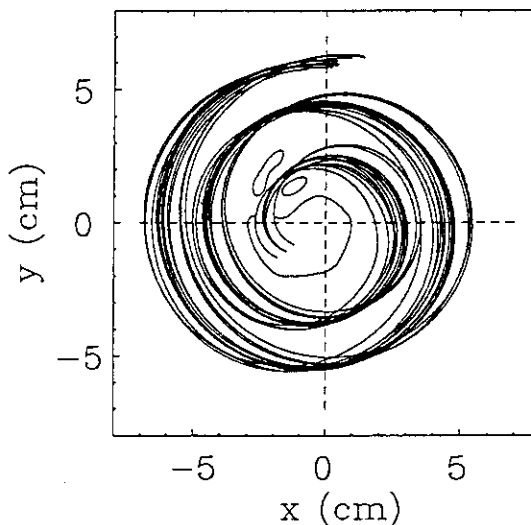


Fig. 2. Trajectories of the particles lying in orthogonal positions on the phase ellipse whose area is $4\text{mm} \times 50\text{mrad} \times \pi$ with injection phases of 0° , $+15^\circ$ and -15° .

for 70 MeV protons with injection phases of 0° , $\pm 10^\circ$, $\pm 20^\circ$ and $\pm 30^\circ$ are shown in Fig. 1. Without the phase defining slits, the central particles within an injection phase of $\pm 30^\circ$ can reach the entrance of the deflector. Turn numbers for the central particles with injection phases of -20° and -30° are, however, estimated to be more than those with the other phases by 100~200 turns. Figure 2 shows trajectories of the particles lying orthogonal positions on the phase ellipse of which the area is $4\text{mm} \times 50\text{mrad} \times \pi$ with injection phases of 0° , $+15^\circ$ and -15° . The beams are horizontally focused at the slit(I) position. An effective phase acceptance is $\pm 15^\circ$ for the slit(I) gap of 6mm.

III. ACCEPTANCE

Horizontal and vertical acceptances of the cyclotron for the injection phases of 0° are shown in Fig. 3. The acceptances in both directions are more than 300π mm·mrad, which covers injection beam emittances of 100π to 200π mm·mrad in the horizontal direction and 100π mm·mrad in the vertical direction. The calculated acceptances are defined as follows; horizontal and vertical deviations of particles are within a distance of ± 10 mm from the central particle up to a radius of 25 cm where the isochronous field starts.

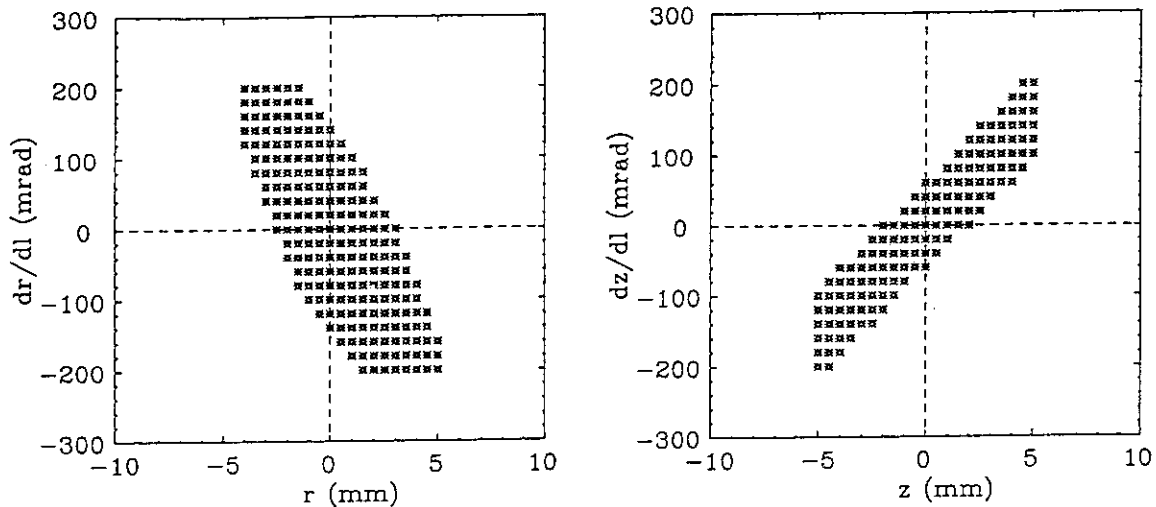


Fig. 3. Horizontal and vertical acceptances of the cyclotron for the injection phases of 0° .

8.9 STATUS OF ION SOURCES

Takayuki NARA, Watalu YOKOTA, Yoshiteru NAKAMURA, Mitsuhiro FUKUDA, Takashi AGEMATSU, Susumu OKUMURA, Ikuo ISHIBORI and Kazuo ARAKAWA

Department of Advanced Radiation Technology, JAERI

I. SOURCE OPERATION

Ion generation has been newly made for C^{5+} , Ne^{6+} , Ne^{7+} , $^{36}Ar^{8+}$, $^{36}Ar^{10+}$ by the ECR source from gases and accelerated by the cyclotron as listed in Table 1. For ions of ^{36}Ar , enriched gas was used. The total operating time for the ECR source in 1992 FY is 1831 hours, and 250 hours are allocated for metallic ion generation and beam characteristics measurement.

Two troubles occurred in the 14.3-GHz klystron power amplifier for the 1st stage. The one was a burst in a rubber tube in which forced air flowed to cool the klystron tube. The rubber deteriorated by strong heat. The other was an increase of an over body current of the tube. It occurred immediately after turning-on and RF power output was not obtained. The total operating time of the tube was about two thousand hours. The tube was replaced with a stored one. During the klystron amplifier was in trouble, the source was operated without the 1st stage RF power and ion beams were generated sufficiently for research experiments.

The multi-cusp ion source has been operated to generate H^+ . The life time of tungsten filaments depends on the operating condition, and is above two hundred hours for moderate operation with beam currents of around 100 μA . We tested a LaB₆ filament for the sake of longer lifetime. It can be operated with filament and emission currents comparable to those of tungsten filament. The arc plasma easily fired and H^+ beam of 40 μA was extracted. Further test will be carried out for higher current.

Table 1. Beam currents and transmission between the source and the cyclotron entrance.

ion	extraction voltage (kV)	beam current (e μ A)		trans- mission (%)
		ion source	cyclotron entrance	
$^4He^{2+}$	10.2	160	130	81
	8.5	240	206	86
	3.4	38	25	67
$^{12}C^{5+}$	14.3	3.0	2.4	80
$^{20}Ne^{6+}$	9.1	17	12.8	75
$^{20}Ne^{7+}$	11.7	4	3.3	82
$^{36}Ar^{8+}$	10.2	18.0	15.7	87
$^{36}Ar^{10+}$	8.2	9.0	7.7	86
$^{40}Ar^{8+}$	10.1	58	54.5	94
$^{40}Ar^{11+}$	9.4	3.0	2.8	93
$^{40}Ar^{13+}$	11.7	0.5	0.39	77
$^{84}Kr^{20+}$	8.8	0.4	0.33	83

II. METALLIC ION GENERATION BY ECR ION SOURCE

We tried to generate metal ions of aluminum (Al), molybdenum (Mo), and boron (B) by direct insertion of a rod into plasma. Rods of Al_2O_3 , Mo_2C and BN were inserted radially into the 2nd stage plasma by remotely controlled motor drive and could be positioned by 50 μm steps. Though the insertion depth has not been optimized, we observed ion beam currents enough for acceleration by the cyclotron as listed in Table 2. Beam currents of Al ions were stable and easily optimized. The Mo ion beam currents were less stable and the total currents of all the isotopes were comparable to that of Al. Ion beam of B were unstable and small compared with the other two metallic ions in spite of low charge state.

Vapor pressures of possible products from the solid or liquid phases of the examined materials are different by factor to some orders at high temperature. It was found that facility of ion generation and beam stability appeared strongly dependent on the vapor pressure difference of the products. Since vapor pressure can be estimated by thermodynamic calculation and we will be able to choose proper materials without ion generation test from now on.

Table 2. Maximum beam current of metallic ions.

material	support gas	ion	current($e\mu\text{A}$)
Al_2O_3	O_2	$^{27}\text{Al}^{8+}$	5
		$^{27}\text{Al}^{6+}$	17
		$^{27}\text{Al}^{4+}$	43
		$^{27}\text{Al}^{3+}$	62
Mo_2C^*	N_2	$^{98}\text{Mo}^{17+}$	5
		$^{98}\text{Mo}^{15+}$	6
		$^{98}\text{Mo}^{13+}$	7
		$^{98}\text{Mo}^{11+}$	2
		$^{98}\text{Mo}^{10+}$	4
		$^{98}\text{Mo}^{9+}$	4
BN	N_2	$^{11}\text{B}^{3+}$	5
		$^{11}\text{B}^{2+}$	5

* natural abundance of ^{98}Mo is 24%

Additionally we tried to generate B ion from LaB_6 of which the vapor pressure is fitted to the above selection criterion, and the obtained ion beam was very stable. The vapor pressures for BN are not fitted and this appears to give rise to an instability of B ion beams.

8 . 1 0 DEVELOPMENT OF BEAM ATTENUATOR

Susumu OKUMURA, Yoshiteru NAKAMURA, Watalu YOKOTA,
Mitsuhiro FUKUDA, Takayuki NARA, Takashi AGEMATSU,
Ikuo ISHIBORI and Kazuo ARAKAWA

Ion Accelerator Division, JAERI

The control of beam current over a very wide range is required frequently for experiments and beam adjustments in the cyclotron. The analysis of single-event upsets of integrated circuits requires extremely low beam current such as a few particles/second; on the other hand, the study of irradiation effect on materials requires several micro ampere or more.

A beam current has been controlled by adjusting parameters of the ion source. In this method, the beam quality such as the size or the emittance is not preserved, so that the time for adjusting the cyclotron parameter is additionally needed to recover the initial state as before. However, when adjusting beam current less than 1nA, the above parameter adjustment is impossible because beam monitors are not sensitive to such a low beam current.

To achieve quick control of the beam current over a wide range without parameter adjustment, we have developed beam attenuators. The beam attenuator can reduce the beam current by using a mesh restricting transmissible beam. The mesh is made of stainless steel with a thickness of about eighty micrometers. Holes of the mesh were pierced by chemical etching. We have prepared five different hole patterns as shown in Fig.1. A beam attenuator unit has two or three air-actuators to insert different meshes into the beam line.

Three beam attenuator units have been installed in the injection line of the cyclotron separately, as shown in Fig.2. It is designed that the beam current can be reduced by a factor of 1 to 10^{-9} depending on the combination of mesh insertion

REFERENCES

- 1) Y.Miyazawa, M.Hemmi, T.Chiba, and M.Kase, RIKEN Accel.Progr.Rep. 18 (1984) 197.

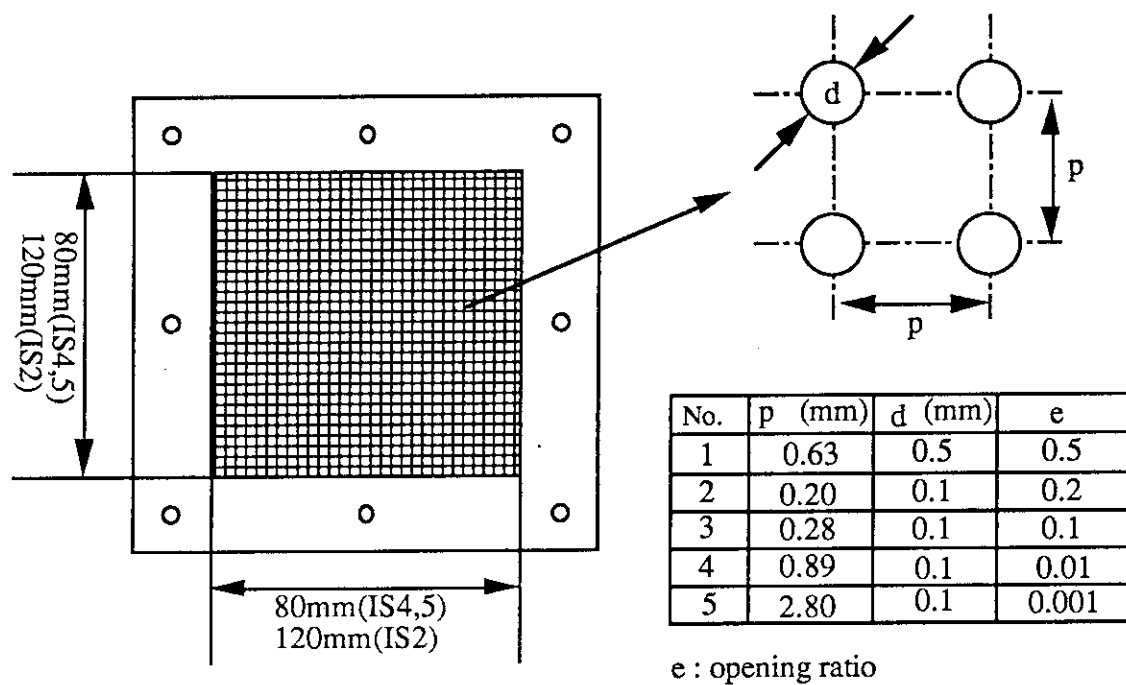


Fig. 1 Hole pattern of the mesh.

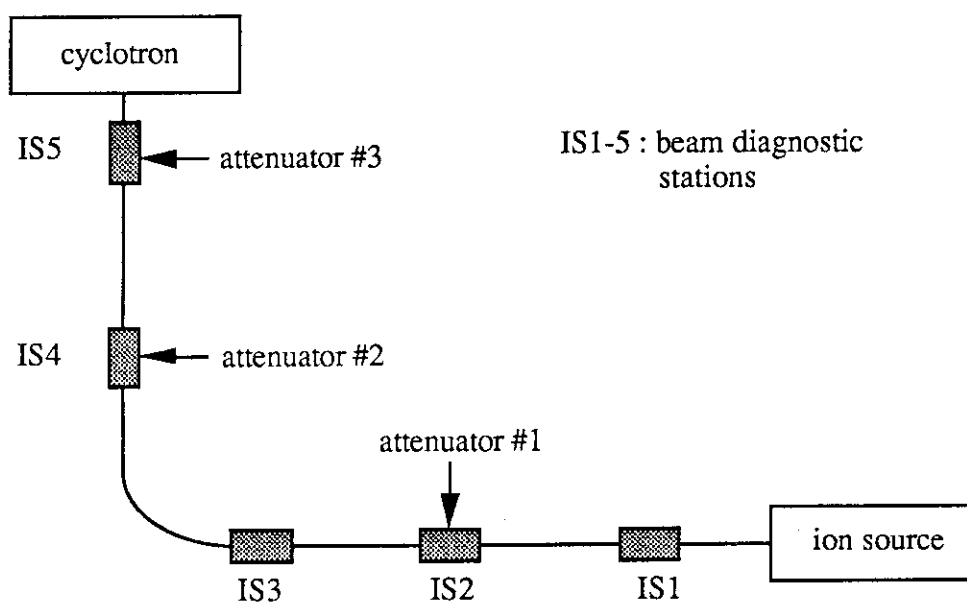


Fig. 2 Schematic layout of beam attenuators in the injection line.

8. 1. 1 DEVELOPMENT OF PARALLEL PLATE AVALANCHE COUNTER FOR FLUENCE-RATE MEASUREMENT

Susumu OKUMURA, Yoshiteru NAKAMURA, Watalu YOKOTA,
Mitsuhiro FUKUDA, Takayuki NARA, Takashi AGEMATSU,
Ikuro ISHIBORI and Kazuo ARAKAWA

Ion Accelerator Division, JAERI

Uniform and high-energy ion beam irradiation of a large area up to $100 \times 100 \text{ mm}^2$ by beam scanning is used for R&D on radiation resistant materials and semiconductor devices for space environment and nuclear fusion reactors and on biotechnology. The cyclotron beam is two-dimensionally scanned by using a pair of deflection electromagnets. The horizontal scanning frequency is 50 Hz and the vertical one is 0.5, 1.0, 2.5 and 5.0 Hz.

To ensure two-dimensional uniformity over an irradiated area, the measurement and monitoring technique of the fluence distribution has been developed. At the first place, cellulose-triacetate (CTA) film dosimeters¹⁾ was applied to the measurement as an integrated dosimetric method. However, it takes long time more than half a day to get the final result of the dose map giving relative fluence distribution and the dosimeter is not sensitive to the integrated dose or fluence. For these reasons, we started to develop a real-time fluence rate mapping system. This system is composed of a parallel plate avalanche counter (PPAC) for positional detection of passing particles and three beam attenuator units to reduce fluence-rate without change of relative fluence distribution. The reduction is required from the limitation of maximum counting rate which the PPAC can handle.

The PPAC is a kind of proportional counters with parallel plane electrodes. We have built a two-dimensional position sensitive PPAC²⁾. Figure 1 shows the configuration of the electrodes. One of the two cathodes is used for horizontal positional detection and the other for vertical one. The effective area is $120 \times 120 \text{ mm}^2$. The gap between the cathode and the anode is 4mm. The anode is a 4 micron thick mylar film, both sides of which were evaporated with a gold layer $40 \mu \text{ g/cm}^2$ thick. The cathodes are also 4 micron thick mylar films; the inner side of each evaporated with a gold layer $80 \mu \text{ g/cm}^2$ thick has 80 strips of 1.25 mm wide with 0.25 mm spacing. The strips are connected to each other by a register of 510 ohm. The positional information is given by the charge division method.

In a vacuum chamber connected with the cyclotron beam line, the PPAC is filled with isobutane gas circulating by a mass flow controller and an outlet valve at a pressure of 10 torr. The window foils (12-50 μm mylar) of the PPAC can contain the gas without any

support. The anode voltage is on the order of 700 V and the cathodes are grounded through high resistors.

The PPAC can be operated at a maximum counting rates of about 10^3 particles/s. However, the typical counting rate for irradiation experiments is more than 10^{10} particles/s. To attenuate the fluence rate without any change of the beam quality, we installed three beam attenuation units³⁾ in the injection line of the cyclotron. The units can control the beam current in an overall range of the attenuation ratio from 1 to 10^{-9} depending on the combination of meshes having uniformly spaced holes. Adjustment of attenuation units provides proper beam current for the measurement of the PPAC.

We are now planning to test the characteristics of the PPAC and to measure the fluence distribution irradiated by the cyclotron beam.

REFERENCES

- 1) H.Sunaga, T.Agematsu, R.Tanaka, K.Yoshida, and I.Kohno Radioisotopes 37(2) (1988) 83.
- 2) Y.Eyal and H.Stelzer, Nucl.Instr.and Meth. 155(1978) 157.
- 3) S.Okumura, Y.Nakamura, W.Yokota, M.Fukuda, T.Nara, T.Agematsu, I.Ishibori and K.Arakawa, in this report.

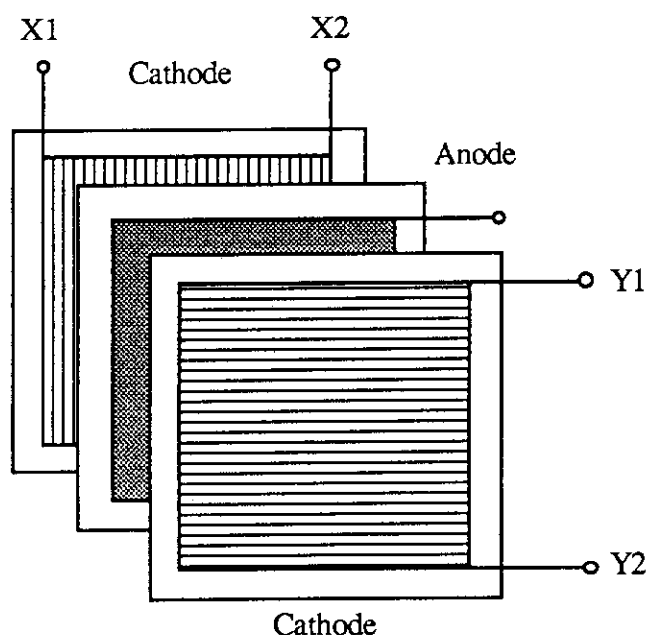


Fig. 1 Configuration of the electrodes in PPAC.

8.12

PERFORMANCE AND SOME OPERATION RESULTS OF THE
VACUUM SYSTEM FOR THE CYCLOTRON

Yoshiteru NAKAMURA, Ikuo ISHIBORI, Susumu OKUMURA,
Takayuki NARA, Watalu YOKOTA, Mitsuhiro FUKUDA,
Takashi AGEMATSU, Kazuo ARAKAWA and Toshihiro YOSHIDA*

Department of Advanced Radiation Technology, JAERI

* Beam Operation Co., Ltd.

I. OPERATION AND MAINTENANCE OF THE VACUUM SYSTEM

The vacuum system^{1),2)} of the JAERI AVF cyclotron has been operated steadily without any serious troubles since the starting of the evacuation in October 1990. We had a few minor typical troubles as follows; 1) the leakage of compressed air into the No. 2 resonator occurred at the copper pipe joint of the contact finger, 2) the leakage of open air also happened at the X-ring of the No. 2 phase slit, 3) some vacuum gauge controllers and fast closing gate valves became malfunction occasionally.

Eight cryogenic pumps (CRYO's) with pumping speeds of 1600 L/s and 4000 L/s were thoroughly overhauled after an operation time of 12000 h, with exchange of their charcoal adsorbers, disassembling and cleaning of the refrigerators. Operating oil and oil eliminators for rotary pumps were replaced with new ones, all the secondary batteries for magnetic suspended turbo molecular pumps (MSTMP's) were also exchanged.

Three portable evacuation systems equipped with Leybold 340M type MSTMP's were newly prepared for utilization as auxiliary evacuation systems for beam transport lines. The number of operations of all metal gate valves was around 100 times at the maximum with the exception of fast closing gate valves, while first maintenance check is recommended after 200 operations.

II. ESTIMATION OF PRESSURE DISTRIBUTION IN THE BEAM TRANSPORT
LINES

The beam transport lines with an overall length of 200 m are divided into 18 vacuum sections, which are designed for systematic vacuum control. We also considered effective location of the vacuum pumps so that the pressure distribution in the beam lines can be kept under the designed value of 3.4×10^{-5} Pa. From the basic calculation model as shown in Fig. 1, the differential pressure along the beam line is estimated by the equation,

$$dP / dx = \rho \{ q (L - x) + Q_0 + Q_L \},$$

where P is pressure (Pa), x the distance from the pump (m), ρ pumping resistance per unit length of the beam duct ($s/m^3 \cdot m$), q outgassing rate per unit length ($Pa \cdot m^3/s \cdot m$), L whole

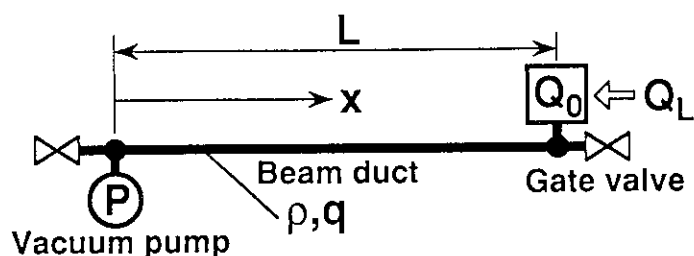


Fig. 1 A basic calculation model for pressure distribution in the beam transport line.

length of the beam duct (m), Q_0 outgassing rate in a beam diagnostic station ($\text{Pa}\cdot\text{m}^3/\text{s}$) and Q_L leakage rate from the diagnostic station ($\text{Pa}\cdot\text{m}^3/\text{s}$). Since the beam line is consisted of circular duct made of aluminum alloy A6063 of 104 mm in diameter, and the standard diagnostic station has one set of a pair of X and Y slits, a Faraday cup, a profile monitor and an alumina monitors, p is 7.35, q 2.17×10^{-8} and Q_0 3.8×10^{-7} . The value of Q_L can be neglected because it is regulated below $3.1 \times 10^{-10} \text{ Pa}\cdot\text{m}^3/\text{s}$ which is much less than the above Q_0 value.

The pressure distribution in a vacuum section including a rotary shutter³⁾ as a large outgassing source (outgassing rate: $1.2 \times 10^{-6} \text{ Pa}\cdot\text{m}^3/\text{s}$) can be given from a practical calculation model as shown in Fig. 2. As an example of the calculation, figure 3 shows the pressure distribution in the vacuum section "VLB0" along LB

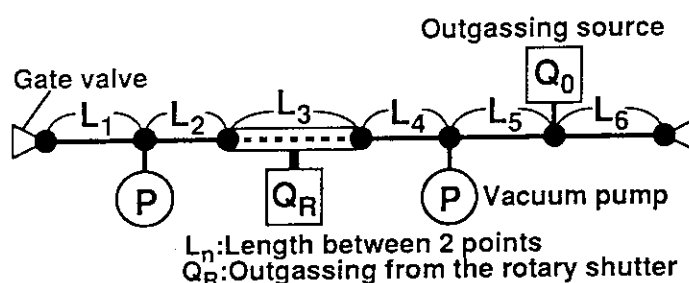


Fig. 2 A calculation model for the actual beam line.

course. The maximum pressure is $3.4 \times 10^{-5} \text{ Pa}$ at the center of the rotary shutter, though two

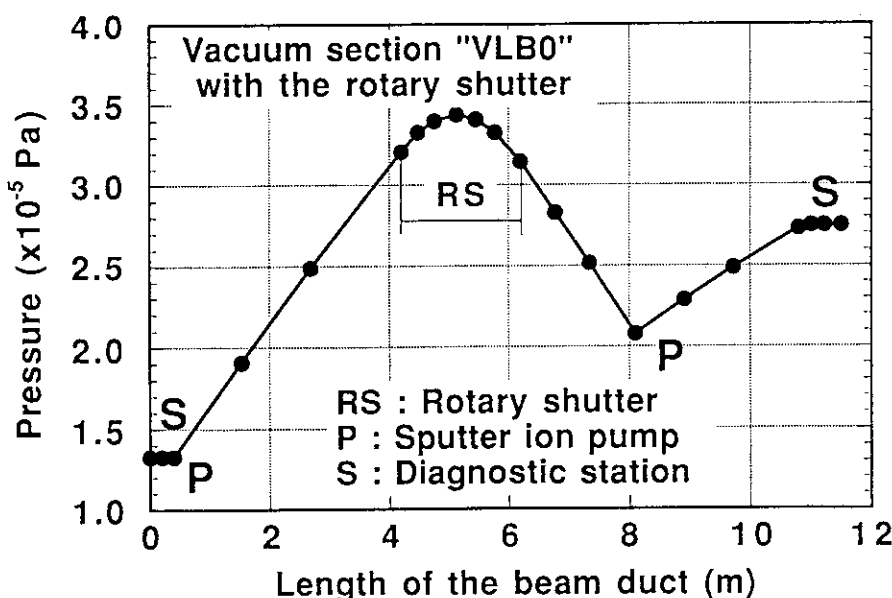


Fig. 3 An example of calculated pressure distribution in the vacuum section "VLB0" including the rotary shutter.

sputter ion pumps (SIP's) are positioned at both sides of the shutter. As a result of the calculation of internal pressure distribution, these pressures were evaluated within the designed value of $3.4 \times 10^{-5} \text{ Pa}$ for all the vacuum sections.

III. MEASUREMENT OF PUMPING CHARACTERISTICS

An example of measured results of evacuation curve for the cyclotron vacuum chamber is shown in Fig. 4. The MSTMP line was opened at 17 min after rotary pump operation, followed by two-decades pressure drop, and then four CRYO's were started. The temperature of the CRYO's panel usually drops below 15 K after 90 min operation. In this example, the CRYO's operation stopped for 3.5 h because of a trouble of the vacuum gauge controller. However, the pressure reached about 1×10^{-4} Pa 20 h later, a steady state of the pressure around 1×10^{-5} Pa was achieved at 300 h through several cyclotron operations.

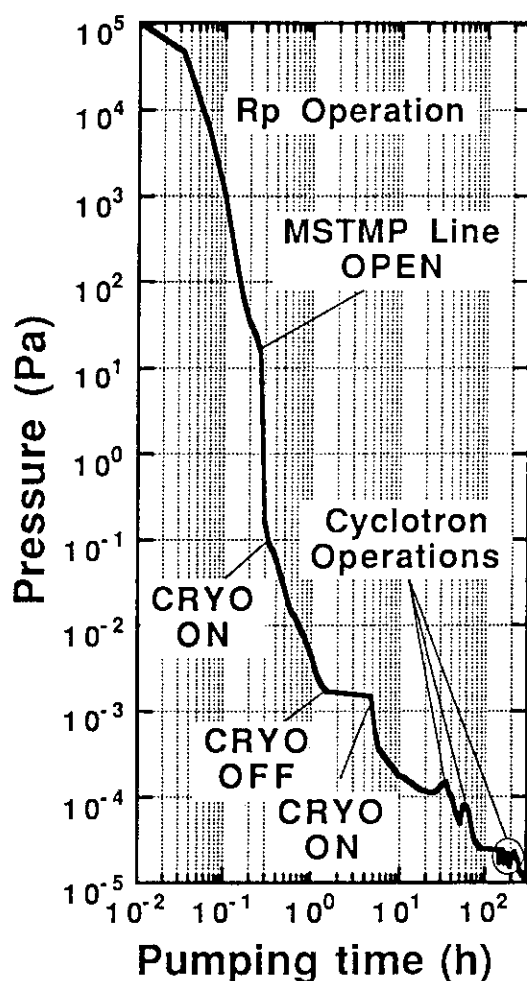


Fig. 4 An example of evacuation curve of the cyclotron vacuum chamber.

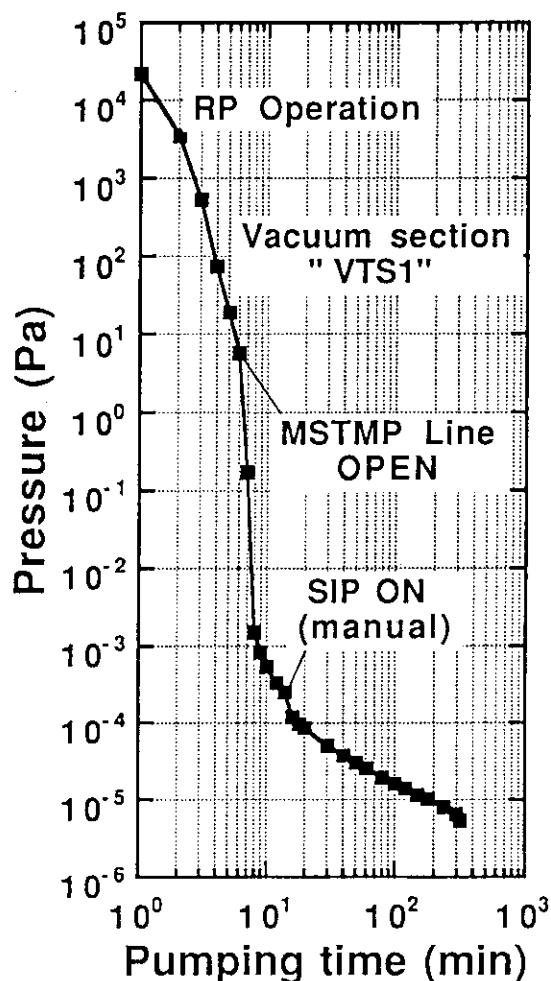


Fig. 5 An evacuation curve of the vacuum section "VTS1" in the beam transport line.

Figure 5 shows a measured result of the vacuum section "VTS1" including the 80 degrees analyzing magnet in the beam transport line. Two MSTMP's lines were opened 6 min after evacuation start, continued by the rapid decrease to 5.4×10^{-4} Pa. Two SIP's were manually driven at 14 min and the pressure gradually decreased to 7×10^{-5} Pa at 5 h. This evacuation ability is excellent because the elapsed time from atmospheric pressure to designed one is required within 8 h.

IV. RESIDUAL GAS ANALYSIS

The measurement of the residual gas in the vacuum chamber with good condition is necessary for the detection of the vacuum troubles. Figure 6 shows a spectrum of residual gas at the total pressure of 1.4×10^{-5} Pa measured by a quadrupole mass analyzer of MSQ-150A type with the resolution of $M/e=150$. Typical peaks of OH^+ ($M/e=17$) and H_2O^+ ($M/e=18$) were observed, and many small peaks in hydrocarbons also appeared, these seem to come from lubrication oil or grease.

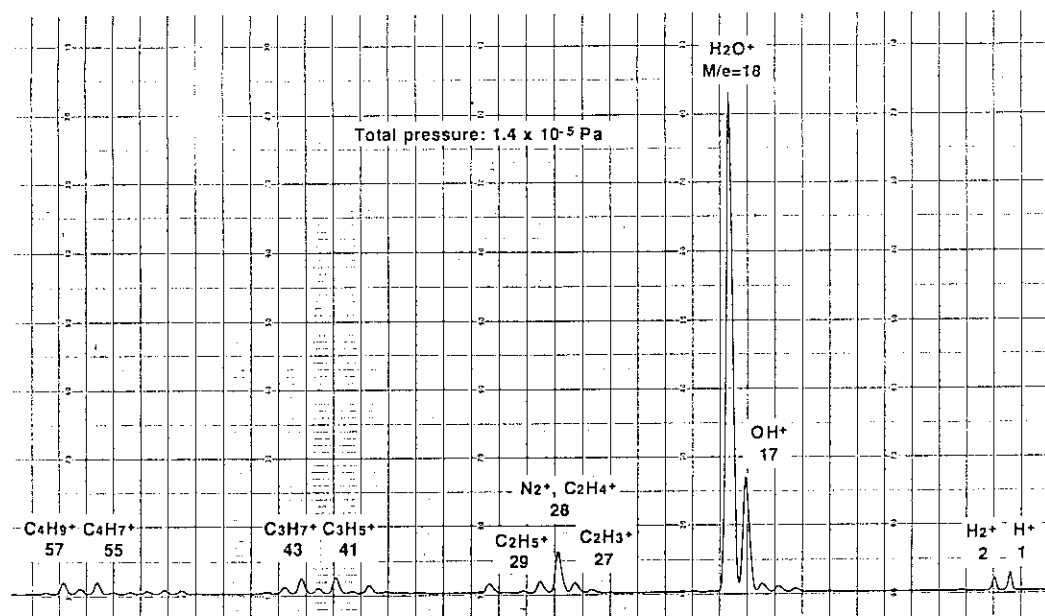


Fig. 6 A residual gas spectrum in the cyclotron vacuum chamber at a steady state pressure of 1.4×10^{-5} Pa.

V. PRESENT STATUS

The pressure in the cyclotron vacuum chamber reaches about 7×10^{-6} Pa in a good condition. The pressure has been maintained to $5-8 \times 10^{-6}$ Pa in the ion injection line, and ranged from 6×10^{-6} to 7×10^{-5} Pa in the majority of 18 vacuum sections of the beam transport lines. However, those pressures in several vacuum sections including the rotary shutters are higher than the designed value of 3.4×10^{-5} Pa, because of the large outgassing from the shutters.

REFERENCES

- 1) Y. Nakamura, K. Arakawa *et al.*, Proc. 8th Symp. Accel. Technol., Saitama, Japan (1991) pp.194-196
- 2) A. Arakawa, Y. Nakamura *et al.*, "1. AVF Cyclotron" in JAERI-M 93-047 (JAERI TIARA Annual Report vol. 1) (1992) pp.34-39
- 3) S. Tanaka, Y. Nakamura and H. Watanabe, Proceedings of "Fall Meeting of the Atomic Energy Society of Japan", M55 (1991) p.807

8.13 RADIATION RESISTANCE OF ELECTRONIC CONTROLLER

Watalu YOKOTA, Yoshiteru NAKAMURA, Kazuo ARAKAWA and Takashi AGEMATSU

Department of Advanced Radiation Technology, JAERI

I. INTRODUCTION

A number of electronic controllers are used in the cyclotron system, and various kinds of semiconductor components in them are sensitive to ionizing radiations. The JAERI cyclotron system has several area with high dose-rate radiation level around the cyclotron and the beam lines during and after operation. Some of the controllers cannot be installed away from the radiation area or shielded from radiation. For this reason, we need information about evaluation and prediction of the radiation resistance or the life time of the controllers. The radiation resistance of semiconductor components has been studied so far, mainly for use in space environments. On the other hand, that for accelerator facilities or the resistance of electronic circuits have been scarcely examined except for electron-positron collider facility³⁾. We tested a vacuum gauge controller by using ^{60}Co γ -rays and single board computers UDC (Universal Device Controller), interface for cyclotron devices, by using ^{60}Co γ -rays and high energy neutrons. In addition, integrated doses of γ -rays and neutron secondarily produced by ion beams were measured at several points around the cyclotron for the evaluation of the controller's life time.

II. UDC AND VACUUM GAUGE CONTROLLER

A UDC is a 8-bit single board computer constructing the bottom of triple layers in the hierarchical control system and makes specific control of each device. The total number of the UDC's is about 420, and some of them have to be installed close to the devices in radiation environment. The semiconductor components in a UDC are summarized in Table 1. The software is programmed in two EPROM's. All the I/O lines are electrically insulated by photo couplers driven by logic IC's.

The vacuum gauge controller is of BALZERS TPG-300. The main semiconductor components are a CPU, a SRAM and an EPROM.

Table 1 Semiconductor components of a UDC.

CPU	i8344	1
EPROM	128k	1
	256k	1
SRAM	256k	1
Transistor Array		41
Keyboard Controller		7
Logic IC		28
Photo coupler		25

III. IRRADIATION AND RESULT

The ^{60}Co γ -ray irradiation was carried out at a gamma-ray facility at JAERI, Takasaki. Eleven UDC's were irradiated and each was connected with a personal computer (PC) through an optical fiber. Monitoring processes run in the UDC's to check memory data and I/O status, being triggered by the commands from the PC every twenty minutes. The irradiation was continued until the UDC's completely broke down at a dose rate of 0.88 Gy/h (Si). The off-line check was also made a few months after the irradiation. The vacuum controller was also irradiated by ^{60}Co γ -ray until it was functionally disordered at a dose rate of 8.4 Gy/h (Si).

Seven UDC's were irradiated by 14-MeV neutron at the FNS (Fusion Neutronic Source) facility⁴⁾ at JAERI, Tokai. The fluence ranged from 1.3×10^{12} (equivalent to 4.8×10^2 Gy (Si)) to 1.6×10^{13} n/cm² (40 Gy) by varying the distance from the source to the UDC's. The off-line check was made after three months, when the neutron induced radioactivation of the UDC's cooled down.

In the on-line check of UDC during the γ -ray irradiation, the first error was observed at 44 Gy (Si) on an average. Some errors were attributed to those of photo couplers. However, no disorder was found by the off-line check. The radiation damage might be recovered by annealing after irradiation. The other errors were caused by breakdown of the EPROM and the SRAM, and the data in memories were partly changed or completely erased. In the case of neutron irradiation, all the photo couplers of single transistor type were broken and some of Darlington photo transistor type exposed at the lowest fluence were alive. Several errors might be caused by failures of the logic IC's driving the photo couplers, but could not be discriminated from those alone by the photo coupler failures. The critical dose for the UDC's is roughly estimated at 40 Gy (Si) or less and there is no appreciable difference of the doses between γ -rays and neutrons.

The vacuum controller was functionally disordered at 97 Gy (Si) and the dose was roughly equal to that for UDC's. Though the broken part was not assigned, the failure of the EPROM and the SRAM is suspected in the same manner as the UDC's.

IV. MEASUREMENT OF ACCUMULATED DOSE

The integrated absorbed doses accumulated at a number of points in the cyclotron vault and the switching magnet room were measured by using alanine dosimeter⁵⁾. The dosimeters were exposed to a mixed radiation of γ -ray and neutrons, and the contribution of neutrons to the integrated dose is estimated at about 95 %. The absorbed dose in alanine dosimeters is approximately evaluated from a dose-response curve for ^{60}Co γ -rays, since the dosimeter sensitivity to neutron is about 0.55 times that to ^{60}Co γ -rays on the average over the energy range of 1 to 15 MeV⁶⁾.

Figure 1 shows the measured value of doses accumulated for 17 months, from March 12 in 1991 to August 19 in 1992. The dose was 1.3×10^3 Gy (Si) at the beam diagnostic station TS1 where the beams were often stopped and monitored for the cyclotron adjustment, 2.3×10^2 Gy (Si) near the deflector trolley, and 3.7 to 6.5 Gy (Si) at the shielding wall surface. The critical doses of UDC's and the vacuum gauge controller is about ten times the observed dose at the wall surface.

The authors are thankful to Mr. K. Hoshika of Sumitomo Heavy Industries, Ltd. for his preparation and off-line check of the UDC's. They thank Mr. T.Kojima for his evaluation of dose absorbed in alanine dosimeters.

REFERENCES

- 1) K.Marks and P. Measel, IEEE Trans. Nucl. Sci., NS-29, No.6(1982) 1662
- 2) D. Schiff et al., IEEE Trans. Nucl. Sci., NS-32, No6(1985) 4050
- 3) S.Battisti et al., Nucl. Instr. and Method, 136 (1976) 451
- 4) T.Nakamura et al., Proc. of 3rd IAEA Technical Committee Mtg. and Workshop on Fusion Reactor Design and Technology, II, (1982) 65
- 5) T. Kojima, R. Tanaka, Radioisotopes, 41, No.6(1992)pp.28.38
- 6) H. Schraube et al., Appl. Radiat. Isot., 40, No.10-12(1989)pp.941-944

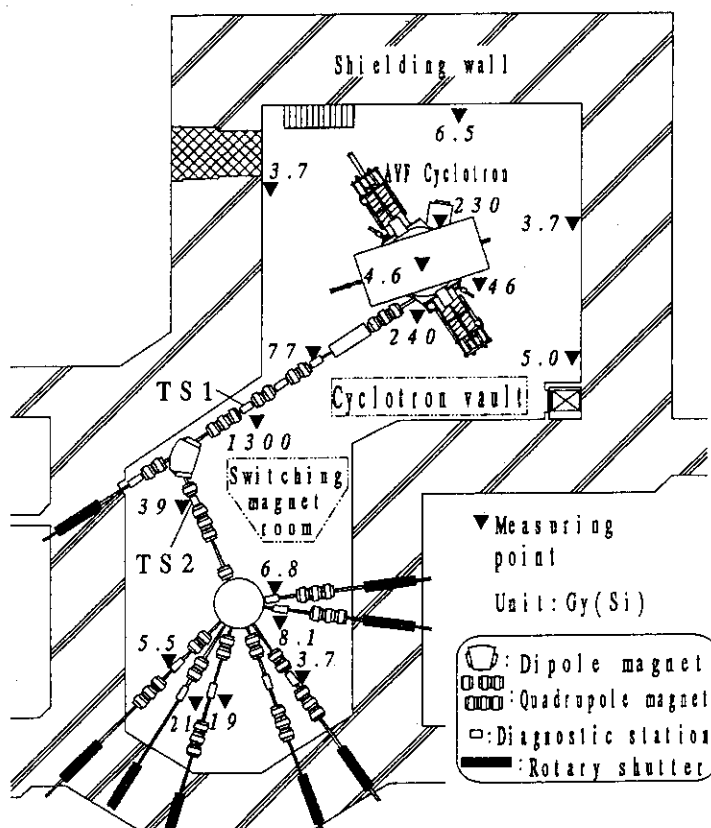


Fig. 1 Accumulated dose for 17 months around the cyclotron.

8.14 SOME TRIALS FOR EFFECTIVE OPERATION OF NEGATIVE ION SOURCES FOR TANDEM ACCELERATOR

Yuichi SAITOH, Satoshi TAJIMA, Isao TAKADA, Kiyoshi MIZUHASHI

Department of Advanced Radiation Technology, JAERI

Two negative ion sources connected with the 3 MV tandem accelerator have been operated since 1991. The one is a charge exchanging RF ion source (NEC; Alphasross) exclusively for negative helium ions, and the other a cesium sputter ion source (NEC; SNICS) for various ion species. We have made an effort to find operating conditions to effectively increase ion beam current from the SNICS, and also find the conditioning method of the Alphasross to quickly attain stable operation after maintenance.

The characteristics of the SNICS was examined in different physical conditions of sputter cathodes made from the materials of interest.

The effects of hardness and shape of the cathodes were tested for three different samples made from nickel powder; the first one is pressed by 50 kg/cm² (soft), the second one 200 kg/cm² (hard), and the third one is the soft cathode with a drilled hole in 1.5 mm diameter and 2 mm deep. The results are shown in Fig. 1. The initial current for the soft cathode was almost the same as the hard one, and exceeded the hard one after fifteen hours operation. It comes from growth of a conical depression

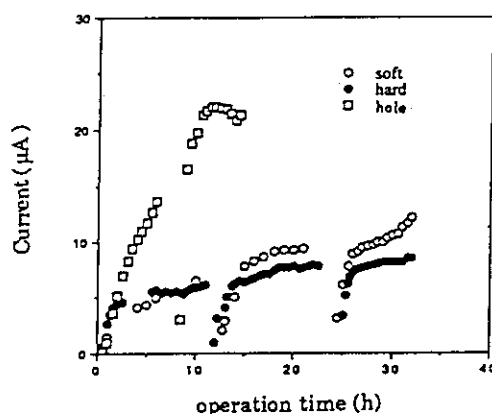


Fig. 1. Ion beam current with respect to operation time in different physical conditions of the sputter cathode.

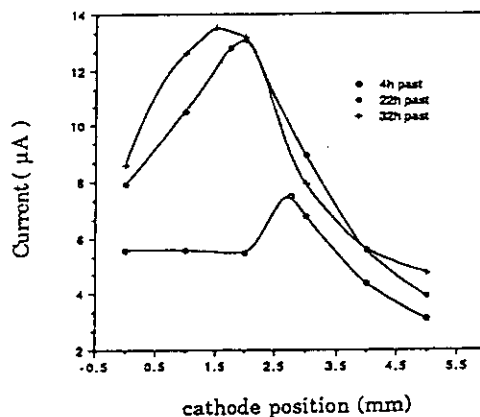


Fig. 2. Ion beam current for the hard cathode in each operating time as functions of cathode position

caused by cesium sputtering at the top of the cathode. The depth of the soft one was deeper than the hard one after the thirty hours operation. The current for the predrilled cathode increased more quickly than the others. This can be explained that the hole makes the beam emittance better.

The influence of geometrical position of the above three cathodes was examined to measure the beam current for various cathode positions in the ion chamber. The result of the hard cathode is shown in Fig. 2, in which the deepest position inside the chamber is defined at 0 mm. It was obvious that the optimum position of the cathode giving the maximum beam current shifted inside with time. The shifting distance corresponded to the depth of the depression made by sputtering. It indicates that there exists a optimum position of the cathode, and the variation of the beam current results from the displacement of the cathode surface caused by the sputtering from the optimum point. It is recommended to adjust the position after about ten hours operation to keep the maximum beam current.

In operation of Alphasross, the probe voltage and current got unstable after the first maintenance and cleaning, as shown in Fig. 3, and did not recover the normal operation for eighty hours. However they were improved by twelve hours operation without rubidium vapor (sleep operation). The improved result is shown in Fig. 4. We supposed that some electrodes in the vacuum chamber were contaminated by Rubidium vapor immediately after the cleaning, and heat given by the sleep operation cleaned the electrode.

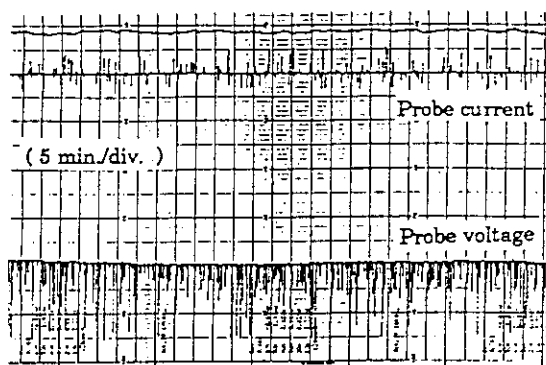


Fig. 3. The probe voltage and current under unstable condition

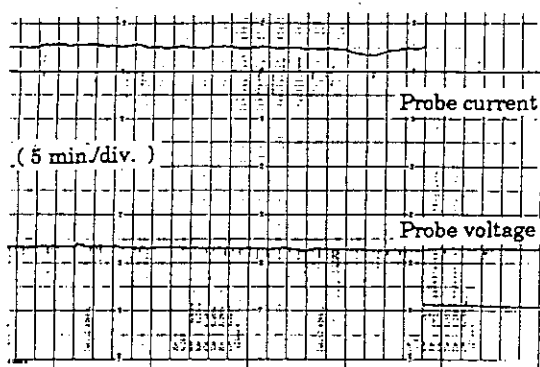


Fig. 4 The probe voltage and current after the sleep operation

9. Buildings and Safety Systems in TIARA Facilities

9.1	Design and Construction of TIARA Facilities	
	H.Watanabe, S.Tanaka, K.Nishimura, I.Takada, Y.Nakamura, K.Mizuhashi, N.Ohnuma, N.Akiyama and M.Maruyama	211
9.2	Radiation Monitoring System in TIARA Facility	
	Y.Nakamura, K.Satoh, K.Nishimura, I.Takada, Y.Iwaya, H.Nonouchi, T.Sasaki and H.Watanabe	221
9.3	Safety Interlock and Display Systems for Cyclotron Facility	
	Y.Nakamura, H.Watanabe, S.Tanaka, T.Agematsu, K.Nishimura and A.Daigo	227
9.4	Personal Access Control System in TIARA	
	K.Nishimura, K.Mizuhashi, A.Iijima and H.Watanabe	232

9.1 DESIGN AND CONSTRUCTION OF TIARA FACILITIES

Hiromasa WATANABE, Susumu TANAKA, Koichi NISHIMURA, Isao TAKADA, Yoshiteru NAKAMURA, Kiyoshi MIZUHASHI, Naoyoshi OHNUMA¹, Nobuyoshi AKIYAMA², and Michio MARUYAMA³

Department of Advanced Radiation Technology, JAERI, ¹JGC Corp.,

²Retired, and ³Beam Operation Co., Ltd.

1. INTRODUCTION

The Takasaki Radiation Chemistry Research Establishment of JAERI has conducted R & D activities for application of gamma-rays and electron beams, and the fruitful results are now widely applied in industrial fields. Considering such circumstances, JAERI has started a new R & D project using ion beams, called Advanced Radiation Technology (ART) project. The idea of the ART project is based on the fact that the application of ion beams is developing into effective means for research not only in fundamental physics but also in many other fields. The project is intended to make use of the characteristics of ion beam in R & D on materials for space and nuclear fusion reactors, new functional materials and biotechnology as described below.

R & D on Materials in Space Environment: For semiconductor devices requiring high reliability for use in telecommunication artificial satellites, priorities are given to those studies as relate to aged deterioration (total dose effects) induced by protons and electrons in space as well as the mechanism of single event effects due to high energy heavy ions, that is required to be clarified urgently. Thus, technologies for upgrading current methods for evaluating anti-radiation characteristics of semiconductor devices for space use together with improvements in radiation resistance are to be developed. Studies will also be undertaken on the space environment resistance of carbon fiber reinforced plastics which is important as the structural materials for artificial satellite.

R & D on Materials for Nuclear Fusion Reactor: For inorganic metal materials used as structural materials for plasma container and as tritium breeder as well as organic composite materials used in super conducting magnets, high energy neutron induced deterioration in the nuclear fusion reactor environment will be assessed by ion beam irradiation and thereby contributing to the progress in the efficient development of relevant materials.

Research on Biotechnology: Cell remodeling technology utilizing excellent controllabilities of ion beams will be developed. Efforts will also be focused on creation of new gene resources by utilizing characteristics of ion beams in terms of high mutation rate than that of X-rays and gamma-rays. In addition, a variety of studies will be conducted

Table 1. Construction program of TIARA facilities scheduled in 1986.

ITEM \ FISCAL YEAR	1986	1987	1988	1989	1990	1991	1992	1993	1994
Buildings	Concept Design	Planning	Construction			(2nd Stage) Construction			
Ion Accelerators			(1st Stage)						
Cyclotron	Concept Design		Manufacturing			Operation			
Tandem Accelerator			Manufacturing			Operation			
Single-ended Accelerator						Manufacturing	Operation		
Ion Implanter						Manufacturing	Operation		
Experimental Apparatus			Manufacturing			(2nd Stage) Manufacturing			
			(1st Stage)						
Research			Research on Ion Beam Technology						
						Research by using Accelerators			

including; studies on chemical reaction induced by heavy ions, research on bionics materials for effective utilization of bio-active materials, and studies of the production of short-lived radioisotopes and synthesis of new labelled compounds useful for medical, agricultural and environmental studies.

Research on New Functional Materials: Researches on creation and modification of materials by application of ions such as implantation and on mechanism of the acquiring functionality will be carried on by tracing material production process through in-situ analysis. Research will also be conducted on advanced analysis technique with ion beams as a probe to meet the needs in the course of the study.

As shown in Table 1, a 6-year construction program of the ion irradiation facilities (TIARA: Takasaki Ion Accelerators for Advanced Radiation Application) was projected to promote the ART project. The construction was scheduled in two stages, the first stage from 1987 to 1990 and the second stage from 1991 to 1992.

2. OUTLINE OF TIARA FACILITIES

2.1 Ion Accelerators

Four ion accelerators have been installed in TIARA, AVF cyclotron completed in October, 1991, 3MV tandem accelerator in June, 1991, 3MV single-ended accelerator and 400kV ion implanter in August, 1993. The main characteristics of the accelerators are shown in Table 2. Details of the cyclotron and tandem accelerator were described in the first annual report^{1,2)} and those of new accelerators will be described in the next annual report.

Table 2. Performances and Characteristics of the ion accelerators in TIARA

Ion Accelerators	Ion particle	Energy (MeV)	Current (μ A)	Characteristics in Beam Use
AVF Cyclotron	H	5 to 90	30	Uniform irradiation in wide area Pulse irradiation Vertical irradiation Secondary neutron utilization
	He	10 to 108	20	
	Ar	100 to 530	2	
	Kr	210 to 520	0.1	
3MV Tandem Accelerator	H	0.8 to 6	5	Microbeam utilization Complex use with other accelerators
	C	0.8 to 15	10	
	Ni	3 to 18	5	
	Au	3 to 18	15	
3MV Single ended Accelerator	H	0.4 to 3	100	Microbeam utilization Complex use with other accelerators Electron generation
	D	0.4 to 3	70	
	He	0.4 to 3	70	
	e ⁻	0.4 to 3	50	
400 kV Ion Implanter	B	0.01 to 0.4	30	Complex use with other accelerators
	P	0.01 to 0.4	30	
	Se	0.01 to 0.4	15	

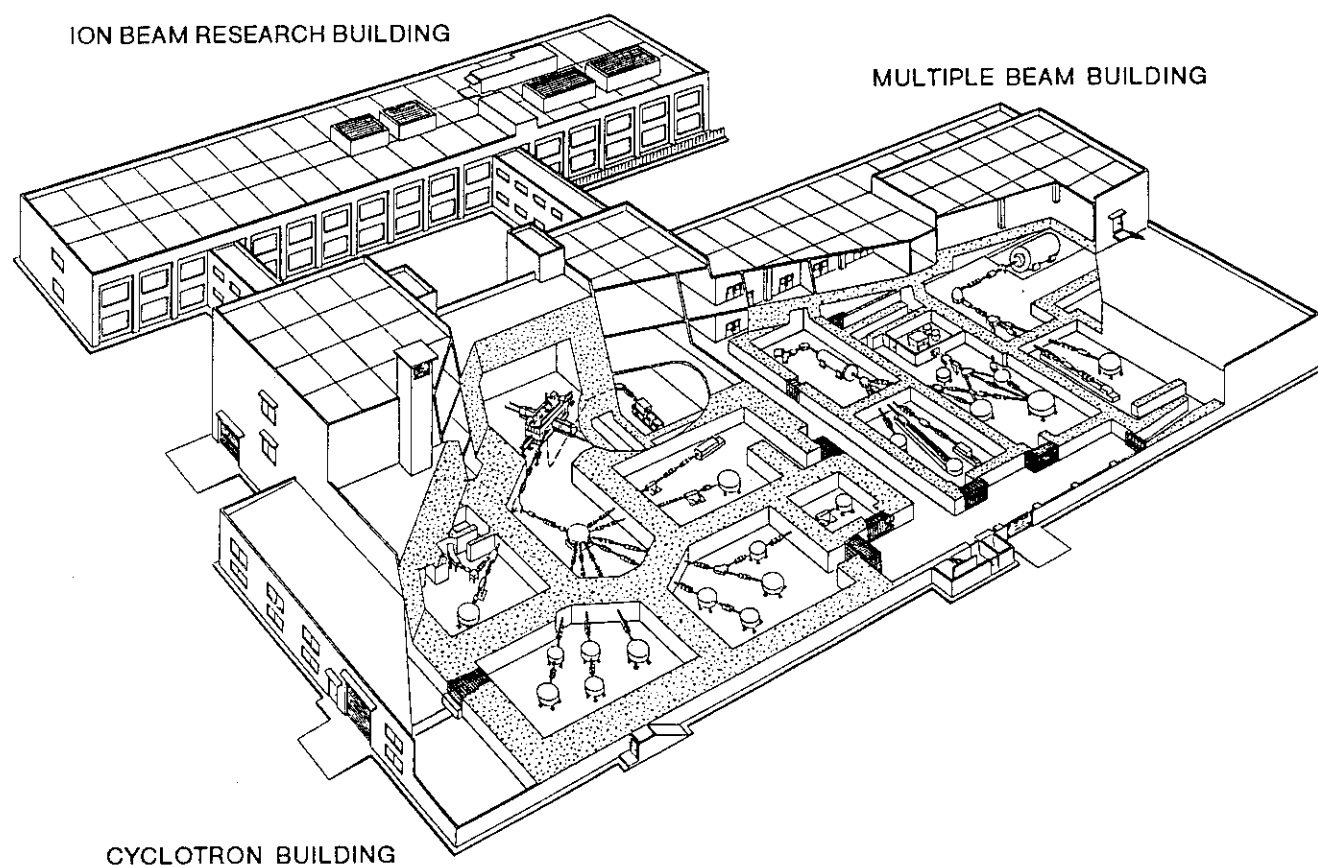
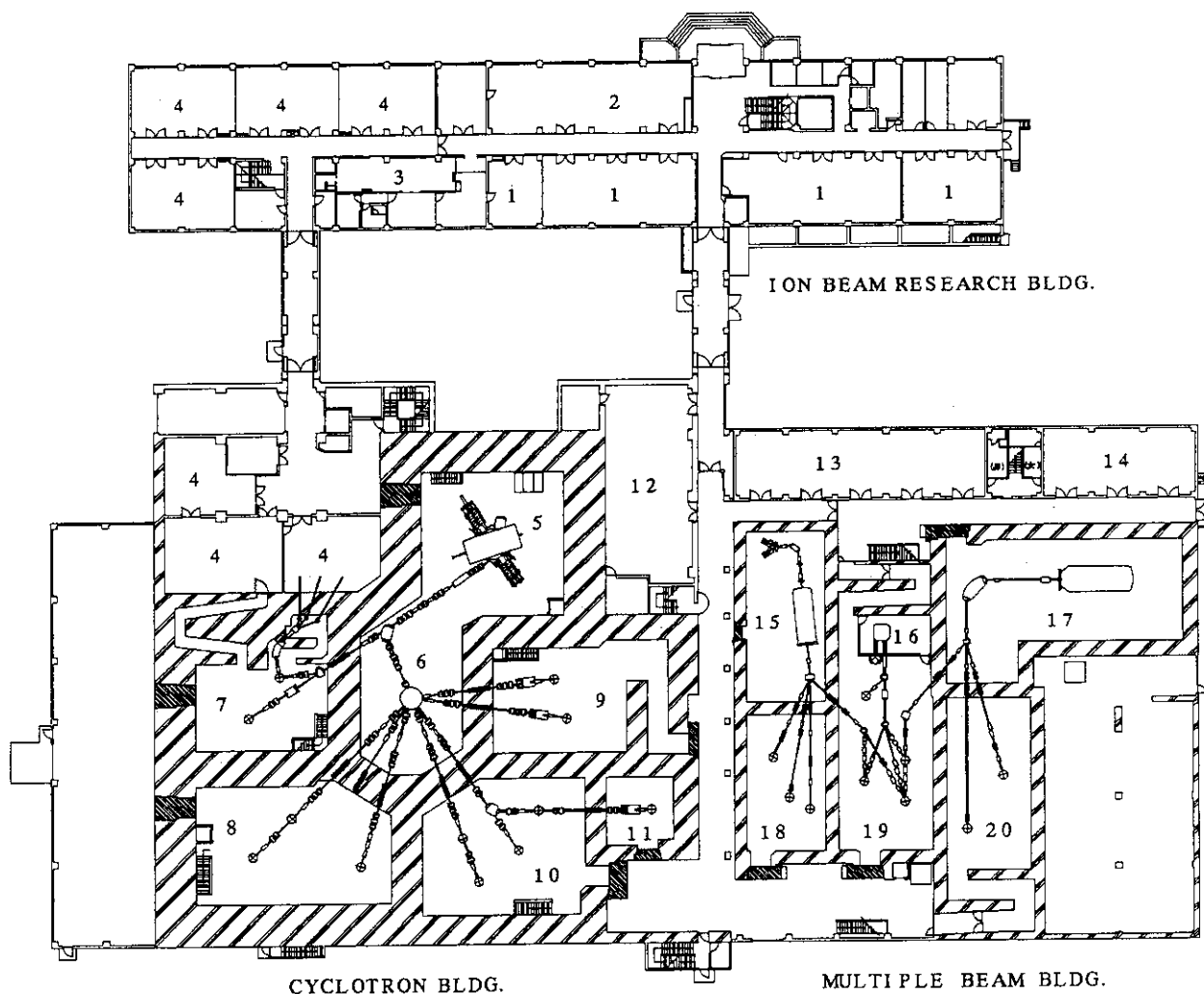


Fig. 1. A Bird's-eye view of TIARA facilities

2.2 Buildings

There are three buildings in TIARA, cyclotron building, multiple beam building, and ion beam research building, all which are of independent structure. As shown in Fig. 1, the cyclotron building and the multiple beam building are neighboring each other, while the ion beam research building is connected to the cyclotron building by two passages. They are combined functionally as a whole.

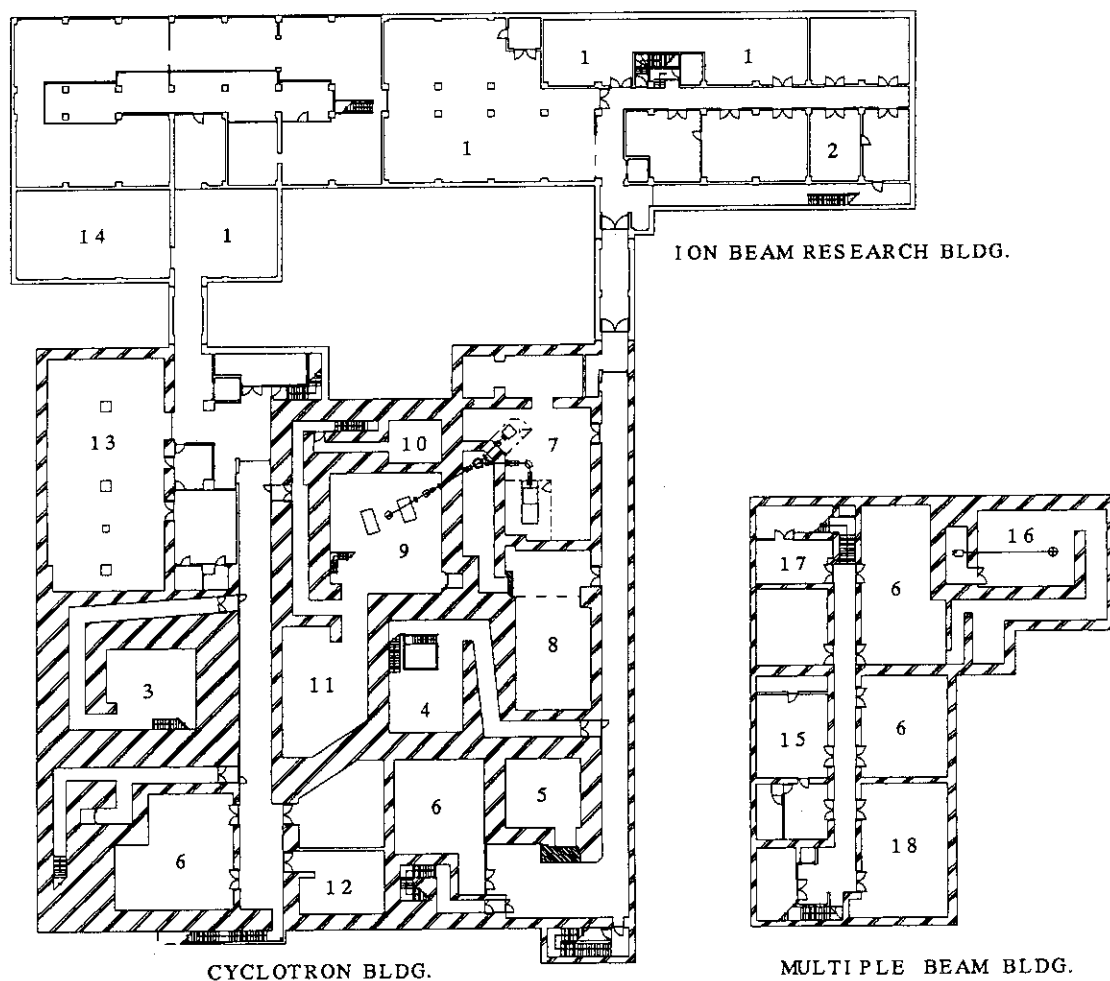
The cyclotron building of reinforced concrete and about 8,100 m² in total floor area from basement to upstairs was constructed for utilization of high energy ion beam from the cyclotron. In the first floor, there are a cyclotron vault, a switching magnet room where ion beams are bent into desired beam courses, and target rooms of two for light ions and three for



1; offices, 2; cyclotron control room, 3; change room, 4; hot-laboratories, 5; cyclotron vault, 6; switching magnet room, 7; light ion room 1, 8; light ion room 3, 9; heavy ion room 1, 10; heavy ion room 3, 11; heavy ion room 4, 12; power supply room for cyclotron, 13; control room for electrostatic accelerators, 14; ion source conditioning room, 15; tandem accelerator room, 16; ion implanter room, 17; single-ended accelerator room, 18; target room 1, 19; target room 2, 20; target room 3.

Fig. 2. A plane figure of first floor in TIARA buildings.

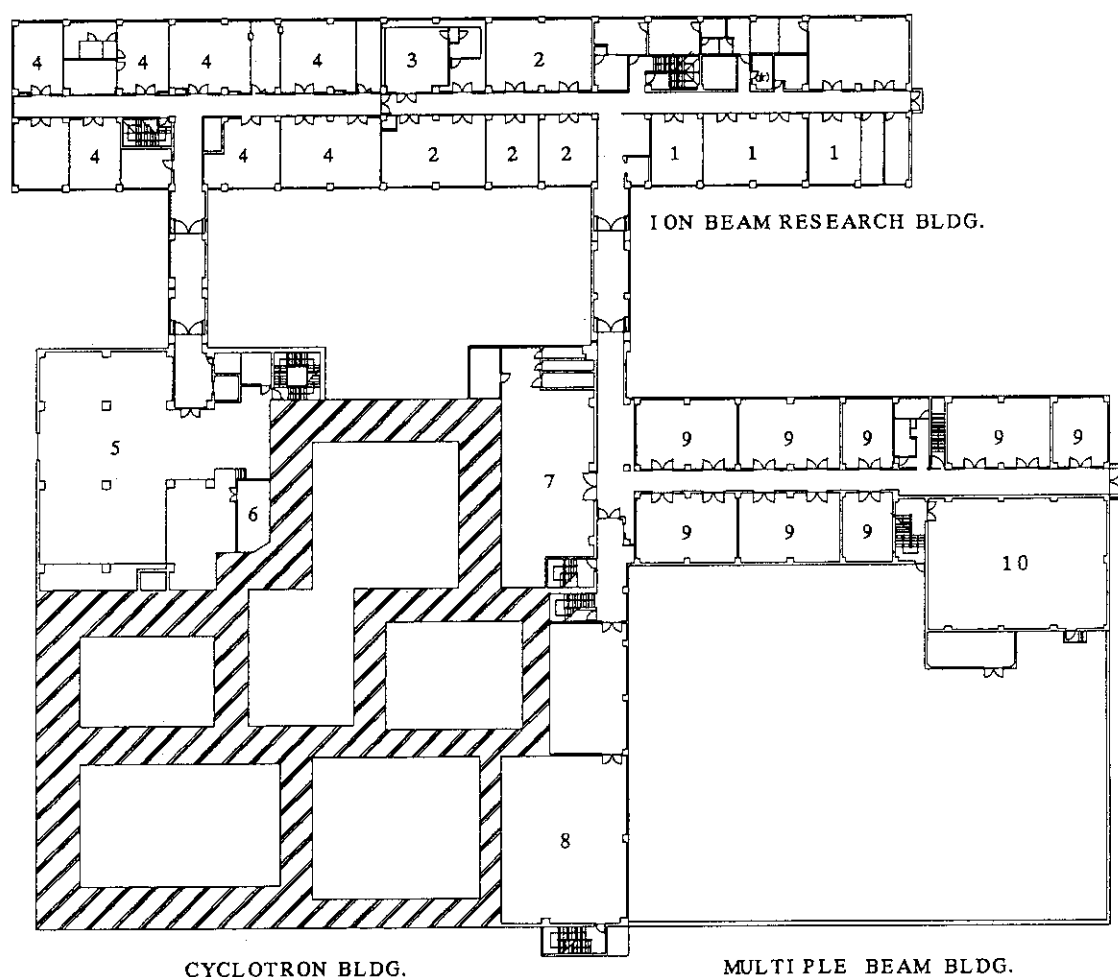
heavy ions, shown in Fig. 2. In the basement, there are three target rooms for utilization of vertical ion beams, an ion source room with two kinds of ion sources, and accelerator utilities such as cooling water system and power distribution system, as in Fig. 3. A cooling room for radioactive accelerator parts, a RI storage room, and treatment rooms for radioactive wastes are also placed in the basement. The multiple beam building of reinforced concrete and about 4,400 m² in total area was constructed for single or multiple use of ion beams from three electrostatic accelerators. As shown in Fig. 2, there are three accelerator rooms, three target rooms, an accelerator control room, and an ion source preparation room, in the first floor. In the basement, there are two target rooms, and cooling water and power supply rooms for accelerators as indicated in Fig. 3. As in Fig. 4, several laboratories are laid and a space



1; machine room for building utilities, 2; control room for building utilities, 3; light ion room 2, 4; heavy ion room 2, 5; heavy ion room 5, 6; preparation and control rooms for beam experiments, 7; ion source room for cyclotron, 8; cooling water room for cyclotron, 9; cyclotron pit-room, 10; cooling room for activated parts, 11; power supply distribution room, 12; RI storage room, 13; room for waste water treatment, 14; storage room for radioactive waste, 15; target room 4, 16; target room 5, 17; machine room for electrostatic accelerators, 18; parts storage room.

Fig. 3. A plane figure of basement in TIARA buildings.

available for visitors is arranged in the second floor. In the target rooms 1 and 3, it is possible to use ion beams independently from the tandem and the single-ended accelerators, respectively. On the other hand, triple-beam and dual-beam experiments are possible in the target room 2 by operating the plural accelerators simultaneously in addition to single-beam utilization. In the target room 4, accessible at any time, the beam from ion implanter is used for material damage observation in real time with an electron microscope. In the target room 5, it is possible to use electron beams from single-ended accelerator by exchange the polarity of the terminal voltage. The ion beam research building with total area of about 4,700 m² is of also reinforced concrete structure with one floor below and two floors above the ground. It is composed of offices and rooms for cyclotron operation, radiation control and facility management, hot laboratories, several laboratories for visitors, and machine rooms, as shown in Fig. 2 to 4.



1;offices, 2;joint use laboratories for visitors, 3;clean room, 4;hot-laboratories, 5; filter room for air exhaust of first class radiation controlled area, 6;radiation monitoring room, 7;machine room for air conditioning, 8;measuring and control room for beam experiments, 9;laboratories, 10;room for visitors.

Fig. 4. A Plane figure of second floor in TIARA buildings.

3. SAFETY DESIGN OF THE FACILITIES

At the design of the facilities, it was defined as a functional policy to take rational design by harmonizing among a human safety, a convenience use, and a construction cost, in addition to abiding by all roles applied.

3.1 General Safety Design

Materials used were selected in consideration of resistant properties in corrosion, weather, fire, radiation and so on. Apparatus was designed to keep easy maintenance and operation in attention to protection of noise and vibration. All systems in the accelerator facility were designed to avoid the complex accident with radiation by the conception "fail to safe". An earthquake-proof design corresponding class B was introduced into the cyclotron base, radioactive waste treatment apparatus and exhaust air filter apparatus. A center computer system by CRT was introduced into the building utility controls of an air-conditioning, a power supply, a cooling water circulation, and so on. By this system, all building utilities can be operated remotely and all status can be watched rationally at the same control room and at the least operators.

3.2 Radiation Safety Design

Radiation Controlled area: The facilities were divided into three radiation areas by wall and/or door to control radiation and radioactive contamination. The first is the radiation controlled area where air or surface of articles may be contaminated by radioisotope using it or operating the cyclotron, such as hot-laboratories, cyclotron vault, light ion rooms, and so on. In the first class radiation controlled area, air exhausters have been installed independently corresponding with the contamination level to be estimated, and air flow is controlled from low contamination level to high level to prevent from the extension of the contamination. Waste water in the first class area is introduced to a storage tank through the exclusive lines, and treated by an evaporator and a condenser. Evaporation residue is solidified by cement in a stainless steel drum, and treated water is reused in the first class area. The second is the radiation controlled area where radiation dose may exceed 0.3 mSv per week without contamination. The accelerator rooms, heavy ion rooms, target rooms, and those surroundings except first class area are controlled as the second class area. In both the first and the second class areas, external radiation level is always observed by radiation monitoring system. The third area is free from radiation control because there is no possibility of both radiation exposure and radioactive contamination, such as accelerator control rooms, offices, cold-laboratories.

Radiation Shielding Design: Characteristic in radiation shielding design of the facilities is that the installed four ion accelerators can be operated simultaneously and many irradiation rooms are independent each other in radiation shielding. The facility design bases of radiation dose rate equivalents were determined as in Table 3 according to a balance between the actual

Table 3. The facility design bases of radiation dose rate equivalents

Area	Occupied Time	Dose Rate Equivalent
a) Radiation controlled area		less than 1 mSv/week
(1) Radiation area such as irradiation room, RI storage room, etc.	48 hs/week	less than 20 μ Sv/h
(2) Another area	168 hs/week	less than 6 μ Sv/h
b) Boundary in radiation controlled area	48 hs/week	less than 300 μ Sv/week (less than 6 μ Sv/h)
c) Outside of radiation controlled area		
(1) Control room, Office	168 hs/week	less than 0.6 μ Sv/h
(2) Another area	48 hs/week	less than 2 μ Sv/h
d) Boundary of the site	168 hs/week	less than 250 μ Sv/3 months (less than 0.1 μ Sv/h)

conditions in use and the law. Radiations assessed in shielding are neutrons and gamma-rays by ion beam irradiation. X-rays are also assessed in the operation of three electrostatic accelerators. The intensities and the angular distributions of radiation sources for shielding design are determined with the combination conditions of ion beams and target that give maximum generation rates of neutrons and/or gamma-rays depend on the condition of beam utilization. Table 4 shows fundamental conditions of beam utilization and maximum neutron generations approved in the accelerator rooms or the irradiation rooms. In the calculation of the dose rate equivalent at various positions, the equivalent was assessed not only by the leakage through shielding materials but also by streaming through maze and/or duct and by sky-shine³⁾.

Countermeasure against Radiation Activation: In the cyclotron system, composed materials are activated by high energy ions and secondary generated neutrons due to the nuclear reaction. To avoid the activation, beam loss is minimized by optimum beam control with computer and by using large diameter beam line duct. In the component parts of beam losing, the material is used that is hard to be activated or in which relatively short life radioisotopes are produced, such as graphite or aluminum. The parts to be not avoid from activation, such as a deflector, a beam slit and a stopper, are exchanged before the radiation level becomes not so high. Water and ion exchange resin taken out of the cyclotron cooling system are also treated as the radioactive wastes. The target as an experimental sample is always assessed with regard to radioactive occurrence in utilizing ion beams. In the second class radiation controlled area, it is very important to assess the possibility of radioisotope production in target, because the radioactive contamination is always inhibited in any case. IRAC cord system⁴⁾ was developed to estimate the isotope production in the various reaction

Table 4. Maximum neutron generation approved in the room

Room Name	Target	Particle	Energy (MeV)	Current (μ A)	Maximum Neutron Generation Approved (neutrons/sec)
Cyclotron Vault	Cu	proton	90	10	8×10^{12}
Switching Magnet Room	Cu	proton	90	10	8×10^{12}
Light Ion Rooms 1 & 2	Cu	proton	90	10	8×10^{12}
Light Ion Room 3	Cu	proton	90	1	8×10^{11}
Heavy Ion Rooms 1 & 2	Cu	$^{14}\text{N}^+$	455	0.8	3×10^{10}
Heavy Ion Room 3	Cu	$^{14}\text{N}^+$	455	0.08	3×10^9
Heavy Ion Rooms 4 & 5	Cu	$^{14}\text{N}^+$	455	0.04	1.5×10^9
Tandem Accelerator Room	C	deuteron	6	1	2×10^{10}
Single-ended Accler. Room	C	deuteron	3	20	3.4×10^{10}
Target Room 1	C	deuteron	6	1	2×10^{10}
Target Room 2	C	deuteron	3	20	} 5.8×10^{10}
	Li	deuteron	0.4	50	
Target Room 3	C	deuteron	3	20	3.4×10^{10}
Target Room 5	(W)	electron	3	100	

conditions. For RI production experiment, a target transfer system from irradiation apparatus to hot-cell with manipulators was designed and equipped according to the building construction to prevent from radiation exposure.

4. SYSTEMS FOR RADIATION SAFETY CONTROL

4.1 Radiation Monitoring System

Radiation monitoring system was installed for many purposes. Neutron monitors were installed in all irradiation rooms and accelerator rooms to observe the neutron generation under fundamental conditions for shielding. Gamma-ray monitors are also installed in all irradiation rooms and accelerator rooms to inhibit the entrance to the room when gamma-ray level is high due to the activation. The monitors for neutron and gamma-ray were equipped in the radiation controlled area to certify the radiation level is low enough to work there. Four monitoring posts with neutron and gamma-ray monitors are located in the neighborhood of the site boundary to certify the radiation level as low as background. Concentrations of activated air and dust in the room where unsealed radioisotope is used are also measured regularly with gas and dust monitors by using an automatically controlled air sampling apparatus. Concentration of gaseous radioisotopes in exhaust air from stack is always observed by a stack gas monitor which is enough to detect the fundamental level controlled.

In addition to the environmental monitoring, the individual monitoring for radiation workers is performed fundamentally by film badge which is a personal dosimeter to detect gamma-rays, fast and thermal neutrons, and beta-rays. In the change room, contamination check is performed by a hand foot cloth monitor. The all articles taken out from the first class area are checked for surface contamination by survey or smear method. Internal exposure of the workers is also controlled by monitoring with a whole body counter in regular intervals.

4.2 Personal Access Control System and Safety Control System

In the large accelerators facilities, it is very important to prevent many workers from radiation accident. The personal access control system was introduced both to control the entrance to the radiation controlled area and to avoid being shut in the irradiation room. The system is composed of sensors (antenna for transmission and receive) and individual definite cards, and personal whereabouts is always defined automatically by holding the card.

In the facilities, there are two safety control stations to construct main components of the interlock systems for cyclotron and three electrostatic accelerators, respectively. The station with programmable controller gives permission or prohibition signals to the accelerator and door operation apparatus by logically judging from many kinds of signals obtained. Those safety signals are displayed at graphic panels in each accelerator control rooms, at status indicate CRT located in the entrance to radiation controlled area, and at operation indicator devices for accelerator operations in the entrance of irradiation rooms and accelerator rooms.

ACKNOWLEDGMENT

The authors would like to acknowledge to Y. Nakayama, S. Takano, T. Sasamoto, Y. Kawakami for construction of TIARA buildings as planned, and all members for their useful suggestions and positive supports.

REFERENCES

- 1) Kazuo ARAKAWA, *et al.*, "1. AVF Cyclotron.", JAERI-M93-047(JAERI TIARA Annual Report vol. 1), p1-54(1993).
- 2) Satoshi TAJIMA, *et al.*, "2. Electrostatic Accelerators.", JAERI-M93-047(JAERI TIARA Annual Report vol. 1), p57-65(1993).
- 3) Susumu TANAKA and Hiromasa WATANABE, "Shielding Design of Ion Accelerator Facility in JAERI Takasaki.", Spring Meeting of the Atomic Energy Society of JAPAN, G12(1991)
- 4) Susumu TANAKA, Hiromasa WATANABE, *et al.*, "IRAC: A code System to Calculate Induced Radioactivity Produced by Ions and Neutrons.", JAERI-M-93-047(JAERI TIARA Annual Report vol. 1), p80-83(1993).

9.2 RADIATION MONITORING SYSTEM IN TIARA FACILITY

Yoshiteru NAKAMURA, Kazuhiro SATOH*, Koichi NISHIMURA,
Isao TAKADA, Yukio IWAYA*, Hideyuki NONOUCHI**
Takashi SASAKI** and Hiromasa WATANABE

Department of Advanced Radiation Technology, JAERI

* Department of Administrative Services, JAERI

** Fuchu Works, Toshiba Co., Ltd.

I. INTRODUCTION

The JAERI AVF cyclotron (K=110 MeV) system^{1),2)} and the 3 MV tandem electrostatic accelerator system^{3),4)} have been already operated in TIARA facility since 1991 and 1990, respectively. Various ions with very wide energy range of 0.8-520 MeV have been also extracted successfully from these accelerators. A radiation controlled area in TIARA facility is divided into the first and second class ones, and radiation safety control in the area has been carried out comprehensively with the support of the radiation monitoring system.

II. BASIC SPECIFICATION AND CONCEPT

Basic specification and concept for the radiation monitoring system⁵⁾ (RMS) are as follows: 1) The RMS is needed to provide excellent reliability and stability, since it is a main equipment for radiation safety control and dependable output signals from the RMS are required to construct an interlock sequence of the operations for the entrance doors and accelerator systems, 2) The RMS can be operated continuously by an uninterruptible power supply connected with engine generating power lines after the stopping of commercial electric power, 3) Good performances such as maintenance-free and durability are also needed on the viewpoints that the RMS has to be always operated and a routine maintenance is scheduled only one time through a year, 4) Module structure was introduced for monitoring racks to improve the interchangeability and the working efficiency when the repairing or the

	Neutrons	High level γ	Low level γ	X - rays	Room gas	Room dust	Exhaust gas	Exhaust dust
Detector	BF ₃	Ion. chamber	SSD	Ion. chamber	Nal scintil.	Plastic scintil.	Plastic scintil.	Plastic scintil.
Energy range (MeV)	~ 17	0.08 - 3	0.08 - 3	0.03 - 1	0.3 - 3 (γ)	0.3 - 3 (β)	0.3 - 3 (β)	0.3 - 3 (β)
Measuring range	$10^0 - 10^5$ cps	$10^{-2} - 10^5$ mSv/h	$10^{-4} - 10^1$ mSv/h	$10^{-4} - 10^1$ mSv/h	$10^1 - 10^5$ cps	$10^0 - 10^4$ cps	$10^1 - 10^5$ cps	$10^0 - 10^4$ cps
Linearity (decade)	± 0.12	± 0.20	± 0.12	± 0.20	± 0.12	± 0.20	± 0.12	± 0.12
Indication	Digital	Digit./Anal.	Digital	Digit./Anal.	Digital	Digital	Digital	Digital
Sensitivity (Bq/cm ³)	—	—	—	—	1×10^{-3}	5×10^{-6}	1×10^{-4}	1×10^{-7}

Table 1 Principal specification and performance for the radiation monitors.

modification is necessary, 5) Most of the radiation detectors were chosen to possess some specifications superior to those of JIS Z-4324 II class.

Principal specification and performance for the radiation monitors are shown in Table 1. In addition, the errors of an indication and an alarm level are within ± 0.3 decades, and the drift during 24 h is less than ± 0.12 decades.

III. DETECTORS FOR RADIATION MONITOR

Dose rates around the wall in the cyclotron vault and the 3 light ion rooms were estimated at 4-16 Sv/h⁶⁾ in case of the maximum proton intensity of 10 μ A and 90 MeV. Operation time converted into maximum operation condition for a year is evaluated at 108 h based on an operation program, therefore an accumulated dose per one year is calculated about 430-1730 Sv at those positions.

At the above radiation environment, the BF₃ detector for neutrons can not be used directly without any countermeasures, because the measuring range is 3-3 $\times 10^5$ μ Sv/h (10⁰-10⁵ cps) and a pre-amplifier consisted of MOS-IC is forecast to have low radiation resistance of about 10² Gy order⁷⁾⁻⁹⁾.

The detector of ionization chamber which has been excluded semi-conductor elements is used for the measurement in high gamma-rays field. This detector of 76.2 mm diameter and 298 mm long is made of aluminum cylindrical chamber filled with argon gas of 5 kg/cm². Ionization current induced by radiation is measured directly using a picoammeter. On the other side, the detector for low level gamma-rays is constructed by a silicon semi-conductor detector (SSD) and a pre-amplifier of MOS-IC. In addition, one X-rays detector with a pre-amplifier is arranged at outer surface of the iron plate shield around the ECR ion source (OCTOPUS)^{10),11)}.

In the irradiation and the accelerator rooms, 15 detectors for gamma-rays are positioned on the shielding wall near the entrance to measure mainly radiation level from the radioactive materials. However, the detectors for neutrons are installed from the standpoint of operation control for the accelerators to ascertain the neutron generation under fundamental conditions concerned to radiation shielding. Eight detectors in the 5 heavy ion rooms and 3 target rooms are mounted in front of the target ports in order to get higher sensitivity, 3 detectors are arranged at maze part in the light ion rooms, and the other 2 detectors in the cyclotron vault and cyclotron pit room are evacuated at shadow space behind the shielding wall as before reason. A number of all detectors amount to 46 channels finally.

IV. GAS AND DUST MONITORS

A flow chart of sampling system for gas and dust monitors is illustrated in Fig. 1. The air exhausted from the first class radiation controlled area is released through a stack after cleaning up by the particular air filters with high efficiency. The air released from the stack is

watched continuously using exclusive gas and dust monitors, because the concentration of radioactivities needs to be always restricted within that of the regulation. This gas monitor of plastic scintillator for released air was improved to be able to measure certainly the concentration of 0.37 mBq/cm^3 which is $1/10$ of the regulation value.

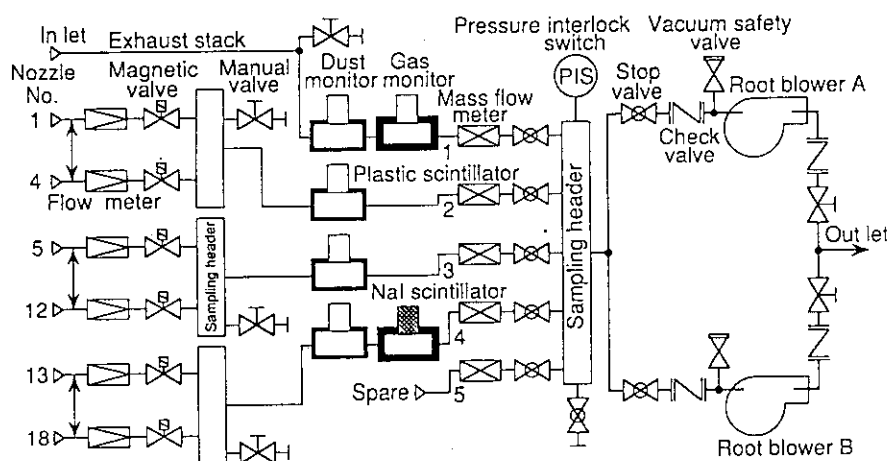


Fig. 1 A flow chart for gas and dust sampling system.

The concentration of radioactive dust in exhausted air from the first class area is measured at regular intervals by the dust monitor through the inlet nozzles No.1 to No. 3. Radioactive dust in hot-laboratory and radioactive wastes treatment

room is also monitored directly by sampling of the room air from No. 5 to No. 11 nozzle. A pair of gas and dust monitor is equipped to inquire into radioactive air and dust through No. 13 to No. 17 nozzle when the high intensity beams and the radioisotopes of considerable amounts are used in the cyclotron vault and pit room, the light ion rooms 1 and 2, and the light ion room 3, a glove box and 3 hot-cells.

The flow rates of sampling air are read off by 4 mass flow meters to calculate the radioactivity concentration, then the measured air is sent to the exhaust line by one of the 2 root blowers with each capacity of $1 \text{ Nm}^3/\text{min}$. The operation of the sampling system is possible either in remote mode or in-situ.

V. DATA ACQUISITION

A connection diagram between the monitoring data and a radiation control computer ($\mu\text{VAX-3400}$) is shown in Fig. 2. Numerical data from neutrons, low level gamma-rays, gas and dust monitors are taken out in turn by way of 4 scanners from 41 digital rate meters. In the analog type monitors for high level gamma-rays and X-rays, the data are treated via 5 logarithmic digital rate meters. The radiation control computer delivers the signals for operating command to 15 magnetic valves (3 spares) through a switch/control unit of HP3488A, and it receives oppositely the operating status of the valves and the measuring data from 4 mass flow meters (1 spare) through a data acquisition unit of HP3421A.

Measuring values of the RMS are transferred every 30 sec to the radiation control computer through two GP-IB extenders communicated by the photo-link interface. Several meteorological data such as temperature, humidity, rainfall, velocity and direction of the wind,

quantity of solar radiation etc. are also sent to the computer every 2 min. These data are stored in two 400 Mbyte hard discs and utilized to CRT status display or making on various materials for radiation safety control.

VI. SOME OPERATION RESULTS

The RMS in the cyclotron building has been operated steadily since an installation in March 1991, and one in the multiple beam building has been completed in March 1993. Four monitoring racks are installed in the cyclotron control room, each of which is assembled into many modules of digital rate meters, high voltage power supplies, a hybrid recorder etc., as shown

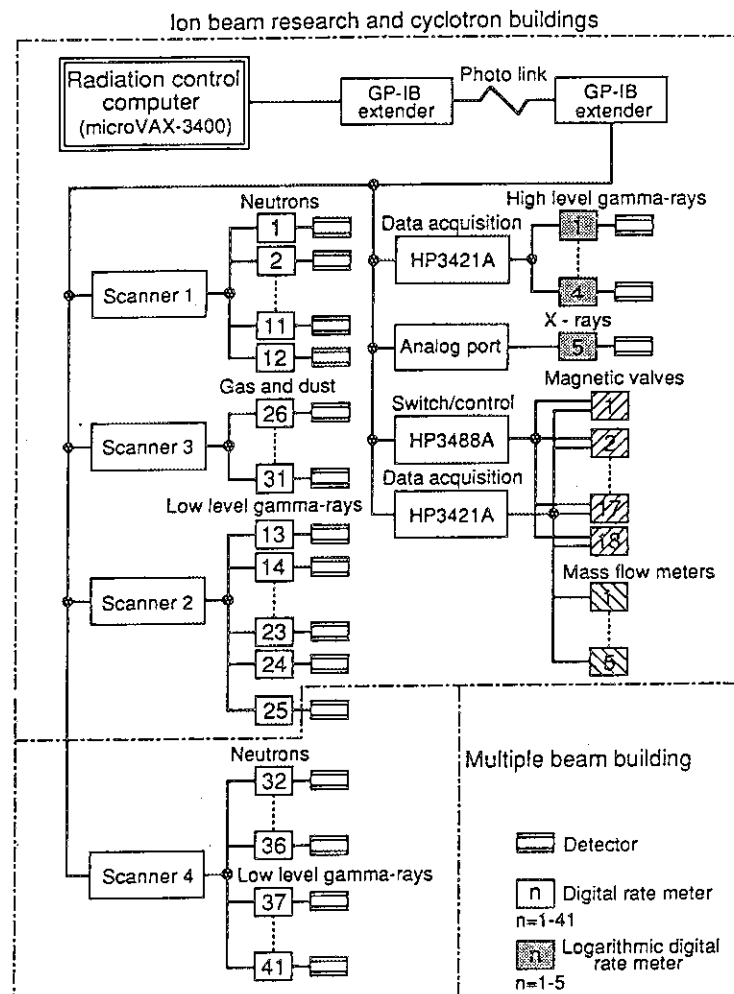


Fig. 2 A connection diagram between the radiation monitoring system and the radiation control computer.

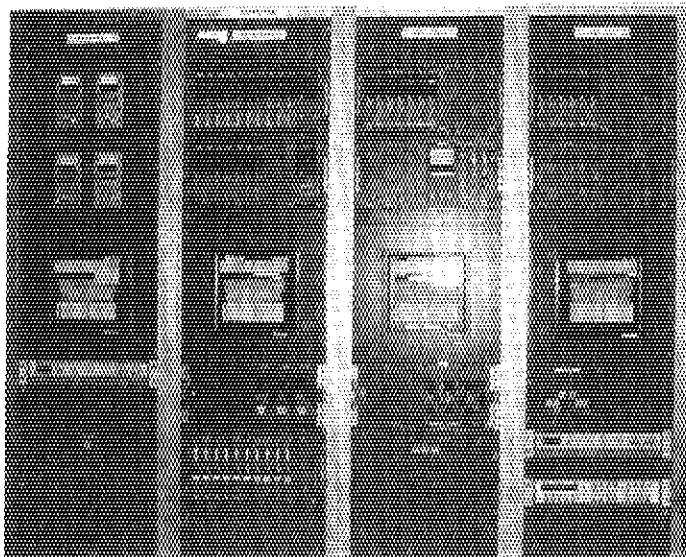


Photo. 1 Front view of the monitoring racks for the radiation monitoring system.

in Photo. 1, and a similar rack is put in the electrostatic accelerators control room.

Counting rate of the neutrons monitor in the cyclotron vault is shown in Fig. 3. Proton beams accelerated to 10-90 MeV were stopped completely by the Faraday cup (TS1) made of a thick copper plate positioned at 9.3 m downstream from the exit of the cyclotron chamber. The detector for neutrons is installed at 12.4 m away from the TS1, along the

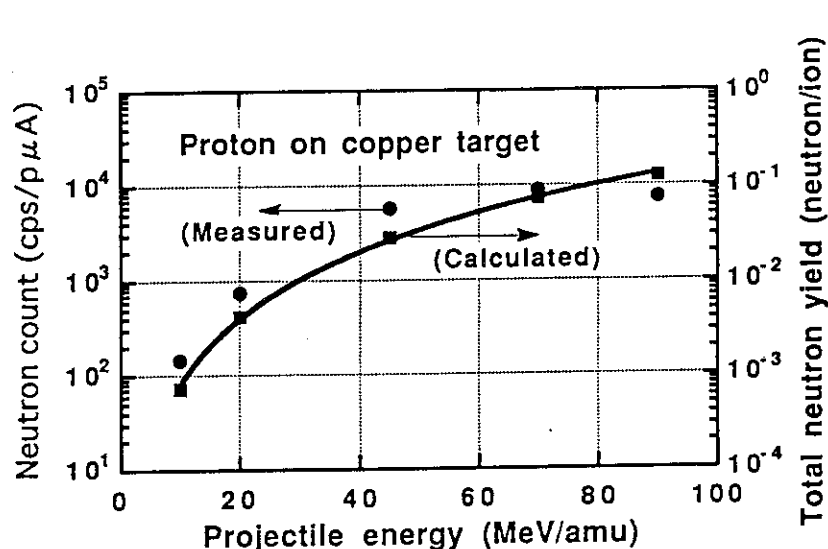


Fig. 3 Neutron count of the radiation monitor in the cyclotron vault. Proton beams were stopped by the Faraday cup in the TS1 diagnostic station downstream the cyclotron.

direction on the deflection angle of 101 degrees. This neutrons detector has been calibrated with averaged energy of 0.33-4.5 MeV using a ^{241}Am -Be source. The measured neutron count accords with the tendency of the calculated total neutron yield⁶⁾.

Furthermore, an example of the indication change of the gamma-rays monitor mounted in the cyclotron vault is shown in

Fig. 4. Although the rapid reduction of the indication was observed first within 30 min after the proton beams of 2.8-3.2 μA with energy of 70 MeV were extracted about 72 h in total from the cyclotron, it took more than 20 h until the indication dropped below the alarm level (50 μSv/h) which was interlocked for the entrance door opening.

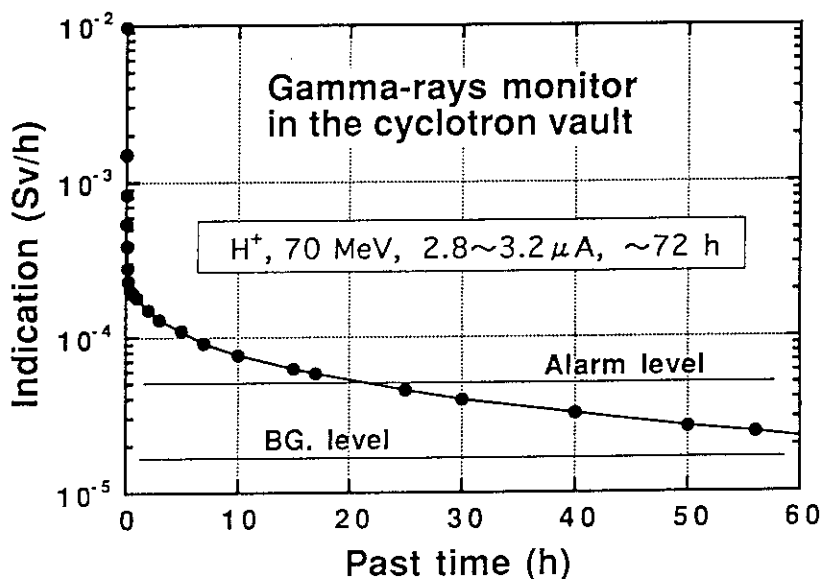


Fig. 4 An example of indication change of the gamma-rays monitor after the cessation of cyclotron operation.

REFERENCES

- 1) K. Arakawa, Y. Nakamura *et al.*, Proc. 13th Int. Conf. Cycl. their Applic., Vancouver, Canada (1992)
- 2) K. Arakawa, Y. Nakamura *et al.*, Proc. 9th Symp. Accel. Sci. Technol., Tsukuba, Japan (1993)
- 3) S. Tajima, I. Takada *et al.*, "2.1 3 MV Tandem Electrostatic Accelerator" in JAERI-M 93-047 (JAERI TIARA Annual Report vol. 1) (1992)

- 4) S. Tajima, I. Takada *et al.*, Proc. 5th Workshop on Tandem Accel. Technol., Tsukuba (1992)
- 5) Y. Nakamura, K. Satoh *et al.*, Proc. 9th Symp. Accel. Sci. Technol., Tsukuba, Japan (1993)
- 6) S. Tanaka, Private communication
- 7) T.V. Nordstrom and C.F. Gibbon, IEEE Trans. Nucl. Sci., NS-28, No.6 (1981)
- 8) G.J. Brucker, E.G. Stassinopoulos *et al.*, IEEE Trans. Nucl. Sci., NS-29, No.6 (1982)
- 9) R.W. Tallon, M.R. Ackermann *et al.*, IEEE Trans. Nucl. Sci., NS-32, No.6, (1985)
- 10) W. Yokota, T. Nara *et al.*, Proc. 13th Int. Conf. Cycl. their Applic., Vancouver, Canada (1992)
- 11) T. Nara, W. Yokota, *et al.*, Proc. 9th Symp. Accel. Sci. Technol., Tsukuba, Japan (1993)

9.3 SAFETY INTERLOCK AND DISPLAY SYSTEMS FOR CYCLOTRON FACILITY

Yoshiteru NAKAMURA, Hiromasa WATANABE, Susumu TANAKA,
Takashi AGEMATSU, Koichi NISHIMURA and Akihiko Daigo*

Department of Advanced Radiation Technology, JAERI

* Toshiba Engineering Co., Ltd.

I. INTRODUCTION

A safety interlock and display systems are fundamental equipments which are necessary for a regulation on prevention for radiation hazards in a radiation facility. They have been requested to equip with higher reliability and assurance in consideration of person security, especially.

II. SAFETY CONTROL STATION

In large radiation facility with several accelerators and many irradiation rooms such as TIARA, the safety interlock and display systems for person security and accelerator operation have to certainly deal with many signals communicated among the systems or the apparatus of various kinds in the facility. Two sets of the safety interlock and display systems in combination with the cyclotron and three electrostatic accelerators have been constructed to communicate efficiently among the systems.

Figure 1 shows the relationship among the various safety systems which are related to the safety interlock and display systems for the cyclotron facility. A safety control station

(SCS) is the nucleus part in these systems. Basic function of the SCS is to gather plenty of safety signals from the other systems, and to deliver the required signals to each system after the reconstruction or the translation of the signals. The SCS is connected with 2 computers for radiation safety control and

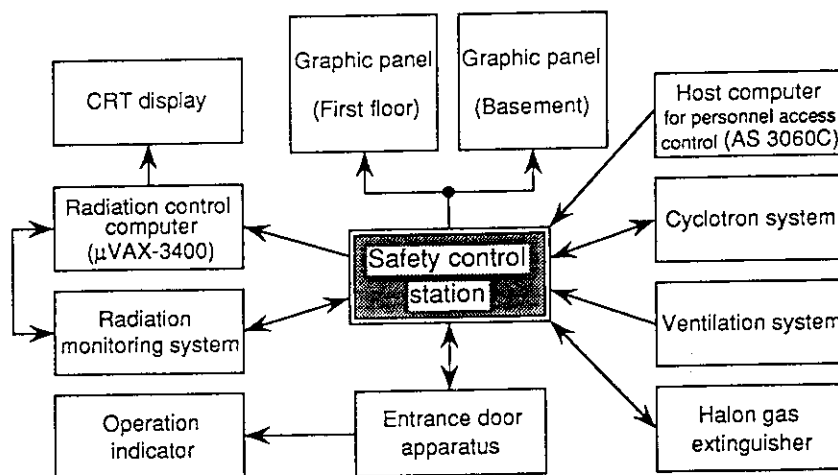


Fig. 1 The relationship among principal devices related to the safety control station.

personnel access control by RS-232C interface. A host computer for personnel access control outputs the status of person's whereabouts to the SCS. A radiation control computer takes in many signals of the conditions of the entrance door, working switch and ventilation, then sends them to 5 CRT displays. These displays are located at each entrance to the radiation controlled areas. A lot of signals are also required for the indication on the 2 graphic panels in the cyclotron control room.

An entrance door apparatus gives three status signals of the entrance door, working switch and emergency door switch to the SCS, receives the interlock signals of the permission and prohibition for the door operation, an indication signal of person existence in the room and an alarm signal for the door closing from it. The cyclotron system is given the permission signals of a cyclotron operation and an irradiation by the SCS, and sends contrarily the signals of 4 kinds which consist of the operation of the cyclotron, the closed state of a pair of a beam line shield (rotary shutter) and a Faraday cup, the choice of a target port and the irradiation mode corresponding the objective irradiation room.

Furthermore, An operation indicator obtains three signals of the cyclotron operation, irradiation mode in the room and entrance permission through the entrance door apparatus from the SCS. The operation indicator, which is installed nearby the each entrance door of the irradiation and accelerator rooms, shows that the accelerator operation and the irradiation mode are built up or not, the entrance into the room is possible or not. A radiation monitoring system outputs alarm signals to the SCS, and gets their reset signals from the SCS. A halon gas extinguisher and a ventilation system give the operation signals of themselves to the SCS and only the former receives the door closing signals from it.

The interlock circuit in the SCS has been built up by a programmable controller of OMRON SYSMAC CH1000H (1024 contacts)³⁾. I/O units are chosen relay contact types of 16, 32 and 64 contacts respectively according to a number of required signals. The internal interlock circuit composed of ladder style can be easily modified using a factory intelligent terminal with 12 inches plasma-display.

The content of input and output signals is listed in Table 1. It is clearly known that most of these signals are needed for the entrance door apparatus which fulfills very important role for person security, although the number of input and output signals is just 137 contacts each.

Table 1 A number of contacts for input and output signals dealt with the programmable controller.

	Input (contacts)	Output (contacts)
Cyclotron system (distributor)	36	6
Entrance door apparatus	39	89
Ventilation system	10	0
Halon gas extinguisher	9	9
Radiation monitoring system	33	4
Host computer (personnel control)	10	0
Radiation control computer	0	29
Total	137	137

III. INTERLOCK FOR ENTRANCE DOOR APPARATUS

In the cyclotron facility, 3 irradiation rooms with vertical beam line are stationed in the basement and connected to the upper irradiation rooms by stairs, as illustrated in Fig. 2. In this case, 2 irradiation rooms have to be regarded as unit irradiation area with 3 entrance doors from the viewpoint of radiation protection. The interlock circuits for 3 doors have to be

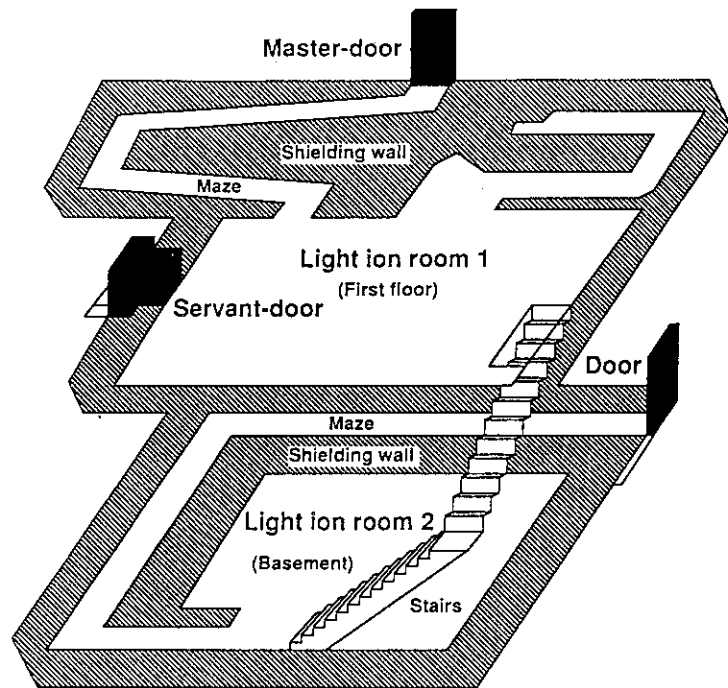


Fig. 2 A model of the entrance doors at the light ion rooms 1 and 2.

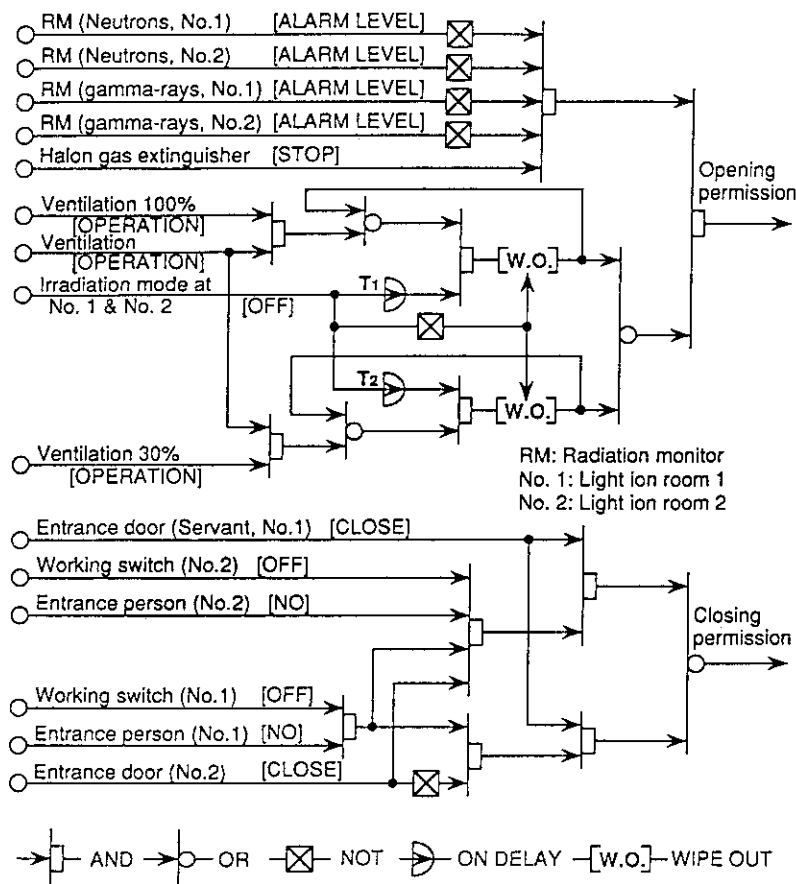


Fig. 3 The interlock circuit for master entrance door of the light ion room 1.

also designed by taking into account the condition of plural doors and their master-servant relations.

Figure 3 shows an example of the interlock circuit for master door of the light ion room 1. This door can be opened by an opening permission signal from the SCS if an irradiation mode is not formed in the irradiation area when 4 radiation monitors indicate safety level, the halon gas is not discharged and the ventilation is operated.

On the other hand, the master door can not be closed on any conditions

unless the servant door has been already closed. This master door is possible to close by a closing permission signal if the door of the light ion room 2 is opened, the working switch is canceled and nobody is in the light ion room 1. In case of the door closing of the light ion room 2, the door can be closed on condition that two working switches are canceled and no one is in the both light ion rooms 1 and 2, as indicated in Fig. 3.

IV. INTERLOCK FOR CYCLOTRON SYSTEM

The cyclotron can not accelerate ion beams without the operation permission signal from the SCS even though all operation conditions for the cyclotron have been satisfied. The accelerated beams can not be also transported to the objective irradiation room without an irradiation permission signal from the SCS. The operation of the cyclotron is allowed when the following 6 conditions have been completed in the cyclotron vault, the switching magnet room, cyclotron pit room, cable passage and power distribution rooms: (1) All the doors are closed, (2) nobody is in the room, (3) all the working switches and the emergency door switches are canceled, (4) the ventilations are operated, (5) halon gases are not discharged and (6) all the beam line shields are closed.

The irradiation mode signals are applied from the cyclotron system to the 5 irradiation areas corresponding to the light ion rooms 1 and 2, the light ion room 3, the heavy ion rooms 1 and 2, the heavy ion room 3, and the heavy ion rooms 3, 4 and 5. The irradiation mode is defined by the first opening of the beam line shield along the objective irradiation room providing that above 6 conditions have been held their ones. However, the cyclotron is stopped as soon as one of the conditions becomes to be not kept during the operation or the irradiation.

V. ALARM CIRCUIT

The SCS can control effectively the information for safety control, because it gathers various signals synthetically. Alarm messages are announced in the control room by a voice module of EPROM if abnormal or alarmed conditions detect in the programmable controller of the SCS. These alarm messages are distinguished into 5 kinds as follows: (1) halon gas is discharged, (2) the emergency door switch is operated, (3) the radiation monitor in the irradiation room exceeds own alarm level when the door is opened, (4) someone is still remained or working switch is operated in the objective area in spite of the condition that the area has been changed to the irradiation mode.

VI. GRAPHIC PANEL

Three graphic panels for the cyclotron facility are shown in Photo. 1. Two large graphic panels on both sides are for safety interlock and display systems, central one is for the cyclotron system. Various information for safety control is easily understood with 2 large

graphic panels (1.8mW×1.8mH, each) which are hung from the ceiling in the cyclotron control room. These panels for first floor and basement are made based on the faithful layout of building planes. The symbolized red and green LED's on the panels indicate their operating conditions such as entrance doors, persons, working switches, emergency door switches, ventilations, halon gases, radiation monitors, beam line shields and target ports.

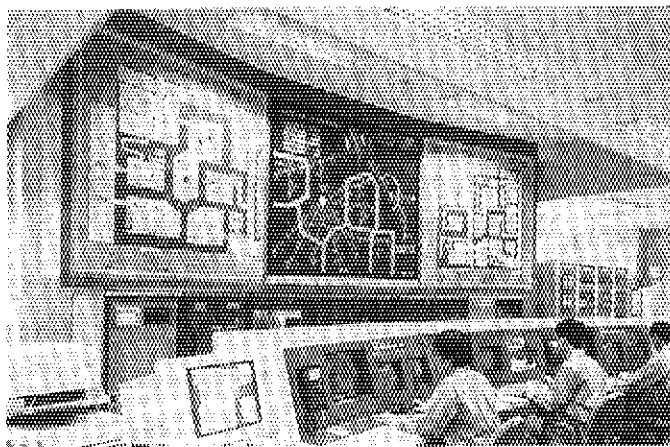


Photo. 1 Three graphic panels for the cyclotron facility.

For example, the symbol of the door at opening position is indicated by red LED as a dangerous signal for person security. Operators and experimenters can easily judge if the irradiation or the entrance to the room is possible because all symbols in the objective room change into green. The red LED on the panels is also flickered to attract attention whenever the

alarm message has been announced or an interlock by-pass switch has been operated for repairing work.

VII. PRESENT STATUS

The safety interlock and display systems have functioned steadily without any troubles since the installation in February 1990. We would expect that not only this system has been useful for operators and users, but also it has contributed enough for radiation safety control.

REFERENCES

- 1) Y. Nakamura, K. Satoh, *et al.*, Proc. 9th Symp. Accel. Sci. Technol., Tsukuba, Japan (1993) pp.434-436
- 2) K. Arakawa, Y. Nakamura, *et al.*, "1. AVF Cyclotron" in JAERI-M 93-047 (JAERI TIARA Annual Report vol. 1) (1993) pp.48-49
- 3) OMRON Co., Ltd., Catalog "Programmable controller SYSMAC C series" (1989)

9.4 PERSONAL ACCESS CONTROL SYSTEM IN TIARA

Koichi NISHIMURA, Kiyoshi MIZUHASHI, Atushi IIJIMA*
and Hiromasa WATANABE

Department of Advanced Radiation Technology, JAERI

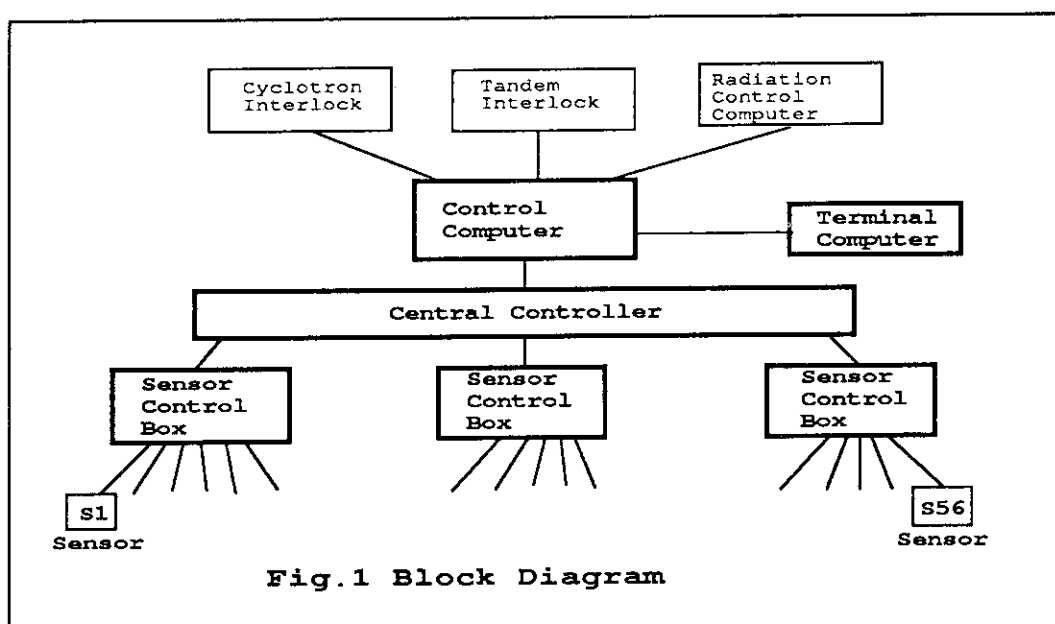
*Toshiba Engineering Co., Ltd.

I. INTRODUCTION

TIARA is the ion accelerators facilities where four accelerator rooms and twelve irradiation rooms are located. In the facilities, a first class and a second class radiation controlled areas are set up to keep the access control of workers. It is also necessary to be absence from the irradiation room when ion beam is utilized. A personal access control system has been introduced in TIARA for personal access control and prevention the workers from radiation exposure in the room.

II. OUTLINE OF THE SYSTEM

The system is composed of a control computer, a central controller, sensor controller, fifty six sensors and about three hundred ID card, as shown in Fig.1. sensor is the main part to communicate without contact with ID card by using induction electromagnetic wave at all time. The sensor sends an ID code signal to the sensor controller when it receives the reflective wave changed in its frequency by ID card. The sensor controller decodes the ID



code from each sensor and communicates with the central controller by using a protocol function. The central controller distinguishes whether the card is right by decoded data. The entrance door to the controlled area is interlocked with the sensor and automatically opens when the worker with ID card is permitted. The control computer defines the personal whereabouts by judging the order of sensor that defects the card and displays the all worker's numbers at every area and room. The computer also informs the personal whereabouts to two safeties monitoring stations which controls the operation conditions of the cyclotron and three electrostatics accelerators through the accelerator interlock systems.

As shown in Photo. 1, the ID card is joined with a personal dosimeter called film badge, which is needed for the entrance to the controlled area. Each card has a characteristic ID code of 22 bits. The card is usually in pause state for save the battery and sends the ID code to the sensor automatically by receiving the start signal from the sensor.

A set of two sensors was installed in each entrance or passage to the radiation controlled areas, the irradiation rooms and accelerator rooms. Photo. 2 shows the sensors installed on the maze wall to the irradiation room.

The sensor can't receive the signal from the card in case that the installed environment is not enough. This case may occur when the electric level around the sensor is higher than that of the signals. To avoid the case, the Optimum location was selected by surveying the noise level before installed.

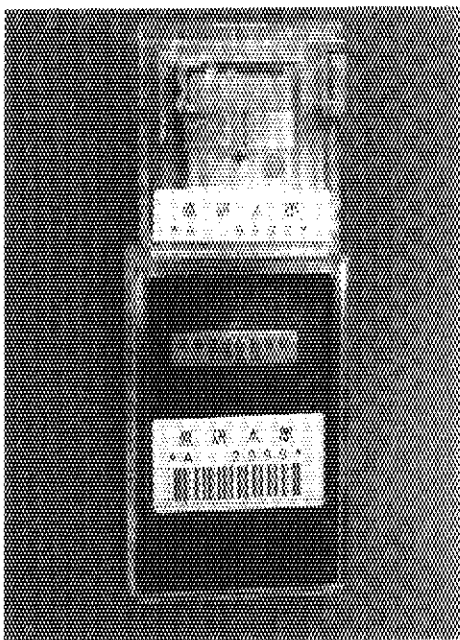


Photo. 1 The ID card joined film badge.



Photo. 2 The sensors installed

10. Status of TIARA 1992

10.1	Utilization of TIARA Facilities	
	Ion Beam Research Administration Division	237
10.2	AVF Cyclotron	
	Group of Cyclotron Operation, Ion Accelerator Division	240
10.3	Status of 3MV Tandem Accelerator and Second-phase Accelerators	
	Construction	
	Group of Electrostatic Accelerators Operation,	
	Ion Accelerator Division	242
10.4	Radiation and Radioactive Waste Controls in TIARA	
	Safety Division and Utilities and Maintenance Division,	
	Department of Administrative Services	244

1 0 . 1 UTILIZATION OF TIARA FACILITIES

Ion Beam Research Administration Division,
Department of Advanced Radiation Technology.

1. Introduction

TIARA is a center of the accelerator facilities for ion beam applications which is composed of three buildings and four ion accelerators, i.e. an AVF cyclotron, a 3MV tandem accelerator, 3MV single-ended accelerator, and 400kV ion implanter. The cyclotron was completed in October 1990 and served for research applications since January 1991. The tandem accelerator was also completed in June 1990 and served since November 1990. The single-ended accelerator and the ion implanter were completed in 1993 and will be served in January 1994.

2. Utilization system

TIARA is opened for public use: it receives applications of the experimental subjects once a year from users in wide areas as well as JAERI staffs, and the subjects are approved after official investigation by the TIARA General Program Committee(GPC). The utilizing time of each accelerator is fairly allotted to the subjects every three periods by Program Advisory Committee under the GPC which are both publicly organized.

Charges for the utilization by visitors are remitted in the case that the outer user have concluded a contract of the joint research (between JAERI and a university or an enterprise) or that of projective joint research between JAERI and universities; the results of research have to be published at the TIARA Research Review Meeting and in the JAERI TIARA Annual Report in these cases. There is another system of visitor use with charges but without duty of the publication.

3. Number of experimental subjects approved in F.Y. 1992

Number of the subject approved for the experiment using cyclotron was 43 and that using tandem accelerator was 20. Subject numbers in each research field are shown in Table 1, and those in each category of relations with users are in Table 2. The subjects for material research in space were numerous in the cyclotron utilization, and those for functional material research in the tandem accelerator utilization.

4. Utilizing times allotted

The utilizing times of each accelerator were allotted every three periods, i.e. 1st(April to July), 2nd(September to December), and 3rd(January to March), in F.Y. 1992 as shown in

Table 1 and 2; where one "day" means daytime from 9 a.m. to 6 p.m. in the case of all periods for the tandem accelerator and 1st period for the cyclotron, but each shift of daytime(9 a.m. to 6 p.m.) and night(6 p.m. to 9 a.m.) is counted as one day in the case of 2nd and 3rd periods for the cyclotron since the cyclotron has been operated continuously from Monday to Friday

The utilization in 3rd period for the tandem accelerator was stopped because of a new beam line construction to the target room 2.

5. TIARA Research Review Meeting

The first TIARA Research Review Meeting was held on 22 and 23, 1992 in Takasaki Radiation chemistry Research establishment, JAERI, where mainly reported were the results of test operation of accelerators completed in F.Y. 1991, the characteristics of experimental apparatus, and the results of ion beam experiments performed in F.Y. 1991. 28 reports and two invited lectures were presented and 147 persons participated in the meeting.

6. JAERI TIARA Annual Report

The first issue of the JAERI TIARA annual Report was published at the end of F.Y. 1992. Included are 25 reports which are mainly on results of research activities performed in F.Y. 1991.

Table 1. Utilization of TIARA in F.Y. 1992 at various research fields.

Accelerators Fields of research	AVF Cyclotron					3MV Tandem Accelerator				
	No. of subject	Utilizing time (days)				No. of subject	Utilizing time (days)			
		1st.	2nd.	3rd.	total		1st.	2nd.	3rd.	total
Materials for space	10	11	13	21	45	1	9	11	-	20
Materials for fusion	3	0	1	0	1	2	2	1	-	3
Biotechnology	9	1	8	9	18	2	9	6	-	15
Functional material	5	0	2	7	9	13	36	30	-	66
RI & nuclear chem.	4	3	4	2	9	0	0	0	-	0
Radiation chemistry	4	2	5	2	9	0	0	0	-	0
Basic technology	5	3	19	9	31	1	9	11	-	20
Others	3	0	0	1	1	1	0	0	-	0
total	43	20	52	51	123	20	65	59	-	124

Table 2. Utilization of TIARA in F.Y. 1992 at various relations with visitors.

Accelerators Relations with visitors		AVF Cyclotron					3MV Tandem Accelerator				
		No. of subject	Utilization time (days)				No. of subject	Utilization time (days)			
			1st.	2nd.	3rd.	total		1st.	2nd.	3rd.	total
JAERI only	Takasaki	7	12	12	14	38	7	31	29	-	60
	Others	5	3	3	1	7	0	0	0	-	0
Cooperative research with university		7	0	4	6	10	10	23	16	-	39
The JAERI-universities collaborative res.program		11	5	23	11	39	1	0	2	-	2
Joint research with private company or governmental institute		10	0	10	15	25	2	11	12	-	23
Cooperative research & Joint research		3	0	0	4	4	0	0	0	-	0
Visitors use with charges		0	0	0	0	0	0	0	0	-	0
Total		43	20	52	5	123	20	65	59	-	124

1 0 . 2 AVF CYCLOTRON

Ion Accelerator Operation Division Department of Advanced Radiation Technology

The JAERI AVF cyclotron is usually operated weekly. One year is divided into 3 beam-time periods, each of which consists of 11 weeks of beam-times and allocated by Program Advisory Committee, intervened by 3 weeks of maintenance and additional beam times and approximately 2 weeks of no cyclotron operation. The experiment plan and beam times allotted once for every period. The weekly operation is usually carried out continuously from Monday morning till Friday evening. Regular yearly overhaul was carried out for 4 weeks in the summer.

The operation for research experiments was started from January 1992 in daily operation mode on a trial basis. The weekly continuous operation was started from September 16 after the yearly overhaul. The total operating time for the FY 1991 and 1992 were 1578 and 2464 hours, respectively. Monthly operating hours for FY 1991 and 1992 are shown in Fig. 1. In FY 1991, the percentage of time used for acceptance tests, operation training and experiments were 71 %, 18 % and 11 %, respectively. The percentage of beam time for experiments was rapidly increased from 18 to 74.4 % in FY 1992. Figure 2 shows the percentage of beam time of accelerated ions for FY 1991 - 1992. Supplied ion species were H^+ , D^+ , $^4He^{2+}$, $^{40}Ar^{8+}$, $^{40}Ar^{11+}$, $^{40}Ar^{13+}$, $^{36}Ar^{8+}$, $^{36}Ar^{10+}$, $^{20}Ne^{6+}$ and $^{20}Ne^{7+}$. The beam time for light ions exceeded 50 % of all as shown in Fig. 2.

The main experiments were research and development on radiation resistant materials for space environment and for nuclear fusion reactor, biotechnology, new functional materials, radioisotope production and nuclear chemistry, radiation chemistry, and ion beam technology.

The accelerator and system troubles happened 341 times from April 1991 to March 1992. The machine troubles disturbed scarcely the scheduled operation.

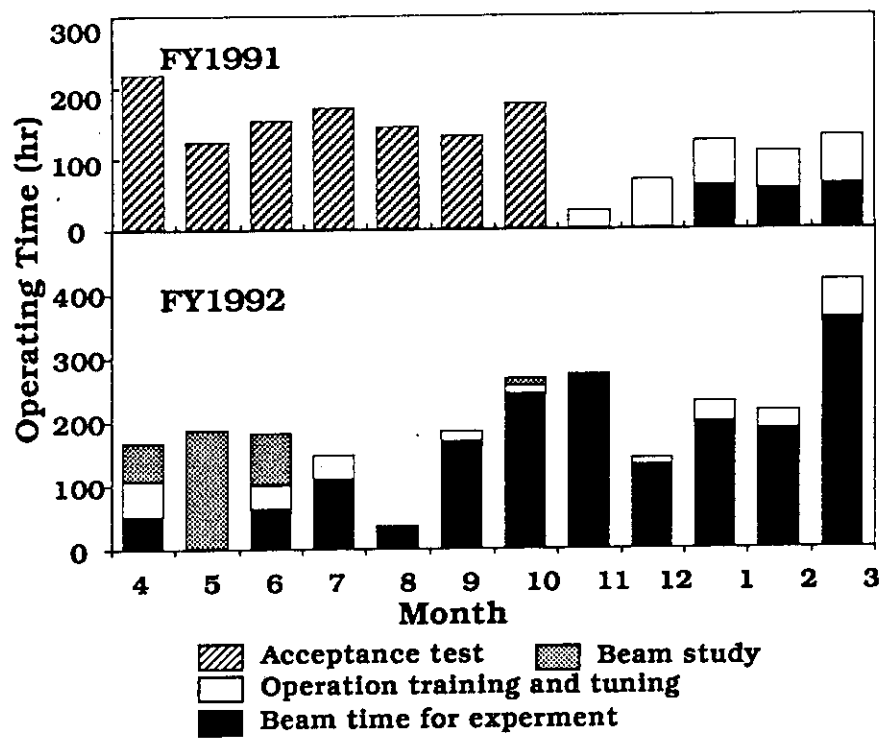


Fig.1 Monthly operation hours for FY 1991 and 1992.

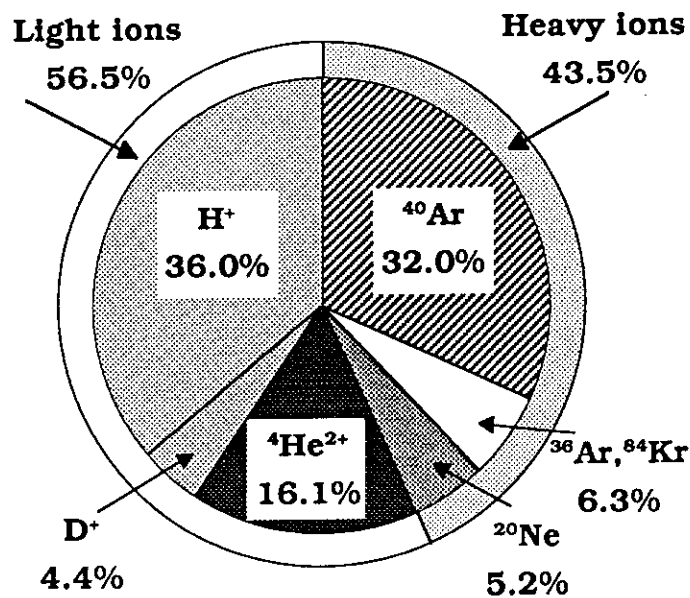


Fig.2 Percentage of beam time of accelerated ions for FY 1991 - 1992

1 0 . 3 Status of 3MV Tandem Accelerator and Second-Phase Accelerators Construction

Ion Accelerator Operation Division

Department of Advanced Radiation Technology

I. Introduction

The tandem accelerator was smoothly operated for experimental utilization from April to December 1992. It was temporarily stopped during the term from January to March 1993, to install two more beamlines providing the beams in the target room No.2.

The second-phase construction of two electrostatic accelerators, a 3MV single-ended accelerator and a 400kV ion implanter, started at Takasaki site from the beginning of February 1993.

II. Operation of the tandem accelerator

The operation time of the tandem accelerator for the two machine times (4-1 and 4-2) in FY 1992 was 1073 hours, and monthly operation times are shown in Fig.1. Fifteen kinds of ion species including eight new ions, ^3He , ^{15}Ni , Si, V, Fe, Cu, Ag and Ce, were provided for experiments. The accelerated particles and their relative beam time are also shown in Fig.2.

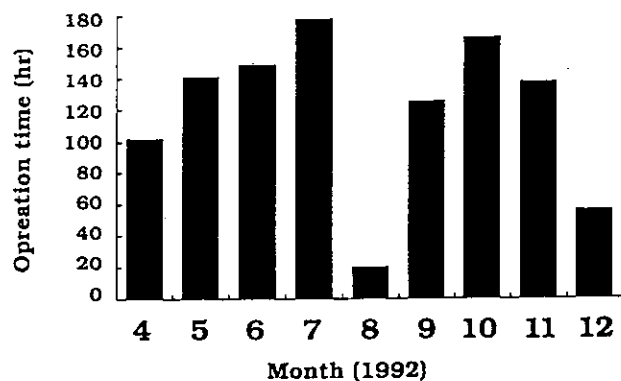


Fig.1 Monthly Operation Times in FY 1992.

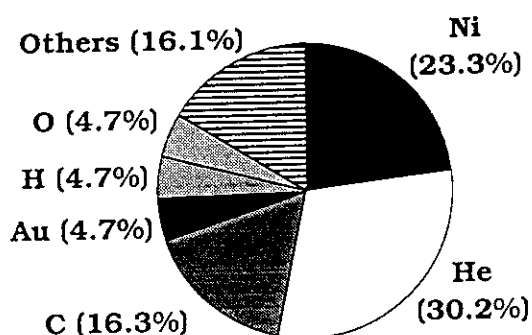


Fig.2 Accelerated Particles and Their Relative Beam Time.

The scheduled overhaul of the tandem accelerator with tank opening was carried out in August. We cleaned up the charging chains and some

high voltage structures and checked the vibration of the pellet chains and resistance value of all the tube grading resistors. The corona needles consumed with discharge were exchanged to new ones. Two ion sources, SNICS and ALPHATROSS, were cleaned up. And also we changed alkali metals, Cs for SNICS and Rb for ALPHATROSS, in the source ovens to new ones.

III. Second-Phase Accelerator Construction

The construction of the single-ended accelerator and the ion implanter has been started at Maebashi and Kuze(Kyoto) sites of Nissin Electric Co. from the beginning of 1992. To confirm the fundamental performances of the machines assembled factory tests were carried out at the both sites in the period of September for December, and passed. The accelerator vessel of the single-ended machine was carried into the Multiple Ion Beam Facility under construction before completion the accelerator room at the end of December 1992 (Fig.3). Alignment works were carried out to fix the setting positions of the accelerators and several magnets before installation of the accelerators and beamlines. The full-scale installation of two accelerators and beamlines started from the beginning of March 1993.

Extension of tandem beamlines, TD and TE, from the switching magnet in the accelerator room to the target room No.2 completed at the end of March by Hakuto(NEC) except the beam transport test.

IV. Summary

After some acceptance tests and a government inspection of the accelerators, the training operation and the accumulation of various operation data will be followed. The operation for experiments will start from September 1992 for the tandem accelerator and from January 1993 for other two.

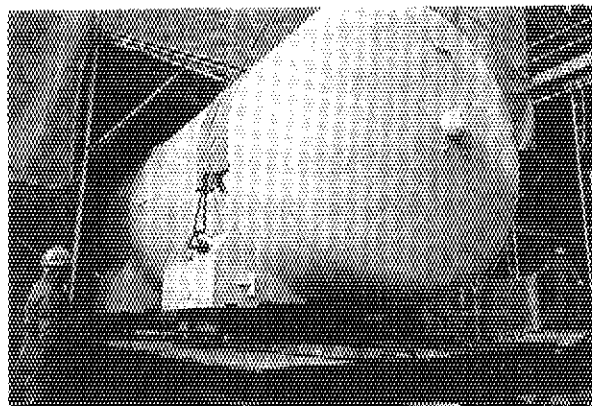


Fig. 3 Pressured Vessel of the Single-ended Accelerator Installed in TIARA Facilities in December 1992.

Reference

- 1) S.Tajima, I.Takada, K.Mizuhashi, Y.Saito, S.Uno, K.Okoshi, Y.Ishii, M.Ishii, K.Yotumoto, R.Tanaka, Proc. 5th Workshop on Tandem Accelerator and Technology, Tukuba(1992) p.15

1 0 . 4 RADIATION & RADIOACTIVE WASTE CONTROLS IN TIARA

Safety Division & Utilities and Maintenance Division,
Department of Administrative Services.

1. Radiation Control

1.1 Individual monitoring

(1) Individual monitoring for the radiation workers

Table 1 shows a distribution on effective dose equivalents of the radiation workers in fiscal 1992. All workers except two were less than 0.2 μSv (minimum detectable dose equivalent) and the two workers were both under 1 μSv who were exposed due to the routine maintenance of the cyclotron.

(2) Individual monitoring for the temporary entrance persons to the radiation controlled areas

Table 2 shows number of persons who have been entered the controlled areas temporally except the radiation workers registered officially. Individual monitoring for the temporary entrance persons was carried out with TLD and the every entrance person was less than minimum detectable dose.

1.2 Monitoring of released radioactivities for gas and dust

Table 3 shows the maximum radioactive concentrations and total activities for gas and dust released from TIARA's stack, during three months in fiscal 1992. The least amount of ^{41}Ar was detected for some time on the operation of the cyclotron, but the radioactive dust released was not detected.

1.3 Monitoring for radiation dose rate and surface contamination

Radiation dose rate monitoring was routinely carried out in/around the controlled areas and surface contamination monitoring was also carried out. No unusual measurement were detected in the same way. Fig. 1 displays a distribution of the dose rate at the controlled area in the cyclotron building as one sample.

1.4 Authorized radioisotopes

Table 4 (a) shows a list of sealed radioisotopes authorized at the end of fiscal 1992. These isotopes are used in TIARA as checking sources for several kinds of radiation detectors. Sixteen nuclides of unsealed type are also authorized mainly for researches of neutron shielding and RI production, as shown in Table 4 (b).

Table 1. Distributions on the effective dose equivalent in fiscal 1992.

Items \ Persons		number of persons			
		1st. quarter	2nd. quarter	3rd. quarter	4th. quarter
Distribution range on effective dose equivalent	HE < 0.2	104	156	177	230
	$0.2 \leq \text{HE} \leq 1.0$	0	1	0	1
	$1.0 < \text{HE} \leq 5.0$	0	0	0	0
	$5.0 < \text{HE} \leq 15.0$	0	0	0	0
	$15.0 < \text{HE} \leq 25.0$	0	0	0	0
	$25.0 < \text{HE} \leq 50.0$	0	0	0	0
	$50.0 < \text{HE}$	0	0	0	0
Persons for radiation control (A)		104	157	177	231
Exposure above 1 mSv	Persons (B)	0	0	0	0
	$(B)/(A) \times 100(\%)$	0	0	0	0
Mass effective dose equivalent (man mSv)		0.0	0.2	0.0	0.2
Mean dose equivalent (mSv)		0.0	0.0	0.0	0.0
Maximum dose equivalent (mSv)		0.0	0.2	0.0	0.2

Table 3. Monitoring results of released activities for gas and dust in fiscal 1992.

Nuclide	Items \ Periods		1st. quarter	2nd. quarter	3rd. quarter	4th. quarter	total
gross- β	dust (Bq/cm ³)	maximum concentration	$< 7.6 \times 10^{-11}$	$< 5.4 \times 10^{-11}$	$< 5.5 \times 10^{-11}$	$< 5.5 \times 10^{-11}$	-
⁶⁴ Cu*	dust (Bq/cm ³)	maximum concentration	$< 5.1 \times 10^{-8}$	$< 4.3 \times 10^{-8}$	-	-	-
	Total released activity(Bq)		0	0	-	-	0
⁶⁵ Zn*	dust (Bq/cm ³)	maximum concentration	-	$< 3.9 \times 10^{-10}$	$< 4.6 \times 10^{-10}$	$< 3.9 \times 10^{-10}$	-
	Total released activity(Bq)		-	0	0	0	0
⁴¹ Ar	gaseous (Bq/cm ³)	maximum concentration	$< 1.1 \times 10^{-4}$	$< 1.1 \times 10^{-4}$	$< 7.1 \times 10^{-5}$	$< 7.1 \times 10^{-5}$	-
	Total released activity(Bq)		7.7×10^7	0	1.1×10^9	3.5×10^8	1.5×10^9

*Noted nuclide was changed from ⁶⁴Cu to ⁶⁵Zn since August '92.

Table 4. List of radioisotopes authorized at the end of fiscal 1992 in TIARA.

(a) Sealed radioisotopes

Authorization No. and Date	Nuclides and amounts	Places used	Places of Storage
No.3469 Aug. 30, '91	^{241}Am 3.7GBq \times 1	Cyclotron building light ion room 1 to 3, heavy ion room 1 to 3, cyclotron vault, light ion and heavy ion preparation rooms, heavy ion measuring room. Multiple beam building target room 1, tandem accelerator room	Cyclotron building
	^{57}Co 370MBq \times 4 $^{119\text{m}}\text{Sn}$ 370MBq \times 4	Cyclotron building ISOL room Ion beam research building hot physical laboratory	Cyclotron building RI storage box in ISOL room

(b) Unsealed radioisotopes

Authorization No. and Date	Places used	Amounts of annual use
No. 5349 Nov. 6, '92	Cyclotron building	^{54}Mn 50MBq
	light ion rooms 1 to 3	^{65}Zn 1GBq
	cyclotron vault	^{56}Co 1GBq
	cyclotron pit room	^{55}Fe 500MBq
	switching magnet room	^7Be 1GBq
	cooling room	^{75}Se 200MBq
	power distribution room	$^{95\text{m}}\text{Tc}$ 200MBq
	hot work room	^{139}Ce 600MBq
	hot laboratory	^{11}C 4GBq
	semi-hot laboratory	^{13}N 4GBq
	RI measuring room	^{15}O 4GBq
	ISOL room	^{52}Fe 200MBq
	Ion beam research building	^{61}Cu 200MBq
	radiation measuring room	^{133}Xe 300MBq
	hot physical laboratory	^{186}Re 600MBq
	hot work room	^{18}F 4GBq
	hot chemical laboratories 1 to 2	

2. Radioactive wastes control

2.1 Solid wastes

Table 5 shows the amounts of solid wastes at various properties and kinds generated in each quarter of fiscal 1992. Main wastes were combustible matter such as globes and incombustible filters for exhaust air. Compressible wastes were generated mainly by the cyclotron maintenance.

2.2 Liquid waste

Liquid waste were almost waste water ('inorganic' in Table 6) generated with chemical experiments and with using air conditioning units installed in each room of the first class radiation controlled area. Larger quantity of the waste water in summer season (2nd. quarter) are due to mainly condensed drain from air by operating the units.

Low level waste water is treated by evaporation and condensed water is reused in the controlled area. Small amounts of residue are generated by evaporation because the radiation level is very low and the waste quantity is very pure so that the waste can be evaporated to high concentration rate.

The evaporation residue is solidified by cement in a stainless steel drum. The residue of ca. 100 liter makes one cement solidify of 200 liter drum.

Table 5. Radioactive solid waste generated in F.Y. 1992.

Items	Amounts of generation in each periods (m ³)					number of package/drum
	1st. quarter	2nd. quarter	3rd. quarter	4th. quarter	total	
Low level	0.14	1.73	0.20	1.14	3.21	
1) Combustible	0.14	0.50	0.20	0.82	1.66	11*
2) Incombustible	0	1.23	0	0.32	1.55	
Compressible	0	0.04	0	0.02	0.06	
Filters	0	1.19	0	0	1.19	11
Incompressible	0	0	0	0	0.00	
Ion exchange resin	0	0	0	0	0.00	
Cement solidify	0	0	0	0.30	0.30	3*
High level	0	0	0	0	0	0
1) Incombustible	0	0	0	0	0	0

*: 200 liter drum

Table 6. Radioactive liquid waste generated in F.Y. 1992.

Items	Amounts of generation in each period (m ³)					number of package/drum
	1st. quarter	2nd. quarter	3rd. quarter	4th. quarter	total	
Low level	9.75	24.77	11.48	4.01	50.01	
1) Inorganic	9.75	24.73	11.48	4.00	49.96	treatment
2) Organic	0	0.04	0	0	0.05	carry over
Organic	0	0	0	0	0	0
Oil	0	0.04	0	0	0.04	carry over
Sludge	0	0	0	0.01	0.01	*
Medium level	0	0.01	0	0	0.01	
1) Inorganic	0	0.01	0	0	0.01	carry over
2) Organic	0	0	0	0	0	
Organic	0	0	0	0	0	
Oil	0	0	0	0	0	
Sludge	0	0	0	0	0	
Evaporation residue	0.01	0	0	0.08	0.09	*

*: treated to cement solidify

Appendix

Appendix 1. List of Publications	253
A1.1 Publications in Journal	253
A1.2 Publications in Proceedings	255
Appendix 2. Type of Research Collaborations	259
Appendix 3. Organization and Personnel of TIARA	260

Appendix 1. List of Publications

A1.1. Publications in Journal

1. S.Furuno, K.Hojou, K.Izui, N.Kamigaki, K.Ono and T.Kino,
In situ observation of structural changes in aluminum during He⁺ and
H₂⁺ dual-ion beam irradiation
J. Nucl. Mater., 191-194 (1992) 1219.
O
2. S.Furuno, K.Hojou, H.Otsu, K.Izui, T.A.Sasaki, T.Tsukamoto and T.Hata,
System for in situ observation and chemical analysis of materials during
dual-ion beam radiation in an electron microscope
J. Electron Microsc., 41 (1992) 273.
O
3. T.Futagami, Y.Aoki, O.Yoda, S.Nagai and D.M.Rück,
XPS studies on the charge states of Cr and Cu atoms implanted into
 α -Al₂O₃ and MgO single crystals
Nucl. Instrum. Methods Phys. Res., Sect. B 80/81 (1993) 1168.
O
4. K.Hojou, S.Furuno, K.N.Kushita, H.Otsu and K.Izui,
In situ observation of damage evolution in SiC crystals during helium
and hydrogen dual-ion beam irradiation
J. Nucl. Mater., 191-194 (1992) 538.
O
5. T.Kamiya and R.Tanaka,
JAERI high energy, heavy ion microprobe system and single ion hit
technique
Nucl. Instrum. Methods Phys. Res., Sect. B 79 (1993) 432
T

6. H.Kudo, K.Shima and T.Ishihara
Secondary electrons induced by fast ions under channeling conditions.
III. Unshadowed electron in target crystal
Phys. Rev., B 47 (1993) 27.
O
7. H.Kudo, E.Yoshida, K.Shima, Y.Nagashima and T.Ishihara
Shadowing pattern imaging with high-energy secondary electrons induced
by fast ions
Jpn. J. Appl. Phys. 31 (1992) L1284.
O
8. T.Okamura, T.Murakami, T.Agematsu, S.Okumura and K.Arakawa,
A visual assistance environment for cyclotron operation
Transactions of the Society of Instrument and Control Engineers 29
(1993) 102.
C
9. O.Yoda, A.Miyashita, K.Murakami, T.Ohyanagi, S.Aoki and N.Yamaguchi,
A laboratory scale apparatus for the time resolved X-ray absorption
spectroscopy using laser plasma as an X-ray source
Jpn. J. Appl. Phys. Suppl. 32-2 (1993) 255.
O
10. O.Yoda, A.Miyashita, T.Ohyanagi and K.Murakami,
Dynamic behaviors of fragments ejected from the surface of carbon
materials by laser ablation
JAERI-M 92-173 (1992).
O

A1.2. Publications in Proceedings

1. K.Arakawa, Y.Nakamura, W.Yokota, M.Fukuda, T.Nara, T.Agematsu,
S.Okumura, I.Ishibori, T.Karasawa, R.Tanaka, A.Shimizu, T.Tachikawa,
Y.Hayashi, K.Ishii and T.Satoh,
Construction and first year's operation of the JAERI AVF cyclotron
Proc. of the International Conference on Cyclotron and Their
Applications (Vancouver, July 6-10, 1991) p.119.
C
2. M.Fukuda, K.Arakawa, Y.Nakamura, W.Yokota, T.Nara, T.Agematsu,
S.Okumura, I.Ishibori and T.Karasawa,
Beam studies of injection to extraction system for JAERI AVF cyclotron
Proc. of the International Conference on Cyclotron and Their
Applications (Vancouver, July 6-10, 1991) p.423.
C
3. K.Harada, R.Kimura, M.Nakachi, S.Oda, M.Kawashima, T.Miki, H.Watanabe,
S.Tano and S.Inaba,
Inhibition by α -particle for cell recovery in *Deinococcus radiodurans*
- Preliminary experiment on earth for the IML-2 Project - (in Japanese)
Proc. of the 8th Space Utilization Symposium
(Tokyo, July 8-9, 1991) p.140.
O
4. K.Harada, R.Kimura, S.Oda, M.Kawashima, T.Miki, N.Mizuma, H.Maki,
M.Saito, H.Watanabe and S.Tano,
Synergistic killing effect of alpha particle beam and hyperthermia on
Deinococcus radiodurans
Proc. of the International Conference on Evolution in Beam Applications
(Takasaki, Nov. 5-8, 1991) p.593.
O

5. M.Inoue and A.Nakamura,
Interspecific hybridization in *Nicotiana*, using radiation-irradiated pollen
Proc. of Symposium on Wide Crosses in Plants and Utilization of Cell and Tissue Culture (Univ. Tokyo, Aug. 27, 1993) p.17.
T
6. M.Inoue, H.Watanabe, A.Tanaka and A.Nakamura,
Effects of ion beam exposure to tobacco pollen
Proc., 83rd Meeting of the Japanese Society of Breeding (Tokyo, April 2, 1993), Japn. J. Breed. 43, Suppl. 1 (1993) 61.
T
7. T.Kamiya, H.Yutoh and R.Tanaka,
JAERI heavy ion microbeam system and single ion hit technique
Proc. of The 1st Meeting the Ion Engineering Society of Japan (Tokyo, June 1-3, 1992) p.105
T
8. T.Kamiya, H.Yutoh and R.Tanaka,
Single ion hit system in heavy ion microbeam apparatus
Proc. of The 3rd Symposium on Beam Engineering of Advanced Material Synthesis (Tokyo, Nov. 24-26, 1992) p.453
T
9. H.Kudo, K.Shima, T.Ishihara, H.Takeshita, Y.Aoki, S.Yamamoto and H.Naramoto,
High-energy shadowing effect and its application to atomic and solid state physics
Proc. of the 15th International Conference on Atomic Collisions in Solids (Ontario, July 26-30, 1993).
T

10. Y.Kumata, Y.Fukumoto, M.Fukuda, K.Arakawa, T.Karasawa and A.Shimizu,
A modified rf system of JAERI AVF cyclotron
Proc. of the International Conference on Cyclotron and Their
Applications (Vancouver, July 6-10, 1991) p.526.
C
11. K.Murakami, T.Ohyanagi, A.Miyashita and O.Yoda,
Laser-plasma soft X-ray absorption spectroscopy of laser-ablated Si
and C particles
Proc. 2nd International Conference on Laser Ablation
(Oak Ridge, April 12-16, 1993).
O
12. S.Nagai,
Deposition of thin carbon films by low energy ion beam
Proc. of the 40th Spring Meeting, the Japan Society of Applied Physics
and Related Societies (Tokyo, Mar. 29 - Apr. 1, 1993) p.1341
O
13. H.Ohno and S.Nagai,
Growth of thin films by low energy ion beam deposition
Proc. of The 3rd Symposium on Beam Engineering of Advanced Material
Synthesis (Tokyo, Nov. 24-26, 1992) p.261
O
14. T.Okamura, T.Murakami, T.Tachikawa, T.Agematsu, S.Okumura and K.Arakawa,
An operator assistance system for JAERI AVF cyclotron
Proc. of the International Conference on Cyclotron and Their
Applications (Vancouver, July 6-10, 1991) p.644.
C

15. S.Okumura, T.Agematsu, W.Yokota, T.Kamiya, M.Fukuda, Y.Nakamura, T.Nara, I.Ishibori, K.Arakawa, M.Maruyama, K.Iso, K.Hoshika and M.Tachibana,
Control system for JAERI AVF cyclotron
Proc. of the International Conference on Cyclotron and Their
Applications (Vancouver, July 6-10, 1991) p.648.

C

16. T.Sekine, M.Koizumi, A.Osa and S.Ichikawa,
Status report of the TIARA-ISOL in JAERI/Takasaki
Proc. of the Specialist Research Meeting on the Nuclear Physics and
Solid State Physics by a Radioactive Nuclear Beam (Mumatori, March 23-
24, 1993) p.19.

O

17. A.Tanaka, H.Watanabe, R.Nozaawa, Q.Hu and S.Kitayama
Characterization of radiation-induced proteins in *Deinococcus*
radiodurans
Proc. of the International Conference on Radiation Effects and
Protection (Mito, March 18-20, 1992) p.160.

O

18. W.Yokota, M.Fukuda, K.Arakawa, Y.Nakamura, T.Nara, T.Agematsu,
S.Okumura, I.Ishibori, T.Tachikawa, Y.Hayashi and Y.Kumata
Performance and beam chopping system for JAERI AVF cyclotron
Proc. of the International Conference on Cyclotron and Their
Applications (Vancouver, July 6-10, 1991) p.581.

C

19. W.Yokota, T.Nara, K.Arakawa, Y.Nakamura, M.Fukuda, T.Agematsu,
S.Okumura, I.Ishibori, T.Tachikawa, Y.Hayashi and K.Ishii
Operation of ion source and beam transport to JAERI AVF cyclotron
Proc. of the International Conference on Cyclotron and Their
Applications (Vancouver, July 6-10, 1991) p.336.

C

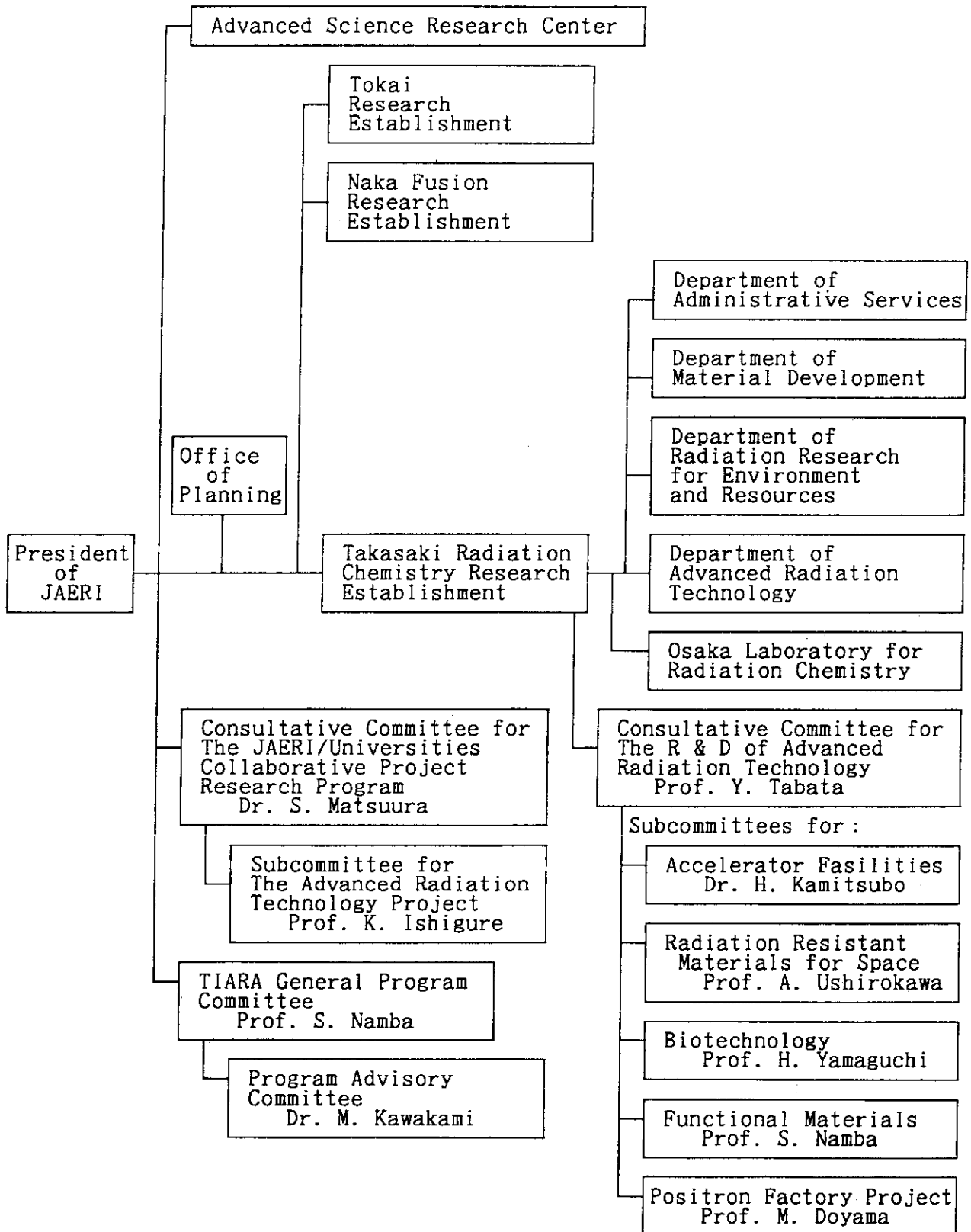
Appendix 2. Type of Research Collaborations

Section of this Report	Research Program Number	Type of Research Collaborations*	Section of this Report	Research Program Number	Type of Research Collaborations*
1.1	#21002	(JAERI)	5.1	#22012	(JAERI)
1.2	#21001	Joint Research	5.2	#21012	(JAERI)
1.3	#22001	Joint Research	5.3	#21026	(JAERI)
1.4	#21010	Joint Research	5.4	#22008	Coop.Res.Univ.
1.5	#21010	Joint Research	5.5	#22010	Coop.Res.Univ.
1.6	#21008	Joint Research	5.6	#22003	Joint Research
2.1	#22005	(JAERI)	5.7	#22007	Coll.Proj.Res.
2.2	#21020	(JAERI)	6.1	#22013, #22014	(JAERI)
2.3	#21016	(JAERI)	6.2	#22011	(JAERI)
2.4	#21018	Coll.Proj.Res.	6.3	#22017	Coop.Res.Univ.
2.5	#21040	Coll.Proj.Res.	6.4	#22018	Coop.Res.Univ.
2.6	#21013	Coll.Proj.Res.	6.5	#21003	(JAERI)
2.7	#21021, #22006	Coop.Res.Univ.	6.6	#21027	Coll.Proj.Res.
2.8	#21017	Coop.Res.Univ.	6.7	#22009	(JAERI)
2.9	#21014, #22004	Coop.Res.Univ.	6.8	—	(JAERI)
2.10	#21019	Joint Research	6.9	#21024	Coop.Res.Univ. /Intern. Coop.
2.11	#21039	Joint Research	6.10	—	Coop.Res.Univ.
3.1	#21029	(JAERI)	7.1	#21035	Coll.Proj.Res.
3.2	#21037	Joint Research /Coll.Proj.Res.	7.2	#21034	(JAERI)
3.3	#21038	Coll.Proj.Res.	8.1	#22016	(JAERI)
4.1	#21004 #21005 #21031, #21033	(JAERI) Joint Research Coll.Proj.Res.	8.2	#21028	Coll.Proj.Res.
4.2	#21022, #21023	(JAERI)	8.3	#21041	Joint Research
4.3	#21009	Joint Research	8.4	#21042	Joint Research
			8.5 ~ 8.14	—	(JAERI)
			9.1 ~ 9.4	—	(JAERI)

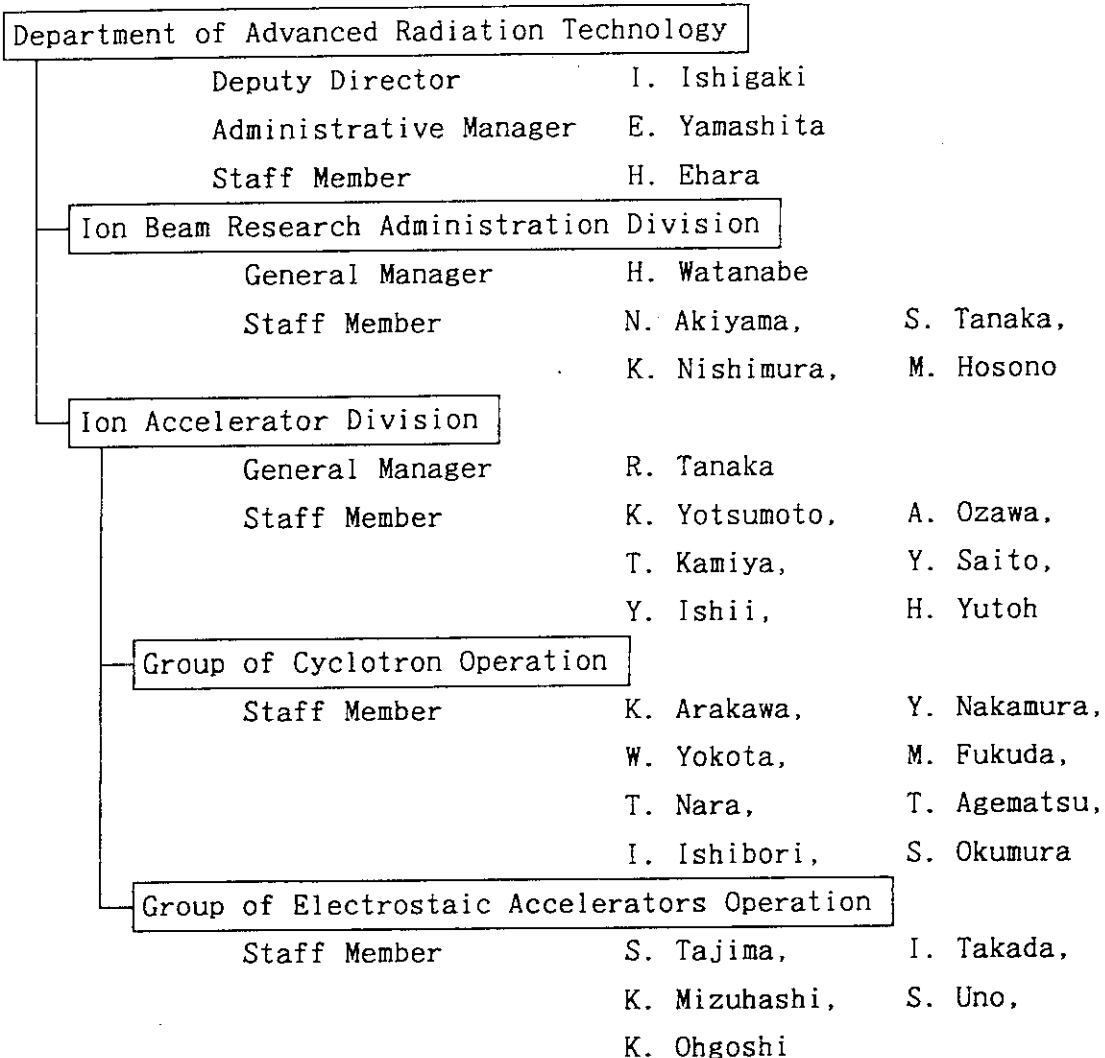
- * Joint Research : Joint research with private company or governmental institution
- Coop.Res.Univ. : Cooperative research with university
- Coll.Proj.Res. : The JAERI-universities collaborative project research program
- Intern. Coop. : International cooperation programs

Appendix 3. Organization and Personnel of TIARA (F.Y. 1992)

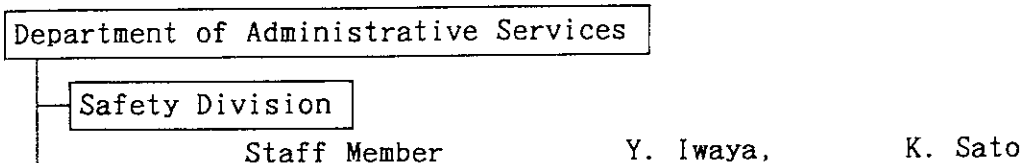
1) Organization for the Research and Development of Advanced Radiation Technology



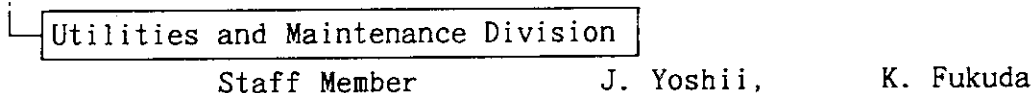
2) Administration and Operation of TIARA *



2) Radiation Monitoring and Control at TIARA



3) Radioactive Waste Treatment and Disposal at TIARA



* for information, contact to : —

Department of Advanced Radiation Technology, Takasaki Radiation Chemistry
Research Establishment, Japan Atomic Energy Research Institute
1233 Wakanuki-machi, Takasaki, Gunma-ken, 370-12, Japan.

Tel. : (81)273-46-9600 ~3; Facsimile : (81)273-46-9690